NORTHWESTERN UNIVERSITY

# Control and Coherence of Next-Generation Superconducting Qubits

A DISSERTATION

SUBMITTED TO THE GRADUATE SCHOOL
IN PARTIAL FULFILLMENT OF THE REQUIREMENTS

for the degree

DOCTOR OF PHILOSOPHY

Department of Physics and Astronomy

By

Daniel Kamrath Weiss

EVANSTON, ILLINOIS

August, 2022

# Abstract

Superconducting-circuit based platforms are strong contenders in the race to build a quantum computer. While the transmon has had extraordinary success as the leading superconducting qubit modality, there are reasons to believe that other types of qubits could possess relative benefits in terms of noise immunity, anharmonicity, or extensibility. In this thesis we explore multiple such next-generation superconducting circuits, focusing specifically on the current mirror and the fluxonium. Kitaev in 2006 proposed the current-mirror circuit, a type of superconducting qubit that should be protected from all types of local noise and could thus possess enhanced coherence times. We explore the spectrum and coherence properties of this device, while also developing numerical methods useful for studying other types of large superconducting circuits. Meanwhile, the highly-anharmonic fluxonium qubit has been shown experimentally to have coherence times competitive with or better than state-of-the-art transmons. Motivated by these results we explore a galvanic-coupling scheme for fluxonium qubits and utilize a framework going beyond typical rotating-wave approximation treatments to perform high-fidelity gates.

# Acknowledgements

First I would like to thank my advisor, Jens Koch. Jens has impressed upon me the necessity as a researcher of owning everything you do: it is never enough to repeat a statement someone else has made without fully understanding it yourself. I learned this from many fruitful discussions with Jens as he probed (and often exceeded) the boundaries of my knowledge. The most important skill Jens taught me is the ability to write a scientific paper and logically communicate an idea. Writing has never been my strong suit and I am a slow learner, so he taught me these lessons three times. I am grateful for it.

I would also like to thank David Ferguson, who was a big part of the first two projects in my PhD and graciously agreed to serve on my committee. His intellect is matched only by his enthusiasm, and I was lucky to get the chance to collaborate with him. I enjoyed the summer I spent with him at Northrop Grumman, where I benefited also from collaborations with Wade DeGottardi and Moe Khalil. I am also grateful to Prof. Andy Geraci for serving on my committee and providing experimental grounding to the proceedings.

In my five years at Northwestern I have been fortunate to follow in the footsteps of many kind and inspiring physicists. Andy Li got the current-mirror project off the ground and entertained many stupid questions from a curious first-year student. I am grateful also for many insightful conversations with Peter Groszkowski. I was fortunate to have Ziwen Huang and Xinyuan You with me for four of my years at Northwestern, and they both were always willing to share knowledge and advice. Sai Pavan Chitta and Yunwei Lu have quickly transitioned from trainees into colleagues, and I benefited from discussions with both of them in our office. I enjoyed collaborating with Matthew Capocci on a project near the end of my PhD, and I look forward to seeing where he takes it. Thanks also to other group members and the wider condensed matter theory community at Northwestern, including Ian Mondragon-Shem, Vinh San Dinh, Brian Baker, Wei-Ting Lin, Robert Regan, Tianpu

Zhou, Danyang Chen, Sandeep Joshi, Joey Yaker and Jason He. All of you helped make my time here productive and enjoyable. Special thanks also to Max Hays who generously allowed me to use his LaTeX template.

A wonderful benefit to working in the Koch group is the near limitless opportunities to collaborate with experimentalists, especially in Dave Schuster's (University of Chicago) and Andrew Houck's (Princeton University) labs. Both Dave and Andrew were generous with their time and advice and I enjoyed getting to work with them and their students. Helin Zhang and I have by now collaborated on multiple Schusterlab fluxonium projects together, and I am always amazed at his physical intuition for problems. To obtain the same level of intuition I would typically need to carry out a lengthy calculation, but he just does it in his head. Thanks also to Chunyang Ding and Yuwei Ma, who shared many experimental and theoretical insights during our collaboration on the two-qubit fluxonium gate project. From the Houcklab, I was lucky to work closely with Jake Bryon, who taught me the value of perseverance in the face of every possible problem a dilution refrigerator could throw your way. I would like to thank my additional Houcklab collaborators who I perhaps spent less time with but who were no less impactful, including Anjali Premkumar, Xanthe Croot and Sara Sussman.

I would like to thank my parents Leisha Self and Jeff Weiss, who made it possible for me to pursue this life as a theoretical physicist. They never once questioned my crazy decision and supported me every step of the way. I would certainly not be here without them. I would also like to thank my siblings, Abby Weiss, Tali Weiss and Aaron Weiss. I feel that we are only growing closer as time goes by and I am thankful for their love and companionship.

Finally I would like to thank my fiancé, Grace Carroll. Words cannot describe the joy I feel coming home to you every day. You celebrated with me during the highest highs and held me through the lowest lows of the PhD journey, and I am certain that this thesis would not exist without you. I can't wait to marry you.

# List of Publications

Chapters 3 and 6 are based largely upon work published in

> Daniel K. Weiss, Wade DeGottardi, Jens Koch, and David G. Ferguson, "Variational tight-binding method for simulating large superconducting circuits", Phys. Rev. Research **3**, 033244 (2021).

Chapters 4 and 7 are based on the preprint (submitted to PRX Quantum)

> Daniel K. Weiss, Helin Zhang, Chunyang Ding, Yuwei Ma, David I. Schuster, and Jens Koch, "Fast high-fidelity gates for galvanically-coupled fluxonium qubits using strong flux modulation", arXiv:2207.03971 (2022).

Chapter 5 and Appendix B are based upon the publication

> Daniel K. Weiss, Andy C. Y. Li, David G. Ferguson, and Jens Koch, "Spectrum and coherence properties of the current-mirror qubit", Phys. Rev. B **100**, 224507 (2019). (Editor's Suggestion)

Additionally, the author contributed theoretical support to the following publication and preprint that were both primarily experimental works and thus are not described extensively in this thesis:

> Helin Zhang, Srivatsan Chakram, Tanay Roy, Nathan Earnest, Yao Lu, Ziwen Huang, Daniel K. Weiss, Jens Koch, and David I. Schuster, "Universal fast-flux control of a coherent, low-frequency qubit", Phys. Rev. X **11**, 011010 (2021).

> Jacob Bryon, Daniel K. Weiss, Xinyuan You, Sara Sussman, Xanthe Croot, Ziwen Huang, Jens Koch, and Andrew Houck, "Experimental verification of the treatment of time-dependent flux in circuit quantization", arXiv:2208.03738 (2022).

The publication by Zhang *et al.* presented experimental results for high-fidelity non-adiabatic gates on a low-frequency and high-coherence fluxonium qubit. D. K. Weiss contributed to the calculation of coherence times, as well as the calculation of matrix elements in the combined fluxonium and resonator system. The preprint from Bryon *et al.* presents experimental results on the correct treatment of time-dependent flux in the context of superconducting circuits. D. K. Weiss performed the bulk of the theoretical analysis and contributed significantly to the writing and editing of the manuscript.

# List of Symbols

| | |
|---|---|
| $a_\mu^\dagger, a_\mu$ | Bosonic creation and annihilation operators associated with a mode $\mu$, obeying the commutation relations $[a_\mu, a_\nu^\dagger] = \delta_{\mu\nu}$ |
| $A$ | Amplitude associated with a drive |
| $B_n$ | Bernoulli numbers |
| CPB | Cooper-pair box |
| $C$ | Capacitance |
| C | Capacitance matrix |
| DMRG | Density-matrix renormalization group |
| $d$ | Hilbert space dimension |
| $e$ | Magnitude of the charge of a single electron |
| $E_C$ | Charging energy associated with a capacitance $C$, $E_C = e^2/(2C)$ |
| $\mathsf{E_C}$ | Charging-energy matrix |
| $E_J$ | Energy associated with a Josephson junction, $E_J = \hbar I_c/(2e)$ |
| $E_L$ | Inductive energy associated with an inductance $L$, $E_L = \Phi_0^2/(2L)$ |
| $E_n, E_{nm}$ | Energy associated with the state $\|n\rangle$ and the energy difference $E_{nm} = E_n - E_m = \hbar\omega_{nm}$ |

| | |
|---|---|
| $h$, $\hbar$ | Planck constant and its reduced version |
| H. c. | Hermitian conjugate |
| $H_0$ | Bare Hamiltonian |
| $H_{\text{eff},n}$ | Effective Hamiltonian at $n^{\text{th}}$ order in perturbation theory obtained using a Schrieffer-Wolff transformation |
| *I* | Shorthand for the 2x2 identity matrix |
| $I_c$ | Critical current associated with a Josephson junction |
| IPAC | Scheme for constructing tight-binding states: improper with anharmonicity correction |
| $J_0$ | Zeroth-order Bessel function of the first kind |
| $k_B$ | Boltzmann constant |
| $\mathcal{L}$ | Lagrangian |
| $\ell_{mm'}$ | Effective harmonic length along the unit vector $\hat{u}_{mm'}$ separating two minima indexed by $m$ and $m'$ |
| $M$ | Number of minima in a single unit cell |
| $N$ | Number of big capacitors in the current-mirror circuit |
| $\mathcal{N}$ | Number of unit cells |
| $N_d$ | Number of degrees of freedom in an arbitrary circuit |
| NISQ | Noisy intermediate-scale quantum |
| $n, n_i$ | Charge-number operator, and the charge-number operator associated with node $i$ |

| | |
|---|---|
| $n_{\text{cut}}$ | Charge-basis cutoff |
| $n_g, n_{gi}$ | Offset charge, and offset charge on a particular node $i$ |
| $n_H$ | Number of nonzero Hamiltonian matrix elements |
| $P$ | Projector, typically onto a low-energy subspace |
| PAC | Scheme for constructing tight-binding states: proper with anharmonicity correction |
| $Q$ | Projector, typically onto a high-energy subspace |
| $Q_{\text{cap}}$ | Quality factor of a capacitor |
| RSA | Acronym for Rivest-Shamir-Adleman, the inventors of the RSA cryptosystem |
| RWA | Rotating-wave approximation |
| $S$ | Generator of a Schrieffer-Wolff transformation |
| $S(\omega)$ | Noise-spectral density $S(\omega) = \int_{-\infty}^{\infty} e^{i\omega t} dt \langle \delta\lambda(t)\delta\lambda(0)\rangle$ |
| $\mathcal{S}$ | Squeezing operator |
| $s_{\text{max}}$ | Excitation number cutoff |
| $T$ | Temperature |
| $T_1$ | Relaxation or depolarization time |
| $T_\phi$ | Pure-dephasing time |
| $T_2$ | Overall dephasing time $1/T_2 = 1/2T_1 + 1/T_\phi$ |
| $\mathcal{T}$ | Translation operator |

| | |
|---|---|
| $V$ | Perturbing Hamiltonian |
| $X$ | Shorthand for the Pauli matrix $\sigma_x$ |
| $Y$ | Shorthand for the Pauli matrix $\sigma_y$ |
| $Z$ | Shorthand for the Pauli matrix $\sigma_z$ |
| $\Gamma^{(m)}$ | Inverse inductance matrix associated with the $m^{\text{th}}$ minimum |
| $\Gamma_1, \Gamma_2, \Gamma_\varphi$ | Depolarization, dephasing and pure-dephasing rates |
| $\delta\lambda(t)$ | Amplitude of a classical noise source |
| $\eta_{\text{avg}}$ | Average relative deviation |
| $\eta_{\text{min,max}}$ | Minimum and maximum relative deviations, respectively |
| $\Xi$ | Normal-mode matrix |
| $\rho$ | Density matrix |
| $\Sigma_{\text{max}}$ | Global excitation number cutoff (maximum Manhattan length of an excitation number vector) |
| $\sigma_x, \sigma_y, \sigma_z$ | Standard Pauli matrices |
| $\Phi_0$, $\phi_0$ | Superconducting flux quantum $\Phi_0 = h/2e$ and its reduced version $\phi_0 = \hbar/2e = \Phi_0/2\pi$ |
| $\phi, \phi_i$ | Node variable, and node variable associated with site $i$ |
| $\phi_{\text{ext}}$ | Reduced external flux $\phi_{\text{ext}} = 2\pi\Phi_{\text{ext}}/\Phi_0$ |
| $\omega$ | Frequency (in units of radians) |
| $\omega_\mu$ | Frequency of system $\mu$ |

| | |
|---|---|
| $\omega_{ij}$ | Frequency associated with the transition between states $\|i\rangle$ and $\|j\rangle$, $\omega_{ij} = E_{ij}/\overline{h}$ |
| $\mathbb{1}$ | Identity operator |
| :: | Normal-ordering symbol |
| $\langle \cdots \rangle$ | Ensemble average over the enclosed quantity |
| $\|0\rangle, \|1\rangle$ | Qubit ground and first-excited states given in Dirac notation |
| $\|n\rangle$ | The $n^{\text{th}}$ excited state of a system in Dirac notation |

To avoid excessive use of subscripts and superscripts, in Chapter 7 we use slightly modified notation from that described above, specifically for node variables and external fluxes.

| | |
|---|---|
| $\varphi_i$ | Node variable associated with site $i$ |
| $\phi_i$ | Reduced external flux through the $i^{\text{th}}$ loop |

*To my family*

# Contents

# List of Tables

# List of Figures

# 1 Introduction

The field of quantum information and computation has grown in leaps and bounds since its inception in the 1980s and 1990s. Benioff in 1980 first considered the interaction between quantum mechanics and computation [1]. This was followed by Feynman in 1981 who famously proposed using a quantum computer to efficiently simulate nature, precisely because nature itself is quantum mechanical [2]. Interest exploded in 1994 when Peter Shor published his eponymous algorithm for factoring integers in polynomial time on a hypothetical quantum computer [3, 4]. The fastest-known classical factoring algorithm takes super-polynomial time [5]. As such the believed hardness of the problem of factorization is the basis of the widely used RSA cryptosystem [6]. If successfully implemented on a quantum computer of sufficient size, Shor's algorithm breaks RSA. There now exist a number of quantum algorithms that provide speedup over known classical counterparts, including Grover's search algorithm [7] and algorithms for simulating chemical reactions [8]. An exhaustive list can be found in the "Quantum Algorithm Zoo" [9].

Researchers are actively investigating a multitude of physical platforms to serve as the building blocks of a quantum computer, including trapped ions [10], neutral atoms [11], nitrogen-vacancy centers in diamond [12], and superconducting circuits [13, 14]. In this dissertation we will focus only on superconducting circuits. This platform holds great promise for realizing a quantum computer, owing in part to the large coupling strengths that are achievable [15] (leading to fast gate times), in-situ tunability [14] and existing advanced fabrication and lithography techniques [16]. A downside of strong coupling is that the interaction with the environment is correspondingly strong. As such, superconducting qubits generally suffer from relatively short coherence times as compared to, e.g., trapped ion qubits [10, 13]. However, as we will discuss below, researchers have made extraordinary progress in recent years in improving the coherence times of superconducting qubits.

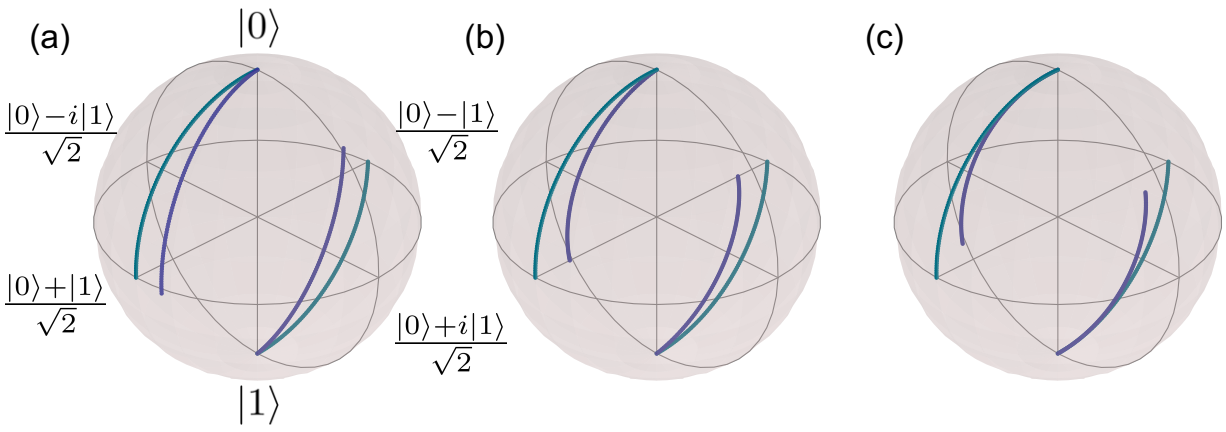


**Figure 1.1:** Degradation of gate fidelities under decoherence and imperfect control. An $X/2$ gate maps the state $|0\rangle$ or $|1\rangle$ to $\frac{1}{\sqrt{2}}(|0\rangle + |1\rangle)$ or $\frac{1}{\sqrt{2}}(|0\rangle - |1\rangle)$, respectively (green trajectories). (a) An imperfect implementation of the $X/2$ gate with a small amount of rotation along the *Y* axis (blue trajectories). (b-c) Implementations of the $X/2$ gate without any unwanted $Y$ rotation but in the presence of (b) depolarization and (c) pure dephasing (blue trajectories). In all three cases, gate fidelities are less than unity.

Especially in the current noisy intermediate-scale quantum (NISQ) era [17], improving coherence times and gate fidelities is critical for increasing the circuit depth, i.e., the number of consecutive quantum gates in a computation [18]. Looking further afield, quantum algorithms require implementation on a quantum computer that is *fault tolerant* [4, 19]. That is to say, the decoherence rates and gate infidelities associated with the physical qubits must be below certain thresholds in order for errors to be correctable. The thresholds vary based on the error-correction scheme: the surface code [20] has a relatively low threshold of just $1\%$ for the per-operation error rate, while the 2D Bacon-Shor code with nearest-neighbor connectivity has a more stringent threshold of $2 \cdot 10^{-5}$ [21]. In the surface code, the number of physical qubits necessary to implement a single logical qubit varies with the error rate [20]. Thus the price paid for such a generous error threshold is that implementation with physical qubits with error rates only just below the threshold requires $> 10^5$ physical qubits per logical qubit [20]. Suppressing this number below $10^3 - 10^4$ physical qubits necessitates two-qubit gate fidelities in excess of $0.999$.

Progress towards higher two-qubit gate fidelities [22, 23, 24] can be made by focusing on the two main factors contributing to errors: decoherence and imperfect control. Decoherence occurs

due to both depolarization and pure dephasing. Depolarization refers to unwanted transitions such as relaxation and excitation, while pure dephasing occurs due to variations in the energy difference between the qubit states. Imperfect control could refer to parasitic terms in the Hamiltonian (such as the ubiquitous static *ZZ* interaction [25, 26, 27, 28]), or to unwanted operators activated by the experimenter while executing a gate. The effects of depolarization, pure dephasing and imperfect control can be visualized by utilizing the Bloch sphere representation of qubit operations [Fig. 1.1]. The north and south pole correspond to the qubit states $|0\rangle$ and $|1\rangle$, respectively, and operations on the qubit are rotations on the Bloch sphere. One very useful aspect of this representation is the ability to include and visualize the detrimental effects of decoherence. Consider as an example the implementation of an $X/2$ gate. If the gate was executed perfectly and decoherence was absent, then the state $|0\rangle$ or $|1\rangle$ would be mapped to the state $\frac{1}{\sqrt{2}}(|0\rangle+|1\rangle)$ or $\frac{1}{\sqrt{2}}(|0\rangle-|1\rangle)$, respectively. The gate fidelity is lowered if the $X/2$ gate is accompanied by an additional unwanted rotation about the *Y* axis, see Fig. 1.1(a). If instead the experimenter has perfect knowledge of the Hamiltonian but the qubit is subject to depolarization or pure dephasing, gate fidelities also suffer, see Fig. 1.1(b)-(c).

In order to obtain the highest-possible gate fidelities, it is thus necessary to achieve the longest-possible coherence times while simultaneously maintaining exquisite understanding of and control over the system Hamiltonian. In this thesis, we explore both avenues of optimization.

## 1.1 Optimizing coherence

To envision how to continue improving the coherence of superconducting qubits, it is useful to give a partial historical account of the development of the fluxonium qubit [29, 30]. Recent experiments on this qubit modality have demonstrated coherence times ranging from hundreds of microseconds [31, 32] to milliseconds [33]. These results represent an improvement of nearly six orders of magnitude relative to the first experiments on Cooper-pair boxes (CPB) [34]. The invention of the CPB in 1998 by Devoret and collaborators established the quantum coherence of a single Cooper pair [35]. In 1999 Nakamura and collaborators demonstrated coherent control over the quantum state of the CPB [34]. Coherence times for the CPB were of the order of a single nanosecond or shorter

[34], limited by low-frequency charge noise [36]. To combat this noise the quantronium was introduced in 2002 by Devoret and collaborators [37]. This device is a generalization of the CPB and allows for the offset charge to be biased at a so-called "sweet spot." At this point the quantronium is first-order insensitive to charge noise and thus enjoyed an orders-of-magnitude jump in coherence times relative to the CPB, with relaxation and dephasing times $T_1, T_2$ on the order of microseconds and hundreds of nanoseconds, respectively [37]. To suppress the detrimental effects of charge noise even further, in 2007 Schoelkopf, Girvin, Devoret and coworkers introduced the transmon, which essentially is a capacitively shunted CPB [38]. This modification exponentially suppresses the charge sensitivity of the qubit transition frequency. State-of-the-art transmons have coherence times in the hundreds of microseconds range [39, 40]. Nevertheless, there are drawbacks to the transmon: it has a reduced anharmonicity relative to the CPB or quantronium and higher-lying levels remain charge sensitive. The fluxonium, introduced by Devoret, Glazman and collaborators in 2009 [29, 30, 41] addresses these issues via the introduction of a shunt inductor. This addition eliminates sensitivity to a dc charge offset [29] and allows for flux tunability, which can be used to control the spectrum of the fluxonium. By biasing the device at the half-flux sweet spot, the fluxonium can have an order-of-magnitude larger anharmonicity than the transmon [32] while remaining first-order insensitive to flux noise. As mentioned above, state-of-the-art fluxonium devices [33] have achieved coherence times greater than the best published results for transmons [39, 40].

This history demonstrates the power of hardware-level protection from noise. In particular it motivates the systematic design of qubits that are protected from *all types of local noise*. In 1997 Kitaev addressed this question in his seminal paper on quantum computing with anyons [42] and introduced the toric code on a lattice, a system with a ground-state degeneracy that is exponentially protected against local perturbations. Inspired by Kitaev's work, Ioffe, Feigel'man, Douçot and coworkers in 2002 proposed arrays of rhombus qubits that implement the crucial features of Kitaev's proposal: an exponentially protected ground-state degeneracy along with vanishing matrix elements of local operators between different logical states [43, 44, 45, 46, 47]. Each rhombus is four sided, with a Josephson junctions on each side [48, 49]. If biased appropriately, the circuit

exhibits an effective $\cos(2\phi)$ potential, where the lowest-energy wave functions localized in the minima at $\phi = 0$ and at $\phi = \pi$ form the qubit states. Gershenson, Ioffe and coworkers have experimentally realized chains of rhombi [50, 51]. Kitaev in 2006 proposed the current-mirror circuit [52], which is similarly a $\cos(2\phi)$ qubit but qualitatively different from the rhombus-based circuits. In 2013 Brooks, Kitaev and Preskill modified the current-mirror design and introduced the $0 - \pi$ circuit. This device was experimentally realized in an unprotected parameter regime by Houck and coworkers in 2019 [53]. Today there is continuous progress on protected circuits and while there has not yet been an experimental demonstration of a fully-protected superconducting circuit, researchers are actively working towards this goal. In this thesis we will focus in detail on characterizing the spectrum, coherence properties and origin of protection of the current-mirror circuit.

## 1.2 Optimizing control

To execute a quantum gate, the experimenter typically implements an external drive. This is modeled as a time-dependent addition to the bare Hamiltonian (which describes the system when the drives are turned off), either causing transitions or introducing relative phases. In superconducting circuits, these drives are typically voltage or current pulses at resonant frequencies [14, 15, 54]. Most often, the analysis of the time evolution in the presence of these drives makes use of the rotating-wave approximation (RWA) [14], simplifying the analysis by rendering the Hamiltonian time independent. However, the RWA is only valid for drive strengths that are sufficiently weak compared with the frequencies of relevant transitions. Strong drives are useful for speeding up gate times, and fast gates are necessary for qubits with limited coherence times. For low-frequency qubits [31, 55, 56], drive strengths yielding high-fidelity gates can approach or even exceed qubit frequencies. In such cases, the validity of the RWA is called into question or made totally inapplicable.

Many researchers have explored beyond-the-RWA physics, most famously Bloch and Siegert [57] who in 1940 derived the leading-order shift of the resonance frequency due to strong drive

effects. In 1973 Cohen-Tannoudji and collaborators provided a fully quantum-mechanical calculation of the Bloch-Siegert shift [58]. In an influential 1965 analysis, Shirley derived similar results by utilizing Floquet theory, replacing the time-dependent and finite-dimensional Hamiltonian with a time-independent and infinite-dimensional Hamiltonian [59]. Many authors have since utilized Floquet theory [60, 61, 62, 63, 64] for both perturbative and nonperturbative analyses of phenomena due to intense fields.

A different technique that provides an exponential solution for the propagator and can also include beyond-the-RWA effects is the expansion due to Magnus [65, 66, 67, 68]. The Magnus expansion has proved widely useful in numerous fields of physics and mathematics, see Ref. [67] and references therein for an extensive review. In recent years, the Magnus expansion has been utilized for optimizing the shape of pulse envelopes [68], analyzing the effects of frequency chirps [69], correcting for leakage errors [70] and accelerating adiabatic gates [71]. In this thesis we utilize the Magnus expansion to predict and correct for strong-drive effects for high-fidelity gates on fluxonium qubits.

## 1.3 Structure of the thesis

This thesis is loosely structured into two main sections. The first section includes the next three chapters, which outline the main ideas that motivate and underlie this thesis. The second section includes the following three chapters which build on the foundation of the previous three and describe our main results.

In Ch. 2 we discuss in detail the modeling of how noise sources couple to qubits and thus motivate the study of hardware-level protection. We introduce the fluxonium and current-mirror circuits, which are the main focus of this thesis. To aid in the numerical diagonalization of the protected current-mirror circuit, in Ch. 3 we introduce the theory of tight binding and discuss its application to superconducting circuits. Considering the optimization of control, in Ch. 4 we derive the Magnus expansion and demonstrate its application in cases where the RWA fails. Continuing on now to the main results of this thesis, in Ch. 5 we introduce an effective model for the current-

mirror circuit and obtain quantitative predictions for the spectrum and coherence of the device. In Ch. 6 we apply the tight-binding method to the current-mirror circuit and obtain numerical results that are beyond those obtainable with more standard exact-diagonalization techniques. In Ch. 7 we shift our attention to the optimization of gate fidelities in high-coherence qubits and discuss a coupling scheme and control protocol for low-frequency fluxonium qubits. We summarize our results and provide an outlook in Ch. 8.

# 2 Decoherence

Superconducting circuits inevitably experience decoherence due to uncontrollable coupling to the environment. This coupling generally results in both depolarization and pure dephasing.

Depolarization is a catch-all term to describe unwanted transitions mediated by the environment. In high-frequency qubits where $\hbar\omega \gg k_B T$, depolarization is typically dominated by relaxation processes $|1\rangle \rightarrow |0\rangle$. Here $\omega$ denotes the qubit frequency and $T$ the temperature of the environment. In lower-frequency qubits where $\hbar\omega \lesssim k_B T$, excitation processes $|0\rangle \rightarrow |1\rangle$ also become important due to the presence of thermal photons at the qubit frequency. For the protected qubits discussed in this thesis, transitions between the qubit states are generally suppressed for reasons that will become clear later. The dominant depolarization processes in this case are transitions *upwards* $|0\rangle, |1\rangle \rightarrow |n\rangle, n > 1$. Adding up the rates of all relevant transitions yields the depolarization rate $\Gamma_1$, and taking the inverse yields the depolarization time $T_1 = 1/\Gamma_1$.

Pure dephasing is the dissipation-free loss of relative-phase information. It is a purely quantum phenomenon, arising from the ability of the environment to distinguish between two quantum states. The detrimental effects of pure dephasing can be understood by considering a Ramsey experiment [72]. The experimentalist initializes the superposition state $|\psi\rangle = \frac{1}{\sqrt{2}}(|0\rangle + |1\rangle)$, and pure-dephasing processes force this state into a classical mixed state $\lim_{t\rightarrow\infty} |\psi(t)\rangle\langle\psi(t)| = \frac{1}{2}(|0\rangle\langle 0| + |1\rangle\langle 1|)$. The pure-dephasing time $T_\phi = 1/\Gamma_\phi$ is thus the timescale associated with the decay of the off-diagonal component $c_0 c_1^*$ of the density matrix

$$|\psi(t)\rangle\langle\psi(t)| = \begin{pmatrix} |c_0|^2 & c_0 c_1^* \\ c_0^* c_1 & |c_1|^2 \end{pmatrix}, \tag{2.1}$$

where $c_0, c_1$ are the time-dependent coefficients in the decomposition $|\psi(t)\rangle = c_0|0\rangle + c_1|1\rangle$. Depolarization processes also generally cause dephasing, combining with pure dephasing to give the overall dephasing rate [73, 74, 75]

$$\Gamma_2 = \frac{\Gamma_1}{2} + \Gamma_\phi. \tag{2.2}$$

The dephasing time is then defined as $T_2 = 1/\Gamma_2$.

## 2.1 Noise modeling

We follow the standard formalism for modeling the coupling of a qubit to the environment: in this analysis we treat the noise classically and assume the Hamiltonian depends on a noisy parameter $\lambda(t) = \lambda_0 + \delta\lambda(t)$ (for instance, the offset charge in a CPB or transmon qubit) [38, 75, 76, 77, 78, 79, 80]. Taylor expanding the Hamiltonian about $\lambda = \lambda_0$ up to second order yields

$$H \approx H_0 + \frac{\partial H_0}{\partial \lambda}\delta\lambda(t) + \frac{1}{2}\frac{\partial^2 H_0}{\partial \lambda^2}\delta\lambda^2(t), \tag{2.3}$$

where the derivatives are evaluated at $\lambda = \lambda_0$. The noise is characterized by its spectral density $S(\omega) = \int_{-\infty}^{\infty} e^{i\omega t} dt \langle \delta\lambda(t)\delta\lambda(0)\rangle$, which is the Fourier transform of the auto-correlation function $\langle \delta\lambda(t)\delta\lambda(0)\rangle$. Here we assume that the noise is Gaussian with zero mean, and that it has a short auto-correlation time compared with the timescale of a typical experiment. In addition we assume that the noise-spectral density is well behaved as $\omega \to 0$ (we relax this assumption in Ch. 5 for the important case of $1/f$ noise sources).

To evaluate the effects of the perturbing operator $V(t)$ [the two rightmost terms in Eq. (2.3)], we expand it in the basis of the eigenstates $|n\rangle$ of $H_0$

$$V(t) = \sum_n v_{nn}(t)|n\rangle\langle n| + \sum_{\substack{n,m \\ n\neq m}} v_{nm}(t)|n\rangle\langle m|. \tag{2.4}$$

The diagonal terms generally cause pure dephasing while the off-diagonal terms induce depolar-

ization. The diagonal coefficients are given by

$$v_{nn}(t) = \langle n|\partial_\lambda H_0|n\rangle \delta\lambda(t) + \frac{1}{2}\langle n|\partial_\lambda^2 H_0|n\rangle \delta\lambda(t)^2 = \partial_\lambda E_n \delta\lambda(t) + \frac{1}{2}\langle n|\partial_\lambda^2 H_0|n\rangle \delta\lambda^2(t), \tag{2.5}$$

where the second equality is obtained straightforwardly by differentiating the eigenvalue equation $H_0(\lambda)|n(\lambda)\rangle = E_n(\lambda)|n(\lambda)\rangle$ with respect to $\lambda$ and operating from the left by the bra $\langle n(\lambda)|$, where we have made the dependence on $\lambda$ explicit. For pure dephasing we distinguish between operating at or away from a sweet spot, where $\partial_\lambda E_n = 0$ and the linear contributions of the noise vanish. At this bias point second-order effects of the noise become important for pure dephasing. The off-diagonal coefficients are approximated by

$$v_{nm}(t) = v_{nm}\delta\lambda(t), \quad v_{nm} = \langle n|\partial_\lambda H_0|m\rangle, \quad n \neq m, \tag{2.6}$$

neglecting the second-order contributions which are subdominant when considering depolarization [75].

Assuming that the noise can be treated perturbatively, it is convenient to transform into the interaction picture defined by the unitary $U_0(t) = \exp(-iH_0 t/\hbar)$. The interaction-frame Hamiltonian is

$$H_I = U_0^\dagger H U_0 - i\hbar U_0^\dagger \dot{U} = \sum_n v_{nn}(t)|n\rangle\langle n| + \sum_{\substack{n,m \\ n\neq m}} v_{nm}(t)|n\rangle\langle m|e^{i\omega_{nm}t}, \tag{2.7}$$

where $\omega_{nm} = (E_n - E_m)/\hbar$. Expanding the state at time $t$ as $|\psi(t)\rangle = \sum_n c_n(t)|n\rangle$, the equations of motion for the coefficients $c_n(t)$ are

$$i\hbar\dot{c}_n(t) = \sum_m v_{nm}(t)e^{i\omega_{nm}t}c_m(t). \tag{2.8}$$

In the following we obtain solutions to Eq. (2.8) by making suitable approximations. We first discuss depolarization before returning to pure dephasing.

### 2.1.1 Depolarization

The probability of a transition from $|i\rangle \rightarrow |n\rangle$ from first-order time-dependent perturbation theory is [81]

$$P_{ni}(t) = \left| -\frac{i}{\hbar} \int_0^t dt' v_{ni} e^{i\omega_{ni}t'} \delta\lambda(t') \right|^2 = \frac{1}{\hbar^2} |v_{ni}|^2 \int_0^t dt' \int_0^t dt'' e^{i\omega_{ni}t''} e^{-i\omega_{ni}t'} \delta\lambda(t'')\delta\lambda(t'), \tag{2.9}$$

In a typical $T_1$ measurement, one averages over many experiments and thus noise realizations. Taking an ensemble average yields

$$\langle P_{ni} \rangle(t) = \frac{1}{\hbar^2} |v_{ni}|^2 \int_0^t dt' \int_0^t dt'' e^{i\omega_{ni}(t''-t')} \langle \delta\lambda(t''-t')\delta\lambda(0) \rangle, \tag{2.10}$$

where we have utilized the time translation symmetry of the noise. Introducing $\tau = t'' - t'$ yields

$$\langle P_{ni} \rangle(t) = \frac{1}{\hbar^2} |v_{ni}|^2 \int_0^t dt' \int_{-t'}^{t-t'} d\tau e^{i\omega_{ni}\tau} \langle \delta\lambda(\tau)\delta\lambda(0) \rangle. \tag{2.11}$$

Under the assumption of a short autocorrelation time of the noise, the inner integral is dominated by the values of $\tau$ near zero. It is thus a good approximation to take the limits of integration to $\pm\infty$ [80]. We recognize the inner integral as $S(\omega_{ni})$ and the outer integral immediately yields a factor of $t$

$$\langle P_{ni} \rangle(t) = \frac{1}{\hbar^2} |v_{ni}|^2 S(\omega_{ni}) t, \tag{2.12}$$

valid only for sufficiently small values of $t$ where we can apply first-order perturbation theory. Dividing by $t$ then yields the rate for transitions $|i\rangle \rightarrow |n\rangle$, which is known as Fermi's Golden Rule [75, 78, 80, 81]

$$\Gamma_{ni} = \frac{1}{\hbar^2} |v_{ni}|^2 S(\omega_{ni}). \tag{2.13}$$

For a system where the two lowest-energy states $|0\rangle, |1\rangle$ are the qubit states, the full depolarization rate is $\Gamma_1 = \Gamma_{\text{rel}} + \Gamma_{\text{exc}} + \Gamma_{\text{esc}}$, where

$$\Gamma_{\text{rel}} = \frac{1}{\hbar^2}|v_{10}|^2 S(+|\omega_{10}|), \quad \Gamma_{\text{exc}} = \frac{1}{\hbar^2}|v_{10}|^2 S(-|\omega_{10}|), \quad \Gamma_{\text{esc}} = \frac{1}{\hbar^2}\sum_{\substack{i=0,1 \\ n>1}} |v_{ni}|^2 S(-|\omega_{ni}|), \tag{2.14}$$

describing the rates for relaxation, excitation and escape from the qubit subspace, respectively. We generally assume that the noise source is in thermal equilibrium [80] and therefore obeys detailed balance

$$S(-\omega) = S(\omega)\exp(-\hbar\omega/k_B T). \tag{2.15}$$

Thus qubit excitation is suppressed relative to qubit relaxation. However, for low-frequency qubits where $\hbar\omega \lesssim k_B T$, all of relaxation, excitation and escape processes can meaningfully contribute to depolarization.

### 2.1.2 Pure dephasing

We now turn our attention to calculating pure dephasing rates. We first consider the case when the first-order terms dominate, before discussing pure dephasing at a sweet spot where the second-order terms must be included. In the context of pure dephasing, we ignore the terms causing transitions in Eq. (2.4). In this case the dynamical equations (2.8) for the coefficients $c_n(t)$ are independent and can immediately be solved, yielding

$$c_n(t) = c_n(0)\exp\left[-\frac{i}{\hbar}\int_0^t \partial_\lambda E_n \delta\lambda(t')dt'\right]. \tag{2.16}$$

Let us suppose that at time $t = 0$ we have a superposition of the qubit states $|\psi(0)\rangle = c_0(0)|0\rangle + c_1(0)|1\rangle$. The off-diagonal component of the density matrix at time $t$ is

$$\rho_{01}(t) = c_0(0)c_1^*(0)\exp\left[-\frac{i}{\hbar}\partial_\lambda E_{01}\int_0^t \delta\lambda(t')dt'\right], \tag{2.17}$$

defining $\partial_\lambda E_{01} = \partial_\lambda E_0 - \partial_\lambda E_1$. The exponential encodes the decay of the coherence. To characterize the timescale associated with this decay (as in a typical Ramsey experiment), one averages over multiple repeated measurements. Thus, we calculate the ensemble average $\langle \rho_{01} \rangle(t)$. Indeed, because the noise $\delta\lambda$ is a random Gaussian signal, the phase of the exponential is itself a random Gaussian process. The quantity $\langle e^{-i\phi(t)} \rangle$ is then known as the characteristic function [82] of the random variable $\phi(t)$. For a Gaussian random variable with zero mean, the characteristic function is $\langle e^{-i\phi(t)} \rangle = e^{-\frac{1}{2}\langle \phi^2(t) \rangle}$ [80, 82], yielding

$$\langle \rho_{01} \rangle(t) = c_0(0) c_1^*(0) \exp\left[ -\frac{1}{2\hbar^2} |\partial_\lambda E_{01}|^2 \int_0^t dt' \int_0^t dt'' \langle \delta\lambda(t' - t'') \delta\lambda(0) \rangle \right]. \tag{2.18}$$

Changing variables and extending the bounds of integration in the same manner as discussed in the context of Eq. (2.11), we recognize the inner integral as $S(0)$ and obtain [75, 83, 84]

$$\langle \rho_{01} \rangle(t) = c_0(0) c_1^*(0) \exp\left[ -\frac{1}{2\hbar^2} |\partial_\lambda E_{01}|^2 S(0) t \right], \tag{2.19}$$

from which we read off the pure-dephasing rate

$$\Gamma_\phi = \frac{1}{2\hbar^2} |\partial_\lambda E_{01}|^2 S(0). \tag{2.20}$$

This result agrees with those of Refs. [75, 83] after accounting for the differing factors of $2\pi$ in the definition of $S(\omega)$. Some authors refer to this as a "Golden-Rule type" result [75]. Note however that we were not forced to employ perturbation theory to derive Eq. (2.20), whereas Fermi's Golden Rule typically relies on first-order perturbation theory. If the qubit is biased at a sweet spot, second-order effects of the noise can become important. We include such effects in Ch. 5 for the important case of $1/f$ noise.

## 2.2 Protection

With the expressions for the rates of depolarization and pure dephasing in hand, we now consider in detail the principle behind protected qubits. Hardware-level noise protection is obtained by simultaneously suppressing the matrix elements relevant for relaxation and excitation as well as the dispersion of the qubit energy difference relevant for pure dephasing, see Eqs. (2.14) and (2.20). To gain intuition, we first consider qubits that are protected from either depolarization or pure dephasing but not both. Following this we discuss possible realizations of fully-protected qubits.

### 2.2.1 Partially protected qubits

To obtain hardware-level protection from pure dephasing, the first step is to suppress the linear dispersion of the qubit energy with a noisy external parameter, see Eq.(2.20). This is typically known as operating at a sweet spot [37, 85]. Further protection from pure dephasing can be obtained by exponentially suppressing the dispersion. A famous example of a qubit protected from dephasing in this manner is the transmon qubit [38, 86]. The Hamiltonian of the transmon is [38]

$$H_{\text{tmon}} = 4E_C(n - n_g)^2 - E_J \cos(\phi), \tag{2.21}$$

where $n_g$ is the offset charge, $E_C$ is the charging energy and $E_J$ is the Josephson energy. The operator $n$ plays the role of momentum and its spectrum is integer valued, counting the number of Cooper pairs on the superconducting island of the transmon [38, 87]. The gauge-invariant phase $\phi = 2\pi\Phi/\Phi_0$ is defined in terms of the superconducting phase $\Phi$ across the junction, where $\Phi_0 = h/2e$ is the superconducting flux quantum. These operators obey the funny-looking commutation relation $[e^{i\phi}, n] = -e^{i\phi}$ [87]. We cannot write the commutation relation in terms of $\phi$ by itself because that operator is not meaningful in this context, as the Hamiltonian and therefore the wave functions are periodic in $\phi$.

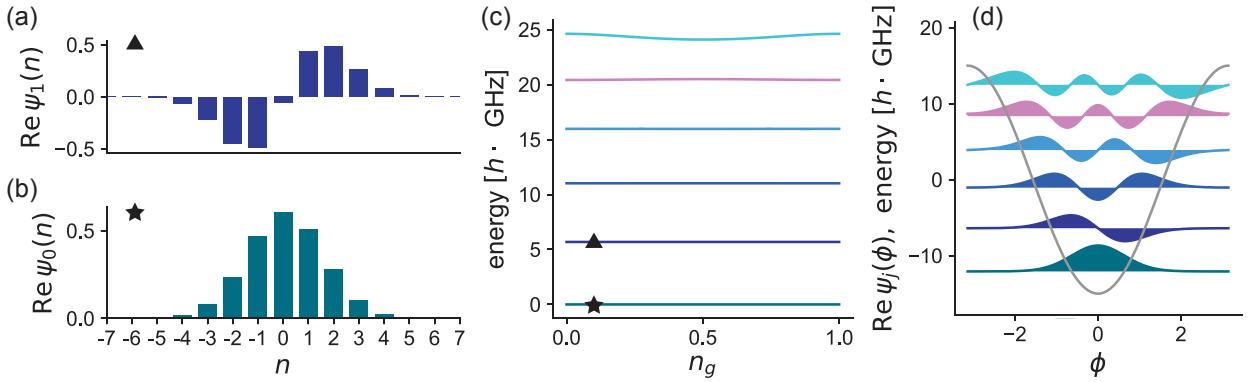


**Figure 2.1:** Wave functions and spectrum of the transmon. (a)-(b) Wave functions in the charge basis of the two lowest-lying states of the transmon at $n_g = 0.1$. The delocalization of the eigenstates in charge space is the origin of protection from dephasing due to charge noise. (c) Spectrum as a function of offset charge $n_g$. For the lowest-lying levels, the spectrum is flat before charge-sensitivity is re-established by the higher-lying states. (d) Wave functions in phase space. The qubit wave functions are localized in the same potential well and thus do not have disjoint support. Numerical results were obtained using transmon parameters $E_J/h = 15$ GHz, $E_C/h = 0.3$ GHz.

One source of external noise causing dephasing in the transmon is fluctuations in the value of $n_g$. The transmon's protection from such charge fluctuations derives from operating in the parameter regime $E_J \gg E_C$, leading to delocalization of the qubit wave functions in charge space [see Fig. 2.1(a)-(b)]. This nature of the qubit wave functions prevents the charge-number operator $n$ [the operator that couples to $n_g$, see Eq. (2.21)] from discriminating between the qubit states. Observe that this feature generally leads to a vanishing of the linear dispersion of the qubit frequency, as $\partial_\lambda E_{01} = \langle 0|\partial_\lambda H_0|0\rangle - \langle 1|\partial_\lambda H_0|1\rangle$. Indeed the charge dispersion of the qubit frequency is exponentially suppressed in the transmon regime [see Fig. 2.1(c)] [38]. This "sweet-spot everywhere" approach yields protection from dephasing due to charge noise.

There is a cost however to the protection gained from pure-dephasing processes. The qubit states are localized in the same potential well in position (phase) space [see Fig. 2.1(d)], and thus matrix elements $|\langle 0|\mathcal{O}|1\rangle|$ with respect to some local operator $\mathcal{O}$ (for instance the charge-number operator $n$) are typically of order unity. Thus the transmon is not protected from relaxation.

One straightforward means to suppress $\langle 0|\mathcal{O}|1\rangle$ and obtain protection from relaxation is to engineer the qubit wave functions to be localized in different regions of variable space. The wave functions are then said to have "disjoint support" [88, 89]. As long as the perturbing operator $\mathcal{O}$ is

a local operator (like charge or phase, as opposed to a displacement operator), the matrix element $\langle 0|\mathcal{O}|1\rangle$ is exponentially suppressed, dominated by tails of the qubit wave functions [90]. An example qubit whose wave functions can enjoy disjoint support is the fluxonium qubit [91, 92]. The fluxonium Hamiltonian is [29, 30]

$$H_{\text{fl}} = 4E_C n^2 - E_J \cos(\phi) + \frac{1}{2}E_L(\phi - \phi_{\text{ext}})^2, \tag{2.22}$$

where $E_C$ is the charging energy, $E_J$ is the Josephson energy, $E_L$ is the inductive energy and $\phi_{\text{ext}} = 2\pi\Phi_{\text{ext}}/\Phi_0$ is the reduced flux defined in terms of the magnetic flux $\Phi_{\text{ext}}$. The fluxonium Hamiltonian is not periodic in $\phi$, thus the spectrum of the charge operator $n$ is no longer discrete and $\phi$ is now a meaningful operator. The operators $n$ and $\phi$ are canonically conjugate and obey the standard commutation relation $[\phi, n] = i$.

For parameter choices in the "heavy-fluxonium" regime $E_J \gg E_C \gtrsim E_L$ [91, 92] and away from integer or half-integer values of $\Phi_{\text{ext}}/\Phi_0$, the two lowest-lying wave functions localize in different minima of the fluxonium potential, see Fig. 2.2(a). These states serve as the qubit states and are protected from relaxation by disjoint support [91, 92]. Unfortunately, this qubit is not simultaneously protected from dephasing, as it is linearly susceptible to flux noise [91]. This is clear from the spectrum of the fluxonium, where away from integer or half-integer flux the quantity $\partial_{\Phi_{\text{ext}}} E_{01}$ is nonzero, see Fig. 2.2(b). If instead we bias at e.g. a point of half-integer flux where the spectrum is first-order insensitive to flux noise, the qubit states delocalize and are unprotected from relaxation.

We thus observe that in single-mode circuits like the transmon and the fluxonium, it is difficult if not impossible to obtain full protection from both depolarization and dephasing. In the following we investigate two means for bypassing this limitation. The first strategy involves careful choice of parameters to enhance coherence times in single-mode circuits. The second is considering more complex circuits (with more than one degree of freedom) that may be engineered to have full protection from relaxation and dephasing.

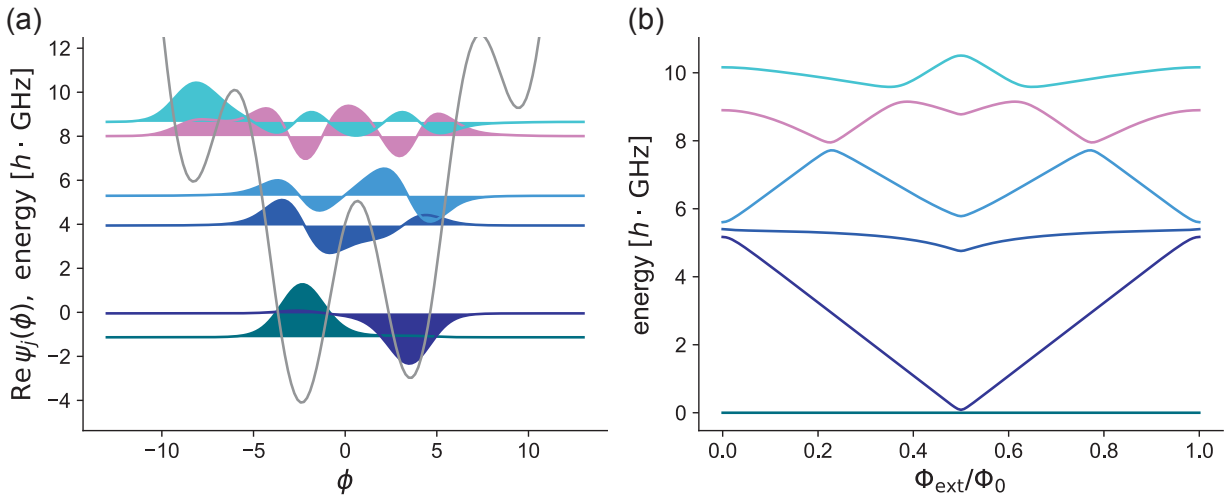


**Figure 2.2:** Wave functions and spectrum of the fluxonium. (a) Wave functions at $\Phi_{\mathrm{ext}} = 0.4\Phi_0$. The two lowest-lying wave functions localize in neighboring minima of the potential. (b) Spectrum as a function of flux. Away from degeneracy points, the energy splitting $E_{01}$ is linearly sensitive to the external flux $\Phi_{\mathrm{ext}}$. Fluxonium parameters used here are $E_J/h = 5$ GHz, $E_L/h = 0.3$ GHz, $E_C/h = 1$ GHz.

### 2.2.2 Partially protected qubits + (premium)

In circuits like the transmon or fluxonium, it is generally only possible to obtain hardware-level protection from depolarization or dephasing, but not both [88]. This limitation may be circumvented by instead operating a dephasing-protected qubit in a frequency regime where the noise-power spectrum relevant for relaxation is suppressed. Thus, while transition matrix elements can be of order unity, the depolarization rate can still be made relatively small. This configuration is achieved in the heavy-fluxonium circuit [91, 92], specifically biased at the half-flux sweet spot $\Phi_{\mathrm{ext}} = 0.5\Phi_0$ [31]. At this point, the energy spectrum of the qubit is only quadratically sensitive to flux noise, see Fig. 2.2(b). It is well known that typical charge noise amplitudes (in units of $2e$) exceed typical flux noise amplitudes (in units of $\Phi_0$) by more than an order of magnitude [41]. Thus the linear suppression of flux noise is sufficient to achieve record dephasing times from hundreds of microseconds to milliseconds [31, 32, 33]. These results stand in contrast to those for CPB qubits biased at charge sweet spots, with dephasing times of the order of a microsecond or less [37, 75, 85].

At the half-flux sweet spot the qubit eigenstates delocalize over the two lowest-energy minima

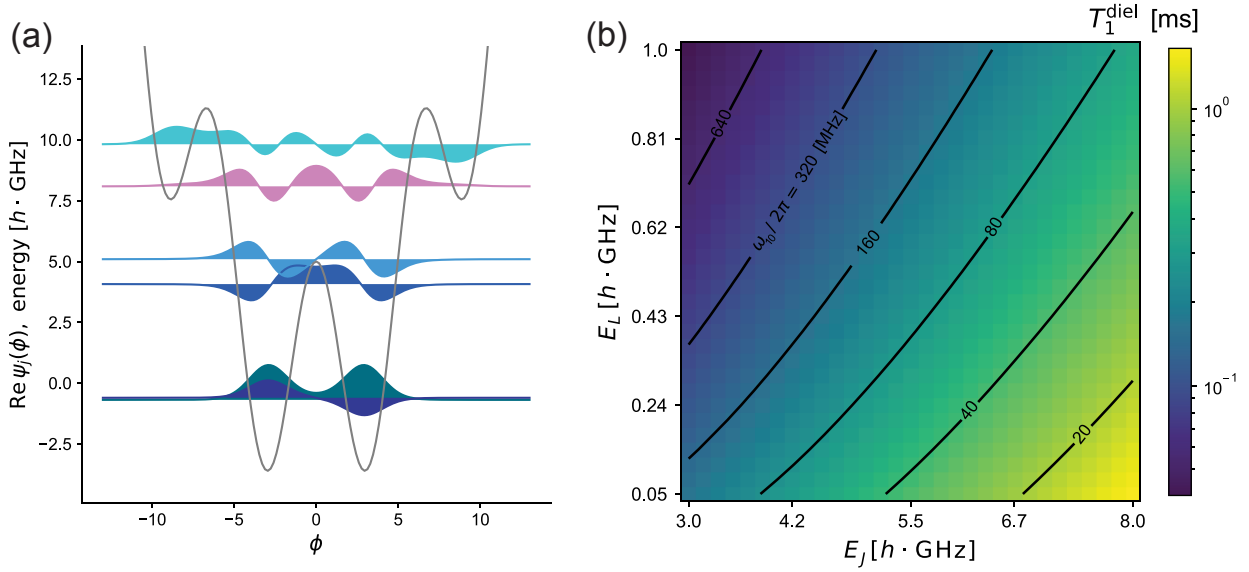


**Figure 2.3:** Fluxonium at the half-flux sweet spot. (a) Wave functions and potential of the fluxonium when biased at $\Phi_{\mathrm{ext}} = 0.5\Phi_0$. The two lowest-lying states delocalize over the neighboring degenerate minima. (b) Qubit frequency $\omega_{10}$ (contour lines) and depolarization time due to dielectric loss $T_1^{\mathrm{diel}}$ (coloring) as a function of $E_J, E_L$. The quantities $\omega_{10}$ and $T_1^{\mathrm{diel}}$ are inversely correlated in this parameter regime. We used the same fluxonium parameters as in Fig. 2.2, as well as $1/Q_{\mathrm{cap}} = 4 \cdot 10^{-6}$ [31].

of the potential, see Fig. 2.3(a). These states have support in the same regions of variable space, and matrix elements relevant for relaxation (such as $\langle 1|\phi|0\rangle$) are not suppressed. Thus there is no hardware-level protection from relaxation. Instead, here we seek to suppress the contribution from the noise-power spectrum in Eq. (2.14). We focus on depolarization due to dielectric loss, which numerous experiments on fluxonium qubits have found to be limiting $T_1$ [31, 32, 33].

This noise channel can be modeled by assuming that the dielectric constant of the relevant capacitor has an imaginary component, leading to a nonzero value for the real part of the admittance [93]. The noise-spectral density at positive frequencies is then [32, 78, 93, 94, 95, 96, 97, 98]

$$S_{\text{diel}}(\omega_{10}) = \frac{\hbar\omega_{10}^2 C}{Q_{\text{cap}}}\left(\coth\left[\frac{\hbar\omega_{10}}{2k_B T}\right]+1\right), \tag{2.23}$$

where $Q_{\text{cap}}$ is the quality factor (which can have a weak frequency dependence [32]), $C$ is the relevant capacitance, $\omega_{10}$ is the qubit frequency, $k_B$ is the Boltzmann constant and $T$ is the temperature. Including both relaxation and excitation and ignoring escape from the qubit subspace (a good approximation for the highly anharmonic fluxonium qubit), the depolarization rate is

$$\Gamma_1^{\text{diel}} = \frac{1}{\hbar^2}(S_{\text{diel}}[\omega_{10}] + S_{\text{diel}}[-\omega_{10}])|\langle 1|\Phi|0\rangle|^2 = \frac{\hbar\omega_{10}^2}{4E_C Q_{\text{cap}}}\coth\left(\frac{\hbar\omega_{10}}{2k_B T}\right)|\langle 1|\phi|0\rangle|^2, \tag{2.24}$$

making explicit use of Eq. (2.15). Consider now the limit of small qubit frequencies $\hbar\omega_{10}/k_B T \ll 1$. In this case we obtain

$$\Gamma_1^{\text{diel}} \approx \frac{\omega_{10} k_B T}{2E_C Q_{\text{cap}}}|\langle 1|\phi|0\rangle|^2. \tag{2.25}$$

By varying for instance the device parameters $E_J$ and $E_L$, we verify the inverse scaling of $T_1^{\text{diel}} \equiv 1/\Gamma_1^{\text{diel}}$ [Eq. (2.24)] and $\omega_{10}$ predicted by Eq. (2.25),[1] see Fig. 2.3(b). A recent experiment has confirmed that dielectric loss remains the dominant contributor to depolarization for qubit frequen-

[1] It is worth stressing here that we are restricting the fluxonium to operate at the sweet spot. Thus while the matrix element $\langle 1|\phi|0\rangle$ generally has nontrivial flux dependence, that is not relevant to our current discussion. Indeed, varying $E_J$ and $E_L$ across a wide range of parameters, $\langle 1|\phi|0\rangle$ is approximately a constant, making $\omega_{10}$ the only varying quantity in Eqs. (2.24)-(2.25) [99].

cies as low as $\omega_{10}/2\pi = 10$ MHz [31]. The depolarization rate can thus be suppressed by effectively modifying the frequency at which the noise-spectral density is sampled. Despite lacking full hardware-level noise protection, the heavy fluxonium biased at the sweet spot has shown record coherence times, from hundreds of microseconds [31, 32] to milliseconds [33].

It is important to ensure that in lowering the qubit frequency, there is no (or very little) corresponding slowdown in gate times. If there were such a trade off, there would be no net benefit because the number of executable gates in a quantum circuit would not increase. If we limit ourselves to gates that are executed by driving on resonance with a particular transition within the framework of the RWA, then indeed there would be a corresponding slowdown [14]. However, recent work [31, 55, 100, 101] has shown that there is no fundamental limit on gate speeds relative to qubit frequencies. Ficheux *et al.* demonstrated a fast and high-fidelity two-qubit gate on qubits with frequencies of $72$ and $136$ MHz by driving non-computational transitions [100]. Campbell *et al.* [55] and Zhang *et al.* [31] demonstrated high-fidelity single-qubit gates in low-frequency qubits using nonadiabatic, non-resonant drives. A schematic of the pulse scheme used in Ref. [31] for a $Y/2$ gate along with associated Bloch-sphere trajectories are shown in Fig. 2.4. Thus, it is not necessarily true that gate times must increase as qubit frequencies are lowered.

### 2.2.3 Fully-protected qubits

A popular strategy to obtain *simultaneous* protection from both relaxation and dephasing in superconducting circuits is to construct a qubit whose potential is effectively "$\cos(2\phi)$" [43, 44, 46, 47, 49, 50, 51, 52, 53, 79, 89, 94, 102, 103]. The unifying idea behind such qubits is that if single-Cooper-pair tunneling can be suppressed in favor of the tunneling of *pairs* of Cooper pairs, then the potential energy of the circuit can effectively be written as $U = -E_2\cos(2\phi) - E_1\cos(\phi)$ with $E_1 \ll E_2$. Indeed this is the idea behind Kitaev's current-mirror qubit [52] which we analyze in detail in Chs. 5-6. If the relevant kinetic energy scales are dominated by the effective potential energy $E_2$, then eigenstates localize in the inequivalent minima at $\phi = 0$ and $\phi = \pi$ (hence, e.g., the name $0 - \pi$ [102]), see Fig. 2.5. The two lowest-energy eigenstates are typically taken to be the qubit

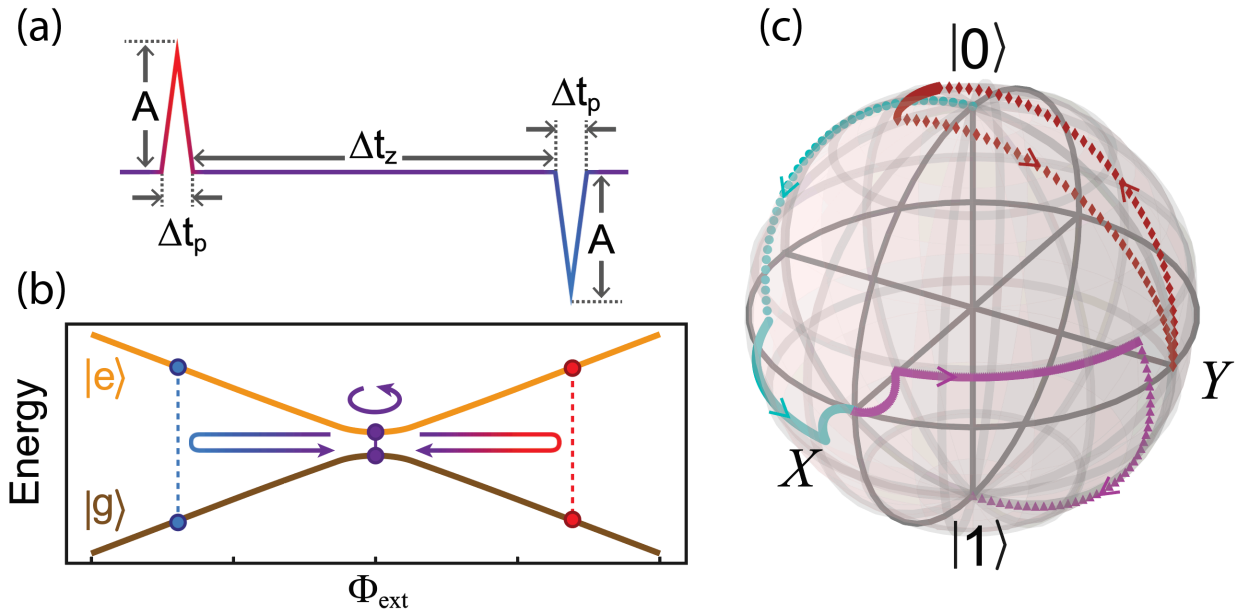


**Figure 2.4:** Non-adiabatic single-qubit gates in a fluxonium qubit. (a) A *Y/2* gate is obtained by using fast, triangle-shaped flux pulses of amplitude $A$ and $-A$ combined with idling at the sweet spot. (b) Schematic of the energy-level diagram of the fluxonium near the sweet spot. (c) Bloch sphere trajectories of the initial states $|0\rangle$ (teal), $(|0\rangle + |1\rangle)/\sqrt{2}$ (purple), and $(|0\rangle + i|1\rangle)/\sqrt{2}$ (red) subject to the *Y/2* pulse. The authors of Ref. [31] utilized the parameters $A/h = 184$ MHz, $\omega_{10}/2\pi = 14$ MHz, $\Delta t_p = 5$ ns, $\Delta t_z = 24$ ns and obtained a *Y/2* gate with fidelity $F = 0.9992$. Figure modified from Ref. [31] with permission of the authors.

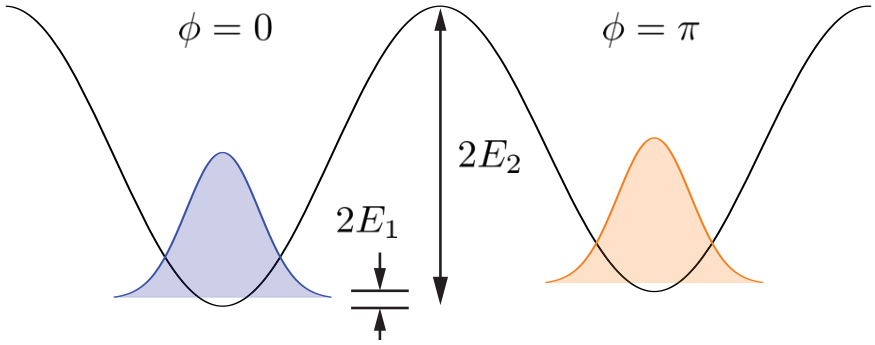


**Figure 2.5:** Principle of a $\cos(2\phi)$ or $0-\pi$ qubit. For a circuit with effective potential energy $U = -E_2\cos(2\phi) - E_1\cos(\phi)$ where $E_1 \ll E_2$, the minima at $\phi = 0$ and $\phi = \pi$ are nearly degenerate. The lowest-energy states localized in each minimum are the qubit states. These states are protected from relaxation by disjoint support. If $E_1$ does not vary with noisy external parameters, then the states are protected from pure dephasing.

states, commonly denoted as $|0\rangle, |1\rangle$ or $|0\rangle, |\pi\rangle$. If $E_1$ is small and moreover does not vary with any noisy external parameters, then we obtain a robust (near-) degeneracy of the ground state. This provides protection from pure dephasing.

Protection from relaxation is due to the disjoint support between the qubit states localized in different potential wells. Notably, if single Cooper-pair tunneling is entirely suppressed $E_1 = 0$, the two minima are exactly degenerate and eigenstates delocalize. Indeed, if the tunnel splitting vanishes then any linear combination of the localized states is itself an eigenstate. This presents an issue for state preparation, which for high-frequency qubits typically consists of passive initialization (simply waiting for a time much longer than $T_1$ so that the qubit has with certainty relaxed to the ground state) [104]. Such a procedure here will not generally prepare the system in the state $|0\rangle$ or $|1\rangle$ but rather in a statistical mixture of the two states. Thus, more sophisticated state-preparation schemes are necessary. Moreover, due to the suppression of local matrix elements, the execution of gates typically relies on global operators [42, 102] or traversals through higher-lying states [53, 103]. The former option appears difficult to physically implement [103]. The latter option has been realized experimentally [53], but is problematic due to the absence of protection from decoherence for the higher-lying states. Protocols and techniques for performing both high-fidelity state preparation as well as physically-realizable protected gates represent important open questions in the

road to realizing a fully-protected superconducting qubit.

# 3 Tight Binding for Superconducting Circuits

*This chapter is based on material published in D. K. Weiss et al., Phys. Rev. Research* **3**, *033244 (2021).*

Research on superconducting qubits has repeatedly encountered physics familiar from models and phenomena in solid-state physics. Examples include the close connection between the Cooper pair box and a particle in a one-dimensional crystal, or the interpretation of the fluxonium Hamiltonian in terms of Bloch states subject to interband coupling [29]. Another analogy, which points to the computational technique developed in this chapter and applied to circuits like the current mirror in Ch. 6, is the consideration of crystal electrons in the tight-binding limit. In this regime, tunneling between electronic orbitals of different atoms is weak, and linear combinations of atomic orbitals constructed by "periodically repeating" localized wave functions serve as a meaningful basis. The tight-binding method then employs this basis in an approximate solution to the Schrödinger equation. An analogous scenario can be encountered for superconducting circuits as shown in Fig. 3.1. Minima of the potential energy may give rise to localized states that are only weakly connected by tunneling to partner states in other potential minima. The "atomic orbitals" which we will refer to as "local wave functions" in this case can be identified with the harmonic oscillator states associated with a local Taylor expansion around each minimum.

We will find this technique useful due to the difficulty of simulating superconducting circuits with an increasing number of degrees of freedom. Large circuits, especially of the size considered for the current mirror [52] or rhombi lattice [47], pose significant challenges for the quantitative analysis of energy spectra and prediction of coherence times. Consequently, the development of more

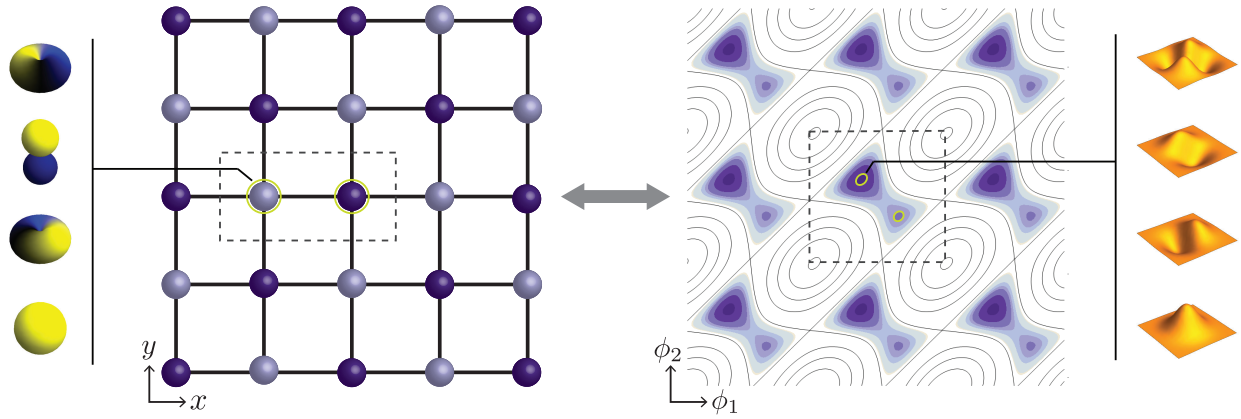


**Figure 3.1:** Comparison between tight binding as applied to solids and superconducting circuits. Left: example of a two-dimensional lattice with a two-atom basis, signified by the grey and blue atoms; far left: example atomic wave functions. Right: potential of the flux qubit, with two inequivalent minima in each unit cell at the chosen value of flux. We only color the potential below a cutoff value to draw the eye to the potential minima locations. Near the minima the potential is approximately harmonic, therefore the local wave functions take the form of harmonic oscillator states, see far right.

efficient numerical tools capable of solving for eigenstates and eigenenergies of large superconducting circuits has emerged as a vital imperative. Strategies recently introduced for that purpose include hierarchical diagonalization [105, 106], adaptive mode decoupling [107], and DMRG methods [108, 109, 110]. We propose variational tight binding as another strategy complementing the former ones [111].

Since the Hilbert space dimension $d$ of even a single transmon circuit is infinite, it is not fully accurate to blame the "growth" of $d$ for the challenges encountered with circuits of larger size. Nonetheless, when representing a Hamiltonian in a basis not specifically tailored for the problem at hand, the dimension of the truncated Hilbert space typically grows exponentially when choosing the truncation level such that a particular level of convergence is reached. This turns the numerical diagonalization of a circuit Hamiltonian into a hard problem. An approach to address this challenge introduced in Ch. 3 consists of constructing basis states which more closely approximate the desired low-energy eigenstates from the very beginning. As long as construction of the tailored basis and decomposition of the Hamiltonian in that basis can be accomplished efficiently, this approach will allow for reduced truncation levels and hence enable coverage of circuit sizes otherwise inac-

cessible numerically.

Our construction of such tailored basis states is based on the observation that low-lying eigenstates of superconducting circuits are often localized in the vicinity of minima of the potential energy, when expressed in terms of appropriate generalized-flux variables. If the potential energy is periodic or at least periodic along certain axes, then the situation resembles the setting of a particle in a periodic potential, as commonly encountered in solid-state physics when considering electrons inside a crystal lattice. In the regime where tunneling between atomic orbitals of different atoms is weak, tight-binding methods are appropriate for band structure calculations [112, 113]. An analogous treatment has previously been applied to small circuits; see, for example, the discussions of tunneling between minima in the flux qubit [114, 115, 116, 117], the derivation of an asymptotic expression for the charge dispersion in the transmon qubit [38], or the analysis of charge noise in the fluxonium circuit [118]. Chirolli and Burkard carry out a full tight-binding description of the low-energy physics of the flux qubit, considering Bloch sums of harmonic oscillator ground-state wave functions localized in each minimum at the half-flux sweet spot [115]. Motivated by the new interest in circuits of increased size and complexity, we build upon this research in two specific ways. First, we consider multiple basis states in each minimum, to both improve ground-state energy estimates and extract excited-state energies. Second, we consider minima that are not necessarily identical, and introduce an efficient means of calculating matrix elements between states localized in such inequivalent minima. These techniques allow us to demonstrate that tight-binding methods can be adapted for efficient computation of energy spectra of large circuits.

## 3.1 Local-wave function construction

The starting point for this treatment is the full circuit Hamiltonian $H = T + V$. To stress the analogy with the setting of an infinite crystal, we first focus on a purely periodic potential $V(\vec{\phi})$, as realized by a circuit that does not include any inductors. (Including inductors is possible, which we comment on further in Sec. 3.2.) In terms of the node variables $\vec{\phi} = (\phi_1, \ldots, \phi_{N_d})^T$, where $N_d$ is the number of degrees of freedom, the potential energy obeys the periodicity condition $V(\vec{\phi} + 2\pi\vec{j}) = V(\vec{\phi})$

with $\vec{j} \in \mathbb{Z}^{N_d}$ and thus forms a (hyper-)cubic Bravais lattice. Within the central unit cell defined by $\vec{\phi} \in [-\pi, \pi)^{\times N_d}$, the potential energy will exhibit a set of $M$ minima located at positions $\vec{\theta}_m$, $m = 0, 1, \ldots, M$, where $m$ orders the minima from lowest to highest in energy.[1] In the language of solid-state physics, this set of minima corresponds to the multi-atomic basis associated with the Bravais lattice.

The analogy with solid-state physics is further strengthened by considering a gauge where the offset charge dependence is shifted from the Hamiltonian to the wave functions [115, 119]. In this representation, solutions $|\psi\rangle$ to the full Hamiltonian $H$ obey quasiperiodic boundary conditions

$$\mathcal{T}_{\vec{\theta}}|\psi\rangle = e^{-i\vec{n}_g \cdot \vec{\theta}}|\psi\rangle, \tag{3.1}$$

for every $\vec{\theta}$ in the Bravais lattice, where $\mathcal{T}$ is the translation operator and $\vec{n}_g = (n_{g1}, \cdots, n_{gN_d})^T$ is the vector of offset charges. We recognize Eq. (3.1) as an expression of Bloch's theorem with wavevector $-\vec{n}_g$ (typically denoted as $\vec{k}$ in a solid-state context).

The construction of the local wave functions now proceeds by diagonalizing the individual harmonic oscillator Hamiltonians obtained by Taylor expansion around each minimum. We emphasize that the following discussion is quite general, and is equivalent to but rather simpler than similar treatments of harmonic-mode diagonalization in the literature [120, 121]. Expanding around the $m^{\text{th}}$ minimum up to second order we obtain the harmonic Hamiltonian $H'_m = T + V_m$, where

$$V_m = \frac{1}{2} \sum_{i,j} \phi_0^2 \phi_i^{(m)} \Gamma_{ij}^{(m)} \phi_j^{(m)}. \tag{3.2}$$

Here, $\phi_0 = \hbar/2e$ is the reduced flux quantum, $\Gamma_{ij}^{(m)} = \phi_0^{-2} \partial_{\phi_i} \partial_{\phi_j} V|_{\vec{\theta}_m}$ the inverse of the inductance matrix and $\vec{\phi}^{(m)} = \vec{\phi} - \vec{\theta}_m$ the "position" relative to the minimum location. The local Hamiltonian then takes the form

$$H'_m = \frac{1}{2} \sum_{i,j} \left( n_i 8 \frac{e^2}{2} (\mathsf{C})_{ij}^{-1} n_j + \phi_0^2 \phi_i^{(m)} \Gamma_{ij}^{(m)} \phi_j^{(m)} \right), \tag{3.3}$$

[1] Degenerate minima pose no issue, and the ordering is decided arbitrarily.

where $n_i$ is the charge number operator for node $i$ obeying the commutation relation $[\phi_j^{(m)}, n_k] = i\delta_{jk}$ and C is the capacitance matrix. Hereafter, explicit references to $m$ will be omitted for notational simplicity. To obtain the eigenstates of the coupled oscillator Hamiltonian Eq. (3.3) we first determine its normal modes. This is accomplished most efficiently based on the corresponding classical Lagrangian

$$\mathcal{L}' = \frac{1}{2}\phi_0^2 \sum_{i,j} \left( \dot{\phi}_i \mathsf{C}_{ij} \dot{\phi}_j - \phi_i \Gamma_{ij} \phi_j \right). \tag{3.4}$$

(We emphasize that all variables appearing in Eq. (3.4) are classical.) Using the usual oscillatory solution ansatz $\vec{\phi} = \vec{\xi}_\mu e^{-i\omega_\mu t}$ reduces the equations of motion to the generalized eigenvalue problem $\Gamma\vec{\xi}_\mu = \omega_\mu^2 \mathsf{C}\,\vec{\xi}_\mu$ [122]. Here, Latin indices refer to node variables, and Greek indices to normal mode variables. The eigenmode vectors $\vec{\xi}_\mu$ are only determined up to normalization, $\vec{\xi}_\mu^T \mathsf{C}\,\vec{\xi}_\mu = c_\mu$, implying $\vec{\xi}_\mu^T \Gamma \vec{\xi}_\mu = \omega_\mu^2 c_\mu$, where $c_\mu$ is undetermined. Normalization will be fixed when we return to the quantum-mechanical description, in such a way that the Hamiltonian for each mode takes the standard form

$$H'_\mu/\hbar\omega_\mu = \frac{1}{2}\left( -\frac{\partial^2}{\partial\zeta_\mu^2} + \zeta_\mu^2 \right). \tag{3.5}$$

Here, $\vec{\zeta} = (\zeta_\mu)$ collects the normal-mode variables related to the original generalized fluxes via $\vec{\phi} = \Xi\vec{\zeta}$, where $\Xi$ is the matrix of column vectors $\vec{\xi}_\mu$ and encodes both the normal-mode directions and oscillator lengths. In these new variables, both bilinear forms in $\mathcal{L}'$ are diagonal. Legendre transform and quantization thus readily yield

$$H' = \frac{1}{2}\sum_\mu \left[ -\left(\frac{\hbar}{\phi_0}\right)^2 \frac{1}{c_\mu}\frac{\partial^2}{\partial\zeta_\mu^2} + \left(\phi_0\omega_\mu\right)^2 c_\mu \zeta_\mu^2 \right]. \tag{3.6}$$

To cast $H'$ into the form suggested by Eq. (3.5) we now choose $c_\mu = (2e)^2/\hbar\omega_\mu$ as our normalization constants. We denote the eigenstates of $H'$ by $|\vec{s}, m\rangle$. Here, $\vec{s}$ collects the excitation numbers $s_\mu = 0, 1, \ldots$ for each mode $\mu$ and $m$ specifies the minimum of interest.

## 3.2 Bloch summation and the generalized eigenvalue problem

Solution of the Schrödinger equation $H|\psi\rangle = E|\psi\rangle$ proceeds by expressing the Hamiltonian $H$ in matrix form using an appropriate basis. We construct this basis by periodic repetition over the entire Bravais lattice of the local wave functions $|\vec{s}, m\rangle$ defined in the central unit cell, subject to quasiperiodic boundary conditions [Eq. (3.1)]

$$|\psi_{\vec{n}_g,\vec{s},m}\rangle = \frac{1}{\sqrt{\mathcal{N}}}\sum_{\vec{j}} e^{-i\vec{n}_g\cdot(2\pi\vec{j}+\vec{\theta}_m)}\mathcal{T}_{2\pi\vec{j}}|\vec{s}, m\rangle, = \frac{1}{\sqrt{\mathcal{N}}}\sum_{\vec{j}}|\vec{s}, m; \vec{j}\rangle, \tag{3.7}$$

implicitly defining the kets $|\vec{s}, m; \vec{j}\rangle$ which are localized in minimum $m$ in the unit cell located at $2\pi\vec{j}$ and are offset-charge dependent. Here, $\mathcal{N}$ is the number of unit cells. It is straightforward to show that $|\psi_{\vec{n}_g,\vec{s},m}\rangle$ satisfies the quasiperiodicity condition (3.1). We now represent the Schrödinger equation in terms of these basis states. Due to their lack of orthogonality, this transforms the Schrödinger equation into the generalized eigenvalue problem

$$\frac{1}{\mathcal{N}}\sum_{\vec{s},m}\sum_{\vec{j},\vec{j}'}\Big(\langle\vec{s}', m'; \vec{j}'|H|\vec{s}, m; \vec{j}\,\rangle - E\langle\vec{s}', m'; \vec{j}'|\vec{s}, m; \vec{j}\,\rangle\Big)b_{\vec{s},m} = 0, \tag{3.8}$$

where $E$ is the eigenenergy and $b_{\vec{s},m}$ are the coefficients in the decomposition

$$|\psi_{\vec{n}_g}\rangle = \sum_{\vec{s},m} b_{\vec{s},m}|\psi_{\vec{n}_g,\vec{s},m}\rangle. \tag{3.9}$$

Eq. (3.8) can be simplified by performing one of the sums over lattice vectors [112]. We express the kets explicitly in terms of the translation operators

$$|\vec{s}, m; \vec{j}\rangle = e^{-i\vec{n}_g\cdot(2\pi\vec{j}+\vec{\theta}_m)}\mathcal{T}_{2\pi\vec{j}}|\vec{s}, m; \vec{0}\rangle, \tag{3.10}$$

and note that the operator $\mathcal{T}_{2\pi\vec{j}}$ commutes with the Hamiltonian. The summation yields a factor of $\mathcal{N}$ and we obtain

$$\sum_{\vec{s},m}\sum_{\vec{j}}\Big(\langle\vec{s}\,',m';\vec{0}\,|H|\vec{s},m;\vec{j}\,\rangle - E\langle\vec{s}\,',m';\vec{0}\,|\vec{s},m;\vec{j}\,\rangle\Big)b_{\vec{s},m}=0. \tag{3.11}$$

Formally, Eq. (3.11) now has the standard form of a generalized eigenvalue problem with two semidefinite positive Hermitian matrices and can be handled numerically by an appropriate solver. To perform the diagonalization, the crucial remaining task consists of the efficient evaluation of the matrix elements and state overlaps in Eq. (3.11) which we cover in Ch. 6. Note that an alternative route to this equation is application of the variational principle to $\langle\psi_{\vec{n}_g}|H|\psi_{\vec{n}_g}\rangle = E\langle\psi_{\vec{n}_g}|\psi_{\vec{n}_g}\rangle$ [123]; the benefit of this viewpoint is that the eigenenergies thus obtained represent upper bounds to the true eigenenergies of the system [123, 124].

Our analysis thus far has assumed a purely periodic potential, allowing for a direct analogy with the theory of tight binding as applied to solids. Including inductive terms in the potential immediately implies that associated degrees of freedom are no longer subject to (quasi-)periodic boundary conditions. Alternatively, we can say that the unit cell extends along the relevant axes. To include such inductive potential terms, we therefore do not perform periodic summation in Eq. (3.7) along these non-periodic directions.

## 3.3 Example: transmon

We now consider the simple example of applying the previously developed theory to the transmon. The Hamiltonian of the transmon is [38]

$$H_{\text{tmon}} = 4E_C(-i\partial_\phi - n_g)^2 - E_J\cos(\phi), \tag{3.12}$$

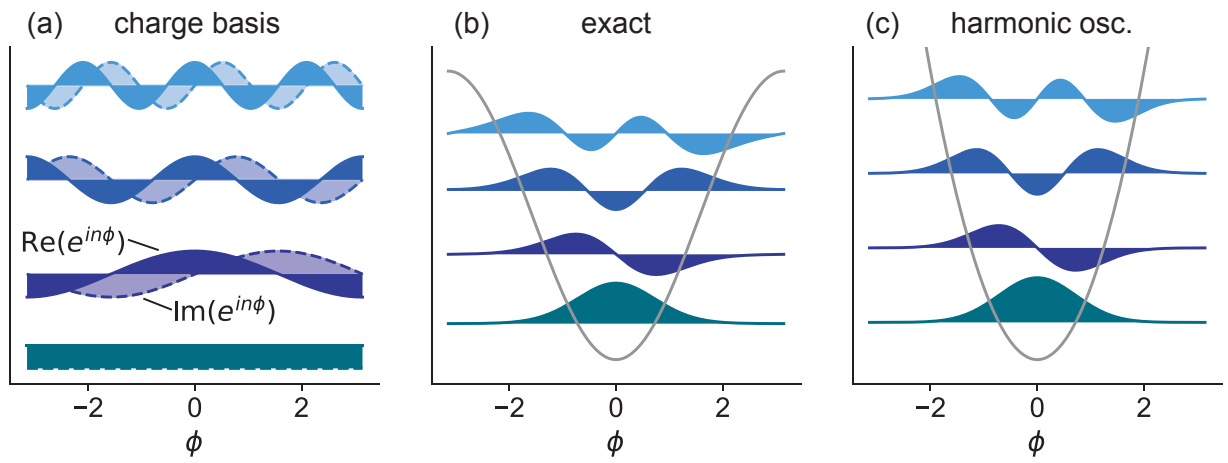


**Figure 3.2:** Comparison of charge-basis and harmonic-oscillator states to exact transmon eigenfunctions. (a) The real and imaginary parts of the charge-basis states . (b) Exact transmon eigenstates for $E_J/E_C = 30$ obtained from diagonalization in the charge basis. (c) Harmonic-oscillator states with oscillator length $\Xi = (8E_C/E_J)^{1/4}$.

where we write the conjugate momentum in the $\phi$ basis as $n = -i\partial_\phi$. The gauge transformation to remove the offset charge from the Hamiltonian is $U = e^{-in_g\phi}$, yielding

$$\bar{H}_{\text{tmon}} = e^{-in_g\phi} H_{\text{tmon}} e^{in_g\phi} = -4E_C\partial_\phi^2 - E_J \cos(\phi). \tag{3.13}$$

Before the gauge transformation, the wave functions obeyed periodic boundary conditions $\psi(\phi + 2\pi) = \psi(\phi)$. The transformed wave functions $\bar{\psi}(\phi) = e^{-in_g\phi}\psi(\phi)$ now obey quasiperiodic boundary conditions $\bar{\psi}(\phi + 2\pi) = e^{-i2\pi n_g}\bar{\psi}(\phi)$, c.f. Eq.(3.1).

Expanding the potential around the only minimum in the central unit cell at $\phi = 0$ yields the local Hamiltonian

$$\bar{H}'_{\text{tmon}} = -4E_C\partial_\phi^2 + \frac{E_J}{2}\phi^2. \tag{3.14}$$

Because the transmon has only a single degree of freedom, the capacitance and inverse inductance matrices are just numbers and we obtain $\Xi = (8E_C/E_J)^{1/4}$. This is the well-known expression for the harmonic length of the transmon [38].

Deep in the transmon regime $E_J \gg E_C$ [38], the local wave functions (harmonic-oscillator

states) qualitatively match the exact transmon wave functions obtained numerically, see Fig. 3.2. Of course, the harmonic-oscillator states must be periodically repeated in the manner shown in Eq. (3.7) to obtain wave functions that obey the correct boundary conditions. On the other hand, the Hamiltonian $H_{\text{tmon}}$ is typically expressed in the charge basis for a numerical analysis of eigenvalues and eigenstates, identifying $\cos(\phi) = \frac{1}{2}(\sum_n n|n\rangle\langle n+1| + \text{H.c.})$. Here, the state $|n\rangle$ corresponds to the number $n$ of Cooper pairs having passed through the junction of the transmon. In the transmon regime, individual charge-basis states are not good approximations to transmon eigenstates, see Figs. 2.1 and 3.2. This implies that we generally need fewer tight-binding states as compared to charge basis states to obtain a specified level of numerical accuracy. For the small-scale example of the transmon, this numerical benefit likely does not outweigh the increase in complexity of the tight-binding method relative to diagonalization in the charge basis. However, we show in Ch. 6 that for larger circuits, the tight-binding method allows for the numerical analysis of circuits that are out of the reach of charge-basis diagonalization.

# 4 Control

*This chapter is based on the recent preprint (submitted for publication) D. K. Weiss et al., arXiv:2207.03971 (2022).*

In search of two-qubit gate fidelities exceeding the current state-of-the-art, it is worth re-examining the framework routinely used for developing the pulse trains which generate the gates of interest. Most commonly, this framework is intimately linked to the use of the rotating-wave approximation (RWA) [125]. This approximation is highly convenient as it can help remove fast time dependence from the Hamiltonian, yields an intuitive picture of the dynamics, and makes calculations particularly simple [14]. However, the range of validity of the RWA is limited and reliance on it constrains the parameter space explorable for maximizing gate fidelities.

Indeed, strong drives beyond the reach of the RWA have been shown to yield high-fidelity gates [31, 55], see also Fig. 2.4. To predict the time evolution in this regime we employ a Magnus expansion [65, 66, 67]. In the following we first derive the general form of the Magnus expansion, before applying it to the textbook example of a two-level system subject to a transverse drive. We identify two regimes of interest for applying the Magnus expansion. The first is where the qubit frequency is larger than the drive amplitude. Here, the first-order effects reduce to the RWA results, while higher-order terms in the Magnus expansion yield corrections to the RWA. The second is the regime where the drive strength overwhelms the qubit frequency. This case represents an extreme breakdown of the RWA, where it ceases to have any validity whatsoever.

## 4.1 Magnus expansion derivation

In the following, we closely follow Ref. [66]. We assume an exponential solution $U(t) = \exp[\Omega(t)]$ to the differential equation

$$\frac{dU(t)}{dt} = \lambda A(t)U(t), \tag{4.1}$$

where we have introduced the order-counting parameter $\lambda$ that is set to 1 at the end of the calculation. The time-dependent Schrödinger equation is a special case of Eq. (4.1), with $A(t) = -iH(t)/\hbar$, where $H(t)$ is the time-dependent Hamiltonian and $U(t)$ is the propagator. The argument $\Omega$ of the exponential is expanded as $\Omega(t) = \sum_{n=1}^{\infty} \lambda^n \Delta_n(t)$, and the goal is to obtain explicit expressions for the $\Delta_n(t)$. To proceed, we make use of the parameter-differentiation formula [66]

$$\frac{d}{d\nu} \exp(\beta\Omega) = \int_0^\beta du \exp([\beta - u]\Omega) \frac{d\Omega}{d\nu} \exp(u\Omega), \tag{4.2}$$

where $\nu$ is some parameter, $\Omega \equiv \Omega(\nu)$ and $\beta$ is independent of $\nu$. This formula can be derived e.g. using the powerful operator-ordering calculus introduced by Feynman [126]. Observe that Eq. (4.2) reduces to the usual expression $\frac{d}{d\nu} e^{\beta\Omega} = \beta \left(\frac{d\Omega}{d\nu}\right) e^{\beta\Omega}$ when the quantities involved are c-numbers as opposed to operators. To cast Eq. (4.2) into a more useful form, we make the substitutions $\beta = 1, u = 1 - x$ and $\nu = t$, yielding

$$\frac{d}{dt} e^{\Omega} = \int_0^1 dx\, e^{x\Omega} \frac{d\Omega}{dt} e^{-x\Omega} e^{\Omega}. \tag{4.3}$$

Equating Eqs. (4.1) and (4.3) we obtain

$$\int_0^1 dx\, e^{x\Omega} \frac{d\Omega}{dt} e^{-x\Omega} = \lambda A(t). \tag{4.4}$$

To expand the left-hand side of Eq. (4.4), we utilize the Baker-Campbell-Hausdorff (BCH) formula [66, 127, 128, 129, 130]

$$e^S H e^{-S} = \sum_{n=0}^{\infty} \frac{1}{n!} (\hat{S})^n (H) = H + [S, H] + \frac{1}{2!}[S, [S, H]] + \ldots, \tag{4.5}$$

introducing notation $\hat{S}(H) = [S, H]$ for the adjoint action of the operator $S$. We obtain

$$\lambda A(t) = \int_0^1 dx \sum_{j=0}^{\infty} \frac{x^j}{j!} (\hat{\Omega})^j \left( \frac{d\Omega}{dt} \right) = \sum_{j=0}^{\infty} \frac{1}{(j+1)!} (\hat{\Omega})^j \left( \frac{d\Omega}{dt} \right), \tag{4.6}$$

performing the integration straightforwardly. Inserting the definition $\Omega(t) = \sum_{n=1}^{\infty} \lambda^n \Delta_n(t)$ yields

$$\begin{aligned} \lambda A(t) &= \sum_{j=0}^{\infty} \frac{1}{(j+1)!} \overbrace{\left( \sum_{n=1}^{\infty} \lambda^n \Delta_n(t) \right)^j} \left( \sum_{m=1}^{\infty} \lambda^m \dot{\Delta}_m(t) \right) \\ &= \lambda \dot{\Delta}_1(t) + \frac{1}{2!} \lambda^2 [\Delta_1(t), \dot{\Delta}_1(t)] + \lambda^2 \dot{\Delta}_2(t) + \ldots \end{aligned} \tag{4.7}$$

In the last line of Eq. (4.7) we have written out explicitly the terms that contribute up to second order in $\lambda$. We may now obtain expressions for the $\Delta_n(t)$ by equating the coefficients of like powers of $\lambda$. Equating the first-order terms yields

$$\Delta_1(t) = \int_0^t dt' \, A(t'). \tag{4.8}$$

We then insert this result into the second-order equation to obtain

$$\Delta_2(t) = \frac{1}{2} \int_0^t dt_1 \int_0^{t_1} dt_2 [A(t_1), A(t_2)]. \tag{4.9}$$

Higher-order terms are similarly calculated. Explicit formulas for the $\Delta_n(t)$ up to $n = 4$ are given in, e.g., Ref. [66].

We apply the Magnus expansion in the following to a two-level system subject to a transverse

sinusoidal drive, described by the Hamiltonian

$$H = -\frac{\hbar\omega}{2}\sigma_z + A\sin(\omega_d t)\sigma_x, \tag{4.10}$$

where $\omega$ is the qubit frequency, $A$ and $\omega_d$ are the drive amplitude and frequency, respectively and $\sigma_x, \sigma_z$ are the usual Pauli matrices. In Ch. 7, this Hamiltonian will arise in the context of parametric flux drives. Upon rotating into a suitable reference frame, the Magnus expansion allows for an analytic approximation to the time-evolution operator. In particular, we are often interested in the form of the propagator after an integer number of drive periods such that the pulse contains net-zero flux [131].

## 4.2 Relatively weak drive

We consider the regime where the qubit energy is larger than the drive amplitude $\hbar\omega > A$. The typical parameter regime for high-frequency qubits is $\hbar\omega \gg A$, where the RWA is expected to be valid and the formalism employed here is not necessary. If instead the drive amplitude approaches the qubit frequency $\hbar\omega \gtrsim A$, then the RWA may fail and corrections to the RWA are required. To carry out the Magnus expansion in this parameter regime, it is appropriate to move into the interaction picture defined by the unitary

$$U_0(t) = \exp\left(i\frac{\omega}{2}\sigma_z t\right). \tag{4.11}$$

The interaction-frame Hamiltonian is

$$H'(t) = U_0^\dagger H U_0 - i\hbar U_0^\dagger \dot{U}_0 = A\sin(\omega_d t)[\cos(\omega t)\sigma_x + \sin(\omega t)\sigma_y]. \tag{4.12}$$

We include the first two terms in the Magnus series. It is straightforward to calculate higher-order corrections, however we find that they are small and can be neglected for typical parameters utilized

in Ch. 7. At the conclusion of the gate $t = n\tau_d$, we obtain

$$U'(n\tau_d) = \cos(\xi)\,\mathbb{1} - i\sin(\xi)\,(\vec{n}\cdot\vec{\sigma}), \tag{4.13}$$

where

$$\vec{n} = (\sin[\pi n\omega/\omega_d], -\cos[\pi n\omega/\omega_d],\, \varepsilon/\xi), \quad \vec{\sigma} = \left(\sigma_x, \sigma_y, \sigma_z\right), \tag{4.14}$$

and we have defined

$$\xi = \frac{2A\omega_d}{\hbar(\omega_d^2-\omega^2)}\sin\left(\frac{\pi n\omega}{\omega_d}\right), \quad \varepsilon = \frac{A^2\omega_d^2\sin(2\pi n\omega/\omega_d)}{\hbar^2(\omega_d^2-\omega^2)^2} + \frac{A^2\pi n\omega}{\omega_d\hbar^2(\omega_d^2-\omega^2)}. \tag{4.15}$$

We have neglected corrections of order $\mathcal{O}([A/\hbar\omega_d]^3)$ to $\xi$, accounting for the deviation of $\vec{n}$ from being a unit vector. The first-order terms involving $\sigma_x, \sigma_y$ determine the amount of population transfer between the two states. The second-order terms encode the leading-order beyond-the-RWA corrections and are proportional to $\sigma_z$. Indeed, in the resonant limit, the first-order term $\Delta_1(n\tau_d) = -i\frac{n\tau_d}{\hbar}\frac{A}{2}\sigma_y$ reproduces the RWA result [14] while the second-order term $\Delta_2(n\tau_d) = i\frac{n\tau_d}{\hbar^2}\frac{3A^2}{8\omega_d}\sigma_z$ corresponds to the well-known Bloch-Siegert shift [57, 68]. Transforming the propagator back to the lab frame via the identity $U(\tau_n) = U_0(\tau_n)U'(\tau_n)U_0(0)^\dagger$, we find

$$\begin{aligned} U(n\tau_d) &= \exp(i\vartheta\sigma_z)[\cos(\xi)\mathbb{1} - i\varepsilon\,\mathrm{sinc}(\xi)\sigma_z] + i\sin(\xi)\sigma_y \\ &\approx \cos(\xi)\exp\{i[\vartheta - \varepsilon\,\mathrm{tanc}(\xi)]\sigma_z\} + i\sin(\xi)\sigma_y \\ &= \begin{pmatrix} \cos(\xi)e^{i(\vartheta-\mathrm{tanc}[\xi]\varepsilon)} & \sin(\xi) \\ -\sin(\xi) & \cos(\xi)e^{-i(\vartheta-\mathrm{tanc}[\xi]\varepsilon)} \end{pmatrix} \end{aligned} \tag{4.16}$$

defining $\vartheta = \pi n\omega/\omega_d$. The approximate equality is valid for $\mathrm{tanc}(\xi)\varepsilon \ll 1$, and $\mathrm{tanc}(x) = \tan(x)/x$. Specific unitaries can be engineered by varying the drive parameters $A, \omega_d$ which determine the variables $\xi, \epsilon$. Examples of this can be found in Ch. 7.

## 4.3 Relatively strong drive

To carry out a Magnus expansion in the regime where the qubit frequency $\omega$ is small compared to the drive amplitude $A$, it is appropriate to move into the interaction picture with respect to the drive. This transformation is achieved via the unitary

$$U_0(t) = \exp\left(\frac{-i}{\hbar}\int_0^t dt'\, A\sin[\omega_d t]\sigma_x\right) = \exp\left(\frac{-i}{\hbar}\frac{2A}{\omega_d}\sin^2\left[\frac{\omega_d t}{2}\right]\sigma_x\right). \tag{4.17}$$

The interaction-frame Hamiltonian is

$$H' = -\frac{\hbar\omega}{2}\cos\left(\frac{4A}{\hbar\omega_d}\sin^2\left[\frac{\omega_d t}{2}\right]\right)\sigma_z - \frac{\hbar\omega}{2}\sin\left(\frac{4A}{\hbar\omega_d}\sin^2\left[\frac{\omega_d t}{2}\right]\right)\sigma_y. \tag{4.18}$$

We carry out the Magnus expansion in the interaction frame, and truncate the Magnus series after the first term (in Ch. 7 we will find numerically that second-order terms are small and can be neglected). The propagator at time $t = n\tau_d = n2\pi/\omega_d$ is

$$U'(n\tau_d) = \cos\left(\frac{n\pi\omega}{\omega_d}J_0\left[\frac{2A}{\hbar\omega_d}\right]\right)\mathbb{1} + i\sin\left(\frac{n\pi\omega}{\omega_d}J_0\left[\frac{2A}{\hbar\omega_d}\right]\right)\left(\cos\left[\frac{2A}{\hbar\omega_d}\right]\sigma_z + \sin\left[\frac{2A}{\hbar\omega_d}\right]\sigma_y\right), \tag{4.19}$$

where $J_0$ is the zeroth-order Bessel function of the first kind. The propagators in the lab and interaction frames are related by $U(t) = U_0(t)U'(t)U_0^\dagger(0)$. Because the lab and interaction frames coincide at $t = 0$ and $t = n\tau_d$, the propagators in the lab and interaction frames are the same at the conclusion of the pulse. As in the previous section, in some cases it is possible to analytically solve for the variables $A$ and $\omega_d$ that yield a particular quantum gate or unitary. For example, to obtain an identity gate, the general solution is

$$\frac{n\pi\omega}{\omega_d}J_0\left(\frac{2A}{\hbar\omega_d}\right) = 2\pi r, \quad r \in \mathbb{Z}. \tag{4.20}$$

# 5 Current Mirror

*This chapter is based on material published in D. K. Weiss et al., Phys. Rev. B* **100***, 224507 (2019) (Editor's Suggestion).*

In this chapter we analyze the spectrum and coherence properties of the current-mirror circuit, introduced by Kitaev [52] in 2006 as one of the first proposals for an intrinsically protected superconducting qubit. We extend Kitaev's treatment by performing a full circuit analysis of the device, and derive an effective model that describes both the origin of the $\cos(2\phi)$ model and the processes that break degeneracy. Using these results we quantify both the spectrum and coherence times of the current mirror.

## 5.1 Full circuit analysis

The current mirror, shown in Fig. 5.1, consists of two linear arrays of $N$ Josephson junctions each that are capacitively coupled to form a ladder. One end of the ladder is then twisted and connected to the other end, thus producing a Möbius strip. The upper and lower edges of the strip are connected by capacitors (capacitance $C_B$), forming a series of rungs. In a device with $2N$ junctions, there are $N$ such rungs. Each node in the circuit additionally has a small capacitance to ground (capacitance $C_g$, not shown in Fig. 5.1). The Josephson junctions are characterized by their junction capacitance $C_J$ and Josephson energy $E_J$. The scope of this work is concerned with the ideal current-mirror circuit in which all junctions, all capacitor rungs, and all ground capacitances are assumed identical.

The circuit may be described in terms of generalized flux variables $\Phi_i$ for each node $1 \leq i \leq 2N$. To simplify notation, we employ reduced flux variables $\phi_i = 2\pi\Phi_i/\Phi_0$. The circuit Lagrangian for

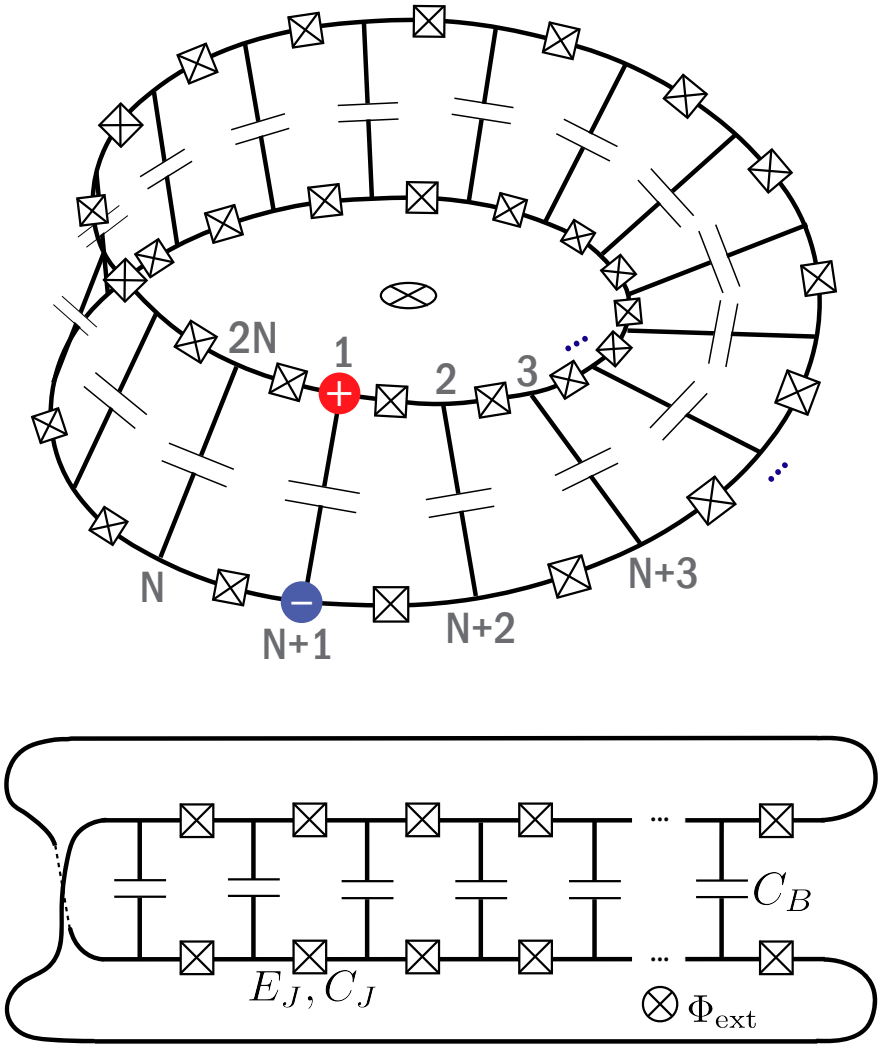


**Figure 5.1:** The current-mirror circuit, consisting of an array of Josephson junctions ($E_J$, $C_J$) capacitively coupled ($C_B$) to form a Möbius strip. Low-energy excitations in the intended parameter regime are Cooper-pair excitons, such as the one shown on rung 1. An external flux $\Phi_{\text{ext}}$ penetrating the interior of the Möbius strip may be used to tune the spectrum of the circuit.

the current mirror is obtained using the method of Devoret [96, 97], and reads

$$\mathcal{L} = \frac{1}{2}\left(\frac{\Phi_0}{2\pi}\right)^2 \sum_{i,j=1}^{2N} \dot{\phi}_i \mathsf{C}_{ij} \dot{\phi}_j + \hbar \sum_{j=1}^{2N} \dot{\phi}_j n_{gj} + {\sum_{j=1}^{2N}}' E_J \cos(\phi_{j+1} - \phi_j - \phi_{\text{ext}}/2N), \tag{5.1}$$

where $n_{gj}$ denotes the offset charge associated with node $j$. An external magnetic flux $\Phi_{\text{ext}} = \phi_{\text{ext}}\Phi_0/2\pi$ may be applied to the interior of the Möbius strip, as shown in Fig. 5.1. The primed sum in Eq. (5.1) is understood modulo $2N$, i.e., $\phi_{2N+1}$ is identified with $\phi_1$. Finally, the capacitance matrix $\mathsf{C}$ is given by [1]

$$\mathsf{C}_{ij} = \begin{cases} C_g + 2C_J + C_B, & i = j \\ -C_J, & i = j \pm 1 \\ -C_B, & i = j \pm N \\ 0, & \text{otherwise.} \end{cases} \tag{5.2}$$

We obtain the Hamiltonian via Legendre transform and quantize it in the usual way by promoting coordinates and conjugate momenta to operators that satisfy the commutation relations $[e^{i\phi_j}, n_k] = -e^{i\phi_j}\delta_{j,k}$. This results in the circuit Hamiltonian

$$H = \sum_{i,j=1}^{2N} 4(\mathsf{E}_{\mathsf{C}})_{ij}(n_i - n_{gi})(n_j - n_{gj}) - {\sum_{j=1}^{2N}}' E_J \cos(\phi_{j+1} - \phi_j - \phi_{\text{ext}}/2N), \tag{5.3}$$

where we have introduced the charging-energy matrix $(\mathsf{E}_{\mathsf{C}})_{ij} = e^2\mathsf{C}^{-1}_{ij}/2$.

Obtaining the spectrum of Eq. (5.3) is challenging due to the large number of circuit degrees of freedom. Exact diagonalization in the charge basis is feasible for $N \leq 3$ in the relevant parameter regime. For circuit sizes $N > 3$, memory requirements for storing the Hamiltonian in the charge basis exceed 1 terabyte when using a charge cutoff of $n_c = 10$ for each node. The predicted intrinsic protection from relaxation and dephasing, however, specifically requires circuits of large size $N \gg 1$ [52]. Therefore, a reduced effective model is needed for a numerical analysis of the circuit's

[1] Indices $i$, $j$ are interpreted modulo $2N$.

spectrum and coherence properties. Such an effective model can be obtained when focusing on the concrete parameter regime affording decoherence protection identified by Kitaev, and is further motivated by Ref. [108]. In this regime, the circuit is predicted to develop a robust ground-state degeneracy, rendering the circuit insensitive to dephasing channels. Further, the two lowest-energy eigenstates $|0\rangle$ and $|\pi\rangle$ should have nearly disjoint support in the multi-dimensional configuration space defined by $\phi_1, \ldots, \phi_{2N}$. As a consequence, all transition matrix elements $\langle 0|\mathcal{O}|\pi\rangle$ of local operators $\mathcal{O}$ are exponentially suppressed, and the circuit is protected from transitions among the computational basis states.

The protected parameter regime is established by a hierarchical ordering of energy scales. First, the Josephson energy is required to be smaller than the junction charging energy, such that Cooper-pair tunneling can be treated perturbatively. Second, the capacitances $C_B$ are expected to be so large that the associated charging energy forms the smallest charging energy in the hierarchy. The protected parameter regime is thus summarized by the conditions

$$N \gg 1, \quad E_J < E_{C_J}, \quad E_{C_B} < E_{C_J} < E_{C_g}, \tag{5.4}$$

where $E_{C_a} = e^2/2C_a$. If offset charges vanish and Josephson tunneling is neglected, the lowest-energy excitations are Cooper-pair excitons (with charging energy $\sim E_{C_B}$) consisting of a Cooper pair and a Cooper-pair hole [52, 108, 132], positioned across a big-capacitor rung, see Fig. 5.1 for an example. In exciton-hopping among adjacent rungs of the ladder, these two charges move together and generate counter-propagating currents – hence the name "current mirror" [52]. We call non-exciton charge excitations "agitons," which incur significantly higher charging energies proportional to $E_{C_J}$ or $E_{C_g}$.[2] The separation into a low-energy subspace including only exciton excitations, and a high-energy subspace including agiton excitons is the key ingredient for the development of the effective model to be described next.

[2]Note that in the presence of charge frustration, the nature of the low-energy excitations changes from Cooper-pair excitons to Cooper-pair and void excitons [52, 108, 132]. We do not consider such effects here, however we remark that in the presence of such charge frustration the overall behavior of the circuit is not expected to change [52].

## 5.2 Effective model

The essential idea behind the effective model is to integrate out high-energy agiton excitations in a perturbative treatment of the Cooper-pair tunneling. The tunneling of a single Cooper pair converts an exciton into an agiton. Since the tunneling amplitude $\sim E_J$ is small compared to the agiton charging energy $\sim E_{C_J}, E_{C_g}$, such an agiton state will take on the role of a virtual intermediate state before the exciton is restored via a second Cooper-pair tunneling step, see Fig. 5.2(a). We capture this physics by employing a Schrieffer-Wolff transformation [14, 133, 134, 135, 136, 137]. The interested reader can find in Appendix A a derivation of the general Schrieffer-Wolff transformation along with associated Mathematica ® code for carrying out the analysis using computer algebra.

The unperturbed Hamiltonian is composed of the charging energy terms

$$H_0 = \sum_{i,j=1}^{2N} 4(\mathsf{E_C})_{ij}(n_i - n_{gi})(n_j - n_{gj}), \tag{5.5}$$

while the perturbing Hamiltonian is composed of the Josephson tunneling contributions

$$V = -\frac{E_J}{2}\sum_{j=1}^{2N} e^{i(\phi_{j+1}-\phi_j)}e^{-i\phi_{\mathsf{ext}}/2N} + \text{H.c.} \tag{5.6}$$

The unperturbed Hamiltonian $H_0$ divides the Hilbert space into the low-energy subspace $\alpha$ that includes the lowest-energy states, spanned exclusively by exciton-charge states and a subspace $\gamma$ that includes agiton charge states. The corresponding unperturbed eigenenergies and eigenstates are denoted $E_{i,\alpha}$, $E_{j,\gamma}$ and $|i,\alpha\rangle$, $|j,\gamma\rangle$. Cooper-pair tunneling acts as a perturbation $V = V_{\mathsf{d}} + V_{\mathsf{od}}$, coupling the two manifolds via its block-off-diagonal component

$$V_{\mathsf{od}} = \sum_{i,j} |i,\alpha\rangle\langle i,\alpha|H_J|j,\gamma\rangle\langle j,\gamma| + \text{H.c.},$$

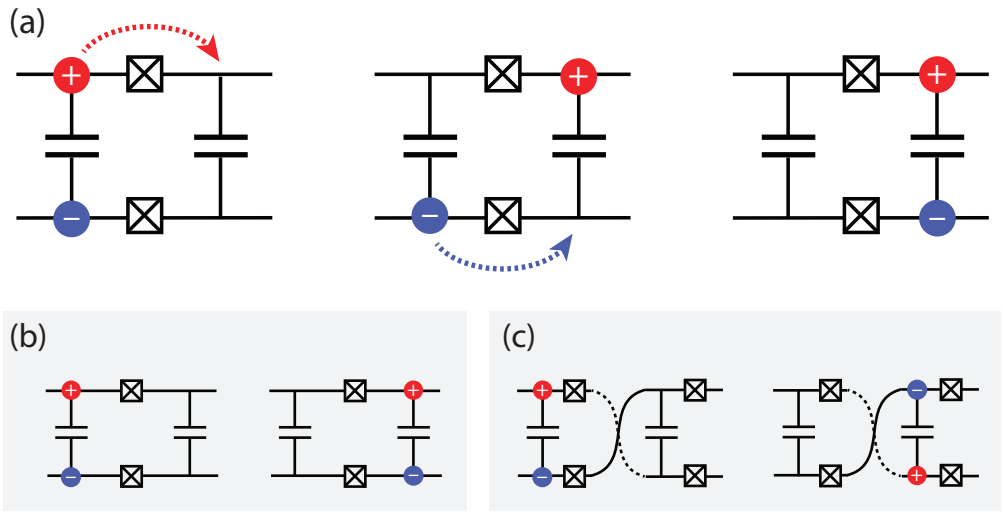


**Figure 5.2:** (a) The tunneling of an exciton from one rung to the next: the Cooper-pair hole tunnels to the right, followed by its partner Cooper pair (or vice versa). (b) Effect of exciton tunneling among regular sites. (c) Exciton tunneling across the stitching point reverses the exciton sign, and corresponds to exciton annihilation on both adjacent rungs.

and individual states within the agiton subspace via its block-diagonal part

$$V_{\mathrm{d}} = \sum_{j,j'} |j,\gamma\rangle\langle j,\gamma|H_J|j',\gamma\rangle\langle j',\gamma|.$$

(Matrix elements between states in the exciton subspace vanish.) Before explicitly carrying out the Schrieffer-Wolff transformation, we first introduce the exciton and agiton variables that allow for analytic expressions for the bare eigenenergies as well as a straightforward interpretation of the effective Hamiltonian.

### 5.2.1 Exciton and agiton variables

We formalize the notion of excitons and agitons by introducing the respective variables

$$\phi_j^{\pm} = \phi_j \pm \phi_{N+j}, \tag{5.7}$$

where $-$ and $+$ correspond to exciton and agiton, respectively. We also correspondingly introduce exciton and agiton charge-number operators

$$n_j^{\pm} = \frac{n_j \pm n_{N+j}}{2}. \tag{5.8}$$

Here, the variable index now ranges from $j = 1, \ldots, N$. These definitions render commutators among the new operators canonical, i.e.,

$$[e^{i\phi_j^{\sigma}}, n_k^{\tau}] = -e^{i\phi_j^{\sigma}} \delta_{jk} \delta_{\sigma\tau}, \qquad \sigma, \tau = \pm. \tag{5.9}$$

We note that quantum numbers of the exciton charge and agiton charge operators obey a simple constraint: for each rung $j$ the two charge quantum numbers must be either both integer, or both half-integer. For instance, a single exciton on rung $k$ corresponds to $n_k^- = 1, n_k^+ = 0$. If, on the other hand, rung $k$ hosts a single Cooper pair on site $k$ (no charge on site $k+N$), then we have $n_k^- = -1/2$ and $n_k^+ = -1/2$. The subspace spanned exclusively by exciton states has quantum numbers $\{n_j^+ = 0\}$ and integer-valued $n_j^-$.

In terms of exciton and agiton variables, the full circuit Hamiltonian is

$$\begin{aligned} H = & \sum_{\sigma=\pm} \sum_{i,j=1}^{N} 4 \left(\mathsf{E}_{\mathsf{C}}^{\sigma}\right)_{i,j} \left(n_i^{\sigma} - n_{gi}^{\sigma}\right) \left(n_j^{\sigma} - n_{gj}^{\sigma}\right) \\ & - \sum_{j=1}^{N-1} 2E_J \cos(\tfrac{1}{2}[\phi_{j+1}^{+} - \phi_j^{+} - \tfrac{\phi_{\mathsf{ext}}}{N}]) \cos(\tfrac{1}{2}[\phi_{j+1}^{-} - \phi_j^{-}]) \\ & - 2E_J \cos(\tfrac{1}{2}[\phi_1^{+} - \phi_N^{+} - \tfrac{\phi_{\mathsf{ext}}}{N}]) \cos(\tfrac{1}{2}[\phi_1^{-} + \phi_N^{-}]), \end{aligned} \tag{5.10}$$

where offset charges $n_{gi}$ have been transformed in a way analogous to Eq. (5.8). Note that the potential energy, comprised of the terms in lines 2 and 3, is $4\pi$-periodic in the $\phi_j^{\pm}$ variables. This is a direct result of $n_j^{\pm}$ taking on half-integer values. Following this coordinate transformation, the charging energy matrix $\mathsf{E}_{\mathsf{C}}$ is brought into block-diagonal form by ordering variables according to

$\phi_1^-, \ldots, \phi_N^-, \phi_1^+, \ldots, \phi_N^+$:

$$\widetilde{\mathsf{E}_\mathsf{C}} = \begin{pmatrix} \mathsf{E}_\mathsf{C}^- & 0 \\ 0 & \mathsf{E}_\mathsf{C}^+ \end{pmatrix}. \tag{5.11}$$

Analytical expressions for these exciton and agiton charging-energy matrices $\mathsf{E}_\mathsf{C}^-$ and $\mathsf{E}_\mathsf{C}^+$ are obtained in Appendix B.

### 5.2.2 Exciton tunneling

The Schrieffer-Wolff transformation proceeds by constructing an effective Hamiltonian

$$H_{\mathsf{eff}} = Pe^S He^{-S} P, \tag{5.12}$$

order-by-order in the small parameters. We have defined the projector onto the low-energy subspace $P = \sum_i |i,\alpha\rangle\langle i,\alpha|$. The generator $S$ of the unitary transformation is anti-Hermitian and purely block off diagonal. Systematic construction of $S$ and of the resulting low-energy Hamiltonian $H_{\mathsf{eff}}$ proceeds via expansion in $V$ and iterative employment of the Baker-Campbell-Hausdorff relation, see Appendix A. To second order, this yields the exciton-hopping terms

$$H_{\mathsf{eff},2} = \frac{1}{2}|i,\alpha\rangle\langle i,\alpha|V|k,\gamma\rangle\langle k,\gamma|V|j,\alpha\rangle\langle j,\alpha| \left( \frac{1}{E_{i,\alpha} - E_{k,\gamma}} + \frac{1}{E_{j,\alpha} - E_{k,\gamma}} \right), \tag{5.13}$$

where here and in the following, summation over repeated Latin indices is implied. In this perturbative path for exciton hopping, a single high-energy virtual state $|k,\gamma\rangle$ is accessed. Calculation of the energy denominators in Eq. (5.13) in principle depends on the states $|i,\alpha\rangle$ and $|j,\alpha\rangle$ and their energies $E_{i,\alpha}$ and $E_{j,\alpha}$, respectively. However, for $N \lesssim 20$ the smallest charging-energy matrix element of the agiton coordinates, $E^+_{C\frac{N}{2}}$, is much larger than the largest charging-energy matrix element of the exciton coordinates, $E^-_{C0}$. Therefore, we may neglect exciton charging energies in the calculation of Eq. (5.13), leading to the simplified expression

$$H_{\mathsf{eff},2} = |i,\alpha\rangle\langle i,\alpha|V|k,\gamma\rangle \frac{1}{-E_{k,\gamma}} \langle k,\gamma|V|j,\alpha\rangle\langle j,\alpha|$$

The virtual state $|k,\gamma\rangle$ accessed depends on the initial state $|j,\alpha\rangle$. For instance, consider an exciton tunneling from rung $\ell$ to rung $\ell+1$. The initial state is given by $|\{n_i^+=0\},\{n_i^-\}\rangle$. There are two possible virtual agiton states, namely

$$|a\pm\rangle = |n_\ell^+ = \mp 1/2, n_{\ell+1}^+ = \pm 1/2, n_\ell^- = n_\ell - 1/2, n_{\ell+1}^- = n_{\ell+1} + 1/2\rangle \tag{5.14}$$

with energies $E_a^\pm$ that can be accessed. We thus find

$$H_{\text{eff},2} = \sum_{\ell=1}^{2N}{}' \Big( |i,\alpha\rangle\langle i,\alpha| e^{i\phi_{\ell+1}} e^{-i\phi_\ell} e^{-i\phi_{\text{ext}}/2N} |a-\rangle \frac{1}{-E_a^-} \langle a- | e^{-i\phi_{\ell+N+1}} e^{i\phi_{\ell+N}} e^{i\phi_{\text{ext}}/2N} |j,\alpha\rangle\langle j,\alpha|$$
$$+ |i,\alpha\rangle\langle i,\alpha| e^{-i\phi_{\ell+1}} e^{i\phi_\ell} e^{i\phi_{\text{ext}}/2N} |a+\rangle \frac{1}{-E_a^+} \langle a+ | e^{i\phi_{\ell+N+1}} e^{-i\phi_{\ell+N}} e^{-i\phi_{\text{ext}}/2N} |j,\alpha\rangle\langle j,\alpha| \Big). \tag{5.15}$$

It is clear from inspection of Eq. (5.15) that the external flux drops out exactly. This indicates weak sensitivity of the circuit to flux, which is only re-established by higher-order terms, as we will demonstrate below.

When neglecting exciton energies as compared to agiton coordinates, the intermediate-state energies become independent of the exciton quantum numbers

$$E_a^\pm = 2\Delta E_j^\pm = 2(E_{\mathsf{C}0}^+ - E_{\mathsf{C}1}^+) \pm 4\left[(\mathsf{E}_\mathsf{C}^+)_{m,j} - (\mathsf{E}_\mathsf{C}^+)_{m,j+1}\right] n_{gm}^+ + \mathcal{O}(E_{C0}^-). \tag{5.16}$$

Here, we have defined $E_{\mathsf{C}0}^+ = (\mathsf{E}_\mathsf{C}^+)_{j,j}$ and $E_{\mathsf{C}1}^+ = (\mathsf{E}_\mathsf{C}^+)_{j,j\pm1}$; see Appendix B for explicit expressions of the charging-energy matrix elements $(\mathsf{E}_\mathsf{C}^+)_{j,k}$. This simplification allows for the sum over initial states to be performed, yielding

$$H_{\text{eff},2} = -\sum_{j=1}^{N-1} J_j \cos(\phi_{j+1}^- - \phi_j^-) - J_N \cos(\phi_1^- + \phi_N^-), \tag{5.17}$$

where the identification $e^{i\phi_j^-} = \sum_n |n_j^- = n+1\rangle\langle n_j^- = n|$ has been used and terms merely introducing energy renormalization of charging energies are omitted. The resulting exciton-hopping

strengths are given by

$$J_j = \frac{E_J^2}{4}\left(\frac{1}{\Delta E_j^+} + \frac{1}{\Delta E_j^-}\right). \tag{5.18}$$

For vanishing agiton offset charges, $n_{gj}^+ = 0$, the exciton-hopping strengths simplify to the uniform expression

$$J = \frac{E_J^2}{2E_{\mathsf{C0}}^+ - 2E_{\mathsf{C1}}^+} = \frac{E_J^2}{2E_{C_J}} + \mathcal{O}\left(\frac{C_g}{C_J}, \frac{1}{N}\right). \tag{5.19}$$

The resulting effective Hamiltonian in the exciton subspace up to second order is

$$\begin{aligned} H_{\mathsf{eff}} = &\sum_{i,j=1}^{N} 4\left(\mathsf{E}_{\mathsf{C}}^-\right)_{i,j}\left(n_i^- - n_{gi}^-\right)\left(n_j^- - n_{gj}^-\right) \\ &- \sum_{j=1}^{N-1} J_j \cos(\phi_{j+1}^- - \phi_j^-) - J_N \cos(\phi_1^- + \phi_N^-). \end{aligned} \tag{5.20}$$

The sign deviation in the final exciton hopping term of Eq. (5.20) occurs as a direct consequence of the Möbius topology. Its origin can be understood with the help of Fig. 5.2, depicting the exciton tunneling process across the twist point. Generally, exciton tunneling is understood as exciton annihilation on one rung and creation on a neighboring rung, see Fig. 5.2(b). However, tunneling across the twist point results in either exciton annihilation or exciton creation on both rungs, see Fig. 5.2(c). We note that the specific location of the twist point is irrelevant to the physics, as variables may be cyclically permuted.

Inspection of the charging energies for excitons, $\mathsf{E}_{\mathsf{C}}^-$, shows that the charge-charge interaction is relatively short-ranged for excitons in the protected regime. Using analytical results from Appendix B, we find the asymptotic expressions

$$\begin{aligned} \left(\mathsf{E}_{\mathsf{C}}^-\right)_{j,j} &= \frac{e^2}{2C_B} + \mathcal{O}\left(\tfrac{C_J}{C_B}, \tfrac{C_g}{C_B}, \tfrac{1}{N}\right), \\ \left(\mathsf{E}_{\mathsf{C}}^-\right)_{j,j+1} &= \frac{e^2 C_J}{4C_B^2} + \mathcal{O}\left(\tfrac{C_J}{C_B}, \tfrac{C_g}{C_B}, \tfrac{1}{N}\right), \\ \left(\mathsf{E}_{\mathsf{C}}^-\right)_{1,N} &= -\frac{e^2 C_J}{4C_B^2} + \mathcal{O}\left(\tfrac{C_J}{C_B}, \tfrac{C_g}{C_B}, \tfrac{1}{N}\right). \end{aligned} \tag{5.21}$$

All other off-diagonal elements are strongly suppressed in higher powers of $C_J/C_B$.

Integrating out the agiton degrees of freedom restores $2\pi$-periodicity of the potential energy in Eq. (5.20), a direct consequence of the elimination of half-integer eigenvalues of $n_j^-$ in the exciton subspace. Inspection reveals that the potential energy has the form of an $N$-dimensional double-well potential, with minima located at $\{\phi_j^- = 0\}$ and $\{\phi_j^- = \pi\}$. The values of the two potential minima are identical, thus providing the basis for the (near-)degeneracy of ground and first excited eigenstates of the current-mirror circuit, as envisioned by Kitaev [52]. This degeneracy is broken by higher-order processes that carry net current around the circuit, or, equivalently, create or annihilate an odd number of excitons. These processes are discussed below.

### 5.2.3 Degeneracy-breaking terms

The leading-order processes that lift the degeneracy among the two potential minima correspond to the annihilation or creation of an odd number $m$ of excitons ($1 \leq m \leq N$), see Fig. 5.3. The circular circuit representation employed in that figure is topologically equivalent to the original Möbius circuit, where it is understood that capacitive connections do not "touch" each other at the center. In principle, constructing the effective Hamiltonian at $N^{\text{th}}$ order $H_{\text{eff},N}$ requires calculation of the generator to order $N-1$, $S = \sum_{n=1}^{n-1} S_n$. In practice, expressions for the generators beyond second order quickly become cumbersome. We sidestep this issue via proofs of the following statements, which allow us to include in the effective Hamiltonian all of the leading-order processes contributing to degeneracy breaking. i) The creation or annihilation of an odd number of excitons leads to degeneracy breaking. ii) Such processes require $N$-th order perturbation theory. iii) Leading-order exciton creation and annihilation leads to sign alternation, i.e., neighboring Cooper-pair charges alternate signs when moving around the circle, see Fig. 5.3. iv) Any process leading to the creation of an odd number of excitons that does not obey sign alternation is of higher order, and is therefore subdominant.

**Proposition 1.** *Degeneracy between the two potential minima at* $\{\phi_j^- = 0\}$ *and* $\{\phi_j^- = \pi\}$ *is broken by perturbative processes that create or annihilate an odd number of excitons. Perturbative processes that leave the exciton number invariant or change it by an even number do not lead to*

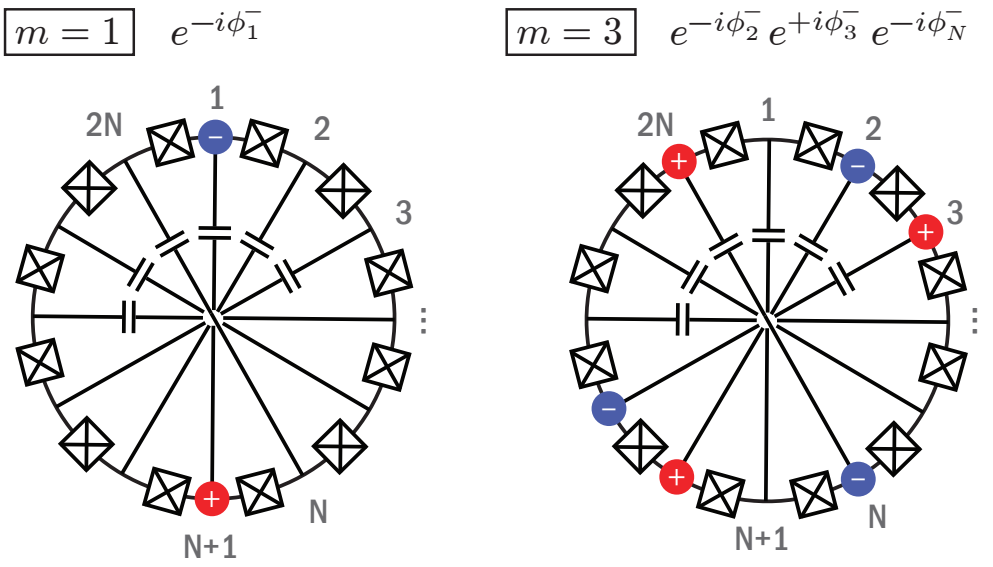


**Figure 5.3:** Creation of an odd number of excitons in the current-mirror circuit, here in its equivalent circular representation. Generation of a single exciton ($m = 1$) on rung $j = 1$ is achieved by the operator $e^{-i\phi_1^-}$. Likewise, $m = 3$ excitons with alternating signs are generated on rungs $j = 2, 3, N$ by the operator $e^{-i\phi_2^-}\, e^{i\phi_3^-}\, e^{-i\phi_N^-}$. The figure shows the configurations obtained when applying these operators to the charge-neutral circuit.

*degeneracy breaking.*

*Proof.* Consider a perturbative process creating or annihilating $m$ excitons at positions $j_1, \ldots, j_m \in \{1, \ldots, N\}$ with exciton signs specified by $s_1, \ldots, s_m \in \{-1, +1\}$. This process contributes a term to the effective Hamiltonian with operator content

$$A = \prod_{k=1}^{m} e^{is_k\phi_{j_k}^-} + \text{H.c.} = 2\cos\left(\sum_{k=1}^{m} s_k\phi_{j_k}^-\right). \tag{5.22}$$

Addition of $A$ to the Hamiltonian amounts to a modification of the potential energy. For even exciton number $m$, the cosine argument is zero at $\{\phi_j^- = 0\}$ and an even integer multiple of $\pi$ at $\{\phi_j^- = \pi\}$, thus changing the two potential minima equally and leaving the degeneracy intact. By contrast, for odd exciton number the cosine argument at $\{\phi_j^- = \pi\}$ is an odd integer multiple of $\pi$, thus leading to an overall sign change between the potential-minima shifts at $\{\phi_j^- = 0\}$ and $\{\phi_j^- = \pi\}$, effectively breaking the degeneracy. □

We will next prove two central statements. First, the leading order for creation or annihilation of an odd number of excitons is order $N$ (where $N$ is the number of big capacitors in the circuit). Second, every such $N$-th order process resulting in odd-number changes in exciton population leads to charge alternation: a '$+$' exciton is always followed by a '$-$' exciton, so that when circling the edge of the Möbius circuit, a Cooper-pair charge is always followed by a Cooper-pair hole, and vice versa. An example of this is

$$\begin{aligned} A_1 &= e^{-i\phi_2^-}\, e^{+i\phi_3^-}\, e^{-i\phi_N^-} + \text{H.c.} \\ &= e^{-i\phi_2} e^{+i\phi_3} e^{-i\phi_N} e^{i\phi_{N+2}} e^{-i\phi_{N+3}} e^{i\phi_{2N}} + \text{H.c.}, \end{aligned}$$

as shown in Fig. 5.3. The 3-exciton creation process described by $B = e^{i\phi_1^-} e^{i\phi_3^-} e^{i\phi_7^-} + \text{H.c.}$, on the other hand, does not obey charge alternation and is of order higher than $N$.

We first prove that odd-number exciton creation with charge alternation requires an $N$-th order process. To assess the minimal order of the perturbative term for exciton creation, we note that the process separates positive and negative charges and moves them in such a fashion to ultimately recover an exciton configuration. Each step of moving a charge along the circuit circumference is achieved by an operator from the perturbing Hamiltonian $H_J$, such as $e^{i\phi_j} e^{-i\phi_{j+1}}$, and increases the order of the perturbative process by one.

Our proof showing that order $N$ is the minimum required order relies on mapping our problem to a special instance of the so-called assignment problem known from combinatorial optimization [138, 139, 140], formulated as follows. Consider two ordered sets $M = \{m_1, m_2, \cdots, m_n\}$ and $P = \{p_1, p_2, \cdots, p_n\}$ which here denote the $n$ positions of minus and plus charges on the circuit. Each minus charge is generated by charge separation and increasing the relative difference to some plus charge. The perturbative order of the creation process is thus ascertained by assigning each minus charge to a plus charge and adding up their "spatial" separations. The order of a process is equal to the cost $C$ of a particular assignment, given by

$$C = \sum_{i,j} C(m_i, p_j) X_{ij}. \tag{5.23}$$

Here, assignments are recorded by the $n \times n$ permutation matrix $X$ with $X_{ij} = 1$ if $m_i$ is assigned to $p_j$; otherwise, $X_{ij} = 0$. Distance between positions on the circle is measured by

$$C(m_i, p_j) = \text{min}\Big[(m_i - p_j) \text{ mod } 2N,\, (p_j - m_i) \text{ mod } 2N\Big]. \tag{5.24}$$

Determining the minimum perturbative order required to achieve the desired exciton creation thus corresponds to finding the optimal assignment $X$ which minimizes the cost $C$. We first show that nearest-neighbor assignment on the circle for creation of an odd number of excitons obeying charge alternation leads to a cost of $N$, and subsequently prove that this assignment is optimal. (Hence, order $N$ is the leading order for odd-number exciton creation.)

**Proposition 2.** *For creation of an odd number of excitons obeying charge alternation, nearest-neighbor assignment has cost $N$.*

*Proof.* The proof proceeds by induction over the (odd) number $m$ of excitons. For the base case $m = 1$ (a single exciton trivially obeys charge alternation), there is only one Cooper-pair creation operator and one annihilation operator. The two generated charges are nearest neighbors with distance $N$, so the cost of the only possible assignment is $N$.

Next, assume that nearest-neighbor assignment indeed has a cost of $N$ for $m = n$ excitons alternating in sign, and show that the same is true for $m = n + 2$ excitons. To do so, decompose the creation operator $A_{n+2}$ for $n + 2$ excitons into creation of $n$ excitons,

$$\begin{aligned} A_n &= e^{-i\phi^-_{i_1}} e^{i\phi^-_{i_2}} \cdots e^{-i\phi^-_{i_n}} \\ &= e^{-i\phi_{i_1}} e^{i\phi_{i_2}} \cdots e^{-i\phi_{i_n}} e^{i\phi_{i_1+N}} e^{-i\phi_{i_2+N}} \cdots e^{i\phi_{i_n+N}}, \end{aligned} \tag{5.25}$$

and creation of two additional excitons, see Fig. 5.4. ("H.c." contributions are omitted from expressions to simplify notation.) For $A_n$, there are two different nearest-neighbor assignments with equal cost $N$: either pairing up $e^{-i\phi_{i_1}}$ and $e^{i\phi_{i_2}}$, or $e^{i\phi_{i_n+N}}$ and $e^{-i\phi_{i_1}}$. To maintain sign alternation,

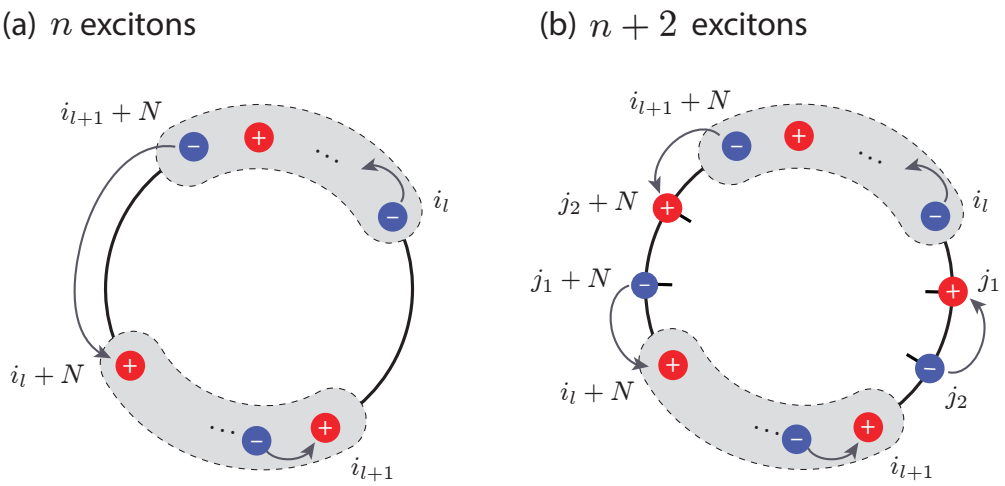


**Figure 5.4:** (a) Nearest-neighbor assignment for an odd number $n$ of excitons with alternating signs. For odd $n$, the assignment of $i_{l+1}+N$ to $i_l+N$ implies that the partner charges $i_{l+1}$ and $i_l$ are not assigned to each other (or vice versa). (b) Creation of $n+2$ excitons with alternating signs is obtained from creation of $n$ and inserting two nearest neighbor excitons with the appropriate signs. The cost for nearest-neighbor assignment remains $N$.

the additional two excitons on rungs $j_1$ and $j_2$ must be nearest neighbors, and $A_{n+2}$ has the form

$$A_{n+2} = e^{-i\phi^-_{i_1}} \cdots e^{-i\phi^-_{i_l}} e^{+i\phi^-_{j_1}} e^{-i\phi^-_{j_2}} e^{+i\phi^-_{i_{l+1}}} \cdots e^{-i\phi^-_{i_n}},$$

where the insertion point is between $i_l$ and $i_{l+1}$.

Without loss of generality, let us assume that for $A_n$, $i_l+N$ and $i_{l+1}+N$ are paired. Since $n$ is odd, this implies that $i_l$ and $i_{l+1}$ are not paired. Insertion of the two additional excitons then leads to the nearest-neighbor assignment shown in Fig. 5.4(b). The new cost of this assignment can be read off from the figure and is given by

$$\begin{aligned} N' = N &- (i_{l+1}+N-i_l-N) + (i_{l+1}+N-j_2-N) \\ &+ (j_1+N-i_l-N) + (j_2-j_1) = N, \end{aligned}$$

thus confirming that creation of $n+2$ excitons with alternating signs also carries cost $N$. □

While nearest-neighbor assignment thus leads to a cost of $N$, it remains to be shown that $N$ is

the minimum possible cost. The situation is straightforward for the assignment problem on the line, which is known to be solved by a greedy assignment, $m_i \to p_i$ [139]. The assignment problem on the circle, which we face here, requires more thought, see Ref. [140]. Therein, Werman et al. show that the circular assignment problem can be reduced to the linear one by identifying an appropriate cutting point. Once this point is used for cutting the circle, linear greedy assignment minimizes the cost. As a corollary to this general result, we can therefore state for our case:

**Corollary 1.** *The optimal assignment for creation of an odd number of excitons with alternating signs consists of nearest-neighbor assignment.*

*Proof.* This follows from the work by Werman et al., and from the fact that greedy assignment for charges with alternating signs results in nearest-neighbor assignment. □

Note that the nearest-neighbor assignment for an odd number of excitons obeying charge alternation leads to either a clockwise or a counter-clockwise assignment, i.e., all assignment arrows pointing from minus charges to plus charges are oriented clockwise or oriented counter-clockwise. A counter-clockwise assignment is shown in Fig. 5.4(b). Since the cost of both assignments is $N$, and we understand cost as order of perturbation theory, both contribute at $N$-th order.

Finally, we show that creation of an odd number of excitons not obeying sign alternation has an optimal cost strictly larger than $N$. To facilitate the proof, we require some additional notation borrowed from Ref. [140]. Given the ordered sets $M = \{m_i\}$ and $P = \{p_i\}$ for locations of minus and plus charges, we define

$$\begin{aligned} F_m(x) &= \left|\{i : m_i < x\}\right|, \\ F_p(x) &= \left|\{i : p_i < x\}\right|. \end{aligned} \tag{5.26}$$

Here, $F_m(x)$ counts the number of minus charges between the origin and position $x$ on the circle; likewise $F_p(x)$ does so for plus charges. The difference

$$F(x) = F_p(x) - F_m(x), \tag{5.27}$$

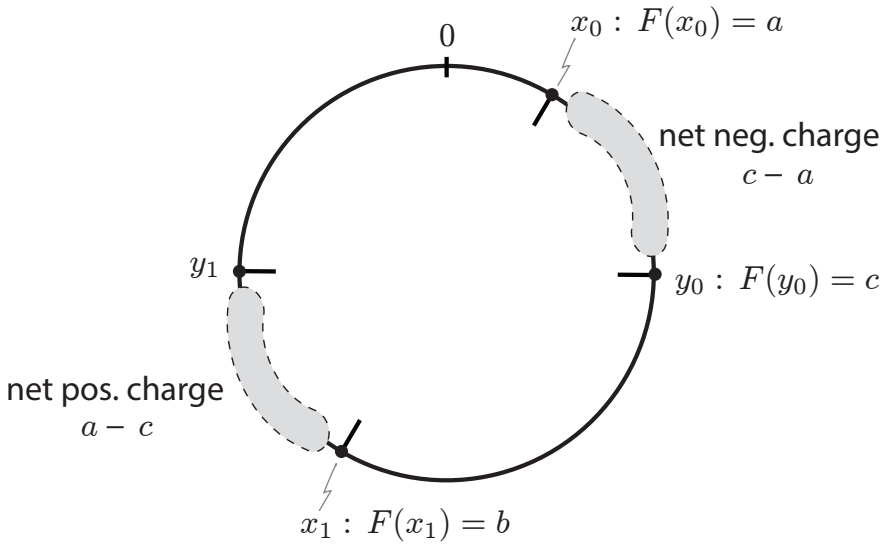


**Figure 5.5:** Visual aid for the proof of Lemma 1, showing that the point antipodal to $F(x_0) =$ max must be a point where $F =$ min.

quantifies the net positive charge between the origin and location $x$. $F$ is a piecewise constant function with discontinuities at charge locations. For an alternating charge configuration, $F$ alternates between either $0$ and $+1$, or $0$ and $-1$, such that $f = \max_x F(x) - \min_{x'} F(x') = 1$. For non-alternating charge configurations, $f$ exceeds 1.

The following three lemmas prove instrumental in the proof that excitons with non-alternating signs require a higher cost.

**Lemma 1.** *Consider a configuration of an odd number of excitons on the circle and let $x_0$ be a position where $F$ is maximal. Then the antipodal point $x_1 = x_0 + N$ marks a position where $F$ is minimal.*

*Proof.* The proof is by contradiction and aided visually by Fig. 5.5. Let $F(x_0) = a =$ max, and let $F(x_1) = b$ at the antipodal point $x_1 = x_0 + N$. Now assume that there exists some other point $y_0$ with $x_0 < y_0 < x_1$ that yields an $F$ even smaller: $F(y) = c < b$. (An analogous argument holds for $y_0 > x_1$.) Then, the interval $[x_0, y_0]$ contains a net negative charge $c - a < 0$. Let $y_1 = y_0 + N$ be the point antipodal to $y_0$. Due to the exciton configuration of charges, the interval $[x_1, y_1]$ must

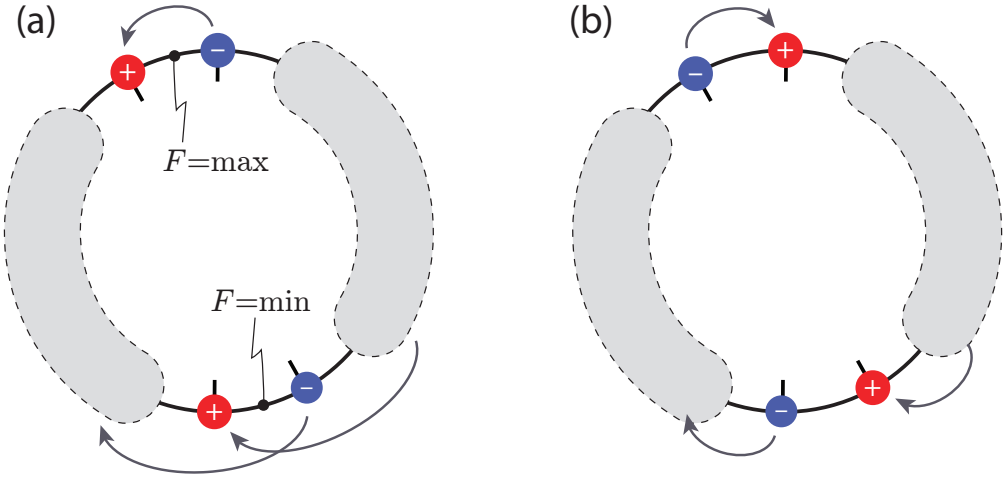


**Figure 5.6:** (a) Configuration of charges adjacent to points of maximal and minimal $F$. Arrows show one of the possible scenarios of optimal assignments. (b) New charge configuration and optimal assignment obtained after swapping the locations of the excitons from (a). The resulting assignment has a cost strictly less than that in (a).

contain the net positive charge $a - c > 0$. As a result, we have

$$F(y_1) = F(x_1) + a - c = a + (b - c) > a = F(x_0),$$

in contradiction to the maximality of $F(x_0)$. □

The following lemma states an important property of the points where $F$ is maximal or minimal. This property regards the assignment arrows (also called "arcs") above these points:

**Lemma 2.** *Consider an odd number of excitons not obeying sign alternation. In the optimal assignment obtained from the algorithm by Werman et al., points of maximal and minimal $F$ must have arcs above them.*

For proof of this lemma the reader is referred to Ref. [140].

**Lemma 3.** *Consider once more an odd number of excitons not obeying sign alternation and antipodal points where $F$ is maximal and minimal, see Fig. 5.6(a). Then the shaded region reached from $F = $ max traveling clockwise must contain net negative charge.*

*Proof.* First, note that the charges surrounding the points of maximum and minimum $F$ must have signs as indicated in Fig. 5.6(a). Since the overall exciton number is odd, the shaded region of interest must contain an odd number of charges, so the net charge $a$ in that region is odd. Further, we have

$$F_{\text{min}} = F_{\text{max}} + a - 2 < F_{\text{max}}.$$

From this, we conclude $a < 2$. We rule out $a = 1$, as this would imply $f = F_{\text{max}} - F_{\text{min}} = 1$ and hence charge alternation. $a = 0$ is not possible since $a$ is odd. Hence, we have $a < 0$, so the net charge in the region of interest is negative. □

These lemmas are now utilized in the proof of the following statement about non-alternating exciton configurations.

**Proposition 3.** *For configurations of an odd number of excitons not obeying sign alternation, the cost of the optimal assignment is strictly larger than* $N$.

*Proof.* The proof is by induction on $f = \max_x F(x) - \min_{x'} F(x')$, starting with the base case $f = 3$. According to Lemma 3, the points of minimal and maximal $F$ must have arcs overhead in the optimal assignment. Since this assignment is obtained by greedy pairing, nested arcs cannot occur. This leaves only two possibilities of optimal assignments for the charges adjacent to the points with extremal $F$. The first is shown in Fig. 5.6(a), where the top two charges are assigned to each other and the bottom ones have crossing arcs. The second possibility places crossing arcs both on the top and bottom pair of charges. By contrast, direct pairing of both the top two charges and the bottom two charges does not yield an optimal assignment as can be seen as follows. Suppose the top two charges are paired. Lemma 3 asserts that the shaded region on the right of Fig. 5.6(a) contains net negative charge. Since minimal cost is achieved by greedy assignment in clockwise fashion, the plus charge on the bottom must be assigned to a negative charge in this shaded region. The negative charge on the bottom must thus be assigned to a positive charge in the shaded region on the left, leading to crossing arcs as shown in the figure.

We assume an optimal assignment of the type depicted in Fig. 5.6(a); the following arguments

also carry over to the case of crossing arcs for both segments. Locate all positions where $F = F_{\text{max}}$ and swap the positions of the two adjacent excitons. This changes the maximum and minimum values of $F$ to $F'_{\text{max}} = F_{\text{max}} - 1$ and $F'_{\text{min}} = F_{\text{min}} + 1$, and hence yields $f' = f - 2$. For $f = 3$, the charge swaps thus produce an exciton configuration with sign alternation. The resulting assignment, shown in Fig. 5.6(b) has a cost strictly lower than the assignment in the non-alternating case of Fig. 5.6(a), completing the proof for the base case of $f = 3$.

For the induction step, assume that any odd-number exciton configuration with $f \leq f_0$ has an optimal-assignment cost strictly greater than $N$, and show that this is true as well for $f = f_0 + 2$. (Note that $f$ can only take on odd-integer values for an odd number of excitons.) The argument is analogous to that employed for the base case $f = 3$. Identifying locations of maximal $F$ and swapping the adjacent excitons, one finds a new configuration with a strictly lower cost and $f' = f - 2 = f_0 > 1$. By the inductive hypothesis, this has an optimal-assignment cost strictly larger than $N$, and so the assertion is proven. □

Based on these results we may now construct the $N^{\text{th}}$ order addition to the effective Hamiltonian capturing leading-order degeneracy breaking. We know that none of the virtual intermediate states are in the low-energy subspace. This is because we have proved that for a state in the low-energy subspace, a perturbative path yielding an odd number of excitons is of order at least $N$. If a state in the low-energy subspace were an intermediate state, we could construct a perturbative path of order strictly less than $N$ that creates an odd number of excitons. Therefore we generally obtain [137]

$$H_{\text{eff},N} = \frac{1}{2}|i,\alpha\rangle\langle i,\alpha| \prod_{\ell=1}^{N-1} (V|k_\ell,\gamma\rangle\langle k_\ell,\gamma|)V|j,\alpha\rangle\langle j,\alpha| \times \left[\frac{1}{\prod_{\ell=1}^{N-1}(E_{i,\alpha} - E_{k_\ell,\gamma})} + \frac{1}{\prod_{\ell=1}^{N-1}(E_{j,\alpha} - E_{k_\ell,\gamma})}\right] \tag{5.28}$$

where $V$ appears $N$ times and there are $N - 1$ energy denominators representing the cost of accessing virtual states from the agiton subspace. Noting that the only relevant terms are those that create or annihilate an odd number of excitons and that obey sign alternation, this expression

reduces to

$$H_{\text{eff},N} = -K \cos\left(\frac{\phi_{\text{ext}}}{2}\right) \sum_{m\leq N}^{\text{odd}} \sum_{i_1<i_2<\cdots<i_m} \cos\left[\sum_{j=1}^{m}(-1)^j \phi^-_{i_j}\right]. \tag{5.29}$$

Here, $K$ is the amplitude for creation and annihilation of an odd number $m$ of excitons with sign alternation. The summation index $m$ of the outer sum counts the number of created/annihilated excitons, and runs over all odd integers in the range of $1$ through $N$. The inner sum accounts for all possible positions $i_j$ of the $m$ excitons. Sign alternation of charges is reflected by the corresponding prefactor in the cosine argument. We observe that the exciton-generating terms also re-establish dependence of the spectrum on the external flux. Simple combinatorics reveals the number of terms in the inner sum of Eq. (5.29) as follows. Given a number of exciton creation/annihilation terms $m$, there are $N-m$ choices of where to place the remaining empty rungs. Therefore there are $\binom{N}{m}$ terms in the inner sum of Eq. (5.29) for each $m$. Summing over all of these contributions yields $\sum_{m\leq N}^{\text{odd}} \binom{N}{m} = 2^{N-1}$ [141].

Given the various perturbative paths and corresponding energy denominators associated with Eq. (5.28) and contributing to Eq. (5.29), it is not immediately clear that all amplitudes can be approximated by the same constant $K$. While it is clear that $K \sim (E_J/2)^N$, the computation and approximation of energy denominators is more involved. To do so, we must track the high-energy virtual states accessed in the perturbative paths.

We illustrate the procedure for the perturbative paths contributing to the creation of a single exciton on rung 1, associated with the operator $\exp(i\phi_1^-)$. As discussed above, the relevant $N$-th order perturbative paths involve either exclusively clockwise transfer of Cooper pairs, or exclusively counter-clockwise transfer. The counter-clockwise contributions are summarized by

$$\begin{aligned} A =& \frac{1}{2}\left(\frac{E_J}{2}\right)^N e^{i\phi_{\text{ext}}/2} \sum_{p\in S_N} |i,\alpha\rangle\langle i,\alpha| \left(\prod_{\ell=1}^{N-1} e^{i\phi_{p(\ell)}-i\phi_{p(\ell)+1}}|k_\ell,\gamma\rangle\langle k_\ell,\gamma|\right) \\ &\times e^{i\phi_{p(N-1)}-i\phi_{p(N-1)+1}}|j,\alpha\rangle\langle j,\alpha| \\ &\times \left[\frac{1}{\prod_{\ell=1}^{N-1}(E_{i,\alpha}-E_{k_\ell,\gamma})} + \frac{1}{\prod_{\ell=1}^{N-1}(E_{j,\alpha}-E_{k_\ell,\gamma})}\right], \end{aligned} \tag{5.30}$$

where the summation is over all permutations $p(n)$ of the numbers $1 \leq n \leq N$. An analogous expression is obtained for clockwise perturbative paths.

The energy denominators in Eq. (5.30) are obtained by tracking the high-energy virtual states accessed. The states involved in one virtual process generally differ from those in another, depending on the permutation $p(n)$. Because there are $N!$ such permutations, the difficulty of carrying out this sum rapidly increases with $N$. As in the calculation of Eq. (5.13), we neglect exciton-charging energies. This approximation leads to a critical simplification of the energy denominators in Eq. (5.30); it allows us to sum over each permutation $p(n)$ where the initial state is a circuit devoid of charge, and to ignore exciton charging energies in the intermediate states as compared to agiton energies. The sum in Eq. (5.30) and its clockwise counterpart can be carried out numerically, yielding the expression $\frac{K}{2}\cos(\phi_{\text{ext}}/2)\exp(i\phi_1^-)$.

To confirm that $K$ is the same for all terms in Eq. (5.29), consider the following. As depicted in Fig. 5.4, to obtain terms with operator content $e^{i(\phi_1^- - \phi_q^- + \phi_r^-)}$ ($r > q$), we needed to sum over terms from Eq. (5.28) of exactly the same form as Eq. (5.30). Here, however, permutations refer to the $N$ integers $[1\,..\,q-1] \cup [q+N\,..\,r+N-1] \cup [r\,..\,N]$. Forming the operator $e^{i(\phi_1^- - \phi_q^- + \phi_r^-)}$ can be related to the formation of $e^{i\phi_1^-}$ by the following substitutions: $e^{i(\phi_q - \phi_{q+1})} \rightarrow e^{i(\phi_{q+N} - \phi_{q+N+1})}, \cdots, e^{i(\phi_{r-1} - \phi_r)} \rightarrow e^{i(\phi_{r+N-1} - \phi_{r+N})}$. To understand the implications of this substitution for the energy denominators, we examine the action of the involved operators on states in the high-energy subspace. Observe that

$$e^{i(\phi_q - \phi_{q+1})} \left| \begin{array}{ll} n_q^- = n_1, & n_{q+1}^- = n_2, \\ n_q^+ = m_1, & n_{q+1}^+ = m_2 \end{array} \right\rangle = \left| \begin{array}{ll} n_q^- = n_1 + \frac{1}{2}, & n_{q+1}^- = n_2 - \frac{1}{2}, \\ n_q^+ = m_1 + \frac{1}{2}, & n_{q+1}^+ = m_2 - \frac{1}{2} \end{array} \right\rangle, \tag{5.31}$$

while

$$e^{i(\phi_{q+N} - \phi_{q+N+1})} \left| \begin{array}{ll} n_q^- = n_1, & n_{q+1}^- = n_2, \\ n_q^+ = m_1, & n_{q+1}^+ = m_2 \end{array} \right\rangle = \left| \begin{array}{ll} n_q^- = n_1 - \frac{1}{2}, & n_{q+1}^- = n_2 + \frac{1}{2}, \\ n_q^+ = m_1 + \frac{1}{2}, & n_{q+1}^+ = m_2 - \frac{1}{2} \end{array} \right\rangle, \tag{5.32}$$

where $n_i, m_i \in \mathbb{Z}$. The crucial insight from this is that the action of the substituted sister operators

yields states that have the same agiton charge numbers, and differ only in the exciton charge numbers. Because the term in Eq. (5.29) involving exp$(i[\phi_1^- - \phi_q^- + \phi_r^-])$ is obtained via a substitution of these sister operators in Eq. (5.30) relative to the term involving exp$(i\phi_1^-)$, their energy denominators will be identical in the approximation that the exciton charging energies are neglected. Similarly, the operators representing the creation of 5, 7,... excitons that include the creation of an exciton on the first rung must all have the same coefficient as exp$(i\phi_1^-)$ by the same reasoning. For identical junction and ground capacitances, the rotational symmetry of the circuit is intact. Therefore, the coefficient of exp$(i\phi_j^-)$ for $j \neq 1$ must be the same as the coefficient of exp$(i\phi_1^-)$. Therefore all terms in Eq. (5.29) must have the same coefficient under the approximations made here.

From numerics for the selected parameter set, we find that $K$ has the functional form $K(N) = 175$ GHz $\times$ exp$(-1.59N)$, quantifying the exponential suppression at large $N$. To establish an analytical bound on $K$ we make one further approximation. Ignoring offset charge, we approximate the charging energy of two unpaired charges anywhere on the circuit by $2\Delta E = 2E_{\mathsf{C}0}^+ - 2E_{\mathsf{C}1}^+$ (and for four unpaired charges by $4\Delta E = 4E_{\mathsf{C}0}^+ - 4E_{\mathsf{C}1}^+$, etc.), as opposed to the exact expression $2\Delta E_{j,k} = 2E_{\mathsf{C}0}^+ - 2(\mathsf{E}_{\mathsf{C}}^+)_{j,k}$ for a Cooper-pair hole on site $j$ and Cooper pair on site $k$. This yields an upper bound for $K$ because $(\mathsf{E}_{\mathsf{C}}^+)_{j,j\pm n} < E_{C1}^+ < E_{C0}^+$ for $n \geq 2$. By counting all paths and extracting the approximate energy denominators, we find

$$K(N) \leq 4\left(\frac{E_J}{2}\right)^N \frac{A_N}{(\Delta E)^{N-1}}, \tag{5.33}$$

where $A_N$ is observed to obey $A_2 = 1$ and $A_{N+1} = A_N(2N-1)/N$. This recursion relation can be solved using Pochhammer symbols, yielding

$$A_N = \frac{(1)_{2N-3}}{(2N-4)!!(2N-4)!}. \tag{5.34}$$

Because there are $2^{N-1}$ degeneracy breaking terms in Eq. (5.29), the relevant bound is not on $K(N)$, but rather $2^{N-1}K(N)$; if $K(N)$ decreases slower than $1/2^{N-1}$, then a ground-state degen-

eracy does not develop at large $N$. Using the large $N$ expression $A_N \sim 2^{N-2}$, we find

$$2^{N-1}K(N) < E_J \left(\frac{2E_J}{\Delta E}\right)^{N-1}. \tag{5.35}$$

Therefore as long as $2E_J < \Delta E$, the degeneracy breaking terms disappear in the large-$N$ limit. The parameters used in this work yield the energy scales $2E_J = 38$ GHz and $\Delta E > 60$ GHz for $N \geq 4$, indicating that a ground state degeneracy should indeed develop.

The resulting full effective Hamiltonian, capturing both exciton tunneling and degeneracy breaking to leading order, is given by

$$\begin{aligned} H_{\text{eff}} = &\sum_{i,j=1}^{N} 4\left(\mathsf{E}_{\mathsf{C}}^{-}\right)_{i,j}\left(n_i^- - n_{gi}\right)\left(n_j^- - n_{gj}^-\right) \\ &- \sum_{j=1}^{N-1} J\cos(\phi_{j+1}^- - \phi_j^-) - J\cos(\phi_1^- + \phi_N^-) \\ &- K\cos\left(\tfrac{\phi_{\text{ext}}}{2}\right)\sum_{m\leq N}^{\text{odd}}\sum_{i_1<\cdots<i_m}\cos\left[\sum_{j=1}^{m}(-1)^j\phi_{i_j}^-\right]. \end{aligned} \tag{5.36}$$

The degeneracy of the two potential minima located at $\{\phi_j^- = 0\}$ and $\{\phi_j^- = \pi\}$ is now weakly broken by $H_{\text{eff},N}$. In the parameter regime of interest, $H_{\text{eff},N}$ is exponentially suppressed, and minima remain near-degenerate. Additionally, the kinetic energy scale $E_{C_B} = 0.2$ GHz is small compared the barrier height $J \approx 2$ GHz, leading to very little tunneling between the two minima. We thus obtain localized, nearly degenerate states for the ground and first-excited states, corresponding to the qubit manifold.

### 5.2.4 Linearization of the effective model

Low-energy excitations of the current-mirror circuit arise as harmonic excitations within the two potential wells of the effective model. To make this statement quantitative, we extract the normal-mode frequencies associated with the linearized version of the second-order effective Hamiltonian (5.20). (Degeneracy-breaking terms proportional to $K$ can be safely neglected in this context.)

The normal-mode analysis is conveniently performed in the Lagrangian picture, where Taylor

expansion of the potential energy about the $\{\phi_j^- = 0\}$ and $\{\phi_j^- = \pi\}$ minima yields

$$\mathcal{L}_{\text{eff}}^{0,\pi} = \frac{1}{2}\left(\frac{\Phi_0}{2\pi}\right)^2 \sum_{i,j}^{N} \dot{\phi}_i^- (\mathsf{C}_-)_{i,j} \dot{\phi}_j^- + \sum_{j=1}^{N-1} \frac{J}{2}(\phi_{j+1}^- - \phi_j^-)^2 + \frac{J}{2}(\phi_1^- + \phi_N^-)^2. \tag{5.37}$$

We seek normal-mode solutions of the form $\vec{\phi}^- = \vec{\xi}_k e^{i\omega_k t}$. As usual, plugging this ansatz into the equation of motion yields the generalized eigenvalue problem $\mathsf{M}\vec{\xi}_k = \omega_k^2 \mathsf{C}_- \vec{\xi}_k$ for the normal-mode amplitudes $\vec{\xi}_k$ and associated eigenfrequencies $\omega_k$. Here, $\mathsf{M}$ denotes the coefficient matrix for the potential bilinear form. Inspection shows that $\mathsf{M}$ and the capacitance matrix $\mathsf{C}_-$ are both real, symmetric, and tridiagonal with additional corner elements. For this reason, they possess the same system of orthonormal eigenvectors, $\mathsf{M}\vec{\xi}_k = m_k \vec{\xi}_k$ and $\mathsf{C}_- \vec{\xi}_k = c_k \vec{\xi}_k$, and the eigenfrequencies are obtained from $\omega_k^2 = m_k/c_k$ with the result

$$\begin{aligned} \omega_k &= \frac{2\pi}{\Phi_0}\sqrt{\frac{4J \sin^2\left[(2k-1)\pi/2N\right]}{C_B + C_g/2 + 2C_J \sin^2\left[(2k-1)\pi/2N\right]}} \\ &= \frac{2\pi}{\Phi_0}\sqrt{\frac{4J}{C_B}}\left|\sin\frac{(2k-1)\pi}{2N}\right| + \mathcal{O}\left(\tfrac{C_g}{C_B}, \tfrac{C_J}{C_B}\right). \end{aligned} \tag{5.38}$$

Normal-mode frequencies are generally four-fold degenerate due to two factors: first, the $0$ and $\pi$ minima contribute equal sets of normal modes; second, one finds $\omega_k = \omega_{N-k+1}$ for all $k \leq \lfloor N/2 \rfloor$. (In the case of odd $N$, the highest normal-mode frequency $\omega_{(N+1)/2}$ is only two-fold degenerate, while the rest remain four-fold degenerate.)

A key insight from Eq. (5.38) is that the eigenfrequencies of the lowest-lying modes scale with $1/N$. Therefore, the circuit size of the current-mirror qubit should not be chosen too large, in order to avoid unwanted thermal population of low-lying excited states. We will argue in Sec. 5.4 that there is indeed a trade-off between depolarization and dephasing times which have opposite behavior as a function of circuit size $N$.

### 5.2.5 Nature of ground-state degeneracy in the full model

We have successfully confirmed the near-degeneracy of the lowest two eigenstates within the effective model. It is instructive to revisit the origin of this degeneracy in the context of the full circuit model [Eq. (5.3)]. We expect low-lying eigenstates to be related to the minima of the potential energy $U = -\sum_{j=1}^{2N} E_J \cos(\phi_{j+1} - \phi_j - \phi_{\text{ext}}/2N)$. Finding its local extrema via $\nabla U = 0$ leads to a set of $2N$ modular equations,

$$\begin{aligned} \phi_1 - \phi_{2N} &\equiv \phi_2 - \phi_1, \\ \phi_{j+1} - \phi_j &\equiv \phi_j - \phi_{j-1}, \qquad 2 \le j \le 2N-1, \\ \phi_{2N} - \phi_{2N-1} &\equiv \phi_1 - \phi_{2N}, \end{aligned} \tag{5.39}$$

where all congruences are modulo $2\pi$. At the minima locations, phase differences between adjacent nodes are thus identical to some constant value $\Delta\phi$. It is convenient to make use of gauge freedom and set $\phi_1 = 0$, to obtain $\phi_j = (j-1)\Delta\phi$, where $1 \le j \le 2N-1$. Solving for $\phi_{2N}$ yields $\Delta\phi = \pi l/N$ with integer $l$ denoting the number of phase windings or vortices. In summary, the local potential minima are labeled by the integer vortex number $l$, and have coordinates

$$(\vec{\phi}_l)_j = \frac{\pi l}{N}(j-1), \qquad |l| < \frac{N}{2} + \frac{\phi_{\text{ext}}}{2\pi}. \tag{5.40}$$

As opposed to the effective-Hamiltonian potential with only two minima at $0$ and $\pi$, one faces a multitude of local minima in the full-circuit model. There is a simple correspondence between minima in the two models, namely

$$\vec{\phi} = \vec{\phi}_l \quad (l = \substack{\text{even}\\\text{odd}}) \qquad \leftrightarrow \qquad \{\phi_j^- = \substack{0\\\pi}\}, \tag{5.41}$$

i.e., minima with even (odd) vortex parity contribute to the effective-model minimum at $0$ ($\pi$). In particular, the ground-state wave function occupies even-$l$ minima, $l = 0, \pm 2, \ldots$, while the nearly degenerate first excited state occupies odd-$l$ minima, $l = \pm 1, \pm 3, \ldots$

**Table 5.1:** Circuit parameters in $h$·GHz used in the numerical analysis, consistent with the conditions (5.4) for the protected regime.

| $E_{C_B}$ | $E_{C_J}$ | $E_{C_g}$ | $E_J$ |
|---|---|---|---|
| 0.2 | 100 | 200 | 19 |

Whether low-lying wave functions span multiple minima depends on whether tunneling between these minima is significant. We thus examine the eigenvalues and eigenvectors of the effective-mass tensor governing the tunneling dynamics, here given by the capacitance matrix C [Eq. (5.2)]. The eigenvectors of C are the real and imaginary parts of

$$(\vec{\zeta}_k)_j = e^{i\pi jk/N}/\sqrt{2N} \tag{5.42}$$

with corresponding eigenvalues

$$\gamma_k = C_g + 4C_J \sin^2\left(\frac{\pi k}{2N}\right) + [1-(-1)^k]C_B. \tag{5.43}$$

Here, $k$ ranges from $1$ to $2N$, and eigenvalues are generally two-fold degenerate (with the exceptions of non-degenerate $k = N$ and $k = 2N$).

From the eigenvalues we infer that the effective masses for even $k$ involve only the small capacitances $C_J$ and $C_g$ (light effective mass), while odd-$k$ eigenvalues involve the large capacitance $C_B$ (heavy effective mass). At the same time, it is only along the directions of odd-$k$ eigenvectors that the values of $\phi_j^-$ variables change, since $(\vec{\zeta}_k)_j = -(\vec{\zeta}_k)_{j+N}$ for odd $k$. Hence, tunneling between minima of different vortex parity is strongly suppressed, confirming the picture of low-lying eigenstates having definite vortex parity.

## 5.3 Spectrum of the current mirror

The simplification achieved with the effective model makes the problem of finding the current-mirror spectrum amenable to numerical diagonalization. The selected current-mirror parameters are given in Tab. 5.1. This choice firmly places the system in the intended protected regime where

the effective model is valid. We note that from the experimental perspective, achieving the small junction capacitance necessary to realize a device with these parameters will likely be the biggest challenge. We compute the eigenspectrum of the effective model as a function of circuit size (number of big capacitors $N$), as well as external flux $\Phi_{\text{ext}}$, using two separate techniques: exact diagonalization and density matrix renormalization group (DMRG).

We first perform exact diagonalization in the exciton-number basis. We employ the simplest truncation scheme by choosing an appropriate exciton-number cutoff $n_c$ for each rung, thus retaining exciton-basis states $-n_c < n_j^- < n_c$. (We find that $n_c = 10$ is sufficient for convergence in our case.) This way, exact diagonalization is feasible up to circuit size $N = 6$, beyond which memory requirements become excessively large [3].

To extend our numerical treatment to current-mirror circuits of sizes $N > 6$, we make use of DMRG methods. These methods have been employed very successfully in simulating one-dimensional quantum systems by an efficient Hilbert-space truncation that only retains largest-weight eigenvectors of the system density matrix at each step in the algorithm [142, 143, 144]. A large class of many-body and spin systems intractable with exact diagonalization can be handled with DMRG. In the context of superconducting circuits, DMRG has previously facilitated the study of capacitively-coupled Josephson junction necklaces by Lee et al. [108]. Since memory efficiency and fast convergence of DMRG algorithms generally rely upon the short-ranged nature of interactions [142], Lee and coworkers eliminated long-ranged capacitive interactions by neglecting junction capacitances. They further applied open boundary conditions which are known to speed up convergence [108, 142, 143, 144].

We proceed in a similar way for the current-mirror circuit, noting that capacitive interactions between rung degrees of freedom are relatively short-ranged in the effective model, see Eqs. (B.8)-(B.9). The long-range interactions produced by the degeneracy-breaking term $H_K$ are known to be weak and do not impede the treatment. The effective Hamiltonian $H_{\text{eff}}$ (5.20) thus essentially describes a one-dimensional exciton model with nearest-neighbor hopping suitable for the DMRG

[3] A truncation scheme using a global exciton-number cutoff will likely succeed in pushing exact diagonalization to slightly larger system sizes, but was not our main interest here.

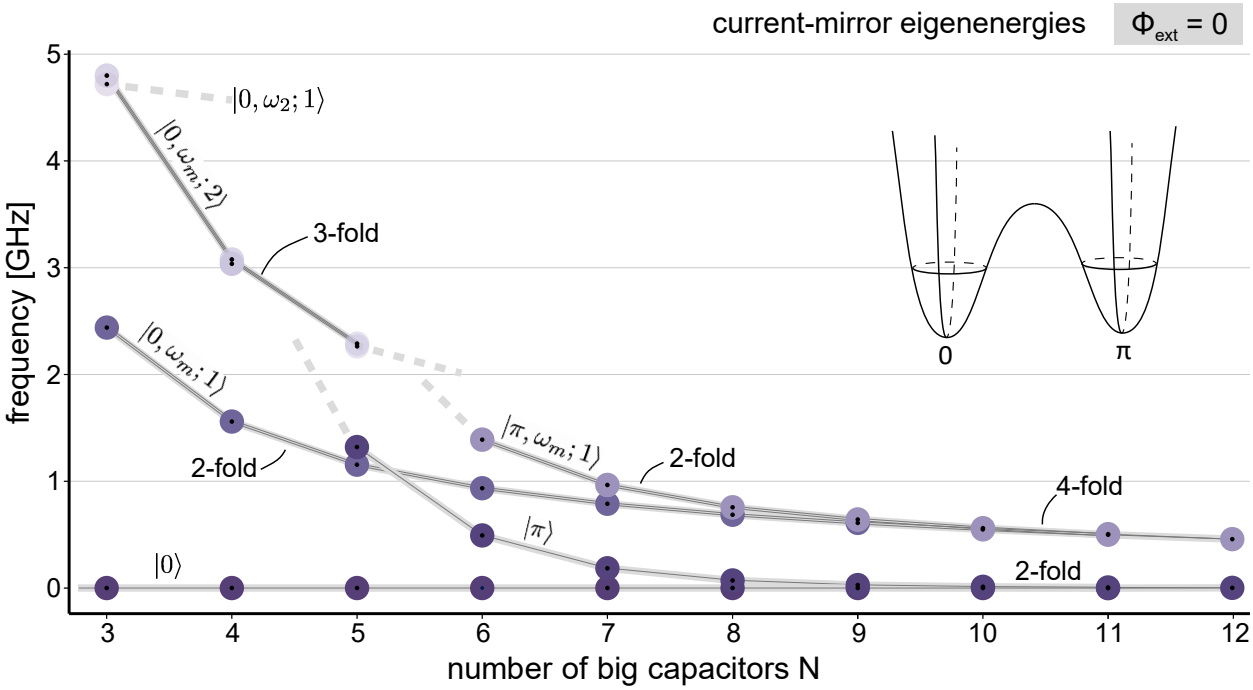


**Figure 5.7:** DMRG results: six lowest eigenenergies of the current-mirror circuit as a function of circuit size $N$ (number of big capacitors), based on the effective Hamiltonian [Eq. (5.36)]. For $N \geq 7$, ground state and first excited state, $|0\rangle$ and $|\pi\rangle$, are the nearly degenerate, lowest eigenstates localized in the $0$ and $\pi$ wells. Other eigenstates correspond to harmonic excitations within the two wells, and are denoted $|\alpha, \omega_k; n\rangle$, where $\alpha = 0, \pi$ labels the well, $k$ is the mode index [see Eq. (5.38)], and $n$ the number of harmonic excitations. $m$ is placeholder for the degenerate modes $\omega_0$ and $\omega_1$. The inset shows a schematic 2d projection of the potential energy with minima at $0$ and $\pi$. (Circuit parameters used: see Tab. 5.1.)

algorithm. The use of open boundary conditions, however, is not appropriate in our case, as the Möbius topology of the current-mirror circuit is crucial for the ground-state degeneracy. We have implemented DMRG for the effective-model Hamiltonian using the ITensor package developed by Stoudenmire and White [145]. In the following, we present DMRG results for circuit sizes up to $N = 12$. To assess the accuracy of DMRG spectra, we have compared against effective-model spectra obtained with exact diagonalization up to 6 big capacitors. We find excellent agreement, with relative deviations less than $2 \times 10^{-6}$. (We have confirmed that even larger circuit sizes can be tackled with DMRG, and the computational bottleneck is no longer memory but runtime.)

The current mirror has been predicted to exhibit ground-state degeneracy in the limit of large $N$ [52]. For experimental realizations, it is a pertinent question what concrete circuit size is required

to enter the protected regime. Results from our DMRG calculations shed new light on this issue. Figure 5.7 shows the lowest six effective-model eigenenergies versus circuit size $N$, for vanishing magnetic flux. We observe that ground and first excited states rapidly approach each other above $N = 6$, consistent with the exponential suppression of the degeneracy-breaking terms. Labeling of qubit states in Fig. 5.7 is guided by the linearized effective model: the two qubit states eventually becoming degenerate are denoted by $|0\rangle$ and $|\pi\rangle$ in reference to the corresponding potential minima. Other low-lying eigenstates can be identified as harmonic excitations in the two wells with excitation energies approximated by multiples of the mode frequencies from Eq. (5.38). A state in the $\alpha$ well ($0$ or $\pi$) with $n$ excitations in mode $k$ is written as $|\alpha, \omega_k; n\rangle$.

For $N = 3$, the $\pi$ well minimum is still significantly above the $0$ well minimum, and the latter hosts three eigenmodes with frequencies $\omega_0 = \omega_1 < \omega_2$. Coincidentally, we have approximately $\omega_2/\omega_0 \approx 2$, leading to the apparent near-degeneracy for the highest energy eigenstates shown at $N = 3$. Only the lowest mode frequencies scale with $1/N$, leading to the disappearance of states involving $\omega_2$ from the low-energy spectrum above $N = 3$. At large $N$, the degeneracy-breaking terms in Eq. (5.36) become exponentially small and the low-energy eigenstates are well described as harmonic excitations in one of the two wells, where each well is itself a 2-dimensional harmonic oscillator with two-fold degenerate mode frequencies.

We have further investigated the case of half-integer flux, $\phi_{\text{ext}} = \pi$, where degeneracy-breaking terms in Eq. (5.20) vanish. Consistent with that, the ground state is nearly degenerate already at $N = 3$. However, operation at this point produces a completely symmetric double-well potential, thus leading to eigenstates that are symmetric and anti-symmetric superpositions of the localized wave functions in each well. These qubit states are not protected from relaxation by disjoint-support arguments, defeating one of the original purposes for considering the superconducting current mirror as a qubit.

Our numerical results have quantified the circuit size required in order to enter the protected parameter regime. For the parameters we have chosen, the qubit states become the lowest-energy eigenstates of the circuit only for $N \geq 6$. Below this, the degeneracy-breaking terms are large enough to push the qubit state in the $\pi$ well above the low-energy excitations in the $0$ well.

## 5.4 Coherence properties

We follow the formalism outlined in Ch. 2 to compute coherence properties of the current-mirror qubit with respect to relevant noise channels. In the context of superconducting qubits, four main noise channels $\lambda$ are likely candidates to dominate decoherence rates: $1/f$ charge noise via offset-charge variations on each node, $1/f$ critical-current noise of each junction, $1/f$ flux noise in the magnetic flux penetrating the Möbius ring, and dielectric loss in the capacitors. The first three channels generally contribute to pure dephasing, while all four are relevant for depolarization.

### 5.4.1 Pure dephasing

In Ch. 2 we calculated pure-dephasing rates assuming that the noise-power spectrum is well behaved at $\omega = 0$. A more elaborate treatment is necessary to obtain the pure-dephasing rate in the case of $1/f$ noise $S(\omega) = 2\pi A_\lambda^2/|\omega|$. We proceed by closely following the analysis presented in Ref. [79]. First we consider the first-order effects of the noise before returning to second-order contributions. We insert the relation $\langle \delta\lambda(t)\delta\lambda(0)\rangle = \frac{1}{2\pi}\int_{-\infty}^{\infty} d\omega e^{-i\omega t} S(\omega)$ into Eq. (2.18) to obtain

$$\begin{aligned}\langle \rho_{0\pi}\rangle(t) &= c_0(0)c_\pi^*(0)\,\mathrm{exp}\left[-\frac{1}{4\pi\hbar^2}|\partial_\lambda E_{0\pi}|^2\int_0^t dt'\int_0^t dt''\int_{-\infty}^{\infty} d\omega e^{-i\omega(t'-t'')}S(\omega)\right] \\ &= c_0(0)c_\pi^*(0)\,\mathrm{exp}\left[-\frac{A_\lambda^2}{\hbar^2}|\partial_\lambda E_{0\pi}|^2 t^2\int_0^\infty d\omega \frac{\mathrm{sinc}^2(\omega t/2)}{\omega}\right].\end{aligned} \tag{5.44}$$

This integral diverges logarithmically as $\omega \to 0$. Thus to proceed we must institute a low-frequency cutoff $\omega_{\mathrm{ir}}$ for the lower-bound on the integral. This cutoff is typically chosen to satisfy $t \ll \omega_{ir}^{-1}$ [75]. Carrying out the integral and expanding in powers of $\omega_{\mathrm{ir}} t$ we obtain

$$\langle \rho_{0\pi}\rangle(t) \approx c_0(0)c_\pi^*(0)\,\mathrm{exp}\left[-\frac{A_\lambda^2 t^2}{\hbar^2}|\partial_\lambda E_{0\pi}|^2\left(\frac{1}{2}\{3-2\gamma\}+\ln\frac{1}{\omega_{\mathrm{ir}}t}\right)\right], \tag{5.45}$$

where $\gamma \approx 0.58$ is the Euler–Mascheroni constant. Typically the constant term is neglected, noting that $\omega_{\mathrm{ir}} t \ll 1$. According to Eq. (5.45) the decay of the coherence is Gaussian, and by convention

the dephasing time is then taken to be the variance

$$\Gamma_{\phi}^{(1),\lambda} = \sqrt{\frac{2A_{\lambda}^2}{\hbar^2}|\partial_{\lambda}E_{0\pi}|^2|\ln \omega_{\mathsf{ir}} t|}. \tag{5.46}$$

If the first-order effects vanish due to operation at a sweet spot (such as $\phi_{\mathsf{ext}} = \pi$), we must calculate the second-order effects. We thus return to Eq. (2.8) and noting that $\partial_{\lambda}E_{0\pi} = 0$, obtain

$$c_n(t) = c_n(0)\exp\left[-\frac{i}{\hbar}\frac{1}{2}\langle n|\partial_{\lambda}^2 H_{\mathsf{eff}}|n\rangle \int_0^t dt'\delta\lambda^2(t')\right]. \tag{5.47}$$

Proceeding in the same way as in Ch. 2, the decay of the coherence is given as

$$\begin{aligned}\langle\rho_{0\pi}\rangle(t) &= c_0(0)c_{\pi}^*(0)\exp\left[-\frac{1}{4\hbar^2}\left(D_{0\pi}^{\lambda,(2)}\right)^2\int_0^t dt_1\int_0^t dt_2\langle\delta\lambda^2(t_2-t_1)\delta\lambda^2(0)\rangle\right] \\ &= c_0(0)c_{\pi}^*(0)\exp\left[-\frac{1}{4\hbar^2}\left(D_{0\pi}^{\lambda,(2)}\right)^2\left\{t^2\sigma^4 + \frac{2t^2}{4\pi^2}\int_{-\infty}^{\infty}d\Omega\int_{-\infty}^{\infty}d\omega\,\mathrm{sinc}^2\left(\frac{(\Omega+\omega)t}{2}\right)S(\Omega)S(\omega)\right\}\right],\end{aligned} \tag{5.48}$$

defining

$$D_{0\pi}^{\lambda,(n)} = \langle 0|\partial_{\lambda}^n H_{\mathsf{eff}}|0\rangle - \langle 1|\partial_{\lambda}^n H_{\mathsf{eff}}|1\rangle, \tag{5.49}$$

and where $\sigma^2 = \langle\delta\lambda^2(0)\rangle = \int_{-\infty}^{\infty}\frac{d\omega}{2\pi}S(\omega)$ is the total noise power. In the second line of Eq. (5.48) we have used Isserlis's theorem [146] to simplify $\langle\delta\lambda^2(t_2-t_1)\delta\lambda^2(0)\rangle = \langle\delta\lambda^2(0)\rangle^2 + 2\langle\delta\lambda(t_2-t_1)\delta\lambda(0)\rangle$. Additionally, we utilized the expression for the autocorrelation function in terms of the noise spectral density $\langle\delta\lambda(t_2-t_1)\delta\lambda(0)\rangle = \frac{1}{2\pi}\int_{-\infty}^{\infty}d\omega\,e^{-i\omega(t_2-t_1)}S(\omega)$. We insert the definition of $S(\omega)$ into Eq. (5.48) and institute an ultra-violet cutoff $\omega_{\mathsf{uv}}$, yielding

$$\begin{aligned}\langle\rho_{0\pi}\rangle(t) = c_0(0)c_{\pi}^*(0)\exp\Bigg\{-\frac{1}{4\hbar^2}\left(D_{0\pi}^{\lambda,(2)}\right)^2\Bigg(t^2\left[2\int_{\omega_{\mathsf{ir}}}^{\omega_{\mathsf{uv}}}\frac{A_{\lambda}^2}{\omega}d\omega\right]^2 \\ + 8A_{\lambda}^4 t^2\int_{\omega_{\mathsf{ir}}}^{\omega_{\mathsf{uv}}}d\Omega\int_{\omega_{\mathsf{ir}}}^{\omega_{\mathsf{uv}}}d\omega\,\mathrm{sinc}^2\left[\frac{(\Omega+\omega)t}{2}\right]\frac{1}{\omega\Omega}\Bigg)\Bigg\}.\end{aligned} \tag{5.50}$$

The integral on the top line of Eq. (5.50) is straightforward to carry out, while we extract the leading-order logarithmic divergence of the integral on the bottom line as $\omega_{\text{ir}} \to 0$. The resulting pure-dephasing rate is

$$\Gamma_{\phi}^{(2),\lambda} = \sqrt{\frac{2A^4}{\hbar^2}\left(D_{0\pi}^{\lambda,(2)}\right)^2 [\ln^2(\omega_{\text{uv}}/\omega_{\text{ir}}) + 2\ln^2(\omega_{\text{ir}}t)]}. \tag{5.51}$$

It is possible in some cases for the second-order effects to meaningfully contribute even when the first-order effects do not vanish. In this case we can carry out the same analysis with minimal modifications, obtaining the overall pure dephasing rate [79]

$$\Gamma_{\phi}^{\lambda} = \sqrt{\frac{2A_{\lambda}^2}{\hbar^2}\left(\partial_{\lambda}E_{0\pi}\right)^2 |\ln\omega_{ir}t| + \frac{2A_{\lambda}^4}{\hbar^2}\left(D_{0\pi}^{\lambda,(2)}\right)^2 \left(\ln^2\frac{\omega_{uv}}{\omega_{ir}} + 2\ln^2\omega_{ir}t\right)}. \tag{5.52}$$

We make the common assumption that different noise channels are statistically independent [30, 75, 76, 77, 80, 147], and thus add individual decoherence rates and take the inverse to obtain the overall pure-dephasing time

$$T_{\phi} = \left(\sum_{\lambda}\Gamma_{\phi}^{\lambda}\right)^{-1}. \tag{5.53}$$

To numerically evaluate Eq. (5.52) we use the frequency cutoffs $\omega_{\text{uv}}/2\pi = 3.0\,\text{GHz}, \omega_{\text{ir}}/2\pi = 1\,\text{Hz}$ as well as the typical measurement time $t = 10\,\mu\text{s}$ [147, 148, 149]. We use standard estimates for the amplitude of charge noise $A_{n_g} = 10^{-4}e$ [150], critical-current noise $A_{I_c} = 10^{-7}I_c$ [151] and flux noise $A_{\Phi_{\text{ext}}} = 1\mu\Phi_0$ [148]. Derivatives of the Hamiltonian appearing in Eq. (5.52) are calculated numerically using a five-point stencil, as analytical evaluation of derivatives is prevented by the difficulty of obtaining a closed, analytical form for the degeneracy-breaking amplitude $K$. For charge noise and critical-current noise, the derivatives are performed by varying the noisy quantity at a single site/junction, keeping all other offset charges/junction critical currents constant.

Figure 5.8 presents our numerical results for the pure-dephasing times of the current-mirror qubit. We find that charge noise is the limiting factor for pure dephasing, which is not unexpected

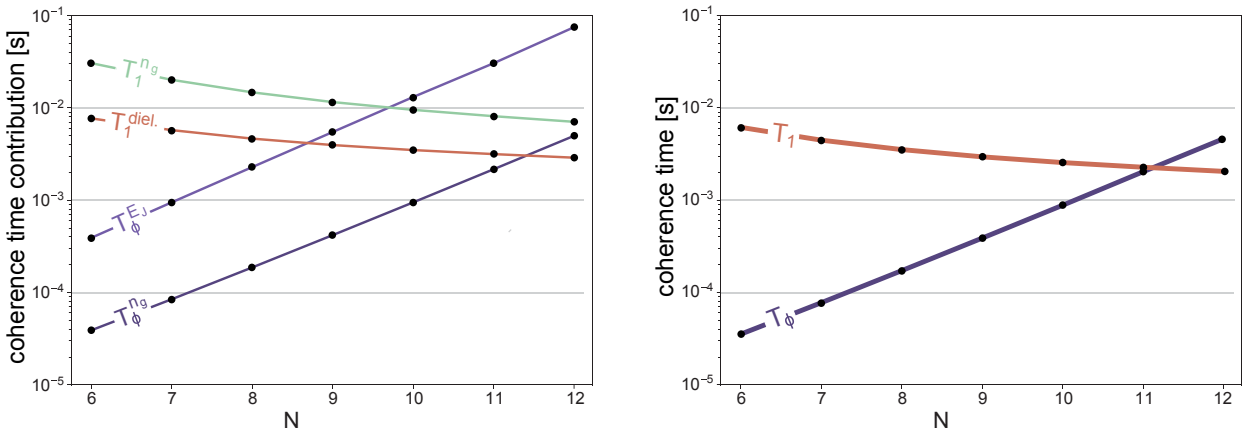


**Figure 5.8:** (a) Pure dephasing and depolarization times $T_\phi^\lambda$ and $T_1^\lambda$, as a function of circuit size $N$. Charge noise limits $T_\phi$, but dephasing times increase exponentially with $N$. Dielectric loss limits $T_1$, with escape from the qubit subspace dominating over relaxation. Due to the $1/N$ scaling of low-energy excitations thermal excitations become more prominent with increasing circuit size. This explains the observed decrease in $T_1^\lambda$ as a function of $N$. (b) Total $T_1$ and $T_\phi$ as a function of circuit size $N$.

given that the current mirror operates at $E_J < E_{C_J}$ – a regime where offset-charge dependence is relevant. Critical-current noise is subdominant, and dephasing due to flux noise is so insignificant that its contributions are outside the range displayed in Fig. 5.8. Dephasing times overall improve as a function of $N$ because the relevant derivatives $\partial K/\partial n_{gj}$ and $\partial K/\partial E_J$ are suppressed as a function of $N$, as a direct consequence of the exponential suppression of $K$ with $N$. (In fact, operating the qubit at the sweet spot $\phi_{\text{ext}} = \pi$ improves offset-charge and critical-current pure-dephasing times by factors of ten or more. However, this operating point is not attractive since protection from relaxation is lost.)

We predict dephasing times on the order of milliseconds for $N$ as small as 10. We expect the exponential decrease of $K$ to persist for higher values of $N$, indicating that pure dephasing times on the order of tens of milliseconds should be possible for $N = 13, 14$.

### 5.4.2 Depolarization

An important merit of the current-mirror qubit is its built-in protection from relaxation. Because of the virtually disjoint support of the $|0\rangle$ and $|\pi\rangle$ wave functions, all matrix elements $\langle 0|M|\pi\rangle$ with

respect to local operators $M$ are exponentially small. This implies that depolarization in the form of escape upward to higher-energy eigenstates outside of the qubit subspace is the main contributor to $T_1$, as opposed to relaxation within the computational subspace.

In addition to the previously studied noise channels, we now also include dielectric loss which is a known contributor to depolarization [94, 152]. The depolarization time $T_1^\lambda = (\Gamma_1^\lambda)^{-1}$ due to channel $\lambda$ is obtained by summing over individual depolarization rates [Eqs. (2.13)-(2.14)],

$$\Gamma_1^\lambda = \Gamma_{\text{rel}}^\lambda + \Gamma_{\text{exc}}^\lambda + \Gamma_{\text{esc}}^\lambda, \tag{5.54}$$

using Fermi's golden rule. Here we explicitly include transitions to eigenstates outside of the qubit manifold. For the $1/f$ noise sources, the analysis presented in Ch. 2 may be applied straightforwardly. For dielectric loss, the situation is slightly modified. Following Refs. [94, 152], we model dielectric loss as dissipation in the dielectric of each capacitor in the current mirror. The operator that mediates transitions in Fermi's golden rule is the charge stored on each capacitor [94]. To find expressions for the charges on the big capacitors and the junction capacitors, we return to the Lagrangian picture. The charge across the $j$-th junction is $\frac{\Phi_0}{2\pi} C_J(\dot{\phi}_{j+1} - \dot{\phi}_j)$. Similarly, the charge across the $j$-th big capacitor is given by $\frac{\Phi_0}{2\pi} C_B(\dot{\phi}_{j+N} - \dot{\phi}_j)$. In order to evaluate matrix elements, these expressions must be rewritten in terms of operators associated with the effective Hamiltonian. The relation

$$\dot{\phi}_i^- = \sum_{j=1}^{N} 8(\mathsf{E}_\mathsf{C}^-)_{i,j} n_j^- /\hbar = 8E_{C_B} n_i^- /\hbar + \mathcal{O}\left(\frac{C_J}{C_B}\right) \tag{5.55}$$

allows us to recast the capacitor charges in terms of exciton charge operators. The final ingredient for predicting depolarization times due to dielectric loss in a capacitor with capacitance $C$ is the form of the noise power spectrum when the noise couples through the charge operator. This is [94, 95]

$$S_{\text{diel.}}(\omega, C) + S_{\text{diel.}}(-\omega, C) = \frac{2\hbar}{CQ(C)} \coth \frac{\hbar\omega}{2k_\mathsf{B}T}, \tag{5.56}$$

where $T$ is the temperature and $Q(C)$ is the quality factor of the dielectric. We use values of

$Q(C_J) = 10^6$ and $Q(C_B) = 10^7$ as well as $T = 15$ mK [94, 95].

While the symmetrized noise power spectrum is useful for discussing relaxation, we are interested mainly in escape from the qubit subspace. These processes only involve the noise power spectrum at negative frequencies, corresponding to absorption of energy from the environment. Assuming the microscopic origin of the noise is a system in thermal equilibrium, the spectrum must obey detailed balance, see Eq. (2.15). This allows us to solve for $S_{\text{diel.}}(-\omega, C)$. If we additionally assume the $1/f$ noise sources are in thermal equilibrium, then their respective noise-power spectra are also suppressed at negative frequencies. Since low-energy excitations in the current mirror scale as $1/N$, we expect $T_1$ to decrease as a function of $N$. Since $T_\phi$ was observed to increase with $N$, we expect there to be an optimal $N$ for operating the current-mirror qubit where $T_1$ and $T_\phi$ are of the same order of magnitude.

We present our results for the depolarization times of the qubit in Fig. 5.8. Dielectric loss is the limiting factor for depolarization at all $N$, which is reasonable given that a circuit of size $N$ by definition has $2N$ junction capacitors and $N$ big capacitors. $1/f$ charge noise is sub-dominant, and contributions from $1/f$ critical-current noise and magnetic-flux noise to depolarization are safely negligible. Our calculations yield depolarization times of multiple milliseconds, on-par with state-of-the-art fluxonium qubits [33]. As seen in Fig. 5.8, past $N = 11$ the qubit ceases to be $T_\phi$ limited and becomes $T_1$ limited.

We emphasize that escape from the qubit subspace is the dominant contributor to depolarization, and relaxation within the qubit subspace is vastly suppressed. Such escape processes are only relevant for transitions inside of each well, because of a similar suppression of matrix elements between states in different wells. Interestingly, if the qubit degree of freedom could be made insensitive to harmonic excitations and merely be linked to overall occupation in the $0$ vs. the $\pi$ well, then $T_1$ times would be dramatically longer than in our above estimates.

# 6 Variational Tight Binding

*This chapter is based on material published in D. K. Weiss et al., Phys. Rev. Research* **3***, 033244 (2021).*

In the previous chapter we derived an effective model for the current-mirror circuit and simulated it using DMRG techniques. In so doing we extracted the spectrum and coherence times of the device. Notably, the effective model cannot capture charge frustration. Thus, we are motivated to simulate the full model of the current-mirror circuit to account for such effects. Unfortunately, naive diagonalization in the charge basis with sparse matrices quickly fails due to memory requirements as we will show below. Additionally we have attempted to simulate the full model of the circuit using DMRG which was not successful due to the explosion of the bond dimension [109]. To make progress in analyzing larger circuits, we require a qualitatively different approach than the ones previously described.

Such an approach is provided by the tight-binding method introduced in Ch. 3. There, we illustrated how tight binding is applied to superconducting circuits in general. Here, we focus on the details of numerical implementation and the efficient computation of the relevant matrix elements. We then apply the method to the examples of the flux qubit and the current mirror.

## 6.1 Efficient computation of matrix elements and overlaps

Solution of the generalized eigenvalue problem [Eq. (3.11)] involves the computation of matrix elements of harmonic-oscillator states at different locations and, possibly, with different normal-mode orientations and oscillator lengths. The calculation of these quantities proceeds either via use of ladder operators or by explicit integration within the position representation. Even though integra-

tion can in principle be accomplished analytically, the expressions become increasingly tedious in higher dimensions. (The integrals are generally two-center integrals that lead to two-variable Hermite polynomials [153]). By contrast, the ladder-operator formalism is more readily adapted for the numerical calculations of the matrix elements in question. Therefore, we focus on this approach.

The matrix elements and overlaps to be evaluated have the form

$$\langle \vec{s}\,', m'; \vec{0}\,|\mathcal{O}|\vec{s}, m; \vec{j}\,\rangle, \tag{6.1}$$

where $\mathcal{O}$ is either the Hamiltonian $H$ or the identity. To facilitate the use of the ladder-operator formalism, we next re-express operators and states in terms of the creation and annihilation operators associated with the $m = 0$ minimum in the central unit cell. Since inequivalent minima differ in locations and curvatures, local wave functions are shifted and possibly squeezed relative to each other,

$$\mathcal{T}_{\vec{\theta}_m}\mathcal{S}_m|\vec{s}\rangle = |\vec{s}, m\rangle, \tag{6.2}$$

where $|\vec{s}\rangle \equiv |\vec{s}, 0\rangle$ and we have taken the location of the $m = 0$ minimum to be the origin, $\vec{\theta}_{m=0} = \vec{0}$. The intuitive interpretation of Eq. (6.2) is based on a two-step process: first the harmonic oscillator states for $m = 0$ are deformed via the squeezing operator $\mathcal{S}_m$ to match the local curvature of the $m^{\text{th}}$ minimum and are then shifted over to the appropriate location of that minimum via the translation operator $\mathcal{T}_{\vec{\theta}_m}$. According to Eq. (6.2), the matrix elements take the form

$$\langle \vec{s}\,', m'; \vec{0}\,|\mathcal{O}|\vec{s}, m; \vec{j}\,\rangle = \langle \vec{s}\,'|\mathcal{S}^\dagger_{m'}\mathcal{T}^\dagger_{\vec{\theta}_{m'}}\mathcal{O}\,\mathcal{T}_{\vec{\theta}_m+2\pi\vec{j}}\mathcal{S}_m|\vec{s}\rangle. \tag{6.3}$$

The expression for the states is readily obtained,

$$|\vec{s}\rangle = \prod_\mu \frac{1}{\sqrt{s_\mu!}}(a^\dagger_\mu)^{s_\mu}|\vec{s} = \vec{0}\,\rangle, \tag{6.4}$$

where we introduce the ladder operators $a_\mu$ obeying the commutation relation $[a_\mu, a^\dagger_\nu] = \delta_{\mu\nu}$. Like-

wise the treatment of the translation operator $\mathcal{T}_{\vec{\theta}} = e^{-i\vec{\theta}\cdot\vec{n}}$ is straightforward: making use of the relation between the number operators and ladder operators

$$n_j = \sum_\mu \frac{-i}{\sqrt{2}} \Xi^{-T}_{j\mu}(a_\mu - a^\dagger_\mu), \tag{6.5}$$

the translation operator can be expressed as

$$\mathcal{T}_{\vec{\theta}} = \exp(-\frac{1}{\sqrt{2}} \vec{\theta}^T \, \Xi^{-T}[\vec{a} - \vec{a^\dagger}]), \tag{6.6}$$

which translates the position variables $\vec{\phi}$ by $\vec{\theta}$. Here we use the compact notation $\vec{a} = (a_1, \cdots, a_{N_d})^T$ and $\vec{a^\dagger} = ({a_1}^\dagger, \cdots, {a_{N_d}}^\dagger)^T$ and denote $\Xi^{-T} = (\Xi^{-1})^T$.

The expression for the squeezing operator can be found by considering a simplified situation of two harmonic Hamiltonians $H_a, H_c$ of the form of Eq. (3.3), but defined at the same center point. The Hamiltonian $H_a$ is diagonalized by the ladder operators $\vec{a}, \vec{a^\dagger}$ and $H_c$ is diagonalized by $\vec{c}, \vec{c^\dagger}$. The respective eigenfunctions $|\vec{s}\rangle_a$ and $|\vec{s}\rangle_c$ are related by a unitary squeezing transformation,

$$\mathcal{S}|\vec{s}\rangle_a = |\vec{s}\rangle_c, \tag{6.7}$$

which is equivalent to $\mathcal{S}\vec{a}\mathcal{S}^\dagger = \vec{c}$. To obtain a concrete expression for $\mathcal{S}$ we note that the bosonic ladder operators are related by a Bogoliubov transformation [154, 155, 156]

$$\begin{pmatrix} u & v \\ v^* & u^* \end{pmatrix} \begin{pmatrix} \vec{a} \\ \vec{a^\dagger} \end{pmatrix} = \begin{pmatrix} \vec{c} \\ \vec{c^\dagger} \end{pmatrix}, \tag{6.8}$$

where $u, v$ are $N_d \times N_d$ matrices. These can be found by considering the two decompositions of

the phase and number operators in terms of the differing sets of ladder operators

$$\begin{pmatrix} \vec{\phi} \\ \vec{n} \end{pmatrix} = \frac{1}{\sqrt{2}} \begin{pmatrix} \Xi & \Xi \\ -i\Xi^{-T} & i\Xi^{-T} \end{pmatrix} \begin{pmatrix} \vec{a} \\ \vec{a^\dagger} \end{pmatrix} \tag{6.9}$$
$$= \frac{1}{\sqrt{2}} \begin{pmatrix} \Xi' & \Xi' \\ -i\Xi'^{-T} & i\Xi'^{-T} \end{pmatrix} \begin{pmatrix} \vec{c} \\ \vec{c^\dagger} \end{pmatrix},$$

where the matrix $\Xi$ is defined for $H_a$ and $\Xi'$ for $H_c$ as in Sec. 3.1. Solving Eq. (6.9) for the ladder operators $\vec{c}, \vec{c^\dagger}$ yields the real-valued Bogoliubov matrices

$$u = \frac{1}{2}\left(\Xi'^{-1}\Xi + \Xi'^{T}\Xi^{-T}\right), \tag{6.10}$$
$$v = \frac{1}{2}\left(\Xi'^{-1}\Xi - \Xi'^{T}\Xi^{-T}\right) \tag{6.11}$$

As shown in Ref. [157], the multimode squeezing operator can now be expressed in terms of $u, v$ as follows:

$$\mathcal{S} = \exp\left(\frac{1}{2}(\vec{a}^{\,T}\ \vec{a^\dagger}^{\,T}) J \ln M (\vec{a}\ \vec{a^\dagger})^T\right), \tag{6.12}$$

where

$$M = \begin{pmatrix} u & v \\ v & u \end{pmatrix}, \quad J = \begin{pmatrix} 0 & \mathbb{1} \\ -\mathbb{1} & 0 \end{pmatrix}. \tag{6.13}$$

Returning now to our original notation, we identify $\mathcal{S}_m$ with $\mathcal{S}$ in Eq. (6.12), where the $m$ dependence carries forward to the Bogoliubov $u, v$ matrices. With Eqs. (6.4),(6.6),(6.12) we have, in principle, collected all ingredients necessary for the evaluation of the matrix elements and overlaps [Eq. (6.3)]. However, numerical implementation necessarily involves truncation, and we will show in the following that normal-ordering operator expressions is essential for maximizing accuracy.

A standard approach for truncating the infinite-dimensional operators $a_\mu, a_\mu^\dagger$ consists of exci-

tation cutoffs $s_{\text{max}}$ applied to each individual mode. This is a fine strategy for moderate sized systems, but quickly becomes intractable for larger systems due to the exponential growth of the Hilbert-space dimension $d_{\text{indv}} = (M+1)(s_{\text{max}}+1)^{N_d}$, where we recall that $M$ corresponds to the number of minima. To mitigate this bottleneck, one can instead use a global excitation number cutoff $\Sigma_{\text{max}}$, which institutes a maximum Manhattan length of the excitation number vector, $\|\vec{s}\|_1 \leq \Sigma_{\text{max}}$ [158]. The Hilbert-space dimension can be found using the "hockey-stick identity" to be

$$d_{\text{global}} = (M+1)\begin{pmatrix} \Sigma_{\text{max}}+N_d \\ N_d \end{pmatrix}. \tag{6.14}$$

While $d_{\text{global}}$ still grows exponentially, the prefactor of the exponential growth is smaller than that associated with $d_{\text{indv}}$. For example, if we consider $M=0$ (a single minimum) $s_{\text{max}} = \Sigma_{\text{max}} = 3$ and $N_d = 5$, we obtain $d_{\text{indv}} = 1,024$ and $d_{\text{global}} = 56$.

Given a specific truncation level, it makes a difference whether operator expressions are normal ordered or not. Denoting the truncated operators as $\tilde{a}_\mu, \tilde{a}_\mu^\dagger$, the nominally identical expressions $\tilde{a}_\mu \tilde{a}_\mu^\dagger$ and $\tilde{a}_\mu^\dagger \tilde{a}_\mu + \delta_{\mu\mu}$ in fact give different results as seen, for instance, in

$$\begin{aligned} \langle s_{\text{max}}|\tilde{a}_\mu \tilde{a}_\mu^\dagger|s_{\text{max}}\rangle &= 0, \\ \langle s_{\text{max}}|(\tilde{a}_\mu^\dagger \tilde{a}_\mu + \delta_{\mu\mu})|s_{\text{max}}\rangle &= s_{\text{max}}+1. \end{aligned} \tag{6.15}$$

Here, the "wrong" result of the first expression can be circumvented by using the normal-ordered version in the second expression. This example is indicative of a general result, that it is beneficial to normal order ladder-operator expressions before further numerical evaluation.

In the following sections where we apply the tight-binding method to several example systems, we find that the sets of basis states constructed with or without squeezing (proper vs. improper tight binding) may yield similar numerical performance. This is naturally the case if minima contributing to the low-energy spectrum have similar curvatures, or if all amplitude of the lowest-energy states is concentrated in the $m=0$ minimum. Whenever possible, omitting squeezing from the construction

of basis states significantly simplifies the numerical treatment.

### 6.1.1 Normal ordering

The translation operator $\mathcal{T}_{\vec{\theta}}$ can be normal ordered via the the Baker-Campbell-Hausdorff (BCH) formula [127, 128, 129, 130], which takes the form $e^X e^Y = e^{X+Y+\frac{1}{2}[X,Y]}$ when $X$ and $Y$ are operators that commute with their commutator $[X, Y]$. This yields

$$\mathcal{T}_{\vec{\theta}} = \mathcal{V}_{\vec{\theta}}^{\dagger} \mathcal{V}_{-\vec{\theta}} \exp\left(-\frac{1}{4}\vec{\theta}^T \Xi^{-T} \Xi^{-1} \vec{\theta}\right), \tag{6.16}$$

where

$$\mathcal{V}_{\vec{\theta}} = \exp\left(\frac{1}{\sqrt{2}}\vec{\theta}^T \Xi^{-T} \vec{a}\right). \tag{6.17}$$

Expressions for commuting $\mathcal{V}$ operators past operators such as $n_j$ and $e^{i\phi_j}$ (which enter $\mathcal{O}$ in Eq. (6.1)) can be easily obtained:

$$\mathcal{V}_{\vec{\theta}}\, \vec{n} = \left(\vec{n} + \frac{i}{2}\Xi^{-T}\Xi^{-1}\vec{\theta}\right) \mathcal{V}_{\vec{\theta}}, \tag{6.18}$$

$$\mathcal{V}_{\vec{\theta}}\, e^{i\phi_j} = e^{i(\phi_j + \frac{1}{2}\theta_j)} \mathcal{V}_{\vec{\theta}}, \tag{6.19}$$

where in Eq. (6.18) we have used the identity [66] $e^X Y = (Y + [X, Y])e^X$, again valid when $X$ and $Y$ commute with $[X, Y]$.

The normal-ordering procedure for expressions involving the squeezing operators is more involved. In general, we must normal order operator expressions

$$\mathcal{S}_{m'}^{\dagger} \mathcal{T}_{\vec{\theta}_{m'}}^{\dagger} \mathcal{O}\, \mathcal{T}_{\vec{\theta}_m + 2\pi\vec{j}} \mathcal{S}_m \tag{6.20}$$

prior to numerical evaluation. Normal ordering of the squeezing operator $\mathcal{S}_m$ [Eq. (6.12)] proceeds

by first placing $\mathcal{S}_m$ in so-called disentangled form [157, 159]

$$\mathcal{S}_m = \exp\left(-\frac{1}{2}\operatorname{Tr} Y\right) \exp\left(-\frac{1}{2}a_\mu^\dagger X_{\mu\nu} a_\nu^\dagger\right) \exp\left(-a_\mu^\dagger Y_{\mu\nu} a_\nu\right) \exp\left(\frac{1}{2}a_\mu Z_{\mu\nu} a_\nu\right), \tag{6.21}$$

where $X = u^{-1}v, Y = \ln u, Z = vu^{-1}$ and we omit the $m$ dependence of these quantities for notational simplicity [154]. The inner term of Eq. (6.21) with $Y$ is not yet normal ordered. This can be rectified via the formula [160]

$$\exp(a_\mu^\dagger Y_{\mu\nu} a_\nu) = :\exp(a_\mu^\dagger (e^Y - \mathbb{1})_{\mu\nu} a_\nu):, \tag{6.22}$$

where $::$ is known as the normal-ordering symbol. Creation and annihilation operators inside the normal-ordering symbol can be commuted without making use of the commutation relations. A trivial example of the use of this superoperator is $:aa^\dagger: = a^\dagger a$.

To commute exponentials and $\mathcal{V}$ operators appearing for example in Eq. (6.21) and Eq. (6.17) we make use of the following normal-ordering formulae [161, 162]

$$\begin{aligned}
\exp(a_\mu Z_{\mu\nu} a_\nu)\exp(a_\mu^\dagger X_{\mu\nu} a_\nu^\dagger) &= \frac{1}{\sqrt{\det(\mathbb{1} - 4ZX)}} \exp(a_\mu^\dagger [(\mathbb{1} - 4XZ)^{-1} X]_{\mu\nu} a_\nu^\dagger) \\
&\quad \times \exp(a_\mu^\dagger [\ln(\mathbb{1} - 4XZ)^{-1}]_{\mu\nu} a_\nu) \exp(a_\mu [(\mathbb{1} - 4ZX)^{-1} Z]_{\mu\nu} a_\nu), \qquad (6.23) \\
\exp(a_\mu^\dagger Y_{\mu\nu} a_\nu)\exp(a_\mu^\dagger Y'_{\mu\nu} a_\nu) &= \exp(a_\mu^\dagger \ln(e^Y e^{Y'})_{\mu\nu} a_\nu), \qquad (6.24) \\
\exp(a_\mu Z_{\mu\nu} a_\nu)\exp(\lambda_\mu a_\mu^\dagger) &= \exp(\lambda_\mu Z_{\mu\nu} \lambda_\nu)\exp(\lambda_\mu a_\mu^\dagger) \\
&\quad \times \exp(a_\mu Z_{\mu\nu} a_\nu)\exp(\lambda_\mu (Z_{\mu\nu} + Z_{\mu\nu}^T) a_\nu), \qquad (6.25) \\
\exp(a_\mu^\dagger Y_{\mu\nu} a_\nu)\exp(\lambda_\mu a_\mu^\dagger) &= \exp(a_\mu^\dagger (e^Y)_{\mu\nu} \lambda_\nu)\exp(a_\mu^\dagger Y_{\mu\nu} a_\nu), \qquad (6.26) \\
\exp(a_\mu^\dagger Y_{\mu\nu} a_\nu)\exp(a_\mu^\dagger X_{\mu\nu} a_\nu^\dagger) &= \exp(a_\mu^\dagger (e^Y)_{\mu\nu} X_{\nu\sigma} (e^Y)^T_{\sigma\tau} a_\tau^\dagger)\exp(a_\mu^\dagger Y_{\mu\nu} a_\nu). \qquad (6.27)
\end{aligned}$$

Here, $X, Y, Y', Z$ and $\vec{\lambda}$ are arbitrary, except for the requirement of $\mathbb{1} - 4XZ$ and $\mathbb{1} - 4ZX$ to be nonsingular in Eq. (6.23). We note that it is relatively straightforward to obtain Eqs. (6.25)-(6.27) from standard applications of the BCH formula [66]. Obtaining Eqs. (6.23)-(6.24) is slightly more difficult, and requires using either Lie algebra techniques [161, 163] or the so-called integration

within ordered products (IWOP) procedure [162].

An instance of Eq. (6.20) relevant for computing wave function overlaps is

$$\mathcal{S}^{\dagger}_{m'} \exp(\vec{\lambda}^T \vec{a}^{\dagger}) \exp(-\vec{\lambda}^T \vec{a}) \mathcal{S}_m, \tag{6.28}$$

identifying

$$\vec{\lambda} = \frac{1}{\sqrt{2}} (\vec{\theta}_m - \vec{\theta}_{m'} + 2\pi \vec{j})^T \Xi^{-T}, \tag{6.29}$$

and neglecting the overall multiplicative factor [c.f. Eq. (6.16)]. To simplify notation, we have suppressed the dependence of $\vec{\lambda}$ on $m, m'$ and $\vec{j}$. We will continue to likewise suppress the $m$ dependence of the various matrices and distinguish between $X_m$ and $X_{m'}$ by using the notation $X$ and $X'$, etc. Applying each of the relations Eq. (6.23)-(6.27) in a few steps of algebra leads to the normal-ordered result

$$\begin{aligned}
\mathcal{S}^{\dagger}_{m'} \exp(\vec{\lambda}^T \vec{a}^{\dagger}) \exp(-\vec{\lambda}^T \vec{a}) \mathcal{S}_m = & \frac{\exp(-\frac{1}{2}[\vec{\lambda}^T \{X + (\mathbb{1} + X)\overline{P^T X'}(\mathbb{1} + X)\}\vec{\lambda} + \mathrm{Tr}\, Y'^{\dagger} + \mathrm{Tr}\, Y])}{\sqrt{\det(\mathbb{1} - X'X)}} \\
& \times \exp(-\frac{1}{2} \vec{a^{\dagger}}^T [\{e^{-Y'}\}^{\dagger} P X \{e^{-Y'}\}^* - Z'] \vec{a^{\dagger}}) \\
& \times \exp(\vec{\lambda}^T [\mathbb{1} + X] P^T [e^{-Y'}]^* \vec{a^{\dagger}}) \\
& \times : \exp(\vec{a^{\dagger}}^T [e^{-Y'^{\dagger}} P e^{-Y} - \mathbb{1}] \vec{a}) : \\
& \times \exp(-\vec{\lambda}^T [\mathbb{1} + \{\mathbb{1} + X\}\overline{P^T X'}] e^{-Y} \vec{a}) \\
& \times \exp(\frac{1}{2} \vec{a}^T [Z - \{e^{-Y}\}^T P^T X' e^{-Y}] \vec{a}),
\end{aligned} \tag{6.30}$$

where $P = (\mathbb{1} - XX')^{-1}$, $\overline{P^T X'} = \frac{1}{2}(P^T X' + X' P)$ and the matrices $X, X'$, etc. can be taken to be symmetric. Similar expressions can be obtained when the operator $\mathcal{O}$ is an explicit function of the ladder operators $\vec{a}, \vec{a^{\dagger}}$.

### 6.1.2 Nearest-neighbor computation

The final step in setting up the generalized eigenvalue problem (3.11), is truncating the sum over vectors $\vec{j}$. A typical truncation scheme is the nearest-neighbor approximation which selects only those unit cells that have the minimal Euclidean distance from the central unit cell. This strategy however does not account for any anisotropy in the harmonic lengths, which results in local wave functions whose Gaussian tails extend further in some directions than in others. We therefore use a different criterion based on the overlap of local wave functions. Whether the unit cell centered at $2\pi\vec{j}$ is a nearest neighbor to the central unit cell now generally depends on the minima under consideration. Specifically, given a minimum $m'$ in the central unit cell, and a minimum $m$ in the unit cell at vector $2\pi\vec{j}$, we determine the nearest-neighbor character by computing the overlap of the two harmonic oscillator ground-state wave functions. For a given overlap threshold value $\varepsilon$, we call the two unit cells nearest neighbors with respect to $m$ and $m'$ if

$$\langle \vec{0}, m'; \vec{0} | \vec{0}, m; \vec{j} \rangle = \sqrt{\frac{2_d^N \det(\Delta_m)^{1/2} \det(\Delta_{m'})^{1/2}}{\det(\Delta_m + \Delta_{m'})}} \exp\left[ -\frac{1}{2} \delta\vec{\theta}^T (\Delta_m^{-1} + \Delta_{m'}^{-1})^{-1} \delta\vec{\theta} \right] > \varepsilon. \quad (6.31)$$

Here, we have defined $\delta\vec{\theta} = 2\pi\vec{j} + \vec{\theta}_m - \vec{\theta}_{m'}$ and $\Delta_m = \Xi_m^{-T}\Xi_m^{-1}$, where $\Xi_m$ is defined relative to minimum $m$. With this definition in place, we truncate the sum over $\vec{j}$ by selecting neighbors up to a certain degree. (Note that the overlap threshold $\epsilon$ must ultimately be adjusted adaptively in order to ensure convergence.)

### 6.1.3 Singular inner products

A possible challenge for the numerical treatment, which we have observed in several cases, is that the overlap matrix $\langle \psi_{\vec{n}_g,\vec{s}',m'} | \psi_{\vec{n}_g,\vec{s},m} \rangle$ may approach singularity (and possibly become indefinite due to rounding errors). This is a familiar problem in quantum chemistry calculations [164, 165] and arises when the set of "basis" states $\{|\psi_1\rangle, |\psi_2\rangle, \ldots, |\psi_h\rangle\}$ is approximately linearly dependent. A common technique for resolving this issue which we have implemented here is the *canonical orthogonalization* procedure of Löwdin [166, 167, 168]. One diagonalizes the inner product matrix to

obtain the eigenvalues $\{\Delta_1, \Delta_2, \ldots, \Delta_h\}$ and matrix of column eigenvectors $U$. The orthonormalized states are [166, 167, 168]

$$|\psi'_k\rangle = \Delta_k^{-1/2} \sum_\ell |\psi_\ell\rangle U_{\ell k}. \tag{6.32}$$

Choosing a cutoff $\Delta_{\text{min}}$ allows for the rejection of states $|\psi'_k\rangle$ where $\Delta_k < \Delta_{\text{min}}$. The Hamiltonian $H$ is then projected onto the deflated basis and we are left with a standard eigenvalue problem.

### 6.1.4 Optimization and anharmonicity correction of the ansatz wave functions

One of the main goals of this chapter is the construction of basis states that closely approximate the low-energy eigenstates of superconducting circuits. We can optimize the tight-binding wave functions (3.7) for this purpose by recognizing that sufficiently far from each minimum location, the potential ceases to be strictly harmonic. The low-energy eigenfunctions typically have spatial spreads that are broader if the leading-order anharmonic term is negative and narrower if it is positive. We take this effect into account and improve the tight-binding wave functions by treating the harmonic length of each mode as a variational parameter. Specifically, we modify the matrix $\Xi$ by optimizing the magnitude of the eigenvectors $\vec{\xi}_\mu$, leaving the directions unchanged, $\vec{\xi}_\mu \to \lambda_\mu \vec{\xi}_\mu$, where $\lambda_\mu$ is optimized. We perform this optimization procedure for the ansatz ground state $|\psi_{\vec{n}_g,\vec{0},m}(\lambda_\mu)\rangle$, making the dependence on $\lambda_\mu$ explicit, minimizing

$$E = \frac{\langle\psi_{\vec{n}_g,\vec{0},m}(\lambda_\mu)|H|\psi_{\vec{n}_g,\vec{0},m}(\lambda_\mu)\rangle}{\langle\psi_{\vec{n}_g,\vec{0},m}(\lambda_\mu)|\psi_{\vec{n}_g,\vec{0},m}(\lambda_\mu)\rangle}. \tag{6.33}$$

The resulting harmonic lengths are then used for all other states defined in the same minimum $m$.[1] We term this optimization scheme "anharmonicity correction," which combined with improper and proper tight binding leads to additional choices for constructing tight-binding states: (IPAC) **imp**roper with **a**nharmonic **c**orrection and (PAC) **p**roper with **a**nharmonic **c**orrection of the $m = 0$ minimum. Recall that the improper scheme calls for the construction of states based only on the

[1] Alternatively, one could optimize the harmonic lengths of a higher-lying basis state [123], which is a possible avenue for future research.

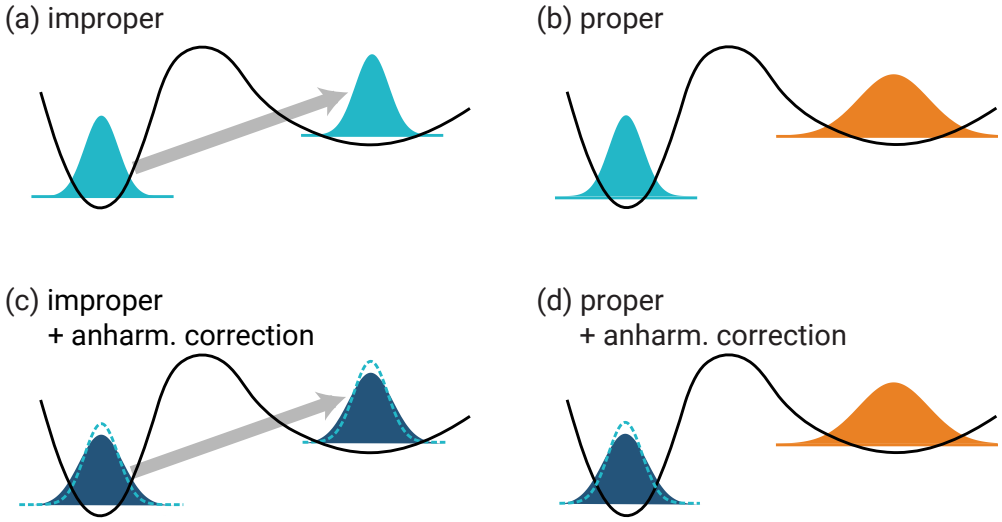


**Figure 6.1:** Schematic of ansatz construction schemes. (a) Improper, where local wave functions are defined according to the curvature of the $m = 0$ minimum and are reused to form the local wave functions of other inequivalent minima. (b) Proper, where local wave functions for every minimum are defined according to the local curvature. (c) Improper with anharmonicity correction, where harmonic length(s) of the ansatz ground-state wave function of the $m = 0$ minimum are optimized to account for anharmonicity corrections to the potential. The resulting wave functions are then also used for $m \neq 0$ minima as in (a). The dashed lines show the unoptimized local ground state wave function defined for the $m = 0$ minimum (the change in the harmonic length due to anharmonicity corrections has been exaggerated). (d) Proper with anharmonicity correction of only the $m = 0$ minimum. Wave functions for the $m = 0$ minimum are defined according to the local curvature and anharmonicity correction scheme, while wave functions for $m \neq 0$ minima are defined only according to the local curvature.

curvature of the $m = 0$ minimum, while the proper scheme constructs states in each minimum according to the local curvature. Therefore IPAC uses anharmonicity correction of the $m = 0$ minimum and applies the resulting states to all minima, while PAC applies anharmonicity correction only to the $m = 0$ minimum, and uses uncorrected states in $m \neq 0$ minima, see Fig. 6.1.

We could further envision the construction of states according to: proper with anharmonicity correction of all minima. However, in the cases considered here, this scheme frequently encounters numerical stability issues far in excess of those of the previously discussed schemes, with no benefit in terms of spectral convergence. In many cases this issue is due to states in $m \neq 0$ minima being optimized with excessively large harmonic lengths, leading to large wave function overlap and hence numerical instability. Resolution of this problem is an interesting open question,

as the proper scheme with anharmonicity correction of all minima could perhaps be useful when applied to other systems.

### 6.1.5 Applicability of tight binding

A natural question to ask is whether the tight-binding method is appropriate for obtaining the eigenspectrum of a given superconducting circuit. A general and systematic answer to this question is difficult to obtain and we do not aim to give a comprehensive answer here. Instead we seek to motivate a "rule-of-thumb" criteria that serves as an indicator of whether the tight-binding method can produce meaningful results.

If the spatial spread of the localized harmonic-oscillator states [eigenfunctions of Eq. (3.6)] is small compared to distances between minima then the tight-binding approach is physically well motivated and we expect tight-binding wave functions to serve as good approximations to low-energy eigenstates. If, on the other hand, the wave functions have large spatial spread and significant overlap, then the weak-periodic-potential approximation is more appropriate for describing the low-energy excitations.

To quantify this discussion, we define length scales to compare the spatial spread of wave functions with the distance between minima. Examining the exponential dependence

$$\exp(-\frac{1}{2}\vec{\phi}^T\Xi^{-T}\Xi^{-1}\vec{\phi})$$

of the local harmonic wave functions, we can extract the effective harmonic length $\ell_{mm'}$ along the unit vector $\hat{u}_{mm'}$ separating two minima $m$ and $m'$

$$\ell_{mm'} \equiv (\hat{u}_{mm'}^T\Xi^{-T}\Xi^{-1}\hat{u}_{mm'})^{-1/2}. \tag{6.34}$$

It is natural to compare $\ell_{mm'}$ to $d_{mm'}/2$, half the distance between the minima. Our rule-of-thumb

for application of the tight-binding method is based on the largeness of the localization ratios

$$r_{mm'} = \frac{d_{mm'}/2}{\ell_{mm'}}, \tag{6.35}$$

compared to unity. This provides a rough threshold for judging whether the tight-binding method might be appropriate.

## 6.2 Tight binding applied to the flux qubit

In order to evaluate the accuracy of the tight-binding method, we first apply it to the familiar case of the three-junction flux qubit. The spectrum of the flux qubit is well understood [114, 169], but applying the method in this context is of interest and nontrivial because the flux qubit has multiple degrees of freedom and multiple inequivalent minima in the central unit cell. Additionally, the flux qubit is typically operated in a parameter regime where tight-binding techniques are applicable. Indeed, many authors have used tight-binding techniques to get analytical estimates of tunneling rates and low-energy eigenvalues [114, 115, 116]. We extend this previous research by using multiple tight-binding basis states in each inequivalent minimum to obtain improved low-energy eigenvalue estimates.

We consider the case where two of the junctions are identical with junction energy $E_J$ and capacitance $C_J$, while the third has junction energy and capacitance reduced by a factor of $\alpha$. The Hamiltonian is [114]

$$\begin{aligned} H_{\text{flux}} = &\sum_{i,j=1}^{2} (n_i - n_{gi}) 4(\mathsf{E}_\mathsf{C})_{ij} (n_j - n_{gj}) - E_J \cos(\phi_1) - E_J \cos(\phi_2) \\ &- \alpha E_J \cos(\phi_1 - \phi_2 + \phi_{\text{ext}}) + E_J(2+\alpha), \end{aligned} \tag{6.36}$$

where $\phi_{\text{ext}} = 2\pi\Phi_{\text{ext}}/\Phi_0$, $\Phi_0 = h/2e$ is the flux quantum, $\mathsf{E}_\mathsf{C} = \frac{e^2}{2}\mathsf{C}^{-1}$ is the charging energy matrix and the constant term is included to ensure that the spectrum of $H_{\text{flux}}$ is positive. The capacitance

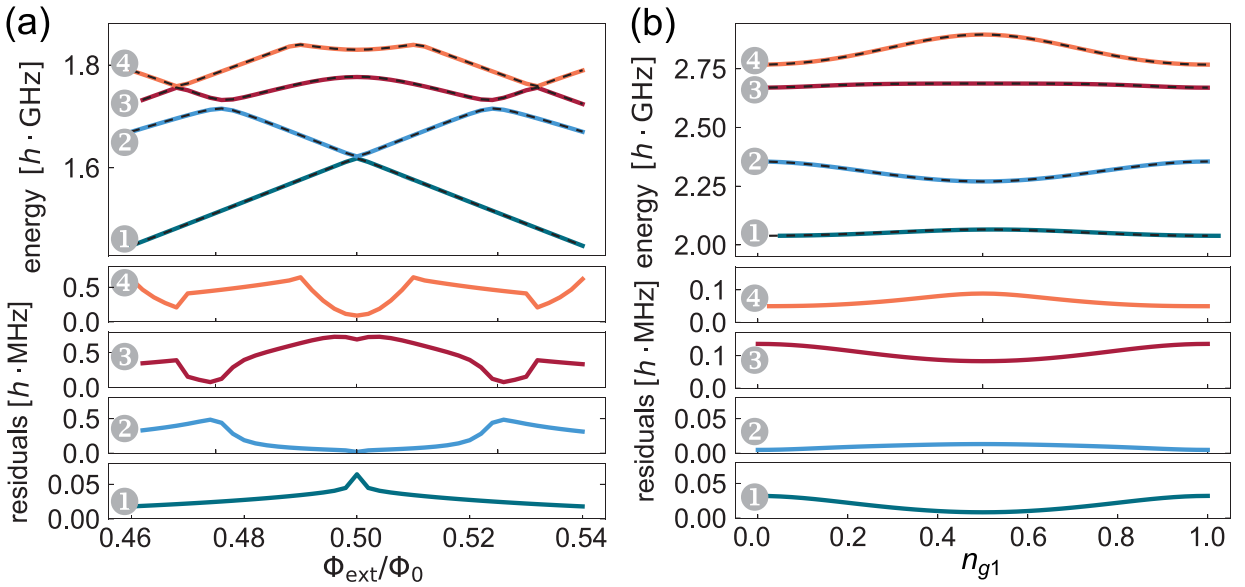


**Figure 6.2:** Spectrum of the flux qubit as a function of (a) flux and (b) offset charge $n_{g1}$, calculated using charge-basis diagonalization (solid) and improper tight binding (dashed). At the magnification level of the two figures, the spectra almost exactly overlap. Below each spectrum is the absolute error of the tight-binding calculation relative to the exact spectrum for each of the four lowest-energy eigenstates. Sub-MHz level agreement is achieved in all cases considered here with $\Sigma_{\text{max}} = 5$, and sub-kHz level absolute error is possible for both parameter sets by increasing $\Sigma_{\text{max}}$. For (a) flux modulation, we choose parameters $E_J/h = 1$ GHz, $E_J/E_{C_J} = 60, E_{C_g}/E_{C_J} = 50, \alpha = 0.8$ and $n_{gi} = 0$ [169]. For (b) tuning $n_{g1}$, we use parameters $E_J/h = 1$ GHz, $E_J/E_{C_J} = 5, E_{C_g}/E_{C_J} = 50, \alpha = 0.8$ and have set $n_{g2} = 0$, $\phi_{\text{ext}} = 0.5$.

matrix C is

$$\mathsf{C} = \begin{pmatrix} C_J(1+\alpha) + C_g & -\alpha C_J \\ -\alpha C_J & C_J(1+\alpha) + C_g \end{pmatrix}, \tag{6.37}$$

where $C_g$ is the capacitance to ground of each island. (See Refs. [114, 169] for details on the derivation of Eq. (6.36)).

In order to demonstrate quantitative accuracy of the tight-binding method, we calculate the flux and offset-charge dependence of the spectrum, see Fig. 6.2. For the parameters considered, the localization ratios are large compared with unity, indicating that the parameter regimes are amenable to tight binding. Figs. 6.2(a-b) show the spectrum as a function of flux and offset charge,

respectively, with improper-tight-binding results overlaying the exact spectrum obtained via charge-basis diagonalization. While the spectra from the two different methods are indistinguishable in the upper panels of Figs. 6.2(a-b), we explicitly visualize the residuals for the four lowest eigenenergies in the lower panels of Figs. 6.2(a-b). For $\Sigma_{\text{max}} = 5$, the residuals are all below 1 MHz for flux and offset-charge variation. Further suppression of the absolute error below 1 kHz is possible by increasing the global excitation number cutoff to $\Sigma_{\text{max}} = 10$.

Even for relatively greedy cutoffs of the global excitation number $\Sigma_{\text{max}}$, the improper-tight-binding method can provide accurate estimates of the eigenspectrum. To compare results obtained using tight-binding methods with results from exact diagonalization, we compute the relative deviation from the exact low-energy spectrum, averaged over the four lowest-energy eigenvalues

$$\eta_{\text{avg}} = \frac{1}{4}\sum_{i=0}^{3}\frac{E_i - \epsilon_i}{\epsilon_i}. \tag{6.38}$$

Here, $\epsilon_i$ is the exact eigenenergy of the state indexed by $i$ and $E_i$ is the approximate eigenenergy. We also define the minimum and maximum relative deviations

$$\eta_{\text{min}} = \min_{i=0,\ldots,3}\left(\frac{E_i - \epsilon_i}{\epsilon_i}\right),$$

with $\eta_{\text{max}}$ defined similarly. To monitor convergence and assess the memory requirements for reaching a desired accuracy, we plot in Fig. 6.3 $\eta_{\text{avg}}$ as a function of nonzero Hamiltonian matrix elements ($n_H$). We use $n_H$ rather than Hilbert-space dimension as a proxy for memory usage to account for the different cases of sparse vs. dense matrix numerics encountered for diagonalization in the charge basis vs. tight binding. For a cutoff as greedy as $\Sigma_{\text{max}} = 1$, corresponding to $n_H = 36$, we find $\eta_{\text{avg}} < 7 \cdot 10^{-3}$ using improper tight binding. Note that for the flux qubit in the parameter regimes considered here, neither the proper-tight-binding technique nor anharmonicity correction provided any appreciable benefit in terms of convergence to the spectrum over improper tight binding.

To benchmark convergence of the tight-binding method, we compare against results obtained

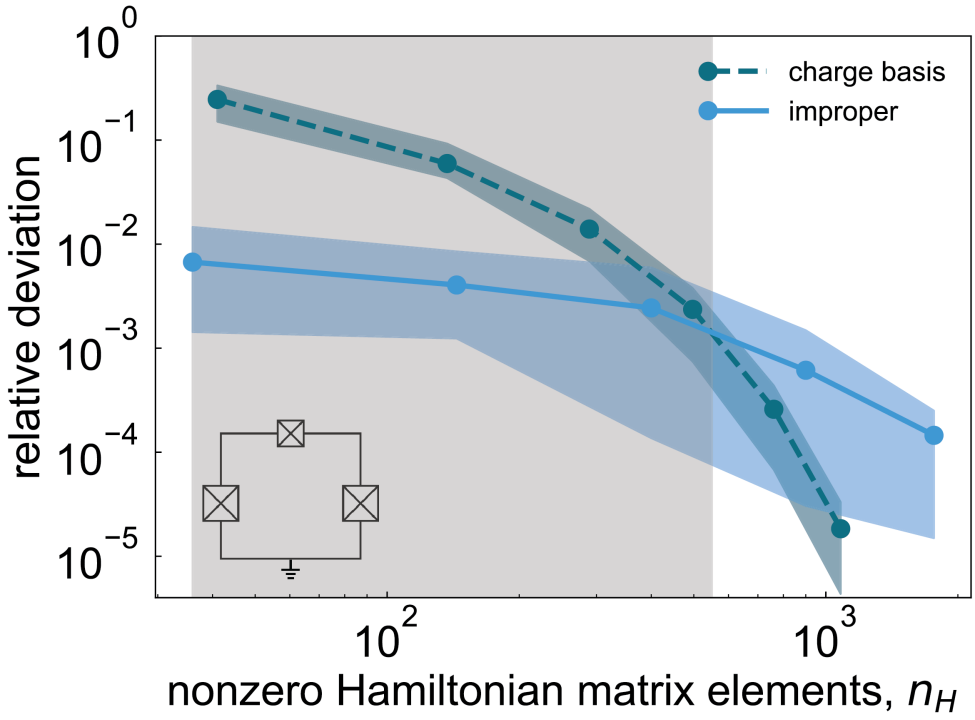


**Figure 6.3:** Comparison of convergence to the exact low-energy flux qubit spectrum between improper tight binding (blue circle, solid line) and approximate diagonalization in the charge basis (green circle, dashed line) as a function of $n_H$. The colored circles represent the average relative deviation $\eta_{\text{avg}}$, while the colored lines are merely a guide to the eye. The colored shaded regions encompass the range between $\eta_{\text{min}}$ and $\eta_{\text{max}}$. The gray shaded region represents the $n_H$ values for which tight binding yields an advantage over charge-basis diagonalization, comparing $\eta_{\text{avg}}$ for a given $n_H$. Improper tight binding allows for an accurate estimate of the low-energy eigenspectrum already at $\Sigma_{\text{max}} = 1$, yielding $\eta_{\text{avg}} < 7 \cdot 10^{-3}$ and maximum absolute error of less than $25$ MHz. We choose the parameters of Fig. 6.2(a), as well as $\phi_{\text{ext}} = 0.47, n_{g1} = 0.2, n_{g2} = 0.3$. We can perform the same calculation for the parameters of Fig. 6.2(b) and obtain similar results, with tight binding outperforming charge-basis diagonalization for small $n_H$. The inset shows a schematic of the flux-qubit circuit.

using *truncated* diagonalization in the charge basis. We compute the average relative deviation $\eta_{\text{avg}}$ using energy estimates obtained via a choice of charge-basis cutoff $n_{\text{cut}}$. By increasing $n_{\text{cut}}$, we increase $n_H$ and can thereby perform a direct comparison with $\eta_{\text{avg}}$ values obtained via tight binding, see Fig. 6.3. The shaded region of Fig. 6.3 indicates where tight binding outperforms approximate diagonalization in the charge basis for a given $n_H$. The advantage region for tight binding is for small values of $n_H$, indicating that when keeping few basis states, tight-binding states yield a closer approximation to the true low-energy eigenstates than charge-basis states. At larger values of $n_H$, charge-basis diagonalization begins to outperform tight binding.

## 6.3 Tight binding applied to the current-mirror circuit

We expect the tight-binding method to be most useful in the study of larger circuits, where keeping a generous number of basis states is not feasible due to memory requirements. To demonstrate the tight-binding method on such a larger circuit, we apply it to the current mirror [52]. The Hamiltonian of the current mirror is given in Eq. (5.3). Eliminating the cyclic degree of freedom corresponding to the net charge on the circuit, we obtain

$$\begin{aligned} H_{\text{CM}} = &\sum_{i,j=1}^{2N-1} (n_i - n_{gi}) 4(\mathsf{E_C})_{ij} (n_j - n_{gj}) - E_J \sum_{i=1}^{2N-1} \cos(\phi_i - \phi_{\text{ext}}/2N) \\ &- E_J \cos(\Sigma_{i=1}^{2N-1} \phi_i - \phi_{\text{ext}}/2N) + 2NE_J, \end{aligned} \tag{6.39}$$

where the circuit contains $2N-1$ degrees of freedom and we remind the reader that $N$ refers to the number of big capacitors. We have added $2NE_J$ to the Hamiltonian to make the spectrum positive definite. As discussed in Ch. 5, the interest in this circuit originates from Kitaev's prediction that quantum information should be protected against relaxation and dephasing in the current mirror [52]. For a representative choice of parameters, one can identify $N \approx 12$ as the ideal value of $N$ [109]. Circuit sizes with such large values of $N$ exceed our capabilities for finding eigenstates and eigenenergies via diagonalization in the charge basis; the maximum value of $N$ where we

can achieve spectral convergence is $N = 3$.[2] We note that we additionally attempted to simulate Eq. (6.39) using DMRG [109, 145], and similarly found a limit of $N = 3$. Due to the long-range interactions present in Eq. (6.39), bond dimensions become prohibitively large, which is a challenge for convergence. Below, we show that the tight-binding method is an advantageous alternative for simulating the current-mirror circuit at larger values of $N$.

Implementation of the tight-binding method for the current-mirror circuit proceeds in a manner analogous to the case of the flux qubit, as neither circuit contains inductors. We choose a set of protected circuit parameters given by $E_{C_B}/h = 0.2$ GHz, $E_{C_J}/h = 35$ GHz, $E_{C_g}/h = 45$ GHz, $E_J/h = 10$ GHz, $\phi_{\text{ext}} = 0$ and $n_{gi} = 0$. To establish qualitatively that the current-mirror circuit with these parameters is amenable to a tight-binding treatment, we fix a value of $N$ and verify that the localization ratios are all of order unity or larger. We observe that the localization ratios generally *increase* with $N$, indicating that the tight-binding method should become increasingly accurate with larger $N$. For an independent quantitative assessment of the validity of tight binding, we will compare spectra obtained with tight-binding methods with exact results. For this purpose we first apply the tight-binding method to the $N = 3$ current-mirror circuit.

We can obtain excellent agreement between spectra obtained via tight binding and exact results, with average relative deviations $\eta_{\text{avg}}$ below $2 \cdot 10^{-5}$, see Fig. 6.4. The best agreement is for the energy of the ground state, for which we obtain agreement to within 16 kHz. For the first- and second-excited states these results correspond to sub-MHz agreement, while for the third-excited state agreement is on the order of a MHz. The use of the anharmonicity correction yields a substantial benefit that is critical for achieving this level of accuracy. We find that the proper-tight-binding method yields nearly identical results to those produced by improper tight binding, and therefore those results are not shown in Fig. 6.4. Our highest accuracy approximations are obtained with $\Sigma_{\text{max}} = 8$, corresponding to $n_H = 1.5 \cdot 10^7$, beyond which we encounter numerical instabilities. We emphasize that one can actually obtain a reasonable approximation to the spectrum based on moderate values of $\Sigma_{\text{max}}$, as shown in Fig. 6.4. For example with $\Sigma_{\text{max}} = 1$ and $n_H = 324$, improper tight binding with anharmonicity correction yields $\eta_{\text{avg}} \approx 8 \cdot 10^{-3}$, corresponding to absolute errors

[2] Our calculations were performed on an Intel Xeon CPU E5-1650 24 core processor with 128 GB RAM.

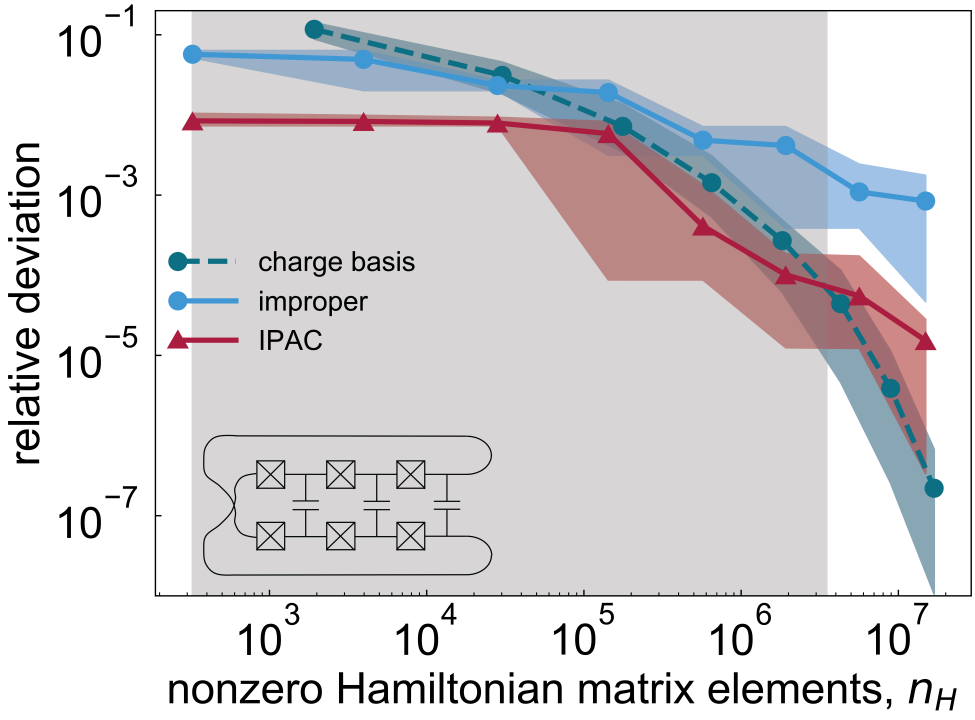


**Figure 6.4:** Performance of the tight-binding method as applied to the $N = 3$ current-mirror circuit. Similarly to the case of the flux qubit, we plot $\eta_{\text{avg}}$ for improper tight binding (blue circle, solid line), improper tight binding with anharmonicity correction (red triangle, solid line) and approximate diagonalization in the charge basis (green circle, dashed line) as a function of $n_H$. Improper tight binding with anharmonicity correction outperforms charge-basis diagonalization across approximately four orders of magnitude in $n_H$, as indicated by the shaded region. The sharp cliff in $\eta_{\text{min}}$ for improper tight binding with anharmonicity correction at $n_H \approx 10^5$ is due to the inclusion of new basis states that contribute to the ground state, yielding $\eta_{\text{min}} \approx 10^{-4}$. The inset shows a schematic of the $N = 3$ current mirror circuit. We choose $\phi_{\text{ext}} = 0$ and $n_{gi} = 0$, with circuit parameters given in the main text.

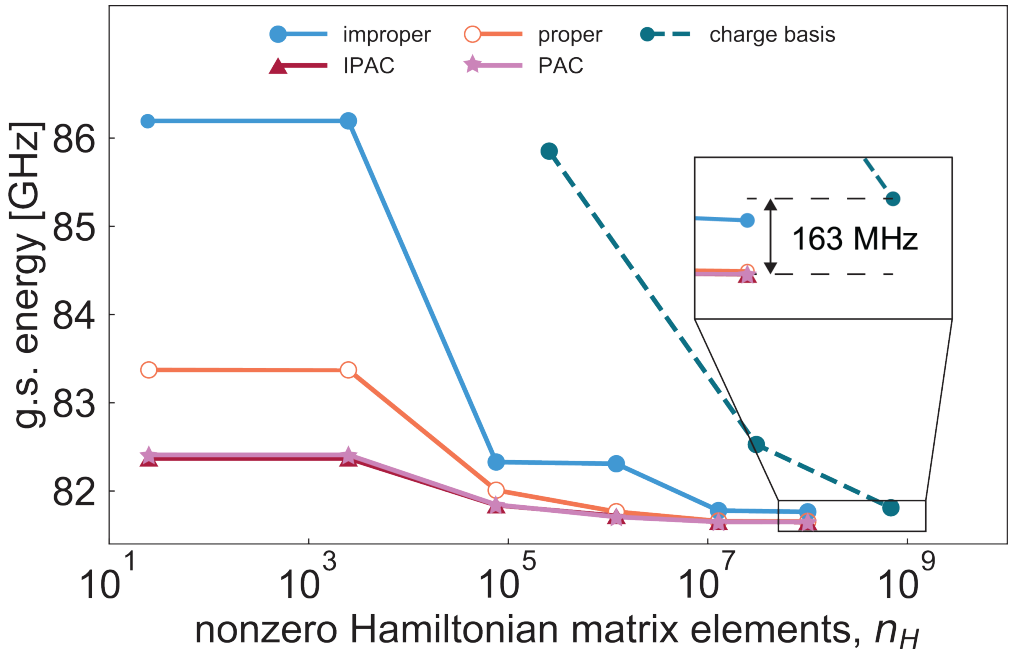


**Figure 6.5:** Comparison of computed ground-state energies for the $N = 5$ current-mirror circuit. Individual curves correspond to results obtained with tight-binding schemes improper (blue solid circle, solid line), improper with anharmonicity correction (red triangle, solid line), proper (orange open circle, solid line) and proper with anharmonicity correction of the global minimum (pink star, solid line), as well as approximate diagonalization in the charge basis (green solid circle, dashed line). Tight-binding techniques consistently yield lower and hence more accurate eigenenergies as compared to charge basis diagonalization, with a difference of 163 MHz between the best results obtained with tight binding and approximate diagonalization in the charge basis, see the inset. We used the same current-mirror circuit parameters here as in Fig. 6.4.

of about $300$ MHz.

We can contrast these results with those obtained using truncated diagonalization in the charge basis. Using the same metric for memory efficiency previously applied to the flux-qubit example, we find that tight binding is advantageous over a wide range of $n_H$ values, see Fig. 6.4. Specifically, to achieve $\eta_{\text{avg}} \approx 8 \cdot 10^{-3}$, truncated diagonalization in the charge basis requires about three more orders of magnitude in memory resources as compared to tight binding. The advantage region for tight binding extends over approximately four orders of magnitude $10^2 \lesssim n_H \lesssim 10^6$, as shown in the shaded area of Fig. 6.4.

To extend toward the regime of ideal $N$, we apply the tight-binding method to obtain the spectrum of the $N = 5$ current-mirror circuit, which has 9 degrees of freedom. We compute the ground-

| $E_0$ [GHz] | | | | | | | $E_1$ [GHz] | | | | | | |
|---|---|---|---|---|---|---|---|---|---|---|---|---|---|
| $\Sigma_{\max}$ | IP | P | IPAC | PAC | $n_{\text{cut}}$ | AD | $\Sigma_{\max}$ | IP | P | IPAC | PAC | $n_{\text{cut}}$ | AD |
| 0 | 86.1951 | 83.3724 | 82.3695 | 82.4101 | 1 | 85.8517 | 0 | 91.4604 | 88.3023 | 84.4859 | 88.3023 | 1 | 87.9608 |
| 1 | 86.1951 | 83.3724 | 82.3695 | 82.4101 | 2 | 82.5268 | 1 | 87.5550 | 84.7936 | 83.4348 | 83.4727 | 2 | 84.1042 |
| 2 | 82.3282 | 82.0090 | 81.8391 | 81.8453 | 3 | 81.8103 | 2 | 85.5667 | 84.7812 | 83.4211 | 83.4566 | 3 | 82.9705 |
| 3 | 82.3087 | 81.7654 | 81.7181 | 81.7059 | | | 3 | 83.5501 | 83.1624 | 82.9354 | 82.9400 | | |
| 4 | 81.7780 | 81.6585 | 81.6501 | 81.6494 | | | 4 | 83.5259 | 82.8765 | 82.7984 | 82.7874 | | |
| 5 | 81.7638 | 81.6544 | 81.6472 | 81.6480 | | | 5 | 82.9122 | 82.7378 | 82.7224 | 82.7236 | | |

**Table 6.1:** Eigenenergies for the ground state and first-excited state of the $N = 5$ current-mirror circuit. Energies were computed using tight-binding schemes (IP) improper, (P) proper, (IPAC) improper with anharmonicity correction, (PAC) proper with anharmonicity correction, as well as (AD) approximate diagonalization in the charge basis. The energies are color coded from least accurate (darkest) to most accurate (lightest). The three tight-binding flavors proper, IPAC and PAC all perform similarly and outperform improper. The most accurate results for $E_0$ and $E_1$ were obtained with tight binding rather than with approximate diagonalization in the charge basis (circuit parameters used are the same as in Fig. 6.4).

state energy $E_0$ and first-excited-state energy $E_1$ using the four tight-binding techniques [improper, proper, (IPAC) improper with anharmonicity correction and (PAC) proper with anharmonicity correction of the $m = 0$ minimum], see Tab. 6.1. By the variational principle, our computed eigenenergies are upper bounds to the true eigenenergies [123, 124, 167]. Therefore, lower eigenenergy values always imply higher accuracy. The proper, IPAC and PAC tight-binding schemes all perform similarly but collectively outperform the improper scheme. The lowest eigenenergies are obtained using IPAC, with bounds $\epsilon_0 \leq 81.6472$ GHz and $\epsilon_1 \leq 82.7224$ GHz. The largest cutoff we can handle is $\Sigma_{\text{max}} = 5$ ($n_H = 1.0 \cdot 10^8$), beyond which we encounter memory issues. We observe that for this circuit, ansatz states localized in minima aside from the $m = 0$ minimum contribute to the low-energy spectrum, and moreover the curvatures of those minima differ from those of the $m = 0$ minimum. Otherwise, there would be no difference between the eigenenergies computed with improper and proper tight binding. Note that schemes IPAC, PAC allow for rough estimates of the eigenspectrum with a greedy cutoff $\Sigma_{\text{max}} = 2$ ($n_H = 7.6 \cdot 10^4$), with calculated $E_0, E_1$ less than $200$ MHz greater than the lowest obtained respective values.

We next compare tight-binding results with those from approximate diagonalization using the truncated charge basis. For $N = 5$ the maximum possible charge cutoff we can handle is $n_{\text{cut}} = 3$, corresponding to a Hilbert-space dimension of $d = 4.0 \cdot 10^7$ and number of nonzero Hamiltonian

matrix elements $n_H = 6.8 \cdot 10^8$. The best estimates for $E_0$ and $E_1$ obtained using approximate diagonalization in the charge basis are in fact *higher* and therefore less accurate than the lowest obtained values using tight-binding methods, see Tab. 6.1. Moreover, the tight-binding methods consistently yield lower eigenenergy approximations across all $n_H$ values. Fig. 6.5 illustrates this point for the ground-state energy $E_0$, and similar results hold for the first-excited-state energy $E_1$. We thus find that the tight-binding method is more memory efficient than charge-basis diagonalization for the $N = 5$ current-mirror circuit. More broadly, this may indicate that the tight-binding method can serve as an interesting and useful method in the context of large circuits.

# 7 High-Fidelity Gates on Galvanically-Coupled Fluxonia

*This chapter is based on the recent preprint (submitted for publication) D. K. Weiss et al., arXiv:2207.03971 (2022).*

In the previous two chapters we focused our attention in large part on quantifying the spectrum and coherence properties of the current-mirror circuit. We have argued that the current-mirror is an interesting example of a protected superconducting qubit that could possess enhanced coherence times. In the process of analyzing the current mirror we developed theoretical and numerical tools allowing for the analysis of other large circuits. Nevertheless the fluxonium qubit has already been shown experimentally to possess coherence times ranging from hundreds of microseconds [31, 32] to milliseconds [33]. These record coherence times, coupled with charge-noise insensitivity and large anharmonicity make the fluxonium promising as the building block of a future quantum processor. Thus to make progress in the near term on enhancing all-important two-qubit-gate fidelities, we focus on coupling low-frequency fluxonium qubits. It is important to note that for such low-frequency qubits, high gate fidelities can be obtained in regimes where the RWA breaks down [31, 55]. To predict dynamics, describe this non-RWA physics, and construct high-fidelity gates we employ a Magnus expansion as introduced in Ch. 4.

Two-qubit gates on capacitively-coupled fluxonia have recently been reported [23, 100, 170, 171, 172], with infidelities on the order of $10^{-2} - 10^{-3}$. These experimental realizations have been accompanied by a flurry of theoretical attention [173, 174, 175, 176, 177, 178, 179]. Fluxonium qubits in these capacitive-coupling architectures have frequencies on the order of 500 MHz - 1 GHz, generally thought to be the ideal frequency range for executing high-fidelity gates in these systems

(considering gate schemes involving population transfer only in the qubit subspace) [173, 174, 176]. However, fluxonia with qubit frequencies less than 200 MHz have consistently achieved the longest coherence times [31, 33], likely because low-frequency operation mitigates dielectric loss [31, 32, 33]. To obtain fast, high-fidelity entangling gates between such low-frequency fluxonium qubits, we revisit galvanic-coupling schemes previously proposed [180, 181, 182] and experimentally implemented [183, 184] for flux qubits. A galvanic-coupling scheme helps yield strong coupling strengths, as those are quantified by phase matrix elements rather than charge matrix elements (as would be the case for capacitive coupling). Phase matrix elements are not suppressed by the qubit frequency [178], making a galvanic-coupling architecture attractive for achieving entangling gates on low-frequency qubits. Moreover, for fluxonium qubits whose inductance is kinetic [30] rather than geometric [185], a galvanic connection can generally yield stronger coupling strengths than those achieved through mutual inductance alone [185]. To make the coupling strength tunable, we generalize the so-called "fluxonium molecule" circuit introduced in Ref. [186] by inserting a coupler Josephson junction as shown in Fig. 7.1.

We bias the heavy-fluxonium qubits at their half-flux sweet spots, as such fluxonia are linearly insensitive to flux noise and thus have achieved record coherence times [31, 32, 33]. To avoid directly exciting the coupler degrees of freedom, the interaction between the qubits and the coupler is chosen to be dispersive. This allows for an effective description in which the coupler is eliminated, but mediates a tunable *XX* interaction. We show that the strength of this effective *XX* coupling changes sign as a function of coupler flux and thus passes through zero. In addition, we find that the parasitic *ZZ* interaction strength is suppressed, which is a general feature of coupled systems of low-frequency fluxonium qubits [100].

We describe how to execute two-qubit gates via sinusoidal modulation of the coupler flux for a duration as short as a few drive periods. Based on our analysis outside the RWA regime, we find that the implemented entangling operations generally differ from named gates by relative phases. We compensate for these phase factors using single-qubit *Z* rotations to obtain a high-fidelity $\sqrt{i\mathrm{SWAP}}$ gate.

Ordinarily, single-qubit gates are designed in the convenient regime where the RWA applies

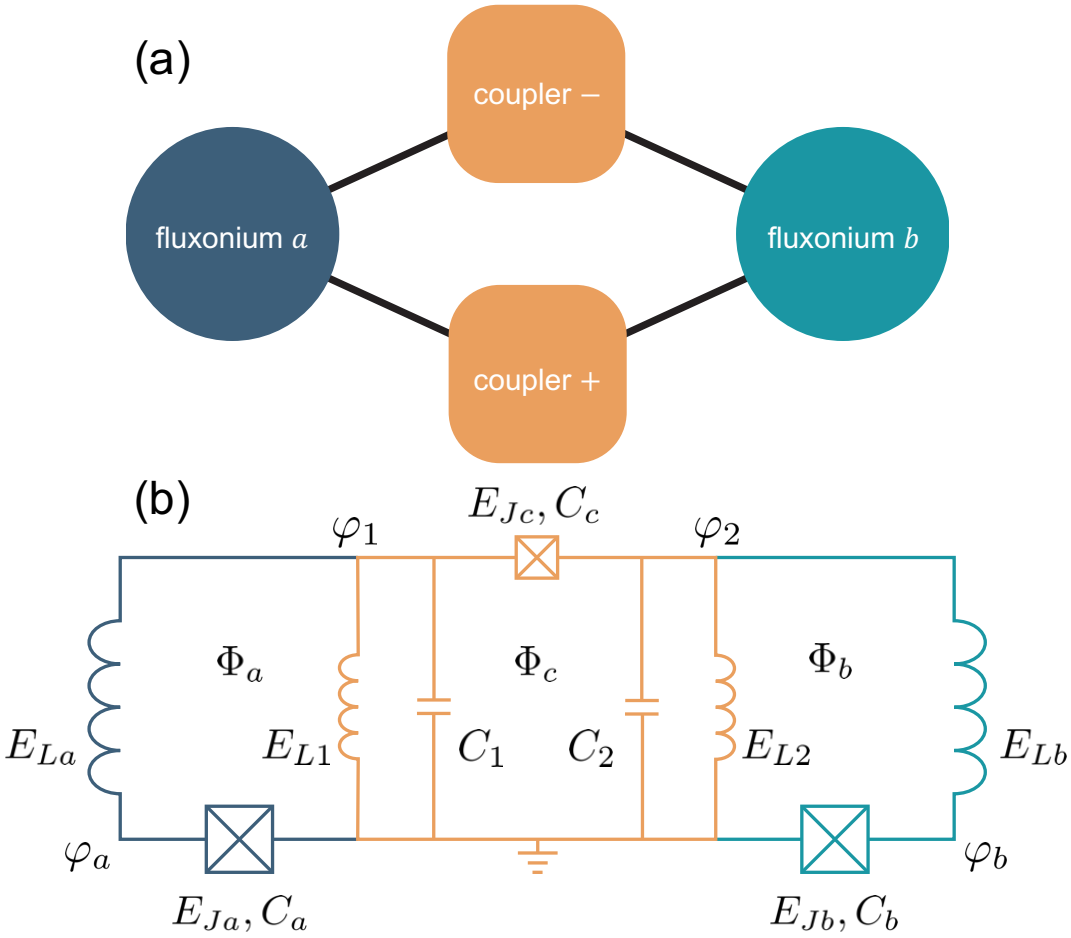


**Figure 7.1:** Galvanically-coupled heavy fluxonia. (a) Schematic of the qubit-coupler interaction. The fluxonium qubits $a, b$ are each coupled to a harmonic coupler mode $\theta_+$ and a flux-tunable coupler mode $\theta_-$, but do not interact directly. (b) Circuit diagram of the device. Qubit $a$ (dark blue) and qubit $b$ (light blue) are galvanically linked to the two coupler modes $\theta_\pm$ (orange). Each loop can be threaded by an external flux $\Phi_\mu$.

[14]. In this scenario, the switch into a frame co-rotating with the drive renders operations simple rotations about fixed axes in the Bloch-sphere picture. Identity gates are obtained by idling and single-qubit *Z* rotations are obtained either e.g. “virtually” by modifying the phase of the drive field in software [187, 188] or “physically” by detuning the qubit frequency from that of the drive [189]. The situation is reversed for systems of heavy fluxonium qubits [91, 92] where drive strengths exceeding the RWA-range are employed – motivating the use of the laboratory frame for qubit operations [31, 55]. In this frame, qubits acquire dynamical phases in the absence of control pulses; in other words, idling yields *Z* rotations of each qubit [31, 55]. To synchronize gates in multi-qubit systems, identity gates of variable time duration must be devised. We show that identity gates can again be implemented using sinusoidal modulation of the qubit fluxes for only a single drive period, resulting in ultra-fast $I$ gates (when compared to the single-qubit Larmor period). Combining the identity gates with single-qubit *Z* rotations assists in achieving high-fidelity entangling gates.

## 7.1 Full-circuit Hamiltonian

To construct the Lagrangian and Hamiltonian of the full circuit shown in Fig. 7.1, we follow the method of Vool and Devoret [96]. The circuit Lagrangian is

$$\mathcal{L} = \frac{\Phi_0^2}{2(2\pi)^2}\left(\sum_{\mu=a,b} C_\mu \dot{\varphi}_\mu^2 + \sum_{i=1,2} C_i \dot{\varphi}_i^2 + C_c[\dot{\varphi}_1 - \dot{\varphi}_2]^2\right) - \frac{1}{2}E_{La}(\varphi_a - \varphi_1)^2 - \frac{1}{2}E_{Lb}(\varphi_b - \varphi_2)^2$$
$$- \frac{1}{2}\sum_{i=1,2} E_{Li}\varphi_i^2 + \sum_{\mu=a,b} E_{J\mu}\cos(\varphi_\mu + \phi_\mu) + E_{Jc}\cos(\varphi_1 - \varphi_2 + \phi_c), \tag{7.1}$$

with node variables and circuit parameters as shown in Fig. 7.1. We have defined the reduced external flux $\phi_\mu = 2\pi\Phi_\mu/\Phi_0$ in terms of the applied magnetic flux through each loop $\Phi_\mu$ and the superconducting flux quantum $\Phi_0 = h/2e$. We consider the case of small deviations from otherwise pairwise equivalent qubit inductors $E_{La}, E_{Lb}$, coupler inductors $E_{L1}, E_{L2}$ and stray capacitances $C_1, C_2$. In the absence of parameter disorder, the coupler modes $\theta_\pm = \varphi_1 \pm \varphi_2$ decouple. Using

these variables the Lagrangian becomes

$$\mathcal{L} = \frac{1}{2}\left(\frac{\Phi_0}{2\pi}\right)^2 \left( \sum_{\mu=a,b} C_\mu \dot{\varphi}_\mu^2 + \frac{1}{2}C\dot{\theta}_+^2 + [C_c + \frac{1}{2}C]\dot{\theta}_-^2 + \frac{1}{2}C\,\mathrm{d}C\,\dot{\theta}_+\dot{\theta}_- \right) \tag{7.2}$$
$$+ \sum_{\mu=a,b} (E_{J\mu}\cos[\varphi_\mu + \phi_\mu] - \frac{1}{2}E_{L\mu}\varphi_\mu^2) - \sum_{i=\pm}\frac{1}{2}E_{Lc}\theta_i^2 + E_{Jc}\cos(\theta_- + \phi_c)$$
$$- \frac{1}{4}(E_L\mathrm{d}E_L + E_L'\mathrm{d}E_L')\theta_+\theta_- + \frac{1}{2}E_{La}\varphi_a(\theta_+ + \theta_-) + \frac{1}{2}E_{Lb}\varphi_b(\theta_+ - \theta_-),$$

where $E_{Lc} = \frac{1}{2}(E_L + E_L')$ and we have introduced notation for the average and relative deviation of the qubit inductors $E_L = \frac{1}{2}(E_{La} + E_{Lb}), \mathrm{d}E_L = \frac{E_{La}-E_{Lb}}{E_L}$, the coupler inductors $E_L' = \frac{1}{2}(E_{L1} + E_{L2}), \mathrm{d}E_L' = \frac{E_{L1}-E_{L2}}{E_L'}$, and the stray capacitances $C = \frac{1}{2}(C_1 + C_2), \mathrm{d}C = \frac{C_1-C_2}{C}$. We perform the Legendre transform to obtain the Hamiltonian and promote our variables to non-commuting operators obeying the commutation relations $[\varphi_\mu, n_\mu] = i$ for $\mu = a, b$ and $[\theta_j, n_j] = i$ for $j = \pm$. The Hamiltonian is $H = H_0 + V + H_{\mathrm{dis}}$, where

$$H_0 = \sum_{\mu=a,b}[4E_{C\mu}n_\mu^2 + \frac{1}{2}E_{L\mu}\varphi_\mu^2 - E_{J\mu}\cos(\varphi_\mu + \pi)] \tag{7.3}$$
$$+ 4E_{C-}n_-^2 + \frac{1}{2}E_{Lc}\theta_-^2 - E_{Jc}\cos(\theta_- + \phi_c) \tag{7.4}$$
$$+ 4E_{C+}n_+^2 + \frac{1}{2}E_{Lc}\theta_+^2,$$
$$V = -\sum_{\mu=a,b}\frac{E_{L\mu}}{2}\varphi_\mu[\theta_+ + (-1)^\mu\theta_-] + \sum_{\mu=a,b}\frac{E_{L\mu}}{2}\delta\phi^\mu[-2\varphi_\mu + \theta_+ + (-1)^\mu\theta_-], \tag{7.5}$$
$$H_{\mathrm{dis}} = \frac{1}{4}(E_L\mathrm{d}E_L + E_L'\mathrm{d}E_L')\theta_+\theta_- - 4E_{C-}\mathrm{d}C n_+ n_- + \mathcal{O}(\mathrm{d}C^2). \tag{7.6}$$

We have neglected higher-order disorder contributions proportional to $\mathrm{d}C^2$ on the assumption that disorder is small. The variable $\mu$ obeys the correspondence $a \to 0, b \to 1$ when appearing in an exponent. Charging energy definitions are $E_{C\mu} = e^2/2C_\mu,\ \mu = a, b, E_{C+} = e^2/(2[C/2]), E_{C-} = e^2/(2[C_c + C/2])$. We have separated the Hamiltonian into bare, coupling and disorder Hamiltonians $H_0, V, H_{\mathrm{dis}}$, respectively. Additionally, we isolated the qubit flux shift away from the sweet spot $\delta\phi_\mu = \phi_\mu - \pi$ and performed the variable transformation $\varphi_\mu \to \varphi_\mu - \delta\phi_\mu$.

The Hamiltonian $H$ is composed of two fluxonium qubits and two coupler degrees of freedom,

where the qubits interact with the coupler via terms in $V$. The coupler $\theta_+$ degree of freedom is harmonic, while the coupler $\theta_-$ degree of freedom is fluxonium like and thus tunable by external flux. It is important to note that there is no term in the Hamiltonian directly coupling the qubits, thus the qubit-qubit interaction is entirely mediated by the coupler. In the case of symmetric qubit inductors, coupler inductors, and stray coupler capacitances, respectively, there are no terms in the Hamiltonian that directly couple the coupler degrees of freedom, simplifying the analysis. However, we show in the following that small parameter disorder does not negatively affect device performance.

The coupler should have the following two desired properties. The first is it must allow for the execution of high-fidelity two-qubit gates. A straightforward way to achieve this goal is to ensure that the interaction of the qubits with the coupler degrees of freedom is dispersive, allowing for an effective description in terms of two coupled qubits. The second requirement is that the two-qubit coupling strength should be sufficiently flux dependent, allowing for tuning from zero to values that allow for fast gates compared with the coherence times $T_1, T_2$ of each qubit. In the next section, we derive the effective Hamiltonian of the system assuming that the qubit-coupler interaction is dispersive. Following this, we discuss specific coupler parameter choices that satisfy the above requirements.

## 7.2 Low-energy effective Hamiltonian

Near the half-flux sweet spots for each qubit, the qubit excitation energies are small compared with the energy needed to excite the coupler or higher-lying fluxonium states. These energy scales naturally define two subspaces: the low-energy subspace defined by the projector onto the computational states $P = \sum_{\ell,m=0,1} |\ell_a, m_b, 0_-, 0_+\rangle\langle \ell_a, m_b, 0_-, 0_+|$ and the high-energy subspace spanned by all other states. We have defined the bare states $|\ell_a, m_b, n_-, p_+\rangle$ that are eigenstates of $H_0$ with eigenenergies $E_l^a + E_m^b + E_n^- + p\omega_+$. The variables $\ell, m, n, p$ correspond to the number of excitations in the degrees of freedom corresponding to the variables $\varphi_a, \varphi_b, \theta_-, \theta_+$, respectively. The coupler $\theta_-$ mode is fluxonium like, however operated in a different parameter regime than the heavy-fluxonium qubits. The bare wave functions and spectra of qubit $a$ and the coupler $\theta_-$ mode

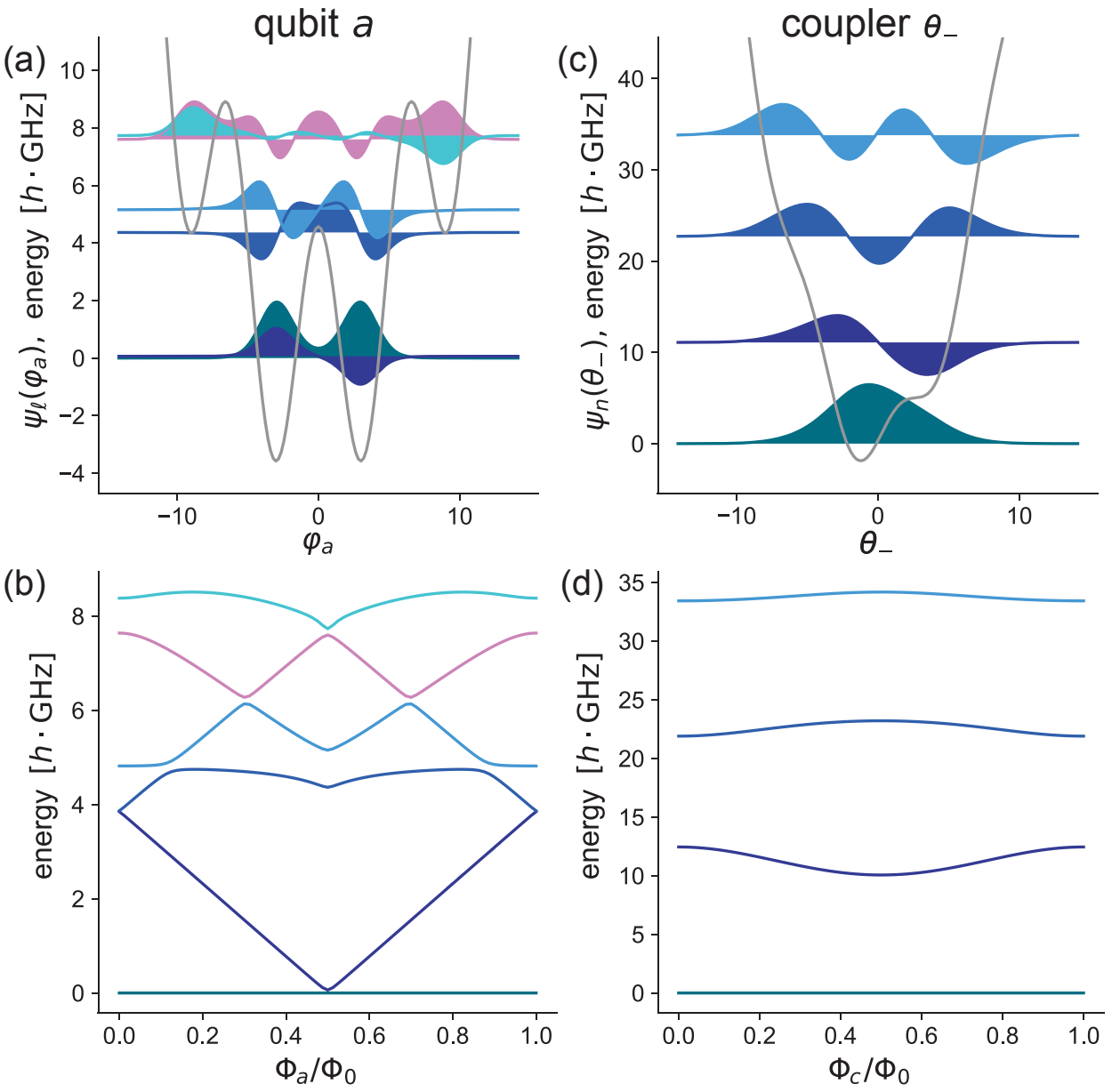


**Figure 7.2:** Bare wave functions and energy spectra. (a) Bare wave functions and potential of qubit $a$ located at the half-flux sweet spot. The bare qubit transition frequency is $\omega_a/2\pi = 62$ MHz, while the energy of the next excited state is 4.4 $h$·GHz above the qubit ground-state energy. (b) Spectrum of qubit $a$ as a function of the qubit flux $\Phi_a$. The wave functions and spectra of qubit $b$ are qualitatively similar to those of qubit $a$. (c) Bare wave functions and potential of the coupler $\theta_-$ mode located at $\Phi_c/\Phi_0 = 0.27$. The energy of the first excited state is more than 10 $h$·GHz above the coupler ground-state energy. (d) Spectrum of the coupler $\theta_-$ mode as a function of the coupler flux $\phi_c$. See Table 7.1 for device parameters.

**Table 7.1:** Circuit parameters in $h$·GHz used throughout this chapter.

| $E_{Ja}$ | $E_{Jb}$ | $E_{Ca}$ | $E_{Cb}$ | $E_L$ | $E_{Jc}$ | $E'_L$ | $E_{C-}$ | $E_{C+}$ |
|---|---|---|---|---|---|---|---|---|
| 4.6 | 5.5 | 0.9 | 0.9 | 0.21 | 3 | 2 | 14.3 | 100 |

are shown in Fig. 7.2. We discuss below in detail the ideal parameter regime in which to operate the coupler modes.

States in different subspaces are coupled by the perturbation $V$, which is small compared with the relevant energy separations. Thus, the interaction is dispersive and we can obtain an effective description of the low-energy physics via a Schrieffer-Wolff transformation [14, 133, 135, 136, 137]. (See Appendix A for a general discussion of the Schrieffer-Wolff transformation along with associated computer-algebra code.) First, we consider the symmetric case $H_{\text{dis}} = 0$. Later, we relax this assumption and allow for parameter disorder.

### 7.2.1 Effective Hamiltonian without parameter disorder

To carry out the transformation, the effective Hamiltonian $H_{\text{eff}} = Pe^{S}He^{-S}P$ and generator $S$ are expanded as

$$H_{\text{eff}} = H_{\text{eff},0} + H_{\text{eff},1} + H_{\text{eff},2} + \cdots , \tag{7.7}$$

$$S = S_1 + S_2 + \cdots . \tag{7.8}$$

We then collect terms of the same order and enforce both that the effective Hamiltonian is block diagonal and that the generator is block off diagonal.

The zeroth- and first-order contributions to the effective Hamiltonian in the computational subspace (neglecting constant terms) are found by applying the projector $P$ onto $H_0$ and $V$ respectively

[14, 133, 135, 136]

$$H_{\text{eff},0} = PH_0P = -\sum_{\mu=a,b} \frac{\omega_\mu}{2}\sigma_z^\mu \tag{7.9}$$

$$H_{\text{eff},1} = PVP = -\sum_{\mu=a,b} \Omega_\mu \sigma_x^\mu \tag{7.10}$$

where $\omega_\mu = E_1^\mu - E_0^\mu$ and

$$\Omega_\mu = E_L \langle 0_\mu|\varphi_\mu|1_\mu\rangle \left[\delta\phi_\mu + (-1)^\mu \frac{\langle 0_\mu|\theta_-|0_\mu\rangle}{2}\right]. \tag{7.11}$$

The Pauli matrices are defined as e.g. $\sigma_x^a = \sum_{m=0,1} |0_a, m_b, 0_-, 0_+\rangle\langle 1_a, m_b, 0_-, 0_+| + \text{H.c.}$

Calculation of the second-order contribution $H_{\text{eff},2}$ to the effective Hamiltonian is facilitated by the first-order generator $S_1$. The expression for the matrix elements of $S_1$ is well known [14] and we obtain

$$S_1 = \sum_{\substack{\mu=a,b\\ j=0,1}} \left( {\sum_{j',n}}' (-1)^{\mu+1} \epsilon_{jj',n}^{\mu,(1)} |j_\mu, 0_-\rangle\langle j'_\mu, n_-| - \sum_{j'} \eta_{jj'}^{\mu,(1)} |j_\mu, 0_+\rangle\langle j'_\mu, 1_+| \right) - \text{H.c.}, \tag{7.12}$$

defining the small parameters

$$\epsilon_{jj',n}^{\mu,(1)} = \frac{g_{jj',0n}^\mu}{E_{jj'}^\mu - E_{n0}^-}, \quad \eta_{jj'}^{\mu,(1)} = \frac{G_{jj'}^\mu}{E_{jj'}^\mu - \omega_+}, \tag{7.13}$$

where $E_{jk}^\mu = E_j^\mu - E_k^\mu, \mu = a, b, -$, and

$$g_{jj',0n}^\mu = \frac{E_L}{2}\langle 0_-|\theta_-|n_-\rangle\langle j_\mu|\varphi_\mu|j'_\mu\rangle, \quad G_{jj'}^\mu = \frac{E_L}{2}\left(\frac{2E_{C+}}{E_{Lc}}\right)^{1/4}\langle j_\mu|\varphi_\mu|j'_\mu\rangle. \tag{7.14}$$

We have introduced annihilation and creation operators $a_+, a_+^\dagger$ for the coupler $\theta_+$ mode via $\theta_+ = \frac{\ell_{\text{osc}}}{\sqrt{2}}(a_+ + a_+^\dagger)$ and $\ell_{\text{osc}} = (8E_{C+}/E_{Lc})^{1/4}$ is the oscillator length. The primed sum in Eq. (7.12) indicates that $n$ is allowed to be zero if $j' \geq 2$, acknowledging that the perturbation $V$ can couple computational states to higher-lying states of the qubit fluxonia without exciting the coupler $\theta_-$

mode. We have neglected contributions proportional to $\delta\phi_\mu$ in Eq. (7.12) as they are comparatively small and can be neglected.

Using the first-order generator, we can compute the second-order effective Hamiltonian in the low-energy subspace via the formula $H_{\text{eff},2} = \frac{1}{2}P[S_1, V]P$ [14, 133, 135, 136], yielding

$$H_{\text{eff},2} = -\sum_{\mu=a,b} \frac{\chi_\mu}{2}\sigma_z^\mu + J\sigma_x^a\sigma_x^b, \tag{7.15}$$

where we have defined $\chi_\mu = \chi_1^\mu - \chi_0^\mu$ and neglected global energy shifts. The qubit-frequency renormalization coefficients are

$$\chi_j^\mu = -\sum_{j'}\left(\sum_n{}' \frac{|g_{jj',n0}^\mu|^2}{\delta_{jj',n}^\mu} + \frac{|G_{jj'}^\mu|^2}{\Delta_{jj'}^\mu}\right), \tag{7.16}$$

defining the energy denominators $\delta_{jj',n}^\mu = E_{n0}^- - E_{jj'}^\mu$ and $\Delta_{jj'}^\mu = \omega_+ - E_{jj'}^\mu$. The two-qubit interaction strength is

$$\begin{aligned} J &= \sum_{n\geq 1} \frac{g_{01,0n}^a g_{01,0n}^b}{2}\left(\frac{1}{\delta_{01,n}^a} + \frac{1}{\delta_{10,n}^a} + \frac{1}{\delta_{01,n}^b} + \frac{1}{\delta_{10,n}^b}\right) \\ &\quad - \frac{G_{01}^a G_{01}^b}{2}\left(\frac{1}{\Delta_{01}^a} + \frac{1}{\Delta_{10}^a} + \frac{1}{\Delta_{01}^b} + \frac{1}{\Delta_{10}^b}\right) \\ &= J_- - J_+, \end{aligned} \tag{7.17}$$

implicitly defining $J_\pm$. Thus, the effective Hamiltonian in the computational subspace up to second order is

$$H_{\text{eff}} = -\sum_{\mu=a,b}\frac{\omega_\mu'}{2}\sigma_z^\mu + J\sigma_x^a\sigma_x^b - \sum_{\mu=a,b}\Omega_\mu\sigma_x^\mu, \tag{7.18}$$

where $\omega_\mu' = \omega_\mu + \chi_\mu$. The Hamiltonian $H_{\text{eff}}$ describes two qubits with frequencies $\omega_\mu'$ coupled via a transverse *XX* interaction with strength $J$ that is tunable with coupler flux $\phi_c$. There are additional single-qubit *X* terms with strength $\Omega_\mu$ that depend on the coupler flux $\phi_c$ as well as the qubit fluxes

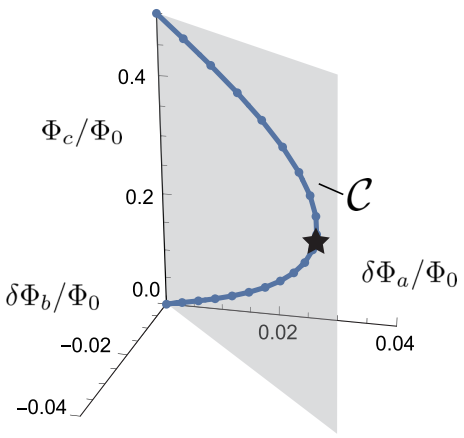


**Figure 7.3:** Sweet-spot contour. As the coupler flux is tuned, the qubit fluxes must be simultaneously adjusted according to $\delta\Phi_\mu/\Phi_0 = (-1)^{\mu+1}\frac{\langle 0_-|\theta_-|0_-\rangle}{4\pi}$ in order to keep the qubits at their sweet spots $\Omega_\mu = 0$. The qubit fluxes are measured as deviations away from the bare sweet-spot locations. The sweet-spot contour $\mathcal{C}$ lies in the semi-transparent gray plane, which bisects the angle between the two qubit-flux axes. The off position where $\Omega_\mu = J = 0$ is marked by a black star.

$\delta\phi_\mu$. We show below that both $J$ and $\Omega_\mu$ can be tuned through zero, yielding two decoupled qubits.

The coefficient $\Omega_\mu$ is defined as

$$\Omega_\mu = E_L\langle 0_\mu|\varphi_\mu|1_\mu\rangle\left[\delta\phi_\mu + (-1)^\mu\frac{\langle 0_-|\theta_-|0_-\rangle}{2}\right], \tag{7.19}$$

and arises at first-order in perturbation theory from two contributions. The first term on the right-hand side is due to a qubit-flux offset from the sweet spot $\delta\phi_\mu$, while the second is from the coupling between the qubits and the coupler $\theta_-$ mode. The matrix element $\langle 0_-|\theta_-|0_-\rangle$ is $\phi_c$ dependent and generally nonzero due to the absence of selection rules for a fluxonium biased away from a sweet spot [90, 190]. Interpreting this second term as an effective flux shift away from the sweet spot for each qubit, we cancel this shift by setting

$$\delta\phi_\mu = (-1)^{\mu+1}\frac{\langle 0_-|\theta_-|0_-\rangle}{2}. \tag{7.20}$$

Thus, we obtain the coupler-flux dependent "sweet-spot contour" shown in Fig. 7.3. It is important

to note that this phenomenon is independent of effects due to geometric flux crosstalk and arises instead directly from coupling terms in $V$.

The two-qubit interaction arises at second-order in perturbation theory, with strength $J = J_- - J_+$. The coefficient $J_-$ ($J_+$) is due to interaction of the qubit with the coupler $\theta_-$ ($\theta_+$) mode. The strength of the interaction $J_-$ is tunable due to the dependence of the matrix elements $\langle 0_-|\theta_-|n_-\rangle$ and energies $E_n^-$ on coupler flux. The coefficient $J_+$ is static, thus the two-qubit interaction is eliminated by tuning $J_-$ to equal $J_+$ in magnitude [26]. We can understand the *XX* nature of the two-qubit coupling by considering the terms appearing in $V$ that mediate the interaction between different subsystems. At the qubit sweet spots and considering only the computational states, the operators $\varphi_\mu$ are off-diagonal and therefore proportional to $\sigma_x^\mu$ with proper choice of phases. Thus, the effective two-qubit interaction consists of a virtual second-order process whereby an excitation is exchanged between the two qubits, or both qubits are co-excited or co-de-excited.

In what follows, we always operate from the dc flux bias point on the sweet-spot contour $\Omega_\mu = 0$ where the two-qubit coupling is turned off $J = 0$, see Fig. 7.3. We do this to keep both qubits at their respective sweet spots and to prevent any unwanted parasitic entanglement between the qubits. We refer to this configuration of dc fluxes as the "off position." Both single- and two-qubit gates are performed by ac flux excursions about this point. Note that the value of the coupler flux $\phi_c$ at the off position is generally parameter dependent.

### 7.2.2 Effective Hamiltonian in the presence of disorder

We now consider how disorder in circuit parameters modifies the form of the effective Hamiltonian Eq. (7.18). This disorder could arise for example from fabrication imperfections. We show below that up to second order, inductive disorder merely results in a modification to Eq. (7.11), while capacitive disorder does not contribute.

From Eq. (7.6) we see that inductive asymmetry adds a disorder term to the Hamiltonian

$$H_{\text{ind}} = \frac{1}{4}(E_L \mathsf{d}E_L + E'_L \mathsf{d}E'_L)\theta_+\theta_-. \tag{7.21}$$

If we assume that the relative deviations are small compared with unity, it is justified to add this term to $V$ and treat it perturbatively. Observe that on the one hand, for virtual transitions mediated by this term, the excitation number of either qubit cannot change. On the other hand, the excitation number of the coupler $\theta_+$ mode must change. Thus, the first-order contributions vanish, and the only second-order terms that contribute beyond a global energy shift are

$$H_{\mathsf{eff},2}^{\mathsf{ind}} = -\frac{1}{2}\sum_{\mu=a,b} g_{\mathsf{ind}}(\eta_{01}^{\mu} + \eta_{10}^{\mu})\sigma_x^{\mu}, \tag{7.22}$$

where we have defined

$$g_{\mathsf{ind}} = \frac{\ell_{\mathsf{osc}}}{4\sqrt{2}}(E_L \mathsf{d} E_L + E_L' \mathsf{d} E_L')\langle 0_-|\theta_-|0_-\rangle. \tag{7.23}$$

Thus up to second order, disorder in the inductors serves only to modify the expressions for the coefficients $\Omega_\mu$. This amounts to a shift in the sweet spot location of each qubit and can be canceled by a corresponding shift of the static qubit fluxes. Thus, small disorder in either the qubit inductors or the coupler inductors does not adversely affect device performance.

We now turn our attention to capacitive disorder $C_1 \neq C_2$ (disorder in the qubit capacitances poses no issue, as the qubits remain decoupled from all other degrees of freedom in the kinetic part of the Hamiltonian). In this case, we proceed as before and treat perturbatively the capacitive disorder term

$$H_{\mathsf{cap}} = -4E_{C-}\mathsf{d}C n_+ n_-. \tag{7.24}$$

Consider the relation between phase and charge matrix elements in fluxonium [178]

$$\langle j_-|n_-|k_-\rangle = i\frac{E_{jk}^-}{8E_{C-}}\langle j_-|\theta_-|k_-\rangle, \tag{7.25}$$

and observe that the charge matrix element vanishes if $j = k$. Thus, any virtual transition mediated by the perturbation (7.24) must excite both the coupler $\theta_-$ mode and the coupler $\theta_+$ mode and thus

does not contribute at second order beyond a global energy shift.

## 7.3 Parameter regime of the coupler

Our derivation of an effective description in terms of two-coupled qubits depends on a dispersive interaction between the qubits and the coupler. Additionally, we require that the coupling strength be sufficiently flux dependent, allowing both for the execution of fast gates and for the interaction to be efficiently turned off. Parameter choices for the coupler must support both of the above goals.

We quantify the dispersiveness of the interaction by calculating the Lamb shift $\chi_a$ (we obtain similar results in the following utilizing instead $\chi_b$). Considering the requirements on flux dependence, we calculate the slope of the coupling strength $J_-$ with respect to $\Phi_c$ at the off position. We target parameters such that $|\partial_{\Phi_c} J_-|/h \approx 100$ MHz/$\Phi_0$ to achieve MHz level coupling strengths (implying fast gates compared with $T_1, T_2$) for small ac flux excursions $\Phi_c \lesssim 0.03\,\Phi_0$ where a linear relationship between the coupling strength $J$ and flux $\Phi_c$ is expected to be valid. This value of the slope also ensures that the device remains insensitive to typical $1/f$ flux noise amplitudes $A_\Phi \approx 1\mu\Phi_0$ [148].

We sweep over $E_{Jc}$ and $E_{C-}$ and calculate $|\partial_{\Phi_c} J_-|$ as well as $\chi_a$ at the off position, see Fig. 7.4. We fix $E_L'/h = 2$ GHz ($E_{Lc}/h = 1.1$ GHz), however we obtain similar results when considering instead larger or smaller values of $E_L'$. It is worth emphasizing that the off position is parameter dependent, thus we reposition the dc fluxes appropriately for each parameter set. For relatively large $E_{Jc}$ and small $E_{C-}$, the lowest-lying states at intermediate flux values localize in minima of the cosine potential. The off position is then generally near the sweet spot, where the vanishing energy difference between the states $|0_-\rangle, |1_-\rangle$, as well as the rapid increase in the value of the matrix element $\langle 0_-|\theta_-|1_-\rangle$ enable flux tunability of $J_-$. These factors in turn imply extreme sensitivity to flux $|\partial_{\Phi_c} J_-|/h \gg 100$ MHz/$\Phi_0$ as well as a breakdown of the dispersive regime. For relatively small $E_{Jc}$ and large $E_{C-}$, flux tunability is lost as the spectrum is nearly harmonic. For decreasing $E_{Jc}$ and $E_{C-}$, excitation energies are suppressed leading to a breakdown of the dispersive interaction. The parameter regime that supports both a dispersive interaction and “Goldilocks” flux dependence

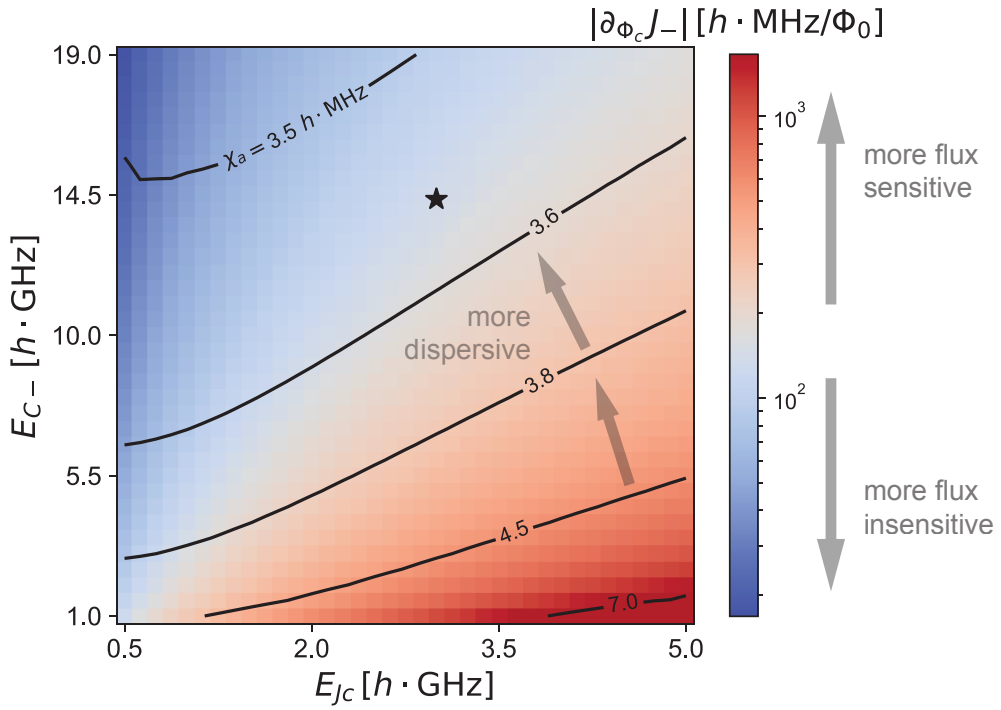


**Figure 7.4:** Flux sensitivity and dispersiveness as a function of the coupler parameters $E_{Jc}$ and $E_{C-}$. Coloring indicates $|\partial_{\Phi_c} J_-|$, i.e., the linear sensitivity of the coupling strength with respect to flux. Contour lines quantify the dispersiveness of the qubit-coupler interaction via the Lamb shift $\chi_a$. Dispersive interaction and suitable flux sensitivity are achieved in the parameter regime $E_{C-} > E_{Jc} \gtrsim E_{Lc}$. The star marks the chosen parameters, Table 7.1.

is thus $E_{C-} > E_{Jc} \gtrsim E_{Lc}$. The parameters $E_{C+}, E_{Lc}$ that define the coupler $\theta_+$ mode are implied by the parameter choices for the coupler $\theta_-$ mode, with the restriction $E_{C+} > E_{C-}$ due to the finite junction capacitance. The parameters used in the remainder of this chapter are given in Table 7.1.

## 7.4 Numerical results

We compute the low-energy spectra of the full-model Hamiltonian $H$ as well as the effective Hamiltonian $H_{\text{eff}}$ and plot the results in Fig. 7.5(a). We vary the coupler flux along the contour $\mathcal{C}$ shown in Fig. 7.3 to ensure that the qubits remain at their sweet spots. Relative deviations between the two spectra are at the level of a percent or less, indicating that the exact results can be accurately described by an effective model of two qubits coupled by a tunable *XX* interaction. The value of the tunable-coupling coefficient $J$ is shown in Fig. 7.5(b) and crosses through zero at $\phi_c \approx 0.27 \cdot 2\pi$. At this position in flux space, the coupler is in the "off" state.

To quantify the on-off ratio of the tunable coupler, we numerically calculate the strength of the parasitic *ZZ* interaction using the formula $\zeta_{ZZ} = E_{\overline{1100}} - E_{\overline{1000}} - E_{\overline{0100}} + E_{\overline{0000}}$ [100]. The eigenenergy $E_{\overline{ijnp}}$ of the dressed state $|\overline{i_a, j_b, n_-, p_+}\rangle$ is found by numerically diagonalizing the full model Hamiltonian $H$. The *ZZ* interaction strength $\zeta_{ZZ}$ is less than $0.3\ h$·kHz at the off position for the parameters considered here, implying an on-off ratio on the order of $10^5$. It is a general feature of coupled systems of low-frequency fluxonia that *ZZ* interaction strengths are suppressed, due to the small repulsions between computational and non-computational states [100].

## 7.5 Drive operators

In the following sections we implement single- and two-qubit gates via ac flux modulation. To analyze the effects of these time-dependent drives, we calculate the matrix elements of the relevant drive operators. Allocating the time-dependent flux in the Hamiltonian in the same way as for static flux generally introduces terms proportional to the time derivative of the external flux [191, 192]. Imposing the constraint that these terms should not appear implies a specific grouping of the flux in

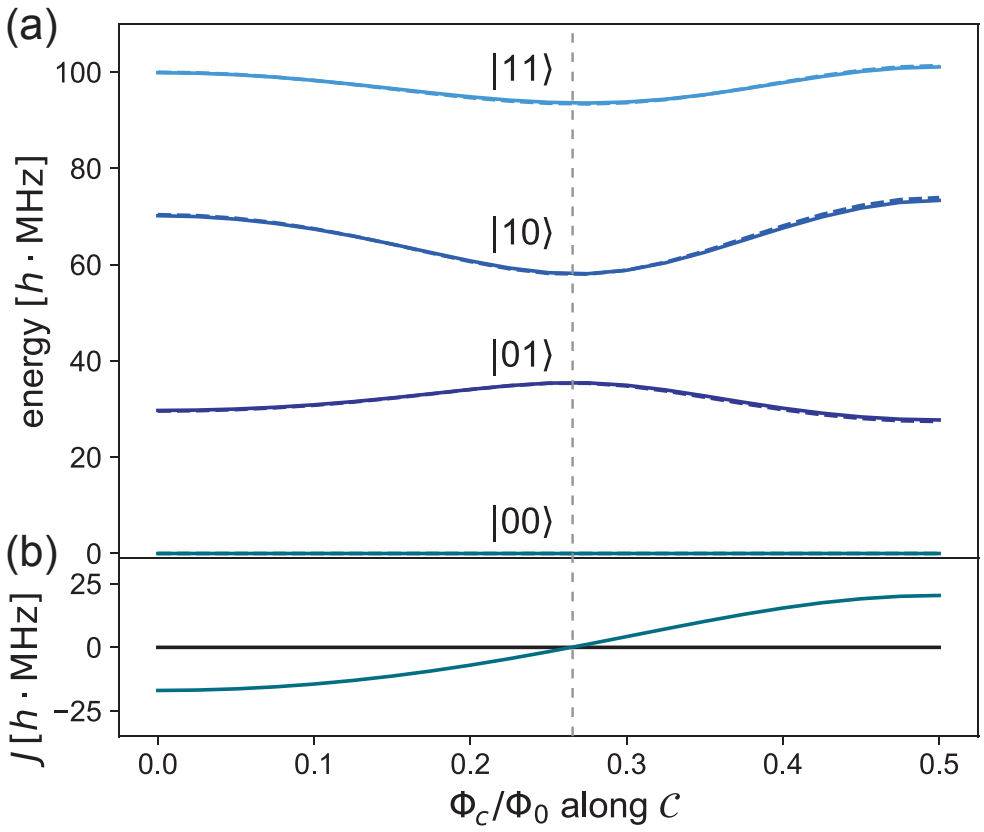


**Figure 7.5:** (a) Low-energy spectrum of the coupled system. As the coupler flux is tuned, the qubit fluxes are adjusted to remain on the sweet-spot contour $\mathcal{C}$, ensuring $\Omega_\mu = 0$. The full lines correspond to the exact spectrum calculated from the full model $H$, while the dashed lines correspond to the spectrum as calculated from the effective Hamiltonian $H_{\text{eff}}$. Eigenenergies are labeled according to the bare state $|ij\rangle \equiv |i_a, j_b, 0_-, 0_+\rangle$ with the largest overlap with the corresponding dressed state when the coupler is in the off state (at $\phi_c \approx 0.27 \cdot 2\pi$, marked by the gray dashed line). (b) Strength $J$ of the effective *XX* coupling. Device parameters can be found in Tab. 7.1.

the full Hamiltonian $H$. For our parameters, we find to a good approximation that the ac qubit fluxes are allocated to their respective inductors, and the ac coupler flux is spread across all four inductors. We first decompose the external fluxes into static $\bar{\phi}_\mu$ and time-dependent $\delta\phi_\mu(t)$ components, where $\bar{\phi}_\mu$ are the dc flux values at the off position. The ac qubit fluxes are already properly allocated, while the appropriate grouping of the coupler flux is obtained via $\theta_- \to \theta_- - \delta\phi_c(t)$. The full time-dependent Hamiltonian is thus $H(t) = H_0 + V + h_a\delta\phi_a(t) + h_b\delta\phi_b(t) + h_c\delta\phi_c(t)$, where

$$h_a = \frac{E_L}{2}(-2\varphi_a + \theta_+ + \theta_-), \tag{7.26}$$

$$h_b = \frac{E_L}{2}(-2\varphi_b + \theta_+ - \theta_-), \tag{7.27}$$

$$h_c = \left(\frac{E_L}{2}\varphi_a - \frac{E_L}{2}\varphi_b - E_{Lc}\theta_-\right). \tag{7.28}$$

Matrix elements of the operators $h_\mu$ with respect to eigenstates of the static Hamiltonian $H_{\text{st}} = H_0 + V$ determine the time evolution, once the time-dependent drives $\delta\phi_\mu(t)$ are specified. The Schrieffer-Wolff transformation allows us to define new basis states that are approximate eigenstates of $H_{\text{st}}$ and thus perturbatively calculate these matrix elements.

The leading-order contributions to select matrix elements of the drive operators $h_\mu$ occur at second order. Thus, to include all relevant corrections to the wave functions that contribute to these matrix elements, we calculate the second-order generator $S_2$ associated with the Schrieffer-Wolff transformation discussed in Sec. 7.2. To simplify the calculation we ignore all contributions from the coupler $\theta_+$ mode due to the inequality $|\eta| < |\epsilon|$ in parameter regimes of interest, yielding [14, 135]

$$S_2 = \sum_{\substack{\mu=a,b\\ j=0,1}} {\sum_{j',n}}' \epsilon^{\mu,(2)}_{jj',n} |j_\mu, 0_-\rangle\langle j'_\mu, n_-| + \sum_{j,k=0,1} {\sum_{j',k',n}}' \epsilon^{ab,(2)}_{jj',kk',n} |j_a, k_b, 0_-\rangle\langle j'_a, k'_b, n_-| - \text{H.c.} \tag{7.29}$$

where we have defined

$$\epsilon^{\mu,(2)}_{jj',n} = -\sum_{j''=0,1} \frac{g^{\mu}_{jj'',00} g^{\mu}_{j''j',0n}}{(E^{\mu}_{jj'} - E^{-}_{n0})(E^{\mu}_{j''j'} - E^{-}_{n0})} + \sum_{j'',n}{}' \frac{g^{\mu}_{jj'',0n'} g^{\mu}_{j''j',n'n}}{(E^{\mu}_{jj''} - E^{-}_{n'0})(E^{\mu}_{jj'} - E^{-}_{n0})},$$

$$\epsilon^{ab,(2)}_{jj',kk',n} = \sum_{\substack{\mu,\nu=a,b \\ \mu\neq\nu}} \left[ \frac{g^{\mu}_{jj',00} g^{\nu}_{kk',0n}}{(E^{\mu}_{jj'} + E^{\nu}_{kk'} - E^{-}_{n0})(E^{\nu}_{kk'} - E^{-}_{n0})} - \sum_{n'}{}' \frac{g^{\mu}_{jj',0n'} g^{\nu}_{kk',n'n}}{(E^{\mu}_{jj'} - E^{-}_{n'0})(E^{\mu}_{jj'} + E^{\nu}_{kk'} - E^{-}_{n0})} \right].$$

At the off position, the effective Hamiltonian $H_{\text{eff}} = -\frac{\omega'_a}{2}\sigma^a_z - \frac{\omega'_b}{2}\sigma^b_z$ (ignoring third-order contributions to the effective Hamiltonian) is diagonal in the basis of the bare computational states $|\ell_a, m_b, 0, 0\rangle, \ell, m \in \{0, 1\}$. Assuming the qubit frequencies are not on resonance $\omega'_a \neq \omega'_b$, the dressed eigenstates are

$$|\overline{\ell_a, m_b, 0_-, 0_+}\rangle = e^{-S}|\ell_a, m_b, 0_-, 0_+\rangle = \left[\mathbb{1} - S_1 - S_2 + \frac{1}{2}(S_1)^2\right]|\ell_a, m_b, 0_-, 0_+\rangle, \tag{7.30}$$

up to second order. With the dressed eigenstates now written in terms of bare states, we may compute matrix elements of the operators $h_\mu$ associated with the ac flux drives.

### 7.5.1 Qubit-flux drive operators

Experimentally, the amplitude of an ac flux drive will typically be no larger than $\delta\Phi_\mu \leq 0.1\Phi_0$ [31]. In this case, we have checked that transitions to higher-lying states mediated by the drive operators $h_a, h_b$ are suppressed. Thus, we need only consider matrix elements of these operators in the computational subspace. Using the expression (7.30) for the dressed states given in terms of the

bare states, we find

$$\langle\overline{\ell m}|h_a|\overline{\ell m}\rangle/E_L = 2\sum_{\ell'\geq 2}\langle\ell_a|\varphi_a|\ell'_a\rangle\epsilon^{a,(1)}_{\ell\ell',0} + \frac{1}{2}\langle 0_-|\theta_-|0_-\rangle, \tag{7.31}$$

$$\langle\overline{\ell m}|h_a|\overline{\ell+1 m}\rangle/E_L = -\langle 0_a|\varphi_a|1_a\rangle - \frac{1}{2}\sum_{n\geq 1}\langle 0_-|\theta_-|n_-\rangle(\epsilon^{a,(1)}_{01,n} + \epsilon^{a,(1)}_{10,n}) \tag{7.32}$$
$$- \frac{1}{2}\frac{\ell_{\mathsf{osc}}}{\sqrt{2}}(\eta^{a,(1)}_{01} + \eta^{a,(1)}_{10}),$$

$$\langle\overline{\ell m}|h_a|\overline{\ell m+1}\rangle/E_L = -\frac{1}{2}\frac{\ell_{\mathsf{osc}}}{\sqrt{2}}(\eta^{b,(1)}_{01} + \eta^{b,(1)}_{10}) + \frac{1}{2}\sum_{n\geq 1}\langle 0_-|\theta_-|n_-\rangle(\epsilon^{b,(1)}_{01,n} + \epsilon^{b,(1)}_{10,n})], \tag{7.33}$$

$$\langle\overline{\ell m}|h_a|\overline{\ell+1 m+1}\rangle/(E_L/2) = -\sum_{n,n'\geq 1}(\epsilon^{a,(1)}_{\ell\ell+1,n}\epsilon^{b,(1)}_{m+1m,n'} + \epsilon^{a,(1)}_{\ell+1\ell,n}\epsilon^{b,(1)}_{mm+1,n'})\langle n_-|\theta_-|n'_-\rangle \tag{7.34}$$
$$+\sum_{n\geq 1}(\epsilon^{ab,(2)}_{\ell\ell+1,mm+1,n} + \epsilon^{ab,(2)}_{\ell+1\ell,m+1m,n})\langle 0_-|\theta_-|n_-\rangle$$
$$+\sum_{n\geq 1}(\epsilon^{a,(1)}_{\ell\ell+1,n}\epsilon^{b,(1)}_{m+1m,n} + \epsilon^{a,(1)}_{\ell+1\ell,n}\epsilon^{b,(1)}_{mm+1,n})\langle 0_-|\theta_-|0_-\rangle,$$

where we have introduced the shorthand $|\overline{\ell,m}\rangle \equiv |\overline{\ell_a, m_b, 0_-, 0_+}\rangle$ for states in the computational subspace, and the labels are understood modulo 2. In Eqs. (7.31)-(7.33), second-order contributions are small and can be neglected, while in Eq. (7.34) the leading-order contributions are at second-order. These analytical approximations indicate that in the computational subspace and at the off position, the operator $h_a$ simplifies dramatically to leading order to $\Omega^a_{\mathsf{ac}}\bar{\sigma}^a_x$. This simplification can be understood by considering each of the matrix elements in Eqs. (7.31)-(7.33) in turn. The diagonal matrix element (7.31) yields a constant contribution at zeroth order, while the first-order contributions are suppressed by small phase matrix elements between computational states and higher-lying states. Thus this matrix element corresponds to the identity up to small corrections and can be ignored. The matrix element (7.32) corresponding to the expected operator $\bar{\sigma}^a_x$ has contributions at zeroth and first-order and is generally nonzero. The matrix element (7.33) vanishes at the off position by definition, see Eq. (7.17). Finally, the leading-order contributions to the matrix element $\langle\overline{\ell,m}|h_a|\overline{\ell+1,m+1}\rangle$ occur at second order and are thus comparatively small. Thus to leading order we obtain $h_a = \Omega^a_{\mathsf{ac}}\bar{\sigma}^a_x$ where $\Omega^a_{\mathsf{ac}} = [(h_a)_{00,10} + (h_b)_{01,11}]/2$ Similar arguments follow for $h_b$, yielding $h_b = \Omega^b_{\mathsf{ac}}\bar{\sigma}^b_x$, where $\Omega^b_{\mathsf{ac}} = [(h_b)_{00,01} + (h_b)_{10,11}]/2$. We find excellent agreement

between the semi-analytic formulas and exact results: for the parameters considered here, we obtain $|\Omega^a_{\mathsf{ac}}|/h = 558, 561$ MHz using Eqs. (7.31)-(7.34) and numerics, respectively. The coefficients associated with all other operators (aside from the irrelevant identity) in the decomposition of $h_a$ are of the order of 2 $h$·MHz or smaller in absolute value, as calculated both from the semi-analytic formulas and exact results.

### 7.5.2 Coupler-flux drive operator

The operator $h_c$ activated by coupler-flux modulation induces both wanted and unwanted transitions in the computational subspace. The latter proceed through virtual excitations of higher-lying states and are discussed in detail in Sec. 7.7.2.1. In the following we focus on the former and compute the matrix elements of $h_c$ in the computational subspace.

The matrix elements of $h_c$ governing the wanted transitions can be obtained within second-order perturbation theory using Eq. (7.30)

$$\langle\overline{\ell m}|h_c|\overline{\ell m}\rangle = -E_{Lc}\langle 0_-|\theta_-|0_-\rangle - E_L\sum_{\ell'\geq 2}\langle \ell_a|\varphi_a|\ell'_a\rangle\epsilon^{a,(1)}_{\ell\ell',0} - E_L\sum_{m'\geq 2}\langle m_b|\varphi_b|m'_b\rangle\epsilon^{b,(1)}_{mm',0}, \tag{7.35}$$

$$\langle\overline{\ell m}|h_c|\overline{\ell+1 m}\rangle = \frac{E_L}{2}\langle 0_a|\varphi_a|1_a\rangle + E_{Lc}\sum_{n\geq 1}\langle 0_-|\theta_-|n_-\rangle(\epsilon^{a,(1)}_{01,n} + \epsilon^{a,(1)}_{10,n}), \tag{7.36}$$

$$\langle\overline{\ell m}|h_c|\overline{\ell m+1}\rangle = -\frac{E_L}{2}\langle 0_b|\varphi_b|1_b\rangle - E_{Lc}\sum_{n\geq 1}\langle 0_-|\theta_-|n_-\rangle(\epsilon^{b,(1)}_{01,n} + \epsilon^{b,(1)}_{10,n}), \tag{7.37}$$

$$\langle\overline{\ell m}|h_c|\overline{\ell+1 m+1}\rangle = -\frac{E_{Lc}}{E_L/2}\langle\overline{\ell m}|h_a|\overline{\ell+1 m+1}\rangle. \tag{7.38}$$

Careful consideration of the above matrix elements indicates that at the off position, $h_c$ can be simplified to

$$h_c = J_{\mathsf{ac}}\bar{\sigma}^a_x\bar{\sigma}^b_x, \tag{7.39}$$

where we have defined the ac *XX* coupling strength

$$J_{\mathsf{ac}} = \frac{1}{2}\left(\langle\overline{00}|h_c|\overline{11}\rangle + \langle\overline{01}|h_c|\overline{10}\rangle\right). \tag{7.40}$$

We detail below how this simplification proceeds. The diagonal matrix element (7.35) is a constant up to small corrections for the same reasons as for $h_a$ and can be ignored. The matrix elements in Eqs. (7.36)-(7.37) approximately vanish at the off position based on the following argument. Equating $J_-$ and $J_+$ and making the approximation that the qubit excitation energies are small compared with those of the coupler degrees of freedom, we find

$$\sum_{n\geq 1} \frac{|\langle 0_-|\theta_-|n_-\rangle|^2}{E^-_{n0}} \approx \frac{1}{2E_{Lc}}. \tag{7.41}$$

This implies that the second terms in Eqs. (7.36)-(7.37) approximately cancel the first terms. The two-qubit matrix element (7.38) which appears at second order is then expected to dominate, as second-order contributions to the matrix elements Eqs. (7.35)-(7.37) are comparatively small and can be neglected. For our parameters, we obtain $|J_{\mathsf{ac}}|/h = 14.3, 18.3$ MHz using the semi-analytic formulas Eqs. (7.35)-(7.38) and exact numerics, respectively. We have checked that the semi-analytic results agree with exact numerics in the limit of large $E_{Lc}$, where the interaction becomes more dispersive.

## 7.6 Single-qubit gates

There are important differences between how single-qubit gates are performed on high frequency qubits like transmons and how they are executed on low-frequency qubits like those studied here. For transmon qubits, drive strengths are typically small compared with the qubit frequency. It is then appropriate to move into a frame co-rotating with the drive frequency (typically on or near resonance with the qubit frequency) and perform the RWA [14, 193]. The rotating-frame Hamiltonian is now time independent, allowing for the relatively straightforward calculation of time-evolution operators (propagators). Observe that in this rotating frame, idling corresponds to an identity op-

eration (assuming a resonant drive). In contrast, to obtain fast gates for low-frequency qubits like heavy fluxonium [31] or superconducting composite qubits [55], drive strengths typically equal or exceed the qubit frequencies. Thus, gates are typically performed in the laboratory frame as it is not appropriate to move into a rotating frame like that described above [31, 55, 56, 194]. In the lab frame, qubit states acquire dynamical phase factors while idling. Indeed we utilize these *Z* rotations in Sec. 7.7 for achieving a high-fidelity $\sqrt{i\text{SWAP}}$ gate. Nevertheless in the absence of drives, we obtain an identity operation (up to an overall sign) only by idling for exact multiples of the Larmor period $\tau_q = 2\pi/\omega_q$, where $\omega_q$ is the qubit frequency. If we now consider multiple qubits with non-commensurate frequencies, it is not obvious how to perform an operation on one qubit without a second qubit acquiring dynamical phase during the gate time. Therefore, we seek an active means of obtaining *variable-time* identity operations for low-frequency qubits. Single-qubit $X/2$ and $Y/2$ gates can be obtained using the techniques described in e.g. Refs. [31, 55], allowing for universal control when combined with arbitrary *Z* rotations achieved by idling.

### 7.6.1 Identity gates

We utilize flux pulses that begin and end at zero and whose shapes are described by sinusoidal functions, but that only last for a single period [55]. This pulse shape is chosen because the external flux averages to zero[1], helping eliminate long-timescale distortions [131]. Recall from Sec. 7.5.1 that turning on a qubit a (b) flux drive activates a *XI* (*IX*) term in the Hamiltonian. This is the expected generalization from the case of a single fluxonium biased at the half-flux sweet spot and subject to a flux drive [31]. For simplicity we thus focus on the case of an isolated fluxonium. The Hamiltonian is $H_{\text{fl}}(t) = H_\pi + H_d(t)$, where

$$H_\pi = 4E_C n^2 - E_J \cos(\varphi) + \frac{1}{2}E_L(\varphi + \pi)^2, \tag{7.42}$$

$$H_d(t) = E_L \varphi \delta\phi \sin(\omega_d t). \tag{7.43}$$

[1] Many other simple pulse shapes achieve net-zero flux, such as those utilized in Ref. [31], and can yield high-fidelity gates. Single-period sinusoids are used here for simplicity.

Projecting onto the computational subspace yields [31]

$$H_q(t) = -\frac{\omega_q}{2}\sigma_z + A\sin(\omega_d t)\sigma_x, \tag{7.44}$$

defining the effective drive amplitude $A = E_L\langle 0|\varphi|1\rangle\delta\phi$ and making use of selection rules at the half-flux sweet spot. For typical heavy-fluxonium parameters such as those chosen for qubits $a$ and $b$, the amplitude of the drive $A$ exceeds the qubit frequency $\omega_q$ for deviations from the sweet spot as small as $\delta\phi = 0.02 \cdot 2\pi$. Indeed, such strong drives have been used to implement fast single-qubit gates with high fidelities [31, 55]. Here, we utilize similarly strong drives for the implementation of identity pulses.

We seek conditions on the drive strength $A$ and frequency $\omega_d$ such that the propagator $U_q(t)$ is equal to the identity operation after a single drive period, $U_q(t = 2\pi/\omega_d) = \mathbb{1}$. Utilizing a Magnus expansion as described in Sec. 4.3, we see that the condition on obtaining an identity gate after a single period of the drive is

$$\frac{\pi\omega_q}{\omega_d} J_0\left(\frac{2A}{\omega_d}\right) = 2\pi r, \quad r \in \mathbb{Z}, \tag{7.45}$$

which is an equation for the variables $A, \omega_d$. Solutions which avoid fixing $\omega_d$ based on the value of $\omega_q$ are those for $r = 0$ which satisfy

$$\frac{2A}{\omega_d} = j_k, \quad k = 1, 2, \ldots, \tag{7.46}$$

where $j_k$ is the $k^{\text{th}}$ zero of $J_0$. Thus, by choosing a combination of drive amplitude $A$ and frequency $\omega_d$ (and thus gate time) obeying Eq. (7.46), we obtain a variable-time identity gate. We note that it is also possible to arrive at Eq. (7.45) using a perturbative analysis in the context of Floquet theory [60].

### 7.6.2 Numerical results

We present numerical results illustrating that the proposed identity gates can be achieved with high fidelity. To calculate the closed-system fidelity of a quantum operation we utilize the formula [195]

$$F = \frac{\mathrm{Tr}(U^\dagger U) + |\,\mathrm{Tr}[U_\mathrm{T}^\dagger U]|^2}{d(d+1)}, \tag{7.47}$$

where $d$ is the dimension of the relevant subspace of the Hilbert space, $U_\mathrm{T}$ is the target unitary and $U$ is the projection onto the $d$ dimensional subspace of the propagator realized by time evolution. This formula is especially useful when considering systems where leakage may be an issue; in such cases, deviations of the operator $U$ from unitarity are penalized by the term $\mathrm{Tr}(U^\dagger U)$. To obtain the propagator associated with time evolution under the Hamiltonian $H_\mathrm{fl}(t)$, it is most appropriate to express $H_\mathrm{fl}(t)$ in the eigenbasis of the static Hamiltonian $H_\pi$. The qubit states are the two lowest-energy states, and we retain up to eight eigenstates to monitor leakage. Diagonalization of $H_\pi$ is done using scqubits [196], while time-dependent simulations are performed using QuTiP [197, 198]. Sweeping over the drive frequency and amplitude of the flux pulse, we monitor the fidelity of an identity operation, taking $d = 2$ and $U_T = \mathbb{1}$ in Eq. (7.47), see Fig. 7.6. Regions of high fidelity appear as "fingers" in the space of inverse gate time (drive frequency $\omega_d$) and effective drive amplitude $A$. The colored lines are given by $A = j_k\omega_d/2$ for $k = 1, 2, 3, 4, 5$, corresponding to the drive parameters that analytically predict identity gates. These lines overlap with the regions of high fidelity computed numerically for large amplitude $A$ compared with the qubit frequency $\omega_q$. For decreasing $\omega_d$ and $A$, the lines begin to deviate from the high-fidelity fingers due to the breakdown of the Magnus expansion [67]. Nevertheless, we find numerically that high-fidelity $F > 0.9999$ identity gates can be achieved across a wide range of inverse gate times $0.5 \lesssim \omega_d/\omega_q \lesssim 7$. Leakage outside the computational subspace is negligible for the parameters considered here.

The time evolution of the qubit states in the lab frame in the form of trajectories on the Bloch sphere during identity pulses is shown in Fig. 7.7. The drive frequencies $\omega_d$ used in Figs. 7.7(a)-(c) are $\omega_d/\omega_q = 5.3, 3.3, 2.1$, with drive amplitudes $A$ obtained from Eq. (7.46) using the Bessel zeros

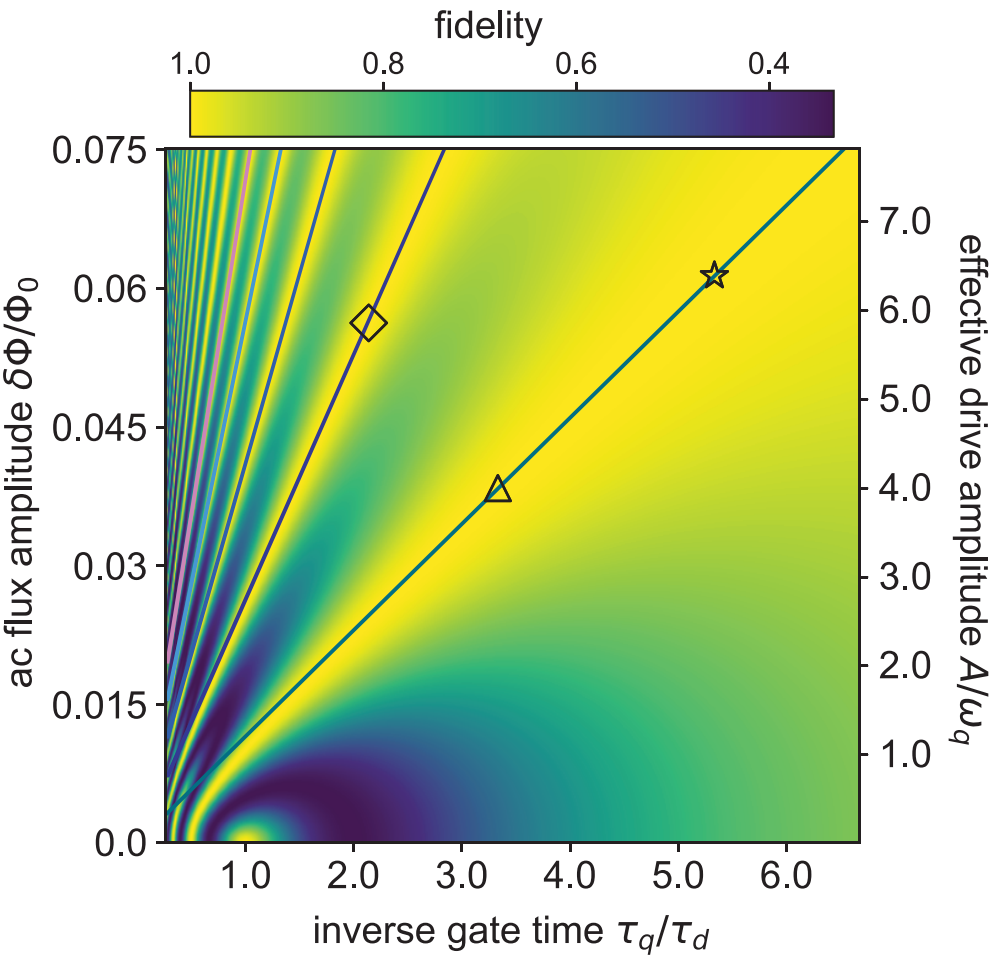


**Figure 7.6:** Variable-time single-qubit identity pulse. We plot the fidelity of an identity operation under a single-period sinusoidal qubit-flux drive. Lines mark locations in amplitude and frequency space where $A = j_k\omega_d/2$ for the first 5 zeroes $j_k$ of $J_0$. Multiple other lines of high fidelity corresponding to larger zeros of $J_0$ are visible in the numerics. These variable-time identity gates are ultra-fast, with gate times that can be small compared to the Larmor period. The point-like region of high fidelity at $\delta\phi = 0$ corresponds to the passive identity operation. The marked points label example drive parameters used for visualizing Bloch sphere trajectories in Fig. 7.7. Numerical simulations are performed using the parameters of qubit $b$ where $\omega_q/2\pi = 37$ MHz.

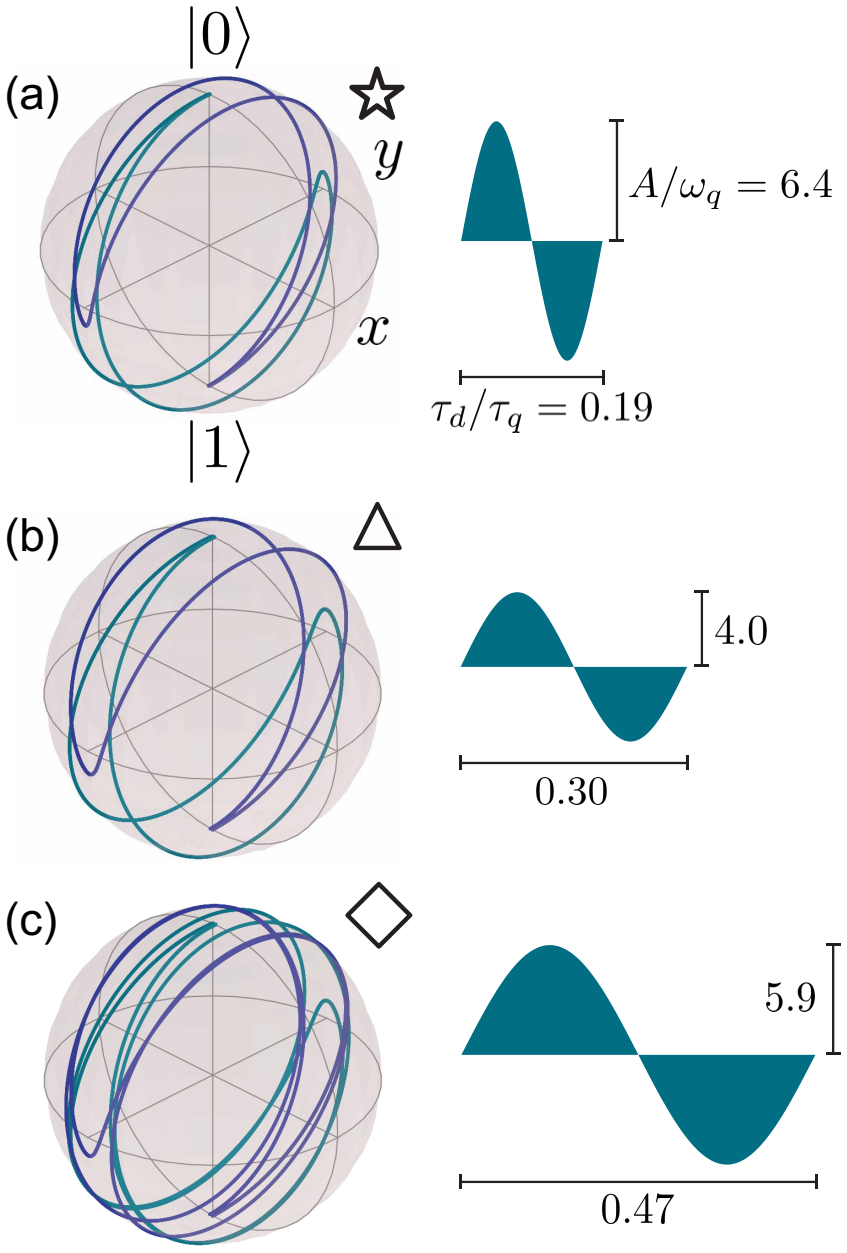


**Figure 7.7:** (a-c) Bloch sphere trajectory in the lab frame of the initial states $|0\rangle$ and $|1\rangle$ subject to the pictured identity gates. The pulse parameters utilized here are marked in Fig. 7.6. Each gate achieves an identity operation with fidelity $F \geq 0.9998$.

$j_1, j_1, j_2$, respectively. In all three cases we obtain fidelities of $F \geq 0.9998$. Numerical optimization of the drive amplitude keeping the drive frequency fixed yields $F > 0.99999$ in each case. The optimized amplitude generally differs from the amplitude derived analytically by less than or of the order of a percent.

## 7.7 Two-qubit entangling gate

When performing two-qubit gates on low-frequency fluxonium qubits, we encounter similar issues to those present for single-qubit gates. To achieve relatively fast gate times compared with $T_1$ and $T_2$, we utilize drive strengths where the RWA is invalid. We perform a Magnus expansion in a frame co-rotating with the qubit frequencies to account for the counter-rotating terms order-by-order. We note that similar results can be obtained using a Floquet analysis [59, 62]. Because single-qubit gates are performed in the lab frame, we then transform the rotating-frame propagator back into the lab frame.

To activate a two-qubit interaction, we consider an ac sinusoidal coupler flux drive $\phi_c(t) = \delta\phi_c \sin(\omega_d t)$. The time-dependent Hamiltonian in the computational subspace is

$$H_{2q}(t) = -\frac{\omega_a'}{2}\bar{\sigma}_z^a - \frac{\omega_b'}{2}\bar{\sigma}_z^b + A\sin(\omega_d t)\bar{\sigma}_x^a\bar{\sigma}_x^b, \tag{7.48}$$

where we recall that gates are performed in the basis of the dressed states as detailed in Sec. 7.5. The Pauli matrices are defined as e.g. $\bar{\sigma}_x^a = \sum_{j=0,1} |\overline{0j}\rangle\langle\overline{1j}| + \text{H.c.}$, etc., utilizing the shorthand $|\overline{i_a j_b}\rangle \equiv |\overline{i_a, j_b, 0_-, 0_+}\rangle$. The effective drive amplitude $A \equiv J_{\text{ac}}\delta\phi_c$ is defined in terms of the ac two-qubit coupling strength $J_{\text{ac}}$ given in Eq. (7.40). For our parameters, $J_{\text{ac}} = 18.3$ MHz. Just as for single-qubit gates, we drive with $\sin\omega_d t$ rather than $\cos\omega_d t$ because we intend to activate the interaction for only one or a few drive periods $n$[2]. In general, the propagator at the final time

[2]The reason we keep the treatment general enough to include multiple drive periods will become clear when we consider time evolution on the full system: for realistic parameters, a single drive period leads to drive amplitudes so large that we obtain fidelity-degrading contributions from high-lying coupler states.

$\tau_n = 2\pi n/\omega_d$ is

$$U(\tau_n) = \mathcal{T} e^{-i\int_0^{\tau_n} H_{2q}(t')dt'} = \begin{pmatrix} a & 0 & 0 & d \\ 0 & b & c & 0 \\ 0 & -c^* & b^* & 0 \\ -d^* & 0 & 0 & a^* \end{pmatrix}, \tag{7.49}$$

where $\mathcal{T}$ is the time-ordering operator and $|a|^2 + |d|^2 = |b|^2 + |c|^2 = 1$. To obtain an entangling gate, we target drive parameters $A, \omega_d$ that yield $|b| = |c| = 1/\sqrt{2}$ and $d = 0$ [3]. We parametrize this gate as

$$\sqrt{\phi\text{SWAP}} = \begin{pmatrix} e^{i\alpha} & 0 & 0 & 0 \\ 0 & e^{i\beta}/\sqrt{2} & e^{i\gamma}/\sqrt{2} & 0 \\ 0 & -e^{-i\gamma}/\sqrt{2} & e^{-i\beta}/\sqrt{2} & 0 \\ 0 & 0 & 0 & e^{-i\alpha} \end{pmatrix}. \tag{7.50}$$

To see that this gate is entangling, note either that it can produce Bell states or that it can be transformed into the entangling gate

$$\sqrt{i\text{SWAP}} = \begin{pmatrix} 1 & 0 & 0 & 0 \\ 0 & 1/\sqrt{2} & -i/\sqrt{2} & 0 \\ 0 & -i/\sqrt{2} & 1/\sqrt{2} & 0 \\ 0 & 0 & 0 & 1 \end{pmatrix}, \tag{7.51}$$

using only single-qubit operations [200]. One such transformation using single-qubit gates is

$$\sqrt{i\text{SWAP}} = R_Z^a(\theta_{a1}) R_Z^b(\theta_{b1}) \sqrt{\phi\text{SWAP}} R_Z^a(\theta_{a2}) R_Z^b(\theta_{b2}), \tag{7.52}$$

[3] A gate with $|a| = |d| = 1/\sqrt{2}$ and $|c| = 0$ is also entangling, yielding a $\sqrt{b\text{SWAP}}$-like gate [199]. Here, we focus instead on entangling gates performed in the $|\overline{01}\rangle, |\overline{10}\rangle$ subspace rather than in the $|\overline{00}\rangle, |\overline{11}\rangle$ subspace.

where

$$R_Z^j(\theta) = \mathsf{exp}(-i\theta\bar{\sigma}_z^j/2), \quad j = a, b.$$

Expressions for the *Z* rotation angles in Eq. (7.52) in terms of $\alpha, \beta$ and $\gamma$ are specified below. The relationship (7.52) provides an explicit recipe for constructing a $\sqrt{i\mathsf{SWAP}}$ gate, given a $\sqrt{\phi\mathsf{SWAP}}$ gate and arbitrary single-qubit *Z* rotations. Quantum algorithms are typically written in terms of named gates like $\sqrt{i\mathsf{SWAP}}$ [201, 202, 203], as opposed to the native gate $\sqrt{\phi\mathsf{SWAP}}$ achieved here. Thus, it may be useful to immediately transform the obtained $\sqrt{\phi\mathsf{SWAP}}$ gate into the more familiar $\sqrt{i\mathsf{SWAP}}$. This is the strategy we pursue here.

Generally, only three of the *Z* rotations in Eq. (7.52) are necessary. We make use of the freedom of the extra *Z* rotation by choosing the angle $\theta_{b2} \in [0, 2\pi)$ that optimizes the overall gate time, including the *Z* rotations. The remaining angles are set to

$$\begin{aligned} \theta_{a1} &= \frac{\pi}{2} + \alpha + \gamma - \theta_{b2}, \\ \theta_{b1} &= \alpha - \beta - \theta_{b2}, \\ \theta_{a2} &= -\frac{\pi}{2} + \beta - \gamma + \theta_{b2}, \end{aligned} \tag{7.53}$$

to satisfy Eq. (7.52). In the following, we find explicit expressions for $\alpha, \beta$ and $\gamma$ in terms of the drive parameters and qubit frequencies. Because we operate in the lab frame, these *Z* rotations are obtained by idling. Idle times for coincident *Z* rotations may differ in general, therefore to synchronize the time spent performing single-qubit gates we make use of the variable-time single-qubit identity gates discussed in Sec. 7.6.

### 7.7.1 Constructing $\sqrt{\phi\mathsf{SWAP}}$

The propagator $\sqrt{\phi\mathsf{SWAP}}$ can be obtained from time evolution under the Hamiltonian $H_{2q}(t)$ as follows. The qubit frequencies $\omega_a', \omega_b'$ are fixed by operating the qubits at their sweet spots, while the drive parameters $A, \omega_d$ may be varied. The Hamiltonian $H_{2q}(t)$ only couples the pairs of states

$|\overline{00}\rangle \leftrightarrow |\overline{11}\rangle$, $|\overline{01}\rangle \leftrightarrow |\overline{10}\rangle$, thus $H_{2q}(t)$ decomposes into a direct sum $H_{2q}(t) = H_-(t) \bigoplus H_+(t)$, where

$$H_\pm(t) = -\frac{\omega_\pm}{2}\Sigma_z^\pm + A\sin(\omega_d t)\Sigma_x^\pm, \tag{7.54}$$

defining $\omega_\pm = \omega_a' \pm \omega_b'$. The Hamiltonians $H_+(t), H_-(t)$ describe dynamics in the $|\overline{00}\rangle, |\overline{11}\rangle$, and the $|\overline{01}\rangle, |\overline{10}\rangle$ subspaces, respectively. The corresponding Pauli matrices are denoted by $\Sigma_j^\pm$, for example $\Sigma_z^+ = |\overline{00}\rangle\langle\overline{00}| - |\overline{11}\rangle\langle\overline{11}|$. For realistic parameters, the two-level-system frequencies $\omega_+$ and $\omega_-$ are large compared with the drive amplitude $A$. To obtain the associated propagators we perform a Magnus expansion, applying results from Sec. 4.2. We retain terms up to second order in the Magnus series as higher-order terms are small and can be neglected. The propagators after $n$ periods of the drive are

$$U_\pm(n\tau_d) = \begin{pmatrix} \cos(\xi_\pm)e^{i(\vartheta_\pm - \mathrm{tanc}[\xi_\pm]\varepsilon_\pm)} & \sin(\xi_\pm) \\ -\sin(\xi_\pm) & \cos(\xi_\pm)e^{-i(\vartheta_\pm - \mathrm{tanc}[\xi_\pm]\varepsilon_\pm)} \end{pmatrix}, \tag{7.55}$$

where quantities in Eq. 7.55 are defined in Sec. 4.2 and the $\pm$ subscripts indicate dependence on the frequencies $\omega_\pm$. For instance we have

$$\xi_\pm = \frac{2A\omega_d}{\omega_d^2 - \omega_\pm^2}\sin\left(\frac{\pi n\omega_\pm}{\omega_d}\right). \tag{7.56}$$

To obtain the $\sqrt{\phi\mathrm{SWAP}}$ gate, we require

$$U_+(\tau_n) = \begin{pmatrix} \cos(\xi_+)e^{i(\vartheta_+ - \mathrm{tanc}[\xi_+]\varepsilon_+)} & \sin(\xi_+) \\ -\sin(\xi_+) & \cos(\xi_+)e^{-i(\vartheta_+ - \mathrm{tanc}[\xi_+]\varepsilon_+)} \end{pmatrix} \stackrel{!}{=} \begin{pmatrix} e^{i\alpha} & 0 \\ 0 & e^{-i\alpha} \end{pmatrix}, \tag{7.57}$$

$$U_-(\tau_n) = \begin{pmatrix} \cos(\xi_-)e^{i(\vartheta_- - \mathrm{tanc}[\xi_-]\varepsilon_-)} & \sin(\xi_-) \\ -\sin(\xi_-) & \cos(\xi_-)e^{-i(\vartheta_- - \mathrm{tanc}[\xi_-]\varepsilon_-)} \end{pmatrix} \stackrel{!}{=} \frac{1}{\sqrt{2}}\begin{pmatrix} e^{i\beta} & e^{i\gamma} \\ -e^{-i\gamma} & e^{-i\beta} \end{pmatrix}. \tag{7.58}$$

The solution for Eq. (7.57) is

$$\xi_+ = \frac{2A\omega_d}{\omega_d^2 - \omega_+^2} \sin\left(n\pi\frac{\omega_+}{\omega_d}\right) = p\pi, \quad p \in \mathbb{Z}, \tag{7.59}$$

which should be interpreted as an equation involving the unknowns $A, \omega_d$. For any nonzero $A$, solutions to Eq. (7.59) for $p = 0$ are

$$\omega_d = n\omega_+/m, \quad (m = 1, 2, 3, \ldots, m \neq n). \tag{7.60}$$

For nonzero $p$, solutions $(A, \omega_d)$ can only be found by numerically solving the full transcendental equation (7.59). We find in the following that to satisfy Eq. (7.58), it is necessary to have the freedom of varying the drive amplitude $A$. Thus, we only consider the case $p = 0$. Setting $m = n$ is excluded in Eq. (7.60) as in this case the left-hand side of Eq. (7.59) does not vanish. However, this restriction is no issue, as motivated by the drive frequency $\omega_d = \omega_-$ used to obtain the $\sqrt{i\text{SWAP}}$ gate when the RWA is valid [14] we do not consider on resonance driving of the $|\overline{00}\rangle \leftrightarrow |\overline{11}\rangle$ transition $\omega_d = \omega_+$. With $\omega_d$ given by Eq. (7.60), the expression for $\varepsilon_+$ simplifies to $\varepsilon_+ = \frac{A^2}{\omega_d^2}\frac{\pi n m}{1-m^2}$ and we satisfy Eq. (7.57) with the phase $\alpha = \vartheta_+ - \varepsilon_+$.

Considering now the requirement (7.58) for $U_-$, the solution is

$$\xi_- = \frac{2A\omega_d}{\omega_d^2 - \omega_-^2} \sin\left(n\pi\frac{\omega_-}{\omega_d}\right) = \pm\frac{\pi}{4} + \pi q, \quad q \in \mathbb{Z}, \tag{7.61}$$

where the $\pm$ indicates that the sign may be absorbed into the phases $\beta, \gamma$. We interpret Eq. (7.61) as an equation for the unknown $A$, as we have fixed $\omega_d$ previously. Solving for $A$ yields

$$A = \pm\frac{\pi(\omega_d^2 - \omega_-^2)}{8\omega_d \sin(\pi n\frac{\omega_-}{\omega_d})}, \tag{7.62}$$

where we have set $q = 0$ to minimize the magnitude of $A$. In general, the fraction on the right-hand side of Eq. (7.62) may be positive or negative, depending on $n$ and the magnitude of $\omega_-$ relative to $\omega_d$. Thus, we choose the sign of $\xi_- = \pm\pi/4$ based on which yields a positive drive amplitude $A$.

With the drive frequency and amplitude given by Eq. (7.60) and Eq. (7.62) respectively, we satisfy Eq. (7.58) with phases $\beta = \vartheta_- - 4\varepsilon_-/\pi$ and $\gamma = 0$ or $\gamma = \pi$ depending on the sign of $\xi_-$.

The previous analysis only leaves us to choose the integers $m, n$, see Eq. (7.60). We make use of this freedom to limit the drive amplitude $A$ in magnitude. Careful inspection of the removable singularity in Eq. (7.62) suggests the usage of a drive frequency $\omega_d$ near $\omega_-$. This can be achieved by a combination of $n$ and $m$ such that their ratio $n/m$ closely approximates $\omega_-/\omega_+$. The optimal choice of $n$ must balance between mitigating the effects of $T_1$ and $T_2$ by keeping gate durations $2\pi n/\omega_d$ as short as possible, and holding at bay unwanted population transfer incurred by strong drive amplitudes $A \sim 1/n$ [see Sec. 7.7.2.1]. With $n$ and $m$ specified as such, we have constructed the $\sqrt{\phi\text{SWAP}}$ gate allowing for the execution of a $\sqrt{i\text{SWAP}}$ gate when combined with single-qubit *Z* rotations.

### 7.7.2 Full-system numerical simulations

This realization of $\sqrt{i\text{SWAP}}$ reaches closed-system (open-system) fidelities as high as $F = 0.9996$ ($F = 0.9994$), which we obtain from numerical simulation of the full system as detailed in the following. Time evolution is based on the Hamiltonian $H(t) = H_0 + V + \sum_{\mu=a,b,c} h_\mu \delta\phi_\mu(t)$, see Eqs. (7.3)-(7.5) as well as Eqs. (7.26)-(7.28) for the flux-activated terms. The dc fluxes entering $H_0 + V$ are set to the off position[4], as is appropriate for performing single- and two-qubit gates. For numerical efficiency, $H(t)$ is expressed in the eigenbasis of the static Hamiltonian $H_0 + V$. The computational states of interest are the four lowest-energy states, with qubit frequencies $\omega_a'/2\pi = 58.1$ MHz, $\omega_b'/2\pi = 35.5$ MHz. Beyond these, we include up to 50 additional states in our simulations. For the parameters considered here, we have $\omega_-/\omega_+ = 0.24$, thus we choose $n/m = 1/4$, yielding $\omega_d/2\pi = 23.4$ MHz. Upon including the effects of decoherence, the choice $n = 2$ and thus $m = 8$, $A/2\pi = 2.9$ MHz optimizes the gate fidelity.

The full gate duration is $t_{\text{tot}} = 2\pi n/\omega_d + \max(t_{a1}, t_{b1}) + \max(t_{a2}, t_{b2})$, where $t_{\mu i} = -\theta_{\mu i}/\omega_\mu$. The equations for the times $t_{\mu i}$ are understood modulo $2\pi$ and the *Z* rotation angles are known in terms

[4] The off position is found by minimizing the energy of the $|\overline{11}\rangle$ state, analogously to how the off position is found based on the effective Hamiltonian $H_{\text{eff}}$. The exact and effective values for the coupler flux at the off position typically have a relative deviation of less than one percent

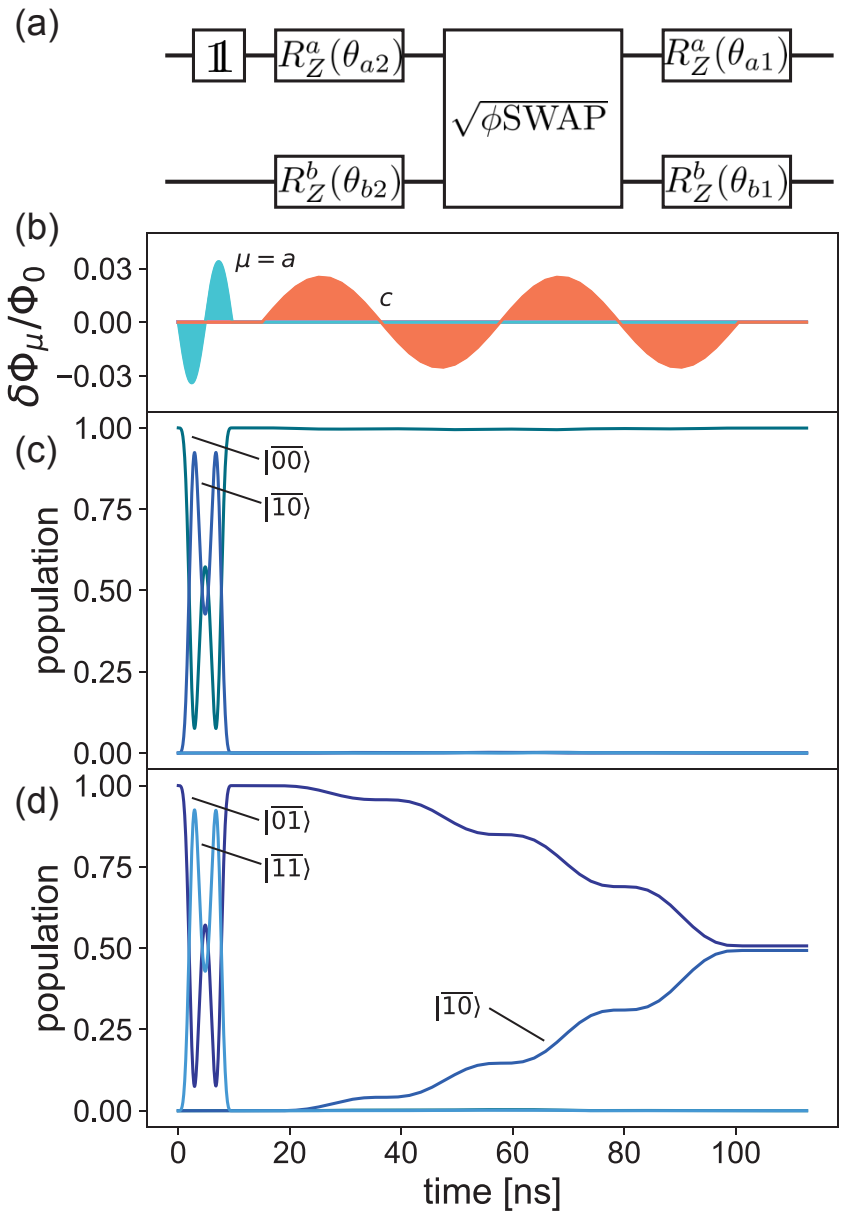


**Figure 7.8:** $\sqrt{i\text{SWAP}}$ gate composed of a $\sqrt{\phi\text{SWAP}}$ gate and corrective $Z$ rotations. (a) Quantum-circuit representation of the flux pulses shown in (b). The qubit flux $\delta\phi_a(t)$ (blue) is modulated to achieve the required identity operation, while the coupler flux $\delta\phi_c(t)$ (orange) is activated to entangle the qubits. Single-qubit $Z$ rotations are obtained during the time spent idling. (c) Time evolution with the initial state $|\overline{00}\rangle$. Population transfer to the $|\overline{11}\rangle$ or other states is negligible during the $\sqrt{\phi\text{SWAP}}$ time window. (b) Time evolution for $|\overline{01}\rangle$ as the initial state. The $|\overline{01}\rangle$ and $|\overline{10}\rangle$ states exchange population during the segment when the coupler flux is nonzero. The closed-system fidelity of the $\sqrt{i\text{SWAP}}$ gate is $F = 0.9996$.

of the phases $\alpha, \beta, \gamma$, see Eq. (7.53). The angle $\theta_{b2}$ is a free parameter and is chosen to minimize the overall gate time by forcing the idle times after the $\sqrt{\phi\text{SWAP}}$ gate to coincide $t_{a1} = t_{b1}$. For our parameters we obtain $t_{\text{tot}} = 113$ ns, where $2\pi n/\omega d = 85$ ns and the single-qubit gates require 28 ns, see Fig. 7.8. For the initial state $|\overline{00}\rangle$, population appreciably varies only during the single-qubit identity-gate segments, see Fig. 7.8(c). Meanwhile, for the state $|\overline{01}\rangle$, population transfer to the $|\overline{10}\rangle$ state occurs during the $\sqrt{\phi\text{SWAP}}$ portion of the gate, see Fig. 7.8(d). Closed-system simulations of this pulse sequence yield a gate fidelity of $F = 0.9996$ for achieving a $\sqrt{i\text{SWAP}}$ gate, calculated using Eq. (7.47), taking $d = 4$ and $U_{\text{T}} = \sqrt{i\text{SWAP}}$. Infidelities at the $10^{-4}$ level are likely due to residual effects from the higher-lying states that cause unwanted transitions in the computational subspace as described in the following.

#### 7.7.2.1 Virtual transitions involving higher-lying states

The full analysis of time evolution when modulating the coupler flux requires consideration of higher-lying states. These states outside the computational subspace, while largely remaining unoccupied, participate as virtual intermediate states in unwanted transitions. We estimate the amount of population transfer between the states $|i\rangle = |\overline{\ell_a, m_b, 0_-, 0_+}\rangle$ and $|f\rangle = |\overline{\ell'_a, m'_b, 0_-, 0_+}\rangle$ with $i \neq f$ at the conclusion of the gate $t = 2\pi n/\omega_d$ using time-dependent perturbation theory up to second-order [81]

$$
\begin{aligned}
T_{\ell m \to \ell' m'} = \Bigg| & \frac{i\langle f|\delta\phi_c h_c|i\rangle\omega_d}{E_{fi}^2 - \omega_d^2}(1 - e^{2\pi i n E_{fi}/\omega_d}) \\
& + \sum_v \frac{\omega_d^2 \langle f|\delta\phi_c h_c|v\rangle\langle v|\delta\phi_c h_c|i\rangle}{E_{vi}^2 - \omega_d^2} \\
& \left( \frac{[2E_{vi} + E_{fi}][1 - e^{2\pi n i E_{fi}/\omega_d}]}{E_{fi}[E_{fi}^2 - 4\omega_d^2]} - \frac{1 - e^{2\pi n i E_{fv}/\omega_d}}{E_{fv}^2 - \omega_d^2} \right) \Bigg|^2 ,
\end{aligned}
\tag{7.63}
$$

where the sum on $v$ is over virtual intermediate states $|v\rangle = |\overline{\ell''_a, m''_b, p_-, q_+}\rangle$ and we have defined $E_{fv} = E_{\overline{\ell' m' 00}} - E_{\overline{\ell'' m'' pq}}$, etc. The top line of Eq. (7.63) represents direct transitions between the states $|i\rangle$ and $|f\rangle$, occurring for nonzero $\langle f|h_c|i\rangle$ (e.g. $|i\rangle = |\overline{0_a, 1_b, 0_-, 0_+}\rangle$ and $|f\rangle = |\overline{1_a, 0_b, 0_-, 0_+}\rangle$).

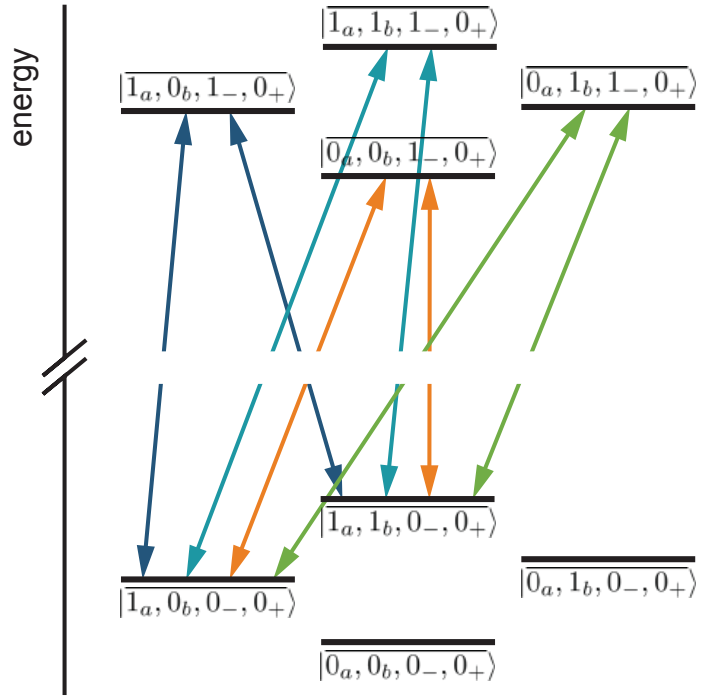


**Figure 7.9:** Schematic of unwanted transitions in the computational subspace. These transitions are due to virtual excitations of the higher-lying states $|\overline{\ell_a, m_b, 1_-, 0_+}\rangle, \ell, m \in \{0, 1\}$ mediated by the drive operator $h_c$. As an example, we show the four perturbative paths contributing to the undesired transition $|\overline{1_a, 0_b, 0_-, 0_+}\rangle \leftrightarrow |\overline{1_a, 1_b, 0_-, 0_+}\rangle$.

These are the wanted transitions discussed previously. The second and third lines of Eq. (7.63) are the second-order contributions and allow for unwanted transitions. Based on numerical calculation of the matrix elements of $h_c$ between the computational states and higher-lying states, we find that the four states $|v\rangle = |\overline{\ell_a, m_b, 1_-, 0_+}\rangle, \ell, m \in \{0, 1\}$ with an excitation in the $\theta_-$ mode dominate the sum on $v$, see Fig. 7.9. (Note that this virtual process is heavily suppressed in the context of qubit-flux drives, due to the comparatively small coefficient $E_L/2 \ll E_{Lc}$ multiplying the operator $\theta_-$ in $h_a$).

These transitions mediated by the higher-lying states can significantly degrade gate fidelities. Indeed, attempting to implement the $\sqrt{\phi\text{SWAP}}$ gate with only a single drive period leads to poor fidelities $F < 0.9$ due to the unwanted transitions. Slowing down the gate by utilizing two drive periods mitigates this issue in large part by reducing the required drive amplitude. It is an interesting

avenue for further research to investigate means for overcoming this limitation on $\delta\phi_c$ to achieve faster gate times without sacrificing fidelity.

#### 7.7.2.2 Decoherence effects

To include the detrimental effects of decoherence on gate fidelities, we numerically solve the Lindblad master equation

$$\frac{d\rho(t)}{dt} = -i[H(t), \rho(t)] + \sum_{\mu=a,b} [\Gamma_1^\mu \mathcal{D}(L_1^\mu)\rho(t) + \Gamma_\phi^\mu \mathcal{D}(L_\phi^\mu)\rho(t)], \tag{7.64}$$

where $\rho(t)$ is the system density matrix and

$$\mathcal{D}(L)\rho = L\rho L^\dagger - \frac{1}{2}\{L^\dagger L, \rho\},$$

is the standard form of the dissipator. The relevant jump operators $L$ are here:

$$L_1^\mu = \bar{\sigma}_-^\mu, \quad L_\phi^\mu = \bar{\sigma}_z^\mu.$$

We neglect decoherence processes due to higher-lying states, noting that their occupation remains minimal throughout the duration of the pulse. We consider two sets of estimates for decoherence rates, one conservative, $\Gamma_\phi = 1/80\,\mu\text{s}, \Gamma_1 = 1/300\,\mu\text{s}$, and one optimistic, $\Gamma_\phi = 1/4000\,\mu\text{s}, \Gamma_1 = 1/1000\,\mu\text{s}$, both consistent with recent experiments [31, 33]. At the conclusion of the gate, we project onto the computational subspace and perform numerical quantum process tomography [174, 197, 198, 204] to obtain the process matrix $\chi$. The open-system gate fidelity is calculated using the formula

$$F = \frac{d\,\text{Tr}(\chi\chi_\text{T}) + \text{Tr}(\chi)}{d+1}, \tag{7.65}$$

see Appendix C for the derivation of Eq. (7.65) based on results presented in Refs. [195, 205, 206]. We have defined $\chi_\text{T}$ as the target process matrix and here $d = 4$. We obtain open-system gate

fidelities of $F = 0.997, F = 0.9994$ for the two cases of conservative and optimistic decoherence rate estimates, respectively.

# 8 Conclusion and outlook

The goal of this thesis has been to make progress on two related fronts. The first was to evaluate and characterize the coherence of noise-protected qubits—specifically the current-mirror qubit—in the hope that such a next-generation device can outperform and eventually supersede the transmon. The second was to improve gate fidelities by going beyond standard treatments based on the RWA, especially in the context of high-coherence and low-frequency fluxonium qubits. These goals are mutually beneficial due to the detrimental effects of both imperfect control and decoherence on gate fidelities. To break out of the NISQ era [17] and make meaningful strides towards achieving quantum error correction, gate fidelities must increase beyond the current state-of-the-art.

The detailed analysis of Kitaev's current mirror faced new challenges not common for previously studied superconducting circuits: the significant increase in the number of degrees of freedom. As a consequence, simulating the full Hamiltonian using exact diagonalization proved intractable for $N > 3$ because of memory requirements. To overcome this obstacle, in Ch. 5 we presented an effective Hamiltonian describing the low-energy subspace of the current-mirror circuit, halving the number of degrees of freedom and, more importantly, reducing the range of interactions. This effective Hamiltonian was derived by treating the Josephson tunneling perturbatively, resulting in second-order exciton tunneling as well as $N$-th order degeneracy-breaking processes. We provided a systematic discussion of the degeneracy-breaking terms, crucial to predicting the behavior of the current-mirror qubit. The effective Hamiltonian thus obtained is amenable to DMRG treatment, and has allowed us to simulate circuits with up to $N = 12$ big capacitors. For the DMRG numerics, computation time rather than memory poses the bottleneck, and therefore simulation of even larger circuits is possible.

Our numerical DMRG results confirmed the development of (approximate) ground-state degen-

eracy for circuit sizes exceeding $N = 6$, tracing the origin of the near-degeneracy to an effective double-well structure with slight asymmetry in the $N$-dimensional configuration space of the effective model. We established a correspondence between the minima in the full model with the minima in the effective model, indicating that even (odd) vortex parity minima contribute to the 0 ($\pi$) minimum. Linearization of the effective-model potential around both minima further yields a good approximation for the circuit's low-energy excitations in terms of harmonic normal modes. An important insight from this analysis is the observed $1/N$ scaling of the energies of low-lying excitations. As a consequence, excessively large circuit sizes $N$ must be avoided as increasing size will eventually lead to depolarization from thermal excitations of the harmonic modes.

Based on the spectral data from DMRG, we have estimated coherence times for the current-mirror qubit for a representative set of parameters. $1/f$ charge noise, critical-current noise, flux noise and dielectric loss were investigated for their contributions to both pure dephasing and depolarization. We find that charge noise is likely to limit $T_\phi$, while dielectric loss limits $T_1$ in our analysis. $T_\phi$ is observed to improve as a function of $N$ because of the decreasing degeneracy-breaking coefficient $K$, while $T_1$ worsens as a function of $N$ because of the energy suppression of low-lying eigenstates, and resulting thermal excitations. $T_\phi$ and $T_1$ intersect near $N = 11$, indicating that $N = 11$ may be considered an ideal operating point of the qubit for the studied parameter set. Coherence times calculations were performed at the charge sweet spot, leaving open for now the characterization in the presence of offset-charge jumps $> 0.1e$ [207].

In Ch. 6 we generalized the well-known method of tight binding for the efficient and accurate computation of the low-energy spectra of superconducting circuits. We demonstrated the method on systems with many degrees of freedom, multiple inequivalent minima, and periodic potentials. Construction of the Hamiltonian proceeds by using ansatz Bloch states formed by appropriate linear combinations of localized wave functions. In terms of the Bloch states, the Schrödinger equation turns into a generalized eigenvalue problem. Solving it yields a spectrum that provides upper bounds to the true eigenenergies. To establish the accuracy of the tight-binding method we applied it to the flux qubit and $N = 3$ current-mirror circuit and achieved excellent agreement with exact results. Additionally, across multiple orders of magnitude in memory usage, eigenenergies

computed using tight binding were found to be more accurate than those calculated using the charge basis. This indicates that for a given limited amount of memory, tight binding states can oftentimes more closely represent the true eigenstates of a circuit as compared to charge-basis states.

To push into the regime of large $N$, relevant for protected current-mirror circuits, we applied the tight-binding method to the $N = 5$ current mirror. For this circuit with nine degrees of freedom, we encounter memory issues before the spectrum converges when using the charge basis. Thus, in the absence of exact results, we compare absolute values of the estimated eigenenergies, which must be upper bounds to the true values. We found that the tight-binding method extracted lower and thus more accurate eigenenergy estimates than those obtained using the charge basis, given our computational resources.

In Ch. 7 we applied our framework for beyond-the-RWA gates to a system of galvanically-coupled fluxonium qubits. The effective *XX* coupling can be switched on and off while maintaining the qubits at their respective sweet spots. Motivated by record coherence times achieved with heavy-fluxonium qubits, we have concentrated on operating at frequencies below $\sim$200 MHz [31, 33]. We proposed gates performed using strong flux modulation that invalidates the RWA, and in particular makes it more natural operate in the lab frame. Using the theory developed in Ch. 4, we presented a protocol that achieves a fast and high-fidelity $\sqrt{\phi\text{SWAP}}$ gate. To transform this into the more familiar $\sqrt{i\text{SWAP}}$ gate, we introduced variable-time identity gates. These gates when combined with *Z* rotations helped us to realize a $\sqrt{i\text{SWAP}}$ gate with fidelity $F > 0.999$. Fidelities are limited by incoherent errors as well as unwanted transitions in the computational subspace mediated by higher-lying states.

We turn next to an outlook on what the author believes are possible interesting directions for future research building on the results of this thesis. These include considering new and improved types of circuits that could exhibit protection, investigating the relative importance of beyond-the-RWA effects in superconducting circuits more broadly and exploring the scalability of the galvanic-coupling architecture introduced for fluxonium qubits.

The circuits underlying the protected rhombus and $0 - \pi$ qubits have been experimentally re-

alized [50, 51, 53]. Reaching the fully protected parameter regime is challenging in part due to stringent parameter requirements, which are similarly present in the case of the current mirror. There has been notable recent progress, for instance in the realization of a superinductance (required for the protected $0-\pi$ circuit [102]) in the context of the so-called "Blochnium" device [208]. However, generally speaking, we lack a systematic understanding of which superconducting circuits do or do not exhibit protection. Indeed there is a significant amount of unexplored space in terms of novel circuit designs. It is possible that there exist other types of protected circuits whose protected parameter regimes are easier to reach with current technologies.

Beyond ideas for new protected circuits, a relatively unexplored frontier is the high-fidelity execution of protected gates on protected circuits. (Unprotected single-qubit gates on a $0-\pi$ qubit have been demonstrated in Ref. [53], however a fidelity was not quoted.) In his seminal paper introducing the current mirror, Kitaev also considered protected gates effected using a quantum switch together with a superinductance [52]. Later proposals from Brooks, Kitaev and Preskill [102] as well as Douçot and Ioffe [47] are based on similar ideas and circuit elements. Recent work based on a detailed analysis of the $0-\pi$ circuit has shown that such a gate scheme will not work in practice [103], irrespective of the difficulties associated with building a quantum switch or superinductance. A very exciting research direction is investigating new and qualitatively different ideas for performing protected gates. This is a gaping hole in the literature that is waiting to be filled.

We have argued in this thesis that effects from strong drives going beyond the RWA are crucial for implementing high-fidelity gates in low-frequency qubits. In the context of two-qubit gates we considered the parameter regime $A/\omega \geq 0.1$, where $A$ is the amplitude of the drive and $\omega$ is the frequency of the relevant transition. In this case neglecting counter-rotating terms can affect fidelities at the level of $10^{-2}-10^{-3}$, necessitating an analysis including these terms to achieve high-fidelity gates. A broader question emerging from this research is the relative importance of these effects on higher-frequency qubits: do such experiments probe parameter regimes where the presence of counter-rotating terms limits gate fidelities? In a recent experiment, Mundada *et al.* coupled two fixed-frequency transmon qubits (separated by 278 MHz) via a flux-tunable coupler

that was modulated at the qubit difference frequency to perform an entangling gate [26]. The drive strengths in this experiment were on the order of a few MHz, thus achieving $A/\omega \geq 0.01$. The reported two-qubit gate infidelities were on the order of $10^{-2}$ [26]. Our preliminary investigations suggest that for such parametrically-activated flux gates, fidelities are impacted at the level of $10^{-4} - 10^{-5}$ when $A/\omega \geq 0.01$. Thus, the experiment in Ref. [26] was not sensitive to the beyond-the-RWA effects discussed here. Nevertheless, if drive strengths increase to achieve faster gates or if infidelities approach the $10^{-4}$ level (consistent with the current state-of-the-art in two-qubit transmon gates [22]), then counter-rotating effects may eventually become limiting and require correction.

Utilizing the galvanic-coupling architecture introduced in Ch. 7 in a future quantum processor will require scaling to arrays of multiple qubits and couplers. One attractive feature of our scheme is the ability to turn the interaction between neighboring qubits off via the tunable coupler. This should help alleviate spectator-qubit effects that can limit two-qubit gate fidelities [209]. It is relatively straightforward to envision extending the device in a 1D array. Generalization to 2D arrays with increased qubit connectivity will require additional modifications, and will be useful for steps towards error-correcting surface codes [20].

We hope that the results presented in this thesis inspire the reader to explore the new and exciting aspects of the world of superconducting quantum circuits. There are clearly many unexplored frontiers, and we have only just scratched the surface of what these circuits have to offer.

# References


[1] Benioff, P., "The computer as a physical system: a microscopic quantum mechanical Hamiltonian model of computers as represented by Turing machines", J. Stat. Phys. **22**, 563 (1980) (cit. on p. 21).

[2] Feynman, R. P., "Simulating physics with computers", Int. J. Theor. Phys. **21**, 467 (1982) (cit. on p. 21).

[3] Shor, P. W., "Algorithms for quantum computation: discrete logarithms and factoring", in Proceedings of the 35th Annual Symposium on Foundations of Computer Science (1994), pp. 124–134 (cit. on p. 21).

[4] Shor, P. W., "Polynomial-time algorithms for prime factorization and discrete logarithms on a quantum computer", SIAM J. Comput. **26**, 1484 (1997) (cit. on pp. 21, 22).

[5] Pomerance, C., "Fast, rigorous factorization and discrete logarithm algorithms", in *Discrete algorithms and complexity*, edited by D. S. Johnson, T. Nishizeki, A. Nozaki, and H. S. Wilf (Academic Press, 1987), pp. 119–143 (cit. on p. 21).

[6] Rivest, R. L., A. Shamir, and L. M. Adleman, "A method for obtaining digital signatures and public-key cryptosystems", Communications of the ACM **26**, 96–99 (1983) (cit. on p. 21).

[7] Grover, L. K., "A fast quantum mechanical algorithm for database search", in Proceedings of the 28th Annual ACM Symposium on Theory of Computing (1996), pp. 212–219 (cit. on p. 21).

[8] Kassal, I., S. P. Jordan, P. J. Love, M. Mohseni, and A. Aspuru-Guzik, "Polynomial-time quantum algorithm for the simulation of chemical dynamics", Proc. Natl. Acad. Sci. **105**, 18681 (2008) (cit. on p. 21).

[9] Jordan, S., *The quantum algorithm zoo*, `https://quantumalgorithmzoo.org` (cit. on p. 21).

[10] Bruzewicz, C. D., J. Chiaverini, R. McConnell, and J. M. Sage, "Trapped-ion quantum computing: progress and challenges", Appl. Phys. Rev. **6**, 021314 (2019) (cit. on p. 21).

[11] Henriet, L., L. Beguin, A. Signoles, T. Lahaye, A. Browaeys, G.-O. Reymond, and C. Jurczak, "Quantum computing with neutral atoms", Quantum **4**, 327 (2020) (cit. on p. 21).

[12] Childress, L. and R. Hanson, "Diamond NV centers for quantum computing and quantum networks", MRS Bull. **38**, 134 (2013) (cit. on p. 21).

[13] Kjaergaard, M., M. E. Schwartz, J. Braumüller, P. Krantz, J. I.-J. Wang, S. Gustavsson, and W. D. Oliver, "Superconducting qubits: current state of play", Annu. Rev. Condens. Matter Phys. **11**, 369 (2020) (cit. on p. 21).

[14] Blais, A., A. L. Grimsmo, S. M. Girvin, and A. Wallraff, "Circuit quantum electrodynamics", Rev. Mod. Phys. **93**, 025005 (2021) (cit. on pp. 21, 25, 40, 53, 57, 63, 120, 124–126, 134, 138, 148, 177, 178, 180, 185).

[15] Blais, A., R.-S. Huang, A. Wallraff, S. M. Girvin, and R. J. Schoelkopf, "Cavity quantum electrodynamics for superconducting electrical circuits: an architecture for quantum computation", Phys. Rev. A **69**, 062320 (2004) (cit. on pp. 21, 25, 187).

[16] Makhlin, Y., G. Schön, and A. Shnirman, "Quantum-state engineering with Josephson-junction devices", Rev. Mod. Phys. **73**, 357 (2001) (cit. on p. 21).

[17] Preskill, J., "Quantum computing in the NISQ era and beyond", Quantum **2**, 79 (2018) (cit. on pp. 22, 155).

[18] Cross, A. W., L. S. Bishop, S. Sheldon, P. D. Nation, and J. M. Gambetta, "Validating quantum computers using randomized model circuits", Phys. Rev. A **100**, 032328 (2019) (cit. on p. 22).

[19] Shor, P. W., "Fault-tolerant quantum computation", in Proceedings of the 37th Conference on Foundations of Computer Science (1996), pp. 56–65 (cit. on p. 22).

[20] Fowler, A. G., M. Mariantoni, J. M. Martinis, and A. N. Cleland, "Surface codes: Towards practical large-scale quantum computation", Phys. Rev. A **86**, 032324 (2012) (cit. on pp. 22, 159).

[21] Svore, K. M., D. P. Divincenzo, and B. M. Terhal, "Noise threshold for a fault-tolerant two-dimensional lattice architecture", Quantum Info. Comput. **7**, 297 (2007) (cit. on p. 22).

[22] Negîrneac, V., H. Ali, N. Muthusubramanian, F. Battistel, R. Sagastizabal, M. S. Moreira, J. F. Marques, W. J. Vlothuizen, M. Beekman, C. Zachariadis, N. Haider, A. Bruno, and L. DiCarlo, "High-fidelity controlled-$Z$ gate with maximal intermediate leakage operating at the speed limit in a superconducting quantum processor", Phys. Rev. Lett. **126**, 220502 (2021) (cit. on pp. 22, 159).

[23] Dogan, E., D. Rosenstock, L. L. Guevel, H. Xiong, R. A. Mencia, A. Somoroff, K. N. Nesterov, M. G. Vavilov, V. E. Manucharyan, and C. Wang, "Demonstration of the two-fluxonium cross-resonance gate", arXiv:2204.11829 (2022) (cit. on pp. 22, 117).

[24] Foxen, B., C. Neill, A. Dunsworth, P. Roushan, B. Chiaro, A. Megrant, J. Kelly, Z. Chen, K. Satzinger, R. Barends, F. Arute, K. Arya, R. Babbush, D. Bacon, J. C. Bardin, S. Boixo, D. Buell, B. Burkett, Y. Chen, R. Collins, E. Farhi, A. Fowler, C. Gidney, M. Giustina, R. Graff, M. Harrigan, T. Huang, S. V. Isakov, E. Jeffrey, Z. Jiang, D. Kafri, K. Kechedzhi, P. Klimov, A. Korotkov, F. Kostritsa, D. Landhuis, E. Lucero, J. Mcclean, M. Mcewen, X. Mi, M. Mohseni, J. Y. Mutus, O. Naaman, M. Neeley, M. Niu, A. Petukhov, C. Quintana, N. Rubin, D. Sank,

V. Smelyanskiy, A. Vainsencher, T. C. White, Z. Yao, P. Yeh, A. Zalcman, H. Neven, and J. M. Martinis, “Demonstrating a continuous set of two-qubit gates for near-term quantum algorithms”, Phys. Rev. Lett. **125**, 120504 (2020) (cit. on p. 22).

[25] DiCarlo, L., J. M. Chow, J. M. Gambetta, L. S. Bishop, B. R. Johnson, D. I. Schuster, J. Majer, A. Blais, L. Frunzio, S. M. Girvin, and R. J. Schoelkopf, “Demonstration of two-qubit algorithms with a superconducting quantum processor”, Nature **460**, 240 (2009) (cit. on p. 23).

[26] Mundada, P., G. Zhang, T. Hazard, and A. Houck, “Suppression of qubit crosstalk in a tunable coupling superconducting circuit”, Phys. Rev. Applied **12**, 054023 (2019) (cit. on pp. 23, 128, 159).

[27] Di Paolo, A., C. Leroux, T. M. Hazard, K. Serniak, S. Gustavsson, A. Blais, and W. D. Oliver, “Extensible circuit-QED architecture via amplitude- and frequency-variable microwaves”, arXiv:2204.08098 (2022) (cit. on p. 23).

[28] McKay, D. C., S. Sheldon, J. A. Smolin, J. M. Chow, and J. M. Gambetta, “Three-qubit randomized benchmarking”, Phys. Rev. Lett. **122**, 200502 (2019) (cit. on p. 23).

[29] Koch, J., V. Manucharyan, M. H. Devoret, and L. I. Glazman, “Charging effects in the inductively shunted josephson junction”, Phys. Rev. Lett. **103**, 217004 (2009) (cit. on pp. 23, 24, 36, 44).

[30] Manucharyan, V., J. Koch, L. I. Glazman, and M. H. Devoret, “Fluxonium : single Cooper-pair circuit free of charge offsets”, Science **326**, 113 (2009) (cit. on pp. 23, 24, 36, 91, 118).

[31] Zhang, H., S. Chakram, T. Roy, N. Earnest, Y. Lu, Z. Huang, D. K. Weiss, J. Koch, and D. I. Schuster, “Universal fast-flux control of a coherent, low-frequency qubit”, Phys. Rev. X **11**, 011010 (2021) (cit. on pp. 23, 25, 37–41, 53, 117, 118, 120, 135, 139, 140, 153, 157).

[32] Nguyen, L. B., Y.-H. Lin, A. Somoroff, R. Mencia, N. Grabon, and V. E. Manucharyan, “High-coherence fluxonium qubit”, Phys. Rev. X **9**, 041041 (2019) (cit. on pp. 23, 24, 37, 39, 40, 117, 118).

[33] Somoroff, A., Q. Ficheux, R. A. Mencia, H. Xiong, R. V. Kuzmin, and V. E. Manucharyan, “Millisecond coherence in a superconducting qubit”, arXiv:2103.08578 (2021) (cit. on pp. 23, 24, 37, 39, 40, 94, 117, 118, 153, 157).

[34] Nakamura, Y., Y. A. Pashkin, and J. S. Tsai, “Coherent control of macroscopic quantum states in a single-Cooper-pair box”, Nature **398**, 786 (1999) (cit. on pp. 23, 24).

[35] Bouchiat, V., D. Vion, P. Joyez, D. Esteve, and M. H. Devoret, “Quantum coherence with a single Cooper pair”, Phys. Scr. **T76**, 165 (1998) (cit. on p. 23).

[36] Nakamura, Y., Y. A. Pashkin, T. Yamamoto, and J. S. Tsai, “Charge echo in a Cooper-pair box”, Phys. Rev. Lett. **88**, 047901 (2002) (cit. on p. 24).

[37] Vion, D., A. Aassime, A. Cottet, P. Joyez, H. Pothier, C. Urbina, D. Esteve, and M. H. Devoret, "Manipulating the quantum state of an electrical circuit", Science **296**, 886 (2002) (cit. on pp. 24, 34, 37).

[38] Koch, J., T. M. Yu, J. Gambetta, A. A. Houck, D. I. Schuster, J. Majer, A. Blais, M. H. Devoret, S. M. Girvin, and R. J. Schoelkopf, "Charge-insensitive qubit design derived from the Cooper pair box", Phys. Rev. A **76**, 042319 (2007) (cit. on pp. 24, 29, 34, 35, 46, 50, 51, 184, 185).

[39] Place, A. P. M., L. V. H. Rodgers, P. Mundada, B. M. Smitham, M. Fitzpatrick, Z. Leng, A. Premkumar, J. Bryon, A. Vrajitoarea, S. Sussman, G. Cheng, T. Madhavan, H. K. Babla, X. H. Le, Y. Gang, B. Jäck, A. Gyenis, N. Yao, R. J. Cava, N. P. de Leon, and A. A. Houck, "New material platform for superconducting transmon qubits with coherence times exceeding 0.3 milliseconds", Nat. Commun. **12**, 1779 (2021) (cit. on p. 24).

[40] Wang, C., X. Li, H. Xu, Z. Li, J. Wang, Z. Yang, Z. Mi, X. Liang, T. Su, C. Yang, G. Wang, W. Wang, Y. Li, M. Chen, C. Li, K. Linghu, J. Han, Y. Zhang, Y. Feng, Y. Song, T. Ma, J. Zhang, R. Wang, P. Zhao, W. Liu, G. Xue, Y. Jin, and H. Yu, "Transmon qubit with relaxation time exceeding 0.5 milliseconds", arXiv:2105.09890 (2021) (cit. on p. 24).

[41] Manucharyan, V. E., "Superinductance", PhD thesis (Yale University, 2012) (cit. on pp. 24, 37).

[42] Kitaev, A., "Fault-tolerant quantum computation by anyons", Ann. Phys. **303**, 2 (2003) (cit. on pp. 24, 42).

[43] Ioffe, L. B. and M. V. Feigel'man, "Possible realization of an ideal quantum computer in Josephson junction array", Phys. Rev. B **66**, 224503 (2002) (cit. on pp. 24, 40).

[44] Ioffe, L. B., M. V. Feigel'man, A. Ioselevich, D. Ivanov, M. Troyer, and G. Blatter, "Topologically protected quantum bits using Josephson junction arrays", Nature **415**, 503 (2002) (cit. on pp. 24, 40).

[45] Douçot, B., M. V. Feigel'man, and L. B. Ioffe, "Topological order in the insulating Josephson junction array", Phys. Rev. Lett. **90**, 107003 (2003) (cit. on p. 24).

[46] Douçot, B., M. V. Feigel'man, L. B. Ioffe, and A. S. Ioselevich, "Protected qubits and Chern-Simons theories in Josephson junction arrays", Phys. Rev. B **71**, 024505 (2005) (cit. on pp. 24, 40).

[47] Douçot, B. and L. B. Ioffe, "Physical implementation of protected qubits", Rep. Prog. Phys. **75**, 072001 (2012) (cit. on pp. 24, 40, 44, 158).

[48] Vidal, J., B. Douçot, R. Mosseri, and P. Butaud, "Interaction induced delocalization for two particles in a periodic potential", Phys. Rev. Lett. **85**, 3906 (2000) (cit. on p. 24).

[49] Douçot, B. and J. Vidal, "Pairing of Cooper pairs in a fully frustrated Josephson-junction chain", Phys. Rev. Lett. **88**, 227005 (2002) (cit. on pp. 24, 40).

[50] Gladchenko, S., D. Olaya, E. Dupont-Ferrier, B. Douçot, L. B. Ioffe, and M. E. Gershenson, "Superconducting nanocircuits for topologically protected qubits", Nat. Phys. **5**, 48 (2009) (cit. on pp. 25, 40, 158).

[51] Bell, M. T., J. Paramanandam, L. B. Ioffe, and M. E. Gershenson, "Protected Josephson rhombus chains", Phys. Rev. Lett. **112**, 167001 (2014) (cit. on pp. 25, 40, 158).

[52] Kitaev, A., "Protected qubit based on a superconducting current mirror", arXiv:cond-mat/0609441 (2006) (cit. on pp. 25, 40, 44, 59, 61, 62, 69, 87, 111, 158).

[53] Gyenis, A., P. S. Mundada, A. Di Paolo, T. M. Hazard, X. You, D. I. Schuster, J. Koch, A. Blais, and A. A. Houck, "Experimental realization of a protected superconducting circuit derived from the $0-\pi$ qubit", PRX Quantum **2**, 010339 (2021) (cit. on pp. 25, 40, 42, 158).

[54] Blais, A., J. Gambetta, A. Wallraff, D. I. Schuster, S. M. Girvin, M. H. Devoret, and R. J. Schoelkopf, "Quantum-information processing with circuit quantum electrodynamics", Phys. Rev. A **75**, 032329 (2007) (cit. on p. 25).

[55] Campbell, D. L., Y. P. Shim, B. Kannan, R. Winik, D. K. Kim, A. Melville, B. M. Niedzielski, J. L. Yoder, C. Tahan, S. Gustavsson, and W. D. Oliver, "Universal nonadiabatic control of small-gap superconducting qubits", Phys. Rev. X **10**, 041051 (2020) (cit. on pp. 25, 40, 53, 117, 120, 139, 140).

[56] Yang, Y. C., S. N. Coppersmith, and M. Friesen, "Achieving high-fidelity single-qubit gates in a strongly driven silicon-quantum-dot hybrid qubit", Phys. Rev. A **95**, 062321 (2017) (cit. on pp. 25, 139).

[57] Bloch, F. and A. Siegert, "Magnetic resonance for nonrotating fields", Phys. Rev. **57**, 522 (1940) (cit. on pp. 25, 57).

[58] Cohen-Tannoudji, C., J. Dupont-Roc, and C. Fabre, "A quantum calculation of the higher order terms in the Bloch-Siegert shift", J. Phys. B **6**, L214 (1973) (cit. on p. 26).

[59] Shirley, J. H., "Solution of the Schrödinger equation with a Hamiltonian periodic in time", Phys. Rev. **252**, 424 (1965) (cit. on pp. 26, 144).

[60] Huang, Z., P. S. Mundada, A. Gyenis, D. I. Schuster, A. A. Houck, and J. Koch, "Engineering dynamical sweet spots to protect qubits from $1/f$ noise", Phys. Rev. Applied **15**, 034065 (2021) (cit. on pp. 26, 140).

[61] Mundada, P. S., A. Gyenis, Z. Huang, J. Koch, and A. A. Houck, "Floquet-engineered enhancement of coherence times in a driven fluxonium qubit", Phys. Rev. Applied **14**, 054033 (2020) (cit. on p. 26).

[62] Petrescu, A., C. L. Calonnec, C. Leroux, A. Di Paolo, P. Mundada, S. Sussman, A. Vrajitoarea, A. A. Houck, and A. Blais, "Accurate methods for the analysis of strong-drive effects in parametric gates", arXiv:2107.02343 (2021) (cit. on pp. 26, 144).

[63] Son, S.-K., S. Han, and S.-I. Chu, "Floquet formulation for the investigation of multiphoton quantum interference in a superconducting qubit driven by a strong ac field", Phys. Rev. A **79**, 032301 (2009) (cit. on p. 26).

[64] Deng, C., J.-L. Orgiazzi, F. Shen, S. Ashhab, and A. Lupascu, "Observation of Floquet states in a strongly driven artificial atom", Phys. Rev. Lett. **115**, 133601 (2015) (cit. on p. 26).

[65] Magnus, W., "On the exponential solution of differential equations for a linear operator", Commun. Pure Appl. Math. **7**, 649 (1954) (cit. on pp. 26, 53).

[66] Wilcox, R. M., "Exponential operators and parameter differentiation in quantum physics", J. Math. Phys. **8**, 962 (1967) (cit. on pp. 26, 53–55, 100, 101).

[67] Blanes, S., F. Casas, J. A. Oteo, and J. Ros, "The Magnus expansion and some of its applications", Phys. Rep. **470**, 151 (2009) (cit. on pp. 26, 53, 141).

[68] Zeuch, D., F. Hassler, J. J. Slim, and D. P. DiVincenzo, "Exact rotating wave approximation", Ann. Phys. **423**, 168327 (2020) (cit. on pp. 26, 57).

[69] Nalbach, P. and V. Leyton, "Magnus expansion for a chirped quantum two-level system", Phys. Rev. A **98**, 023855 (2018) (cit. on p. 26).

[70] Ribeiro, H., A. Baksic, and A. A. Clerk, "Systematic magnus-based approach for suppressing leakage and nonadiabatic errors in quantum dynamics", Phys. Rev. X **7**, 011021 (2017) (cit. on p. 26).

[71] Setiawan, F., P. Groszkowski, H. Ribeiro, and A. A. Clerk, "Analytic design of accelerated adiabatic gates in realistic qubits: general theory and applications to superconducting circuits", PRX Quantum **2**, 030306 (2021) (cit. on p. 26).

[72] Ramsey, N. F., "A molecular beam resonance method with separated oscillating fields", Phys. Rev. **78**, 695 (1950) (cit. on p. 28).

[73] Wangsness, R. K. and F. Bloch, "The dynamical theory of nuclear induction", Phys. Rev. **89**, 728 (1953) (cit. on p. 29).

[74] Redfield, A. G., "The theory of relaxation processes", Adv. Magn. Opt. Reson. **1**, 1 (1965) (cit. on p. 29).

[75] Ithier, G., E. Collin, P. Joyez, P. J. Meeson, D. Vion, D. Esteve, F. Chiarello, A. Shnirman, Y. Makhlin, J. Schriefl, and G. Schön, "Decoherence in a superconducting quantum bit circuit", Phys. Rev. B **72**, 134519 (2005) (cit. on pp. 29–31, 33, 37, 89, 91).

[76] Shnirman, A., Y. Makhlin, and G. Schön, "Noise and decoherence in quantum two-level systems", Phys. Scr. **T102**, 147 (2002) (cit. on pp. 29, 91).

[77] Martinis, J. M., S. Nam, J. Aumentado, K. M. Lang, and C. Urbina, "Decoherence of a superconducting qubit due to bias noise", Phys. Rev. B **67**, 094510 (2003) (cit. on pp. 29, 91).

[78] Schoelkopf, R. J., A. A. Clerk, S. M. Girvin, K. W. Lehnert, and M. H. Devoret, "Noise and measurement backaction in superconducting circuits: qubits as spectrometers of quantum noise", Proc. SPIE **5115**, 356 (2003) (cit. on pp. 29, 31, 39).

[79] Groszkowski, P., A. Di Paolo, A. L. Grimsmo, A. Blais, D. I. Schuster, A. A. Houck, and J. Koch, "Coherence properties of the 0-$\pi$ qubit", New J. Phys. **20**, 043053 (2018) (cit. on pp. 29, 40, 89, 91).

[80] Clerk, A. A., M. H. Devoret, S. M. Girvin, F. Marquardt, and R. J. Schoelkopf, "Introduction to quantum noise, measurement, and amplification", Rev. Mod. Phys. **82**, 1155 (2010) (cit. on pp. 29, 31–33, 91).

[81] Sakurai, J. J. and J. Napolitano, *Modern quantum mechanics*, 2nd ed. (Cambridge University Press, 2017) Chap. 5, p. 358 (cit. on pp. 31, 151).

[82] Papoulis, A., *Probability, random variables, and stochastic processes* (McGraw-Hill, 1991), p. 115 (cit. on p. 33).

[83] Cottet, A., "Implementation of a quantum bit in a superconducting circuit", PhD thesis (Université Paris 6, 2002) (cit. on p. 33).

[84] Huang, Z., "Noise engineering and mitigation in superconducting circuits", PhD thesis (Northwestern University, 2021) (cit. on p. 33).

[85] Metcalfe, M., E. Boaknin, V. Manucharyan, R. Vijay, I. Siddiqi, C. Rigetti, L. Frunzio, R. J. Schoelkopf, and M. H. Devoret, "Measuring the decoherence of a quantronium qubit with the cavity bifurcation amplifier", Phys. Rev. B **76**, 174516 (2007) (cit. on pp. 34, 37).

[86] Schreier, J. A., A. A. Houck, J. Koch, D. I. Schuster, B. R. Johnson, J. M. Chow, J. M. Gambetta, J. Majer, L. Frunzio, M. H. Devoret, S. M. Girvin, and R. J. Schoelkopf, "Suppressing charge noise decoherence in superconducting charge qubits", Phys. Rev. B **77**, 180502 (2008) (cit. on p. 34).

[87] Bishop, L. S., "Circuit Quantum Electrodynamics", PhD thesis (Yale University, 2010) (cit. on p. 34).

[88] Gyenis, A., A. Di Paolo, J. Koch, A. Blais, A. A. Houck, and D. I. Schuster, "Moving beyond the transmon: noise-protected superconducting quantum circuits", PRX Quantum **2**, 030101 (2021) (cit. on pp. 35, 37).

[89] Dempster, J. M., B. Fu, D. G. Ferguson, D. I. Schuster, and J. Koch, "Understanding degenerate ground states of a protected quantum circuit in the presence of disorder", Phys. Rev. B **90**, 094518 (2014) (cit. on pp. 35, 40).

[90] Zhu, G. and J. Koch, "Asymptotic expressions for charge-matrix elements of the fluxonium circuit", Phys. Rev. B **87**, 144518 (2013) (cit. on pp. 36, 127).

[91] Earnest, N., S. Chakram, Y. Lu, N. Irons, R. K. Naik, N. Leung, L. Ocola, D. A. Czaplewski, B. Baker, J. Lawrence, J. Koch, and D. I. Schuster, "Realization of a $\Lambda$ system with metastable states of a capacitively shunted fluxonium", Phys. Rev. Lett. **120**, 150504 (2018) (cit. on pp. 36, 37, 120).

[92] Lin, Y.-H., L. B. Nguyen, N. Grabon, J. San Miguel, N. Pankratova, and V. E. Manucharyan, "Demonstration of protection of a superconducting qubit from energy decay", Phys. Rev. Lett. **120**, 150503 (2018) (cit. on pp. 36, 37, 120).

[93] Masluk, N. A., "Reducing the losses of the fluxonium artificial atom", PhD thesis (Yale University, 2012) (cit. on p. 39).

[94] Smith, W. C., A. Kou, X. Xiao, U. Vool, and M. H. Devoret, "Superconducting circuit protected by two-Cooper-pair tunneling", Npj Quantum Inf. **6**, 8 (2020) (cit. on pp. 39, 40, 93, 94).

[95] Pop, I. M., K. Geerlings, G. Catelani, R. J. Schoelkopf, L. I. Glazman, and M. H. Devoret, "Coherent suppression of electromagnetic dissipation due to superconducting quasiparticles", Nature **508**, 369 (2014) (cit. on pp. 39, 93, 94).

[96] Vool, U. and M. Devoret, "Introduction to quantum electromagnetic circuits", Int. J. Circuit Theory Appl. **45**, 897 (2017) (cit. on pp. 39, 61, 120).

[97] Devoret, M. H., "Quantum fluctuations in electrical circuits", in *Quantum Fluctuations: Les Houches Session LXIII*, edited by S. Reynaud, E. Giacobino, and J. Zinn-Justin (Elsevier, Amsterdam, 1997), pp. 351–386 (cit. on pp. 39, 61).

[98] Burkard, G., R. H. Koch, and D. P. DiVincenzo, "Multilevel quantum description of decoherence in superconducting qubits", Phys. Rev. B **69**, 064503 (2004) (cit. on p. 39).

[99] You, X., "Noise-protected superconducting quantum circuits", PhD thesis (Northwestern University, 2021) (cit. on p. 39).

[100] Ficheux, Q., L. B. Nguyen, A. Somoroff, H. Xiong, K. N. Nesterov, M. G. Vavilov, and V. E. Manucharyan, "Fast logic with slow qubits: microwave-activated controlled-Z gate on low-frequency fluxoniums", Phys. Rev. X **11**, 021026 (2021) (cit. on pp. 40, 117, 118, 132).

[101] Weiss, D. K., H. Zhang, C. Ding, Y. Ma, D. I. Schuster, and J. Koch, "Fast high-fidelity gates for galvanically-coupled fluxonium qubits using strong flux modulation", arXiv:2207.03971 (2022) (cit. on pp. 40, 191).

[102] Brooks, P., A. Kitaev, and J. Preskill, "Protected gates for superconducting qubits", Phys. Rev. A **87**, 052306 (2013) (cit. on pp. 40, 42, 158).

[103] Paolo, A. D., A. L. Grimsmo, P. Groszkowski, J. Koch, and A. Blais, "Control and coherence time enhancement of the 0–$\pi$ qubit", New J. Phys. **21**, 043002 (2019) (cit. on pp. 40, 42, 158).

[104] Kapit, E., "The upside of noise: engineered dissipation as a resource in superconducting circuits", Quantum Sci. Technol. **2**, 033002 (2017) (cit. on p. 42).

[105] Kerman, A. J., "Efficient numerical simulation of complex Josephson quantum circuits", arXiv:2010.14929 (2020) (cit. on p. 45).

[106] Chitta, S. P., T. Zhao, Z. Huang, I. Mondragon-Shem, and J. Koch, "Computer-aided quantization and numerical analysis of superconducting circuits", arXiv:2206.08320 (2022) (cit. on p. 45).

[107] Ding, D., H.-S. Ku, Y. Shi, and H.-H. Zhao, "Free-mode removal and mode decoupling for simulating general superconducting quantum circuits", Phys. Rev. B **103**, 174501 (2021) (cit. on p. 45).

[108] Lee, M., M.-S. Choi, and M. Y. Choi, "Quantum phase transitions and persistent currents in Josephson-junction ladders", Phys. Rev. B **68**, 144506 (2003) (cit. on pp. 45, 62, 86).

[109] Weiss, D. K., A. C. Y. Li, D. G. Ferguson, and J. Koch, "Spectrum and coherence properties of the current-mirror qubit", Phys. Rev. B **100**, 224507 (2019) (cit. on pp. 45, 95, 111, 112).

[110] Di Paolo, A., T. E. Baker, A. Foley, D. Sénéchal, and A. Blais, "Efficient modeling of superconducting quantum circuits with tensor networks", Npj Quantum Inf. **7**, 11 (2021) (cit. on p. 45).

[111] Weiss, D. K., W. DeGottardi, J. Koch, and D. G. Ferguson, "Variational tight-binding method for simulating large superconducting circuits", Phys. Rev. Research **3**, 033244 (2021) (cit. on p. 45).

[112] Slater, J. C. and G. F. Koster, "Simplified LCAO method for the periodic potential problem", Phys. Rev. **94**, 1498 (1954) (cit. on pp. 46, 49).

[113] Löwdin, P. O., "On the non-orthogonality problem connected with the use of atomic wave functions in the theory of molecules and crystals", J. Chem. Phys. **18**, 365 (1950) (cit. on p. 46).

[114] Orlando, T. P., J. E. Mooij, L. Tian, C. H. van der Wal, L. S. Levitov, S. Lloyd, and J. J. Mazo, "Superconducting persistent-current qubit", Phys. Rev. B **60**, 15398 (1999) (cit. on pp. 46, 107, 108).

[115] Chirolli, L. and G. Burkard, "Full control of qubit rotations in a voltage-biased superconducting flux qubit", Phys. Rev. B **74**, 174510 (2006) (cit. on pp. 46, 47, 107).

[116] Tiwari, R. P. and D. Stroud, "Suppression of tunneling in a superconducting persistent-current qubit", Phys. Rev. B **76**, 220505(R) (2007) (cit. on pp. 46, 107).

[117] Chirolli, L. and J. E. Moore, "Enhanced coherence in superconducting circuits via band engineering", Phys. Rev. Lett. **126**, 187701 (2021) (cit. on p. 46).

[118] Mizel, A. and Y. Yanay, "Right-sizing fluxonium against charge noise", Phys. Rev. B **102**, 014512 (2020) (cit. on p. 46).

[119] Girvin, S. M., "Circuit QED: superconducting qubits coupled to microwave photons", in *Quantum Machines: Measurement and Control of Engineered Quantum Systems: Lecture Notes of the Les Houches Summer School: Volume 96, July 2011* (Oxford University Press, 2014) (cit. on p. 47).

[120] Minev, Z. K., Z. Leghtas, S. O. Mundhada, L. Christakis, I. M. Pop, and M. H. Devoret, "Energy-participation quantization of Josephson circuits", arXiv:2010.00620 (2020) (cit. on p. 47).

[121] Rajabzadeh, T., Z. Wang, N. Lee, T. Makihara, Y. Guo, and A. H. Safavi-Naeini, "Analysis of arbitrary superconducting quantum circuits accompanied by a Python package: SQcircuit", arXiv:2206.08319 (2022) (cit. on p. 47).

[122] Goldstein, H., *Classical mechanics* (Addison-Wesley, 1980), pp. 250–253 (cit. on p. 48).

[123] Bishop, R. F., M. F. Flynn, M. C. Boscá, and R. Guardiola, "Paths to optimization in the multistate Rayleigh-Ritz variational method: applications to the double-well quantum anharmonic oscillator", Phys. Rev. A **40**, 6154 (1989) (cit. on pp. 50, 104, 115).

[124] MacDonald, J. K. L., "Successive approximations by the Rayleigh-Ritz variation method", Phys. Rev. **43**, 830 (1933) (cit. on pp. 50, 115).

[125] Rabi, I. I., "Space quantization in a gyrating magnetic field", Phys. Rev. **51**, 652 (1937) (cit. on p. 53).

[126] Feynman, R. P., "An operator calculus having applications in quantum electrodynamics", Phys. Rev. **84**, 108 (1951) (cit. on p. 54).

[127] Baker, H. F., "Alternants and continuous groups", Proc. London Math. Soc. (2) **3**, 24 (1905) (cit. on pp. 55, 100, 178).

[128] Campbell, J. E., "On a law of combination of operators bearing on the theory of continuous transformation groups", Proc. London Math. Soc. (1) **28**, 381 (1897) (cit. on pp. 55, 100, 178).

[129] Campbell, J. E., "On a law of combination of operators", Proc. London Math. Soc. (1) **29**, 14 (1897) (cit. on pp. 55, 100, 178).

[130] Hausdorff, F., "Die symbolische Exponentialformel in der Gruppentheorie", Leipz. Ber. **58**, 19 (1906) (cit. on pp. 55, 100, 178).

[131] Rol, M. A., F. Battistel, F. K. Malinowski, C. C. Bultink, B. M. Tarasinski, R. Vollmer, N. Haider, N. Muthusubramanian, A. Bruno, B. M. Terhal, and L. DiCarlo, "Fast, high-fidelity conditional-phase gate exploiting leakage interference in weakly anharmonic superconducting qubits", Phys. Rev. Lett. **123**, 120502 (2019) (cit. on pp. 56, 139).

[132] Choi, M.-S., M. Y. Choi, T. Choi, and S.-I. Lee, "Cotunneling transport and quantum phase transitions in coupled Josephson-junction chains with charge frustration", Phys. Rev. Lett. **81**, 4240 (1998) (cit. on p. 62).

[133] Schrieffer, J. R. and P. A. Wolff, "Relation between the Anderson and Kondo Hamiltonians", Phys. Rev. **149**, 491 (1966) (cit. on pp. 63, 124–126, 177).

[134] Shavitt, I. and L. T. Redmon, "Quasidegenerate perturbation theories. A canonical van Vleck formalism and its relationship to other approaches", J. Chem. Phys. **73**, 5711 (1980) (cit. on p. 63).

[135] Winkler, R., *Spin-Orbit Coupling Effects in Two-Dimensional Electron and Hole Systems* (Springer, 2003), pp. 201–205 (cit. on pp. 63, 124–126, 134, 177).

[136] Cohen-Tannoudji, C., J. Dupont-Roc, and G. Grynberg, *Atom-photon interactions* (John Wiley & Sons, Ltd, 1998) Chap. 1, pp. 38–48 (cit. on pp. 63, 124–126, 177, 180).

[137] Bravyi, S., D. P. DiVincenzo, and D. Loss, "Schrieffer-Wolff transformation for quantum many-body systems", Ann. Phys. **326**, 2793 (2011) (cit. on pp. 63, 78, 124, 177).

[138] Kuhn, H. W., "The Hungarian method for the assignment problem", Nav. Res. Logist. **2**, 83 (1955) (cit. on p. 71).

[139] Karp, R. M. and S.-Y. R. Li, "Two special cases of the assignment problem", Discrete Math. **13**, 129 (1975) (cit. on pp. 71, 74).

[140] Werman, M., S. Peleg, R. Melter, and T. Y. Kong, "Bipartite graph matching for points on a line or a circle", J. Algorithms **7**, 277 (1986) (cit. on pp. 71, 74, 76).

[141] Gradshteyn, I. S. and I. M. Ryzhik, *Table of integrals, series, and products*, 6th (Academic Press, San Diego, 2000), p. 4 (cit. on p. 79).

[142] Schollwöck, U., "The density-matrix renormalization group", Rev. Mod. Phys. **77**, 259 (2005) (cit. on p. 86).

[143] White, S. R., "Density-matrix formulation for quantum renormalization groups", Phys. Rev. Lett. **69**, 2863 (1992) (cit. on p. 86).

[144] White, S. R., "Density-matrix algorithms for quantum renormalization groups", Phys. Rev. B **48**, 10345 (1993) (cit. on p. 86).

[145] Fishman, M., S. R. White, and E. M. Stoudenmire, "The ITensor software library for tensor network calculations", arXiv:2007.14822 (2020) (cit. on pp. 87, 112).

[146] Isserlis, L., "On a formula for the product-moment coefficient of any order of a normal frequency distribution in any number of variables", Biometrika **12**, 134 (1918) (cit. on p. 90).

[147] Yan, F., S. Gustavsson, A. Kamal, J. Birenbaum, A. P. Sears, D. Hover, T. J. Gudmundsen, D. Rosenberg, G. Samach, S. Weber, J. L. Yoder, T. P. Orlando, J. Clarke, A. J. Kerman, and W. D. Oliver, "The flux qubit revisited to enhance coherence and reproducibility", Nat. Commun. **7**, 12964 (2016) (cit. on p. 91).

[148] Hutchings, M. D., J. B. Hertzberg, Y. Liu, N. T. Bronn, G. A. Keefe, M. Brink, J. M. Chow, and B. L. T. Plourde, "Tunable superconducting qubits with flux-independent coherence", Phys. Rev. Applied **8**, 044003 (2017) (cit. on pp. 91, 130).

[149] Quintana, C. M., Y. Chen, D. Sank, A. G. Petukhov, T. C. White, D. Kafri, B. Chiaro, A. Megrant, R. Barends, B. Campbell, Z. Chen, A. Dunsworth, A. G. Fowler, R. Graff, E. Jeffrey, J. Kelly, E. Lucero, J. Y. Mutus, M. Neeley, C. Neill, P. J. J. O'Malley, P. Roushan, A. Shabani, V. N. Smelyanskiy, A. Vainsencher, J. Wenner, H. Neven, and J. M. Martinis, "Observation of classical-quantum crossover of $1/f$ flux noise and its paramagnetic temperature dependence", Phys. Rev. Lett. **118**, 057702 (2017) (cit. on p. 91).

[150] Zorin, A. B., F.-J. Ahlers, J. Niemeyer, T. Weimann, H. Wolf, V. A. Krupenin, and S. V. Lotkhov, "Background charge noise in metallic single-electron tunneling devices", Phys. Rev. B **53**, 13682 (1996) (cit. on p. 91).

[151] Van Harlingen, D. J., T. L. Robertson, B. L. T. Plourde, P. A. Reichardt, T. A. Crane, and J. Clarke, "Decoherence in Josephson-junction qubits due to critical-current fluctuations", Phys. Rev. B **70**, 064517 (2004) (cit. on p. 91).

[152] Wang, C., C. Axline, Y. Y. Gao, T. Brecht, Y. Chu, L. Frunzio, M. H. Devoret, and R. J. Schoelkopf, "Surface participation and dielectric loss in superconducting qubits", Appl. Phys. Lett. **107**, 162601 (2015) (cit. on p. 93).

[153] Babusci, D., G. Dattoli, and M. Quattromini, "On integrals involving Hermite polynomials", Appl. Math. Lett. **25**, 1157 (2012) (cit. on p. 96).

[154] Javanainen, J., "Noncondensate atoms in a trapped Bose gas", Phys. Rev. A **54**, R3722 (1996) (cit. on pp. 97, 101).

[155] Bogoliubov, N. N., "On a new method in the theory of superconductivity", Nuovo Cimento **7**, 794 (1958) (cit. on p. 97).

[156] Valatin, J. G., "Comments on the theory of superconductivity", Nuovo Cimento **7**, 843 (1958) (cit. on p. 97).

[157] Balian, R. and E. Brezin, "Nonunitary Bogoliubov transformations and extension of Wick's theorem", Nuovo Cimento B **64**, 37 (1969) (cit. on pp. 98, 101).

[158] Zhang, J. M. and R. X. Dong, "Exact diagonalization: the Bose–Hubbard model as an example", Eur. J. Phys. **31**, 591 (2010) (cit. on pp. 99, 182).

[159] Wang, X.-B., S.-X. Yu, and Y.-D. Zhang, "Linear quantum transformation and normal product calculation of boson exponential quadratic operators", J. Phys. A **27**, 6563 (1994) (cit. on p. 101).

[160] Mehta, C. L., "Classical functions corresponding to given quantum operators", J. Phys. A **1**, 385 (1968) (cit. on p. 101).

[161] Ma, X. and W. Rhodes, "Multimode squeeze operators and squeezed states", Phys. Rev. A **41**, 4625 (1990) (cit. on p. 101).

[162] Hong-yi, F., "Normally ordering some multimode exponential operators by virtue of the IWOP technique", J. Phys. A **23**, 1833 (1990) (cit. on pp. 101, 102).

[163] Zhang, W.-M., D. H. Feng, and R. Gilmore, "Coherent states: theory and some applications", Rev. Mod. Phys. **62**, 867 (1990) (cit. on p. 101).

[164] Reed, A. E., L. A. Curtiss, and F. Weinhold, "Intermolecular interactions from a natural bond orbital, donor-acceptor viewpoint", Chem. Rev. **88**, 899 (1988) (cit. on p. 103).

[165] Lu, T. and F. Chen, "Multiwfn: a multifunctional wavefunction analyzer", J. Comput. Chem. **33**, 580 (2012) (cit. on p. 103).

[166] Löwdin, P. O., "Quantum theory of cohesive properties of solids", Adv. Phys. **5**, 1 (1956) (cit. on pp. 103, 104).

[167] Löwdin, P. O., "Group algebra, convolution algebra, and applications to quantum mechanics", Rev. Mod. Phys. **39**, 259 (1967) (cit. on pp. 103, 104, 115).

[168] Löwdin, P. O., "On the nonorthogonality problem", Adv. Quantum Chem. **5**, 185 (1970) (cit. on pp. 103, 104).

[169] You, J. Q., X. Hu, S. Ashhab, and F. Nori, "Low-decoherence flux qubit", Phys. Rev. B **75**, 140515(R) (2007) (cit. on pp. 107, 108).

[170] Xiong, H., Q. Ficheux, A. Somoroff, L. B. Nguyen, E. Dogan, D. Rosenstock, C. Wang, K. N. Nesterov, M. G. Vavilov, and V. E. Manucharyan, "Arbitrary controlled-phase gate on fluxonium qubits using differential ac stark shifts", Phys. Rev. Research **4**, 023040 (2022) (cit. on p. 117).

[171] Bao, F., H. Deng, D. Ding, R. Gao, X. Gao, C. Huang, X. Jiang, H.-S. Ku, Z. Li, X. Ma, X. Ni, J. Qin, Z. Song, H. Sun, C. Tang, T. Wang, F. Wu, T. Xia, W. Yu, F. Zhang, G. Zhang, X. Zhang,

J. Zhou, X. Zhu, Y. Shi, J. Chen, H.-H. Zhao, and C. Deng, “Fluxonium: an alternative qubit platform for high-fidelity operations”, Phys. Rev. Lett. **129**, 010502 (2022) (cit. on p. 117).

[172] Moskalenko, I. N., I. A. Simakov, N. N. Abramov, A. A. Grigorev, D. O. Moskalev, A. A. Pishchimova, N. S. Smirnov, E. V. Zikiy, I. A. Rodionov, and I. S. Besedin, “High fidelity two-qubit gates on fluxoniums using a tunable coupler”, arXiv:2203.16302 (2022) (cit. on p. 117).

[173] Chen, Y., K. N. Nesterov, V. E. Manucharyan, and M. G. Vavilov, “Fast flux entangling gate for fluxonium circuits”, arXiv:2110.00632v1 (2021) (cit. on pp. 117, 118).

[174] Nesterov, K. N., Q. Ficheux, V. E. Manucharyan, and M. G. Vavilov, “Proposal for entangling gates on fluxonium qubits via a two-photon transition”, PRX Quantum **2**, 020345 (2021) (cit. on pp. 117, 118, 153, 191).

[175] Moskalenko, I. N., I. S. Besedin, I. A. Simakov, and A. V. Ustinov, “Tunable coupling scheme for implementing two-qubit gates on fluxonium qubits”, arXiv:2107.11550 (2021) (cit. on p. 117).

[176] Nesterov, K. N., C. Wang, V. E. Manucharyan, and M. G. Vavilov, “Controlled-NOT gates for fluxonium qubits via selective darkening of transitions”, arXiv:2202.04583 (2022) (cit. on pp. 117, 118).

[177] Cai, T. Q., J. H. Wang, Z. L. Wang, X. Y. Han, Y. K. Wu, Y. P. Song, and L. M. Duan, “All-microwave nonadiabatic multiqubit geometric phase gate for superconducting qubits”, Phys. Rev. Research **3**, 043071 (2021) (cit. on p. 117).

[178] Nesterov, K. N., I. V. Pechenezhskiy, C. Wang, V. E. Manucharyan, and M. G. Vavilov, “Microwave-activated controlled-Z gate for fixed-frequency fluxonium qubits”, Phys. Rev. A **98**, 030301(R) (2018) (cit. on pp. 117, 118, 129).

[179] Nguyen, L. B., G. Koolstra, Y. Kim, A. Morvan, T. Chistolini, S. Singh, K. N. Nesterov, C. Jünger, L. Chen, Z. Pedramrazi, B. K. Mitchell, J. M. Kreikebaum, S. Puri, D. I. Santiago, and I. Siddiqi, “Scalable high-performance fluxonium quantum processor”, arXiv:2201.09374 (2022) (cit. on p. 117).

[180] Grajcar, M., Y.-x. Liu, F. Nori, and A. M. Zagoskin, “Switchable resonant coupling of flux qubits”, Phys. Rev. B **74**, 172505 (2006) (cit. on p. 118).

[181] Brink, A. M. van den, A. J. Berkley, and M. Yalowsky, “Mediated tunable coupling of flux qubits”, New J. Phys. **7**, 230 (2005) (cit. on p. 118).

[182] Niskanen, A. O., Y. Nakamura, and J.-S. Tsai, “Tunable coupling scheme for flux qubits at the optimal point”, Phys. Rev. B **73**, 094506 (2006) (cit. on p. 118).

[183] Ploeg, S. H. W. van der, A. Izmalkov, A. M. van den Brink, U. Hübner, M. Grajcar, E. Il’ichev, H.-G. Meyer, and A. M. Zagoskin, “Controllable coupling of superconducting flux qubits”, Phys. Rev. Lett. **98**, 057004 (2007) (cit. on p. 118).

[184] Niskanen, A. O., K. Harrabi, F. Yoshihara, Y. Nakamura, S. Lloyd, and J. S. Tsai, "Quantum coherent tunable coupling of superconducting qubits", Science **316**, 723 (2007) (cit. on p. 118).

[185] Peruzzo, M., F. Hassani, G. Szep, A. Trioni, E. Redchenko, M. Žemlička, and J. M. Fink, "Geometric superinductance qubits: controlling phase delocalization across a single Josephson junction", PRX Quantum **2**, 040341 (2021) (cit. on p. 118).

[186] Kou, A., W. C. Smith, U. Vool, R. T. Brierley, H. Meier, L. Frunzio, S. M. Girvin, L. I. Glazman, and M. H. Devoret, "Fluxonium-based artificial molecule with a tunable magnetic moment", Phys. Rev. X **7**, 031037 (2017) (cit. on p. 118).

[187] McKay, D. C., C. J. Wood, S. Sheldon, J. M. Chow, and J. M. Gambetta, "Efficient $Z$ gates for quantum computing", Phys. Rev. A **96**, 022330 (2017) (cit. on p. 120).

[188] Chen, J., D. Ding, C. Huang, and Q. Ye, "Compiling arbitrary single-qubit gates via the phase-shifts of microwave pulses", arXiv:2105.02398 (2021) (cit. on p. 120).

[189] Lucero, E., J. Kelly, R. C. Bialczak, M. Lenander, M. Mariantoni, M. Neeley, A. D. O'Connell, D. Sank, H. Wang, M. Weides, J. Wenner, T. Yamamoto, A. N. Cleland, and J. M. Martinis, "Reduced phase error through optimized control of a superconducting qubit", Phys. Rev. A **82**, 042339 (2010) (cit. on p. 120).

[190] Zhu, G., D. G. Ferguson, V. E. Manucharyan, and J. Koch, "Circuit QED with fluxonium qubits: theory of the dispersive regime", Phys. Rev. B **87**, 024510 (2013) (cit. on pp. 127, 185).

[191] You, X., J. A. Sauls, and J. Koch, "Circuit quantization in the presence of time-dependent external flux", Phys. Rev. B **99**, 174512 (2019) (cit. on p. 132).

[192] Bryon, J., D. K. Weiss, X. You, S. Sussman, X. Croot, Z. Huang, J. Koch, and A. Houck, "Experimental verification of the treatment of time-dependent flux in circuit quantization", arXiv:2208.03738 (2022) (cit. on p. 132).

[193] Krantz, P., M. Kjaergaard, F. Yan, T. P. Orlando, S. Gustavsson, and W. D. Oliver, "A quantum engineer's guide to superconducting qubits", Appl. Phys. Rev. **6**, 021318 (2019) (cit. on p. 138).

[194] Wu, Y. and X. Yang, "Strong-coupling theory of periodically driven two-level systems", Phys. Rev. Lett. **98**, 013601 (2007) (cit. on p. 139).

[195] Pedersen, L. H., N. M. Møller, and K. Mølmer, "Fidelity of quantum operations", Phys. Lett. A **367**, 47 (2007) (cit. on pp. 141, 153, 191).

[196] Groszkowski, P. and J. Koch, "scqubits: a Python package for superconducting qubits", Quantum **5**, 583 (2021) (cit. on p. 141).

[197] Johansson, J. R., P. D. Nation, and F. Nori, "QuTiP: An open-source Python framework for the dynamics of open quantum systems", Comput. Phys. Commun. **183**, 1760 (2012) (cit. on pp. 141, 153).

[198] Johansson, J. R., P. D. Nation, and F. Nori, "QuTiP 2: A Python framework for the dynamics of open quantum systems", Comput. Phys. Commun. **184**, 1234 (2013) (cit. on pp. 141, 153, 191).

[199] Poletto, S., J. M. Gambetta, S. T. Merkel, J. A. Smolin, J. M. Chow, A. D. Córcoles, G. A. Keefe, M. B. Rothwell, J. R. Rozen, D. W. Abraham, C. Rigetti, and M. Steffen, "Entanglement of two superconducting qubits in a waveguide cavity via monochromatic two-photon excitation", Phys. Rev. Lett. **109**, 240505 (2012) (cit. on p. 145).

[200] Vedral, V., M. B. Plenio, M. A. Rippin, and P. L. Knight, "Quantifying entanglement", Phys. Rev. Lett. **78**, 2275 (1997) (cit. on p. 145).

[201] Huang, C., T. Wang, F. Wu, D. Ding, Q. Ye, L. Kong, F. Zhang, X. Ni, Z. Song, Y. Shi, H.-H. Zhao, C. Deng, and J. Chen, "Quantum instruction set design for performance", arXiv:2105.06074 (2021) (cit. on p. 146).

[202] Mi, X., P. Roushan, C. Quintana, S. Mandrà, J. Marshall, C. Neill, F. Arute, K. Arya, J. Atalaya, R. Babbush, J. C. Bardin, R. Barends, J. Basso, A. Bengtsson, S. Boixo, A. Bourassa, M. Broughton, B. B. Buckley, D. A. Buell, B. Burkett, N. Bushnell, Z. Chen, B. Chiaro, R. Collins, W. Courtney, S. Demura, A. R. Derk, A. Dunsworth, D. Eppens, C. Erickson, E. Farhi, A. G. Fowler, B. Foxen, C. Gidney, M. Giustina, J. A. Gross, M. P. Harrigan, S. D. Harrington, J. Hilton, A. Ho, S. Hong, T. Huang, W. J. Huggins, L. B. Ioffe, S. V. Isakov, E. Jeffrey, Z. Jiang, C. Jones, D. Kafri, J. Kelly, S. Kim, A. Kitaev, P. V. Klimov, A. N. Korotkov, F. Kostritsa, D. Landhuis, P. Laptev, E. Lucero, O. Martin, J. R. McClean, T. McCourt, M. McEwen, A. Megrant, K. C. Miao, M. Mohseni, S. Montazeri, W. Mruczkiewicz, J. Mutus, O. Naaman, M. Neeley, M. Newman, M. Y. Niu, T. E. O'Brien, A. Opremcak, E. Ostby, B. Pato, A. Petukhov, N. Redd, N. C. Rubin, D. Sank, K. J. Satzinger, V. Shvarts, D. Strain, M. Szalay, M. D. Trevithick, B. Villalonga, T. White, Z. J. Yao, P. Yeh, A. Zalcman, H. Neven, I. Aleiner, K. Kechedzhi, V. Smelyanskiy, and Y. Chen, "Information scrambling in quantum circuits", Science **374**, 1479 (2021) (cit. on p. 146).

[203] Arute, F., K. Arya, R. Babbush, D. Bacon, J. C. Bardin, R. Barends, S. Boixo, M. Broughton, B. B. Buckley, D. A. Buell, B. Burkett, N. Bushnell, Y. Chen, Z. Chen, B. Chiaro, R. Collins, W. Courtney, S. Demura, A. Dunsworth, E. Farhi, A. Fowler, B. Foxen, C. Gidney, M. Giustina, R. Graff, S. Habegger, M. P. Harrigan, A. Ho, S. Hong, T. Huang, W. J. Huggins, L. Ioffe, S. V. Isakov, E. Jeffrey, Z. Jiang, C. Jones, D. Kafri, K. Kechedzhi, J. Kelly, S. Kim, P. V. Klimov, A. Korotkov, F. Kostritsa, D. Landhuis, P. Laptev, M. Lindmark, E. Lucero, O. Martin, J. M. Martinis, J. R. McClean, M. McEwen, A. Megrant, X. Mi, M. Mohseni, W. Mruczkiewicz, J. Mutus, O. Naaman, M. Neeley, C. Neill, H. Neven, M. Y. Niu, T. E. O'Brien, E. Ostby, A. Petukhov, H. Putterman, C. Quintana, P. Roushan, N. C. Rubin, D. Sank, K. J. Satzinger, V. Smelyanskiy, D. Strain, K. J. Sung, M. Szalay, T. Y. Takeshita, A. Vainsencher, T. White, N.

Wiebe, Z. J. Yao, P. Yeh, and A. Zalcman, “Hartree-Fock on a superconducting qubit quantum computer”, Science **369**, 1084 (2020) (cit. on p. 146).

[204] Nielsen, M. A. and I. L. Chuang, *Quantum computation and quantum information: 10th anniversary edition* (Cambridge University Press, 2010) Chap. 8 (cit. on pp. 153, 191, 192).

[205] Nielsen, M. A., “A simple formula for the average gate fidelity of a quantum dynamical operation”, Phys. Lett. A **303**, 249 (2002) (cit. on pp. 153, 191).

[206] Horodecki, M., P. Horodecki, and R. Horodecki, “General teleportation channel, singlet fraction, and quasidistillation”, Phys. Rev. A **60**, 1888 (1999) (cit. on pp. 153, 191).

[207] Christensen, B. G., C. D. Wilen, A. Opremcak, J. Nelson, F. Schlenker, C. H. Zimonick, L. Faoro, L. B. Ioffe, Y. J. Rosen, J. L. DuBois, B. L. T. Plourde, and R. McDermott, “Anomalous charge noise in superconducting qubits”, Phys. Rev. B **100**, 140503(R) (2019) (cit. on p. 156).

[208] Pechenezhskiy, I. V., R. A. Mencia, L. B. Nguyen, Y.-H. Lin, and V. E. Manucharyan, “The superconducting quasicharge qubit”, Nature **585**, 368 (2020) (cit. on p. 158).

[209] Krinner, S., S. Lazar, A. Remm, C. Andersen, N. Lacroix, G. Norris, C. Hellings, M. Gabureac, C. Eichler, and A. Wallraff, “Benchmarking coherent errors in controlled-phase gates due to spectator qubits”, Phys. Rev. Applied **14**, 024042 (2020) (cit. on p. 159).

[210] Žitko, R., “Sneg – Mathematica package for symbolic calculations with second-quantization-operator expressions”, Comput. Phys. Commun. **182**, 2259 (2011) (cit. on p. 180).

[211] `https://github.com/dkweiss31/Schrieffer-Wolff` (cit. on p. 180).

[212] Majer, J., J. M. Chow, J. M. Gambetta, J. Koch, B. R. Johnson, J. A. Schreier, L. Frunzio, D. I. Schuster, A. A. Houck, A. Wallraff, A. Blais, M. H. Devoret, S. M. Girvin, and R. J. Schoelkopf, “Coupling superconducting qubits via a cavity bus”, Nature **449**, 443 (2007) (cit. on p. 187).

[213] Kershaw, D., “The explicit inverses of two commonly occurring matrices”, Math. Comput. **23**, 189 (1969) (cit. on p. 188).

[214] Meek, D., “The inverses of some matrices deviating slightly from a symmetric, tridiagonal, Toeplitz form”, SIAM J. Numer. Anal. **17**, 39 (1980) (cit. on p. 188).

[215] Chow, J. M., J. M. Gambetta, L. Tornberg, J. Koch, L. S. Bishop, A. A. Houck, B. R. Johnson, L. Frunzio, S. M. Girvin, and R. J. Schoelkopf, “Randomized benchmarking and process tomography for gate errors in a solid-state qubit”, Phys. Rev. Lett. **102**, 090502 (2009) (cit. on p. 191).

# A Schrieffer-Wolff transformation

In this appendix we derive the Schrieffer-Wolff transformation [14, 133, 135, 136, 137] used extensively throughout this thesis. We follow closely the derivation presented by Bravyi, DiVincenzo and Loss [137] which lends itself to a computer algebra implementation. We present associated Mathematica ® code in Sec. A.2, along with a few selected examples.

## A.1 Analytical Schrieffer-Wolff transformation

Consider the Hamiltonian $H = H_0 + \epsilon V$, where we will treat $\epsilon V$ as a small perturbation on $H_0$. We take the eigenstates $|i\rangle$ and eigenenergies $E_i$ of $H_0$ as known, $H_0|i\rangle = E_i|i\rangle$. A powerful feature of the Schrieffer-Wolff transformation is that it can handle (near) degeneracies. At the outset, we specify the (near-)degenerate subspace(s) spanned by sets of eigenstates from $H_0$. Once this is done, all energy denominators are energy differences between states in different subspaces and thus cannot approach zero (provided that the perturbative treatment itself is valid).

We consider a degenerate subspace defined by a projector $P$ (typically the "low-energy" subspace) along with the complementary subspace defined by the projector $Q = \mathbb{1} - P$ (the "high-energy" subspace). The purpose of the Schrieffer-Wolff transformation is to perturbatively decouple these subspaces to obtain a description of the physics entirely within the low-energy subspace. We introduce a unitary transformation $e^{-S}$ that block diagonalizes the Hamiltonian $H$, specified by an anti-hermitian and block off diagonal generator $S$ [133, 136]. The effective Hamiltonian in the low-energy subspace is then

$$H_{\text{eff}} = Pe^{S}(H_0 + \epsilon V)e^{-S}P. \tag{A.1}$$

Before proceeding, we introduce the notation $\hat{Y}(X) = [Y, X]$ describing the adjoint action of the operator $Y$ on $X$. This notation allows for a compact expression of the unitary transformation

$$\exp(\hat{S})(H_0 + \epsilon V) = \exp(S)(H_0 + \epsilon V)\exp(-S). \tag{A.2}$$

This equality is based on the Baker-Campbell-Hausdorff expansion [14, 127, 128, 129, 130]

$$\exp(S)H\exp(-S) = \sum_{n=0}^{\infty} \frac{1}{n!}(\hat{S})^n(H). \tag{A.3}$$

Splitting the right-hand side of Eq. (A.2) into block-diagonal and block-off-diagonal components, we obtain

$$\exp(\hat{S})(H_0 + \epsilon V) = \cosh(\hat{S})(H_0 + \epsilon V_{\mathsf{d}}) + \sinh(\hat{S})(\epsilon V_{\mathsf{od}}) \tag{A.4}$$

$$+ \cosh(\hat{S})(\epsilon V_{\mathsf{od}}) + \sinh(\hat{S})(H_0 + \epsilon V_{\mathsf{d}}), \tag{A.5}$$

where $V_{\mathsf{d}} = PVP + QVQ$ and $V_{\mathsf{od}} = PVQ + QVP$. Because the generator is block off diagonal, the second line of Eq. (A.4) must be zero

$$\cosh(\hat{S})(\epsilon V_{\mathsf{od}}) + \sinh(\hat{S})(H_0 + \epsilon V_{\mathsf{d}}) = 0. \tag{A.6}$$

Multiplying from the left by $\hat{S}/\sinh(\hat{S})$ (which is defined by its Taylor expansion and well behaved for small $S$) we find

$$\hat{S}\coth(\hat{S})(\epsilon V_{\mathsf{od}}) + \hat{S}(H_0 + \epsilon V_{\mathsf{d}}) = 0. \tag{A.7}$$

To help solve this equation for $S$ we introduce the superoperator

$$\mathcal{L}(X) = \sum_{ij} \frac{\langle i|\mathcal{O}(X)|j\rangle}{E_i - E_j}|i\rangle\langle j|, \tag{A.8}$$

where $\mathcal{O}(X) = PXQ + QXP$. Applying this superoperator to Eq. (A.7) yields

$$S = \mathcal{L}\hat{S}(\epsilon V_{\mathsf{d}}) + \mathcal{L}\hat{S}\coth(\hat{S})(\epsilon V_{\mathsf{od}}), \tag{A.9}$$

noting that $\mathcal{L}\hat{S}(H_0) = \mathcal{L}([S, H_0]) = -\mathcal{O}(S) = -S$. Expanding the generator as $S = \sum_{n=1}^{\infty} \epsilon^n S_n$ ($S_0 = 0$ because $H_0$ is already diagonal) yields

$$\sum_{n=1}^{\infty} \epsilon^n S_n = \mathcal{L}\sum_{n=1}^{\infty} \epsilon^n \hat{S}_n(\epsilon V_{\mathsf{d}}) + \mathcal{L}\sum_{n=0}^{\infty} a_{2n} \left( \sum_{m=1}^{\infty} \epsilon^m \hat{S}_m \right)^{2n} (\epsilon V_{\mathsf{od}}), \tag{A.10}$$

where we have utilized the Taylor expansion

$$\hat{S}\coth(\hat{S})(\epsilon V_{\mathsf{od}}) = \sum_{n=0}^{\infty} a_{2n} (\hat{S})^{2n} (\epsilon V_{\mathsf{od}}). \tag{A.11}$$

The expansion coefficients are $a_n = 2^n B_n / n!$ where the $B_n$ are the Bernoulli numbers. We now proceed by equating the coefficients of terms at each order in $\epsilon$ in Eq. (A.10). This yields a recursive definition for the $S_n$. The first two terms are

$$S_1 = \mathcal{L}(V_{\mathsf{od}}), \tag{A.12}$$

$$S_2 = \mathcal{L}\hat{S}_1(V_{\mathsf{d}}), \tag{A.13}$$

while the higher-order generators are

$$S_n = \mathcal{L}\hat{S}_{n-1}(V_{\mathsf{d}}) + \sum_{j \geq 1} a_{2j} \mathcal{L}\hat{S}^{2j}(V_{\mathsf{od}})_{n-1}, \quad n \geq 3. \tag{A.14}$$

We have defined

$$\hat{S}^k(V_{\mathsf{od}})_m = \sum_{\substack{n_1, \ldots n_k \geq 1, \\ n_1 + \ldots + n_k = m}} \hat{S}_{n_1} \cdots \hat{S}_{n_k}(V_{\mathsf{od}}). \tag{A.15}$$

With the generator in hand we now return to the calculation of the effective Hamiltonian. We

find

$$\begin{aligned}
\exp(\hat{S})(H_0+\epsilon V) &= \cosh(\hat{S})(H_0+\epsilon V_\mathrm{d})+\sinh(\hat{S})(\epsilon V_\mathrm{od}) \\
&= H_0+\epsilon V_\mathrm{d}+[\cosh(\hat{S})-1](H_0+\epsilon V_\mathrm{d})+\sinh(\hat{S})(\epsilon V_\mathrm{od}) \\
&= H_0+\epsilon V_\mathrm{d}+\frac{\cosh(\hat{S})-1}{\tanh(\hat{S})}\tanh(\hat{S})(H_0+\epsilon V_\mathrm{d})+\sinh(\hat{S})(\epsilon V_\mathrm{od}) \\
&= H_0+\epsilon V_\mathrm{d}+\left[-\frac{\cosh(\hat{S})-1}{\tanh\hat{S}}+\sinh(\hat{S})\right](\epsilon V_\mathrm{od}) \\
&= H_0+\epsilon V_\mathrm{d}+\tanh(\hat{S}/2)(\epsilon V_\mathrm{od}).
\end{aligned} \tag{A.16}$$

In the second-to-last equality we have made use of Eq. (A.6) and in the last equality we utilized a standard trigonometric identity. With the Taylor expansion $\tanh(\hat{S}/2)=\sum_{n=1}^{\infty} b_{2n-1}(\hat{S})^{2n-1}$, where $b_{2n-1}=2(2^{2n}-1)B_{2n}/(2n)!$ we obtain

$$H_\mathrm{eff} = PH_0P+P\epsilon V_\mathrm{d}P+\sum_{n=2}^{\infty}\epsilon^n H_{\mathrm{eff},n}, \tag{A.17}$$

$$H_{\mathrm{eff},n} = \sum_{j\geq 1} b_{2j-1}P\hat{S}^{2j-1}(V_\mathrm{od})_{n-1}P. \tag{A.18}$$

We have denoted the effective Hamiltonian at $n^\mathrm{th}$ order by $H_{\mathrm{eff},n}$. As an example, the second-order effective Hamiltonian is

$$H_{\mathrm{eff},2} = \frac{1}{2}P\left[\mathcal{L}(V_\mathrm{od})V_\mathrm{od}-V_\mathrm{od}\mathcal{L}(V_\mathrm{od})\right]P, \tag{A.19}$$

reproducing the known results [14, 136].

## A.2 Computer-algebra implementation

We implement the Schrieffer-Wolff transformation programmatically in Mathematica ® using the SNEG [210] package. We have made the code publicly available on GitHub [211] and additionally describe it below for completeness. We have found this code useful mainly as a means for verifying

analytically derived results. We are certain that the reader can envision more inventive uses of the software.

Import SNEG

```
<< sneg`sneg`;
```

Define the superoperator functions

```
MatrixElementOverListsProj[Op_, PList_, QList_] :=
 Module[{PProj, QProj, bl},
  If[Not[PossibleZeroQ[Op]],
    PProj = PList /. {ket_ -> nc[ket, conj[ket]]};
    QProj = QList /. {ket_ -> nc[ket, conj[ket]]};
    bl = Map[nc[#, QProj] &, Op];
    Return[Total[Outer[nc[#1, #2] &, PProj, bl], 2]],
    Return[0]
    ];
  ]
OffDiagSuperOp[Op_, PList_, QList_] := Module[{},
  Return[MatrixElementOverListsProj[Op, PList, QList]
    + MatrixElementOverListsProj[Op, QList, PList]]
  ]
DiagSuperOp[Op_, PList_, QList_] := Module[{},
  Return[MatrixElementOverListsProj[Op, PList, PList]
    + MatrixElementOverListsProj[Op, QList, QList]]
  ]
LSuperOperator[Op_, H0_, PList_, QList_] :=
 Module[{PProjList, QProjList, PLength, QLength,
   result, Eni, Enj, OffDiagOp, Pidx, Qidx},
  PProjList = PList /. {ket_ -> nc[ket, conj[ket]]};
  QProjList = QList /. {ket_ -> nc[ket, conj[ket]]};
  PLength = Length[PList];
  QLength = Length[QList];
  result = 0;
  OffDiagOp = OffDiagSuperOp[Op, PList, QList];
  For[Pidx = 1, Pidx <= PLength, Pidx++,
   For[Qidx = 1, Qidx <= QLength, Qidx++,
     Eni = nc[conj[PList[[Pidx]]], H0, PList[[Pidx]]];
     Enj = nc[conj[QList[[Qidx]]], H0, QList[[Qidx]]];
     result += Map[nc[PProjList[[Pidx]], #, QProjList[[Qidx]]]
         /(Eni - Enj) &, OffDiagOp];
     result += Map[nc[QProjList[[Qidx]], #, PProjList[[Pidx]]]
         /(Enj - Eni) &, OffDiagOp];
     ];
   ];
  Return[result]
  ]
```

Below we define functions that assist in performing the sum in Eq. (A.15), in particular utilizing the

algorithm presented in Ref. [158] for generating all possible vectors of length $k$ with non-negative entries that sum to $m$. The entries in each vector returned, e.g., by GenerateNextPartition specify the perturbative order of the generator at each position in a product of generators. For instance, the vector $[1, 1, 2]$ corresponds to the product $S_1 S_1 S_2$.

```
GenerateNextPartition[PrevVec_] :=
 Module[{NN, VecLength, NextVec, idx, updateidx},
  NN = Total[PrevVec];
  VecLength = Length[PrevVec];
  updateidx = 0;
  For[idx = VecLength - 1, idx >= 1, idx = idx - 1,
   If[PrevVec[[idx]] != 0,
     updateidx = idx;
     Break[];
     ];
   ];
  NextVec = Table[0, VecLength];
  NextVec[[1 ;; updateidx - 1]] = PrevVec[[1 ;; updateidx - 1]];
  NextVec[[updateidx]] = PrevVec[[updateidx]] - 1;
  NextVec[[updateidx + 1]] = NN - Total[NextVec[[1 ;; updateidx]]];
  Return[NextVec]
  ]
GenerateAllPartitions[k_, m_] :=
 Module[{InitialVec, AllPartitions, PrevVec, NextVec},
  InitialVec = Table[0, k];
  InitialVec[[1]] = m;
  AllPartitions = {InitialVec};
  PrevVec = InitialVec;
  While[PrevVec[[k]] != m,
   NextVec = GenerateNextPartition[PrevVec];
   AllPartitions = Append[AllPartitions, NextVec];
   PrevVec = NextVec;
   ];
  Return[AllPartitions]
  ]
GeneratorSum[H0_, VOp_, Seed_, k_, m_, PList_, QList_] :=
 Module[{AllPartitions, NumPartitions, GenList, NestedCommResult,
   result, genidx, partidx, CurrentPartition, Sgenidx},
  AllPartitions = GenerateAllPartitions[k, m];
  NumPartitions = Length[AllPartitions];
  result = 0;
  For[partidx = 1, partidx <= NumPartitions, partidx++,
   GenList = {};
   CurrentPartition = AllPartitions[[partidx]];
   (* vectors with any entries that are zero do not contribute *)
   If[Not[AnyTrue[CurrentPartition, PossibleZeroQ]],
    For[genidx = 1, genidx <= k, genidx++,
     Sgenidx = ComputeGenerator[CurrentPartition[[genidx]],
       H0, VOp, PList, QList];
     GenList = Append[GenList, Sgenidx]
```

```
    ];
   NestedCommResult = Seed;
   For[genidx = k, genidx >= 1, genidx = genidx - 1,
    NestedCommResult =
      commutator[GenList[[genidx]], NestedCommResult];
    ];
   result += NestedCommResult;
   ];
  ];
 Return[result]
 ]
```

We define the relevant Taylor coefficients

```
amCoeff[m_] := (2^m BernoulliB[m])/m!
b2nminus1Coeff[n_] := (2*(2^(2*n) - 1) BernoulliB[2*n])/(2*n)!
```

Putting everything together, we define the recursive functions for computing the generator and effective Hamiltonian at each order

```
ComputeGenerator[n_, H0_, V_, PList_, QList_] :=
 Module[{S1, S2, Snm1, Sn, Vd, Vod, j, GenSum},
  If[n == 0,
    Return[0],
    If[n == 1,
      Return[LSuperOperator[V, H0, PList, QList]],
      If[n == 2,
        S1 = ComputeGenerator[1, H0, V, PList, QList];
        Vd = DiagSuperOp[V, PList, QList];
        S2 = -LSuperOperator[commutator[Vd, S1], H0, PList, QList];
        Return[S2],
        (* n>=3 *)
        Vd = DiagSuperOp[V, PList, QList];
        Vod = OffDiagSuperOp[V, PList, QList];
        Snm1 = ComputeGenerator[n - 1, H0, V, PList, QList];
        Sn = -LSuperOperator[commutator[Vd, Snm1], H0, PList, QList];
        For[j = 1, 2*j <= n - 1, j++,
         GenSum = GeneratorSum[H0, V, Vod, 2*j, n - 1, PList, QList];
         Sn += amCoeff[2*j]*LSuperOperator[GenSum, H0, PList, QList];
         ];
        Return[Sn]
        ];
      ];
    ];
  ]
ComputeEffectiveHamiltonian[n_, H0_, VOp_, PList_, QList_] :=
 Module[{result, OffDVOp, gensum, j},
  If[n == 0,
    Return[MatrixElementOverListsProj[H0, PList, PList]],
    If[n == 1,
      Return[MatrixElementOverListsProj[VOp, PList, PList]],
```

```
      result = 0;
      OffDVOp = OffDiagSuperOp[VOp, PList, QList];
      For[j = 1, 2*j <= n, j++,
       gensum =
        GeneratorSum[H0, VOp, OffDVOp, 2*j - 1, n - 1, PList, QList];
       result +=
        b2nminus1Coeff[j]*
         MatrixElementOverListsProj[gensum, PList, PList];
       ];
      Return[result]
      ];
    ];
  ]
```

### A.2.1 Example: transmon coupled to a resonator

The Hamiltonian of the coupled system of a transmon and a resonator is $H = H_0 + V$ where [38]

$$H_0 = \sum_j Eq_j \, |j\rangle\langle j| + Er \, a^\dagger a, \quad V = \sum_j g_{j,j+1} |j\rangle\langle j+1| a^\dagger + \text{H.c.} \tag{A.20}$$

We have defined the energy of the $j^{\text{th}}$ excitation of the transmon $Eq_j$, the energy of the resonator $Er$ and the coupling coefficients $g_{i,j}$. We utilize slightly nonstandard notation here for ease of comparison with the software implementation. This Hamiltonian is implemented in Mathematica ® code as

```
Pij[i_, j_] := nc[ket[i, j], bra[i, j]]
dimtmon = 4;
dimres = 4;
Evalsq = Flatten[Table[Subscript[Eq, i], {i, 0, dimtmon - 1}]];
gijs = Flatten[
   Table[ToExpression[StringJoin["g", ToString[i], ToString[j]]],
   {i, 0, dimtmon - 1}, {j, 0, dimtmon - 1}]];
Do[snegrealconstants[Evalsq[[i]]], {i, 1, Length[Evalsq]}]
snegrealconstants[Er]
Do[snegrealconstants[gijs[[i]]], {i, 1, Length[gijs]}]
H0 = Sum[(Evalsq[[i + 1]] + j Er)*Pij[i, j],
{i, 0, dimtmon - 1}, {j, 0, dimres - 1}];
aop = Sum[Sqrt[nocc + 1] nc[ket[Null, nocc],
bra[Null, nocc + 1]], {nocc, 0, dimres - 2}];
tmonplus = Sum[ToExpression[StringJoin["g", ToString[i + 1], ToString[i]]]*
    nc[ket[i + 1, Null], bra[i, Null]], {i, 0, dimtmon - 2}];
Vop = nc[tmonplus, aop] + conj[nc[tmonplus, aop]];
```

To carry out the Schreiffer-Wolff transformation we define the low- and high-energy subspaces. In this case, it is appropriate to treat each state as its own subspace. As an example we consider the case where the low-energy subspace is defined by the state $|j,n\rangle = |1,2\rangle$, where $j$ is the number of transmon excitations and $n$ is the number of resonator excitations. The "high-energy" subspace is then spanned by all the other states (of course, some states in this subspace are lower in energy than the state $|1,2\rangle$: this presents no issue, as the only requirement for carrying out the transformation is that there be a sufficiently large energy gap). The following code computes the second-order effective Hamiltonian in the low-energy subspace

```
In[1]:= PList = {ket[1, 2]};
        QSum = Sum[ket[i, nocc], {i, 0, dimtmon}, {nocc, 0, dimres}] -
           PList[[1]];
        QList = List @@ QSum;
        EffHam2 = ComputeEffectiveHamiltonian[2, H0, Vop, PList, QList];
        Collect[EffHam2, {g10^2, g21^2}]
```

Out[1]= $\left(-\frac{3g10^2}{Er+Eq_0-Eq_1}+\frac{2g21^2}{Er+Eq_1-Eq_2}\right)|1\times2\rangle\cdot\langle1\times2|$,

where, e.g., $|1\times2\rangle$ is the SNEG notation for $|1,2\rangle$. This result agrees with those known in the literature [14, 38, 190]. The fourth-order effective Hamiltonian is likewise straightforward to compute (the third-order term vanishes)

```
In[2]:= EffHam4 = ComputeEffectiveHamiltonian[4, H0, Vop, PList, QList];
        Simplify[Collect[EffHam4, { g21^2 g32^2, g10^4, g21^4, g10^2 g21^2}]]
```

Out[2]= $|1\times2\rangle\cdot\langle1\times2|\left(\frac{9g10^4}{(Er+Eq_0-Eq_1)^3}+\frac{6g10^2g21^2(Eq_0-2Eq_1+Eq_2)}{(Er+Eq_0-Eq_1)^2(Er+Eq_1-Eq_2)^2}+\frac{2g21^2\left(-2g21^2+\frac{g32^2(Er+Eq_1-Eq_2)}{2Er+Eq_1-Eq_3}\right)}{(Er+Eq_1-Eq_2)^3}\right)$.

Finally, to demonstrate the power of the symbolic method, we compute the sixth-order effective Hamiltonian term

```
In[3]:= EffHam6 = ComputeEffectiveHamiltonian[6, H0, Vop, PList, QList];
        Simplify[
         Collect[
          EffHam6, { g21^3 g32^3, g21^2 g32^2 g10^2, g10^6, g21^6,
           g10^2 g21^4, g32^2 g21^4, g10^4 g21^2}]]
```

Out[3]= $2|1\times2\rangle\cdot\langle1\times2|\left(-\frac{27g10^6}{(Er+Eq_0-Eq_1)^5}+\frac{9g10^4g21^2(2Er^2+Eq_0^2+6Eq_1^2+4Er(Eq_1-Eq_2)-8Eq_1Eq_2+3Eq_2^2+Eq_0(-4Eq_1+2Eq_2))}{(Er+Eq_0-Eq_1)^4(Er+Eq_1-Eq_2)^3}+\frac{3g10^2g21^2}{(Er+Eq_0-Eq_1)^3(Er+Eq_1-Eq_2)^4}\left(-6g21^2(Er+Eq_0-Eq_1)^2+4g21^2(Er+Eq_0-Eq_1)(Er+Eq_1-Eq_2)-2g21^2(Er+Eq_1-Eq_2)^2+\frac{g32^2(Er+Eq_0-Eq_1)^2(Er+Eq_1-Eq_2)^2}{(2Er+Eq_1-Eq_3)^2}+\right.\right.$

$$\frac{2g32^2(Er+Eq_0-Eq_1)^2(Er+Eq_1-Eq_2)}{2Er+Eq_1-Eq_3} - \frac{g32^2(Er+Eq_0-Eq_1)(Er+Eq_1-Eq_2)^2}{2Er+Eq_1-Eq_3}\Big) + \frac{-2g21^4g32^2+g21^2g32^4}{(Er+Eq_1-Eq_2)^3(2Er+Eq_1-Eq_3)^2} + \frac{-6g21^4g32^2(Er+Eq_1-Eq_2)+8g21^6(2Er+Eq_1-Eq_3)}{(Er+Eq_1-Eq_2)^5(2Er+Eq_1-Eq_3)}\Big).$$

### A.2.2 Example: two qubits coupled to a resonator

We now apply the Schrieffer-Wolff transformation to the example of two qubits that are each individually coupled to a resonator, but not directly coupled to each other. The Hamiltonian is $H = H_0 + V$, where

$$H_0 = -\frac{Eq_a}{2}\sigma_z^a - \frac{Eq_b}{2}\sigma_z^b + Era^\dagger a, \quad V = gq_a\,\sigma_+^a a + gq_b\,\sigma_+^b a + \text{H.c.} \tag{A.21}$$

We implement this Hamiltonian in Mathematica ® code as

```
Pij[i_, j_, k_] := nc[ket[i, j, k], bra[i, j, k]]
dimres = 5;
snegrealconstants[Eqa, Eqb, Er, gqa, gqb];
H0 = Sum[(-Eqa/2 (-1)^i + -Eqb/2 (-1)^j + k Er) Pij[i, j, k], {i, 0,
    1}, {j, 0, 1}, {k, 0, dimres - 1}];
aop = Sum[
   Sqrt[nocc + 1]
     nc[ket[Null, Null, nocc], bra[Null, Null, nocc + 1]], {nocc, 0,
    dimres - 2}];
q1plus = gqa Sum[nc[ket[1, j, Null], bra[0, j, Null]], {j, 0, 1}];
q2plus = gqb Sum[nc[ket[i, 1, Null], bra[i, 0, Null]], {i, 0, 1}];
Vop = nc[q1plus, aop] + nc[q2plus, aop] +
   conj[nc[q1plus, aop] + nc[q2plus, aop]];
```

We consider the case where the qubits are near resonant, such that the states $|0,1,n\rangle, |1,0,n\rangle$ are approximately degenerate. The indices correspond to the number of excitations in qubit $a$, qubit $b$, and the resonator. As such the low-energy subspace now contains multiple states

```
PList = {ket[0, 1, 2], ket[1, 0, 2]};
QSum = Sum[ket[i, j, k], {i, 0, 1}, {j, 0, 1}, {k, 0, dimres - 1}] -
   Total[PList];
QList = List @@ QSum;
```

The second-order effective Hamiltonian is

```
In[4]:= EffHam2 = FullSimplify[ComputeEffectiveHamiltonian[2, H0, Vop, PList, QList]]
```

Out[4]= $\left(\frac{-2\text{gqa}^2}{\text{Eqa}-\text{Er}}+\frac{3\text{gqb}^2}{\text{Eqb}-\text{Er}}\right)|0\times1\times2\rangle\cdot\langle0\times1\times2|+\frac{\text{Eqa}+\text{Eqb}-2\text{Er}}{2(\text{Eqa}-\text{Er})(\text{Eqb}-\text{Er})}\text{gqa gqb}(|0\times1\times2\rangle\cdot\langle1\times0\times2|+$
$|1\times0\times2\rangle\cdot\langle0\times1\times2|)+\left(\frac{3\text{gqa}^2}{\text{Eqa}-\text{Er}}+\frac{-2\text{gqb}^2}{\text{Eqb}-\text{Er}}\right)|1\times0\times2\rangle\cdot\langle1\times0\times2|$

This reproduces the known result [15, 212].

# B Analytical inverse of the current-mirror capacitance matrix

*This chapter is based on material published in D. K. Weiss et al., Phys. Rev. B* **100***, 224507 (2019) (Editor's Suggestion).*

To obtain analytical expressions for the inverse capacitance matrix of the current-mirror circuit, we first write the capacitance matrix in the $\pm$ coordinates, ordered by exciton variables followed by agiton variables. In these coordinates and with this ordering, the capacitance matrix $\mathsf{C}$ [Eq. (5.2)] is block diagonal

$$\widetilde{\mathsf{C}} = \begin{pmatrix} \mathsf{C}_- & 0 \\ 0 & \mathsf{C}_+ \end{pmatrix}, \tag{B.1}$$

where

$$\mathsf{C}_\pm = \frac{C_J}{2} \begin{pmatrix} x_\pm & -1 & & & \mp 1 \\ -1 & \ddots & \ddots & & \\ & \ddots & \ddots & \ddots & \\ & & \ddots & \ddots & -1 \\ \mp 1 & & & -1 & x_\pm \end{pmatrix}, \tag{B.2}$$

defining $x_\pm = C_\pm / C_J$, $C_+ = C_g + 2C_J$ and $C_- = C_g + 2C_J + 2C_B$. The matrices $\mathsf{C}_\pm$ are symmetric, tridiagonal and Toeplitz. The matrix $\mathsf{C}_+$ is cyclic tridiagonal, and is readily inverted [213], while the anomalous corner elements in $\mathsf{C}_-$ require additional work [214]. One finds

$$(\mathsf{C}_\pm^{-1})_{j,k} = \frac{\mp U_{k-j-1}(x_\pm/2) - U_{N-k+j-1}(x_\pm/2)}{C_J[1 - T_N(x_\pm/2)]}, \tag{B.3}$$

where $T_n$, $U_n$ denote the Chebyshev polynomials of the first and second kind.

Based on these results, we determine asymptotic expressions for the charging-energy matrix elements

$$\left(\mathsf{E}_{\mathsf{C}}^{\pm}\right)_{j,k} = \frac{e^2}{2}(\mathsf{C}_{\pm}^{-1})_{j,k}, \tag{B.4}$$

associated with the agiton and exciton charges $n_j^{\pm}$. In the parameter regime of interest, capacitances follow the hierarchy $C_B \gg C_J > C_g$. Consequently, matrix elements of $\mathsf{E}_{\mathsf{C}}^{+} \sim 1/C_g, 1/C_J$ tend to be large compared to relevant elements of $\mathsf{E}_{\mathsf{C}}^{-} \sim 1/C_B$. Agiton charging energies are long-ranged, with maximum entries along the diagonal and monotonically decreasing towards minimum entries along the $N/2$-th off-diagonal. Asymptotic expressions for the diagonal, and the first and $N/2$-th off-diagonal are given by:

$$E_{C0}^{+} \equiv \left(\mathsf{E}_{\mathsf{C}}^{+}\right)_{j,j} = \frac{e^2}{NC_g}\left[1 + \frac{C_g(N^2-1)}{12C_J} + \mathcal{O}\left(\left\{\tfrac{C_g}{C_J}\right\}^2\right)\right], \tag{B.5}$$

$$E_{C1}^{+} \equiv \left(\mathsf{E}_{\mathsf{C}}^{+}\right)_{j,j\pm1} = \frac{e^2}{NC_g}\left[1 + \frac{C_g(N^2-6N+5)}{12C_J} + \mathcal{O}\left(\left\{\tfrac{C_g}{C_J}\right\}^2\right)\right], \tag{B.6}$$

and

$$E_{C\frac{N}{2}}^{+} \equiv (\mathsf{E}_{\mathsf{C}}^{+})_{j,j\pm\frac{N}{2}} = \frac{e^2}{NC_g}\left[1 - \frac{C_g}{24C_J}\left(N^2+2\right) + \mathcal{O}\left(\left\{\tfrac{C_g}{C_J}\right\}^2\right)\right]. \tag{B.7}$$

For excitons, charging energies are much shorter-ranged with off-diagonal elements decreasing rapidly in powers of $C_J/C_B$. The primarily relevant entries of $\mathsf{E}_{\mathsf{C}}^{-}$ are along the diagonal and first off-diagonal,

$$E_{C0}^{-} \equiv \left(\mathsf{E}_{\mathsf{C}}^{-}\right)_{j,j} = \frac{e^2}{2C_B} + \mathcal{O}\left(\tfrac{C_J}{C_B}, \tfrac{C_g}{C_B}\right), \tag{B.8}$$

$$E_{C1}^{-} \equiv \left(\mathsf{E}_{\mathsf{C}}^{-}\right)_{j,j\pm1} = \frac{e^2 C_J}{4C_B^2} + \mathcal{O}\left(\tfrac{C_J}{C_B}, \tfrac{C_g}{C_B}\right), \tag{B.9}$$

and anomalous corner elements $\left(\mathsf{E}_{\mathsf{C}}^{-}\right)_{1,N} = -E_{C1}^{-}$. These results help us understand the structure of the effective Hamiltonian and allow us to write down analytical expressions for the energies of

virtual intermediate states.

# C Open-system gate fidelity

In this appendix we provide a derivation of Eq. (7.65), for the gate fidelity of a noisy quantum operation:

$$F = \frac{d\,\mathrm{Tr}(\chi\chi_T) + \mathrm{Tr}(\chi)}{d+1}. \tag{C.1}$$

This equation is written in terms of the ideal and realized (either experimentally or numerically) process matrices, $\chi_T$ and $\chi$, respectively. The formula (7.65) is often quoted in this form in the literature [101, 174, 215], while derivations are often written instead in terms of a general quantum channel (completely positive, trace-preserving map) [205, 206] or a sum over Kraus operators [195]. Here, we provide an explicit link between Eq. (7.65) and the results of Refs. [195, 205, 206].

We take as our starting point Eq.(5) of Ref. [195], which gives the gate fidelity for a quantum channel $\mathcal{G}$ achieving the ideal unitary operation $U_0$

$$F = \frac{1}{d(d+1)}\left\{\mathrm{Tr}\left(\sum_k M_k^\dagger M\right) + \sum_k |\,\mathrm{Tr}(M_k)|^2\right\}. \tag{C.2}$$

Here, the quantum channel $\mathcal{G}(\rho)$ has been written in terms of a sum over Kraus operators $\mathcal{G}(\rho) = \sum_k G_k \rho G_k^\dagger$ [204] and the definition $M_k = U_0^\dagger G_k$ has been introduced. Note that the dimension of the relevant subspace is denoted as $d$ instead of $n$ as in Ref. [195] to connect to Eq. (7.65).

To obtain a fidelity formula that does not explicitly depend on the process-dependent Kraus operators $G_k$, we expand in a fixed basis of operators $G_k = \sum_m e_{km}\tilde{G}_m$ [204]. The $\tilde{G}_m$ are typically taken to be (tensor products of) Pauli operators [198]. Inserting this expansion of the Kraus

operators into Eq. (C.1) we obtain

$$F = \frac{1}{d(d+1)} \left\{ \mathsf{Tr}\left( \sum_k \sum_{m,n} e_{kn}^* e_{km} \tilde{G}_n^\dagger \tilde{G}_m \right) + \sum_k \left| \mathsf{Tr}\left( U_0^\dagger \sum_m e_{km} \tilde{G}_m \right) \right|^2 \right\}. \tag{C.3}$$

For the first term on the right-hand side, we obtain

$$\mathsf{Tr}\left( \sum_{m,n} \tilde{G}_n^\dagger \tilde{G}_m \sum_k e_{kn}^* e_{km} \right) = \mathsf{Tr}\left( \mathbb{1} \sum_n \chi_{nn} \right) = d \sum_n \chi_{nn} = d\, \mathsf{Tr}(\chi). \tag{C.4}$$

We have defined the process matrix $\chi_{mn} = \sum_k e_{km} e_{kn}^*$ [204] and the sum on $m$ yields a delta function $\delta_{m,n}$ because the $\tilde{G}_k$ form a basis. Additionally, $\mathbb{1}$ is the $d \times d$ identity matrix. For the second term in Eq. (C.3) we obtain

$$\begin{aligned} \sum_k \left| \mathsf{Tr}\left( U_0^\dagger \sum_m e_{km} \tilde{G}_m \right) \right|^2 &= \sum_k \mathsf{Tr}\left( \sum_m \sum_j e_{km}^* \tilde{G}_m^\dagger u_j \tilde{G}_j \right) \mathsf{Tr}\left( \sum_\ell \sum_i u_i^* \tilde{G}_i^\dagger e_{k\ell} \tilde{G}_\ell \right) \\ &= d^2 \sum_k \sum_{i,j} e_{kj}^* u_j u_i^* e_{ki} \\ &= d^2 \sum_{i,j} \chi_{ij} (\chi_T)_{ji} \\ &= d^2\, \mathsf{Tr}(\chi \chi_T), \end{aligned} \tag{C.5}$$

where we have decomposed the ideal unitary as $U_0 = \sum_j u_j \tilde{G}_j$ and defined the matrix elements of the target process matrix $(\chi_T)_{ij} = u_i u_j^*$. Altogether we find

$$F = \frac{d\, \mathsf{Tr}(\chi \chi_T) + \mathsf{Tr}(\chi)}{d+1}, \tag{C.6}$$

which is Eq. (7.65).